

Spray forming of tubular deposits with close-coupled atomizer (CCA)

Dem Fachbereich Produktionstechnik
der
UNIVERSITÄT BREMEN

zur Erlangung des Grades
Doktor der Ingenieurwissenschaften (Dr.-Ing.)
genehmigte

Dissertation
von
M.Sc. Shohag Hussain

Gutachter:

Prof. Dr.-Ing. habil. Udo Fritsching (Universität Bremen)

Prof. Dr. Claudemiro Bolfarini (Universidade Federal de São Carlos)

Tag der mündlichen Prüfung: 30.08.2022

Acknowledgements

This PhD thesis would not have been possible without the support of many people. First and foremost, I am extremely grateful to my supervisor, Prof. Dr.-Ing. habil. Udo Fritsching. His expertise was invaluable in formulating the research questions and methodology. He read my numerous revisions of the thesis and manuscripts for publications and helped make some sense of the confusion. His insightful feedback pushed me to sharpen my thinking and brought my work to a higher level. I would like to express gratitude to my thesis co-reviewer Prof. Dr. Claudemiro Bolfarini. Many thanks to him for the fruitful scientific discussion and suggestions for the improvement of my work. Additionally, I would like to thank to Prof. Dr.-Ing. habil. Lutz Mädler, who offered his guidance and support from the very beginning of my PhD. His worthwhile scientific discussions, advices and feedback when preparing research questions and manuscripts for publications greatly improved their readability, structure, and scientific argumentation.

Dr. Ing. Volker Uhlenwinkel has guided me during the entire PhD journey as my direct supervisor. I am truly thankful to him, without whom this work would have not been possible. He gave me the opportunity to work in his research group which is well equipped with modern atomization and spray forming facilities and measurement instruments. I always received his scientific and financial supports for the betterment of my research work. His knowledge and experience in the modern atomization and spray forming techniques shaped my knowledge and research work, as well as helped me a lot to refine my thesis topic. I always found him beside me as a guardian and a friend throughout the entire PhD journey.

I would like to acknowledge my colleagues Dr. Chengsong Cui, Lizoel Buss and Dandan Yao for their wonderful collaborations. I am very thankful to them for their help with the experiment and numerical simulation. Special thanks to Aline Weicht for her help with German translations. A big thank to the technicians Stefan Evers, Rainer Lehmann, Frank Peschel, and Horst Woyciechowski who helped me with the experimental setups. I thank to Martina Rickers and Silke Geißler for metallography, Perta Witte for the SEM images, Ellen Mattaei-Schulz for the nitrogen and oxygen content measurements, Mechthild Schröder for surface roughness measurements and Dr. Carsten Kykal for LDA measurements. I am also thankful to Andreas Flunker, Karl Siebels and their teams from the workshops.

I am thankful to the DFG and the project CRC 1232 "From colored states to evolutionary structural materials" for supporting me financially and personally throughout the entire journey. I am really grateful to all the members in the CRC 1232 for their support and collaborations. Special thanks to Dr.-Ing. Lydia Achelis for her guidance and support as graduate coordinator and also to Claudia Sobich for her communicational supports.

I would like to thank my friends, lab mates, colleagues and research team – Dr.-Ing. Nils Ellendt, Dr.-Ing. Nevaf Ciftci, Eric Gärtner, Farhad Mostaghimi, Erika Soares Barreto, Lucas Barcelos Otani, Saeedeh Imani Moqadam, Marcel Hesselmann, Anna Strauch, Dustin Schröder, Dr.-Ing. Ilya Okulov, Dr.-Ing. Norbert Riefler, Dr.-Ing. Matthias Steinbacher, Krischan Sandmann, Malte Stodt, Nithin Mohan Narayan and Dilyan Kamenov for a cherished time spent together in the lab, and in social settings. A big thank you goes to the students who contributed in this thesis: Nicole Temple, Md. Kamrujjaman, Rupanker Das and Sarah Armstrong.

I could not have completed this dissertation without the support of my friends and family who provided stimulating discussions as well as happy distractions to rest my mind outside of my research. Finally, I would like to thank my parents, my sisters and my beautiful wife for their wise counsel and sympathetic ear. You are always there for me with your unconditional trust and endless patience.

I dedicate this PhD thesis to my family.

Contents

Acknowledgements	A
Contents.....	I
Summary.....	III
Zusammenfassung	V
1 Introduction and Motivation	1
2 State of the Art	4
2.1 Spray forming process	4
2.1.1 Spray forming of tubular deposits	6
2.2 Atomization techniques	9
2.2.1 Particle size distribution.....	9
2.2.2 Atomizer design.....	11
2.2.3 Free-fall atomizer.....	11
2.2.4 Close-coupled atomizer.....	13
2.2.5 Hot gas atomization (CCA)	16
2.3 Porosity in spray forming process.....	19
2.3.1 Types of porosity	19
2.3.2 Influences on porosity in spray forming	20
2.3.3 Porosity and thermal behaviour of tubular deposits	28
2.4 In-situ measurement in the spray forming process	32
2.4.1 In-situ measurement techniques	32
2.4.2 Previous droplet studies in molten metal sprays	33
2.5 Summary of the State of the Art.....	36
3 Objectives and Outline of Thesis	37
4 Methodology and Experiments	41
4.1 Close-coupled atomizer for spray forming	42
4.1.1 Hot gas atomization.....	43
4.1.2 Powder production for particle size analysis.....	43
4.2 Materials selection.....	43
4.3 In-situ spray and deposit analysis	45
4.3.1 Deposit surface temperature.....	45
4.3.2 Substrate temperature.....	45

4.3.3	Particle velocity (LDA)	46
4.4	Ex-situ materials characterization	47
4.4.1	Surface roughness	48
4.4.2	Porosity analysis	49
4.4.3	Metallography	50
4.4.4	Powder characterization	51
5	Results and Discussion	53
5.1	Comparison of CCA with FFA	53
5.2	Optimizing process parameters for CCA	56
5.2.1	Microstructure and porosity analysis	56
5.2.2	In-situ temperature measurement	63
5.2.3	Temperature and process parameters	66
5.2.4	Grain size, deposit surface temperature, and GMR	70
5.2.5	Porosity and deposit surface temperature	71
5.2.6	Empirical model for maximum deposit surface temperature	73
5.3	Hot gas atomization	76
5.3.1	Spray condition	76
5.3.2	Particle size	78
5.3.3	Particle velocity and thermal conditions	82
5.3.4	Spray-formed deposits with hot gas atomization	89
5.4	Spray forming of Al alloys tubes	103
5.4.1	Spray forming setup and deposit	103
5.4.2	Porosity and process parameters	107
6	Conclusions and Outlook	113
6.1	Conclusion	113
6.2	Outlook	116
	Bibliography	118
	Appendix	131
	Symbols and Abbreviations	139
	Figures	144
	Tables	152
	List of Publications	154

Summary

The spray forming process is a rapid solidification process for production of metal preforms. In spray forming a superheated molten metal stream is atomized into small droplets by means of high-speed protective gas (e.g. N₂, Ar or He) jets. The atomized semi-solid particles are deposited on a substrate into “near-net-shape” deposit, depending on the demands, e.g. billet, plate, ring, tube, strips. The refined grain structure of the as-sprayed materials due to its high cooling rate ($10^3 - 10^6$ K/s) provides a better mechanical behaviour than materials via conventional ingot casting or powder metallurgy techniques. Intermetallic refinement and macro segregation free microstructure allow to produce numerous new or adapted alloys with specific alloying elements.

Spray forming of tubes may provide even faster cooling of the deposited materials compared to other forms like billets. This process can be used to produce coating on rods or tubes, clad tubes at a high production rate compared to other production techniques. In practice, spray-formed tubes or rings typically are produced by free-fall atomizers (FFA), which typically have low yield. In addition, the larger particles ($d_{50.3} = 100 - 200 \mu\text{m}$) of a FFA spray may induce high porosity in early stage of deposition. A recent study [ELLE14] showed that high yields and low porosities for small diameter tubes can be achieved with close-coupled atomizers (CCA).

The aim of this PhD thesis is to understand the effect of the process conditions and to develop a process route of spray-formed tubes by CCA. A central hypothesis is proposed that less porosity and increased yield can be achieved by higher impact velocities of the spray droplets in CCA spray. Based on the central hypothesis four working hypotheses are derived: i) the deposit porosity can be reduced by smaller droplets by a CCA, ii) the droplet velocity can be increased further by using hot gas atomization, iii) a decreased deformation time during impact will result in high density materials and will extend the process window, and iv) the developed knowledge is transferable to other alloy systems. Therefore, a CCA needs to be adopted for spray forming of tubes with a provision of using hot gas in order to achieve higher droplet velocities. In-situ temperature and particle velocity measurement should be introduced during the atomization process to support the process understanding and development.

As a result of the CCA adaptation, better porosity level have been achieved by smaller particles of a CCA compared to a FFA for AISI 52100 tubular deposits. However, high porosities are found at the deposit end positions due to lower melt mass flow rate and

shadowing effects by the rebound particles. The porosity increases in the vicinity of the substrate with increasing gas-to-melt ratio (GMR), where mostly cold porosities are found. In-situ deposit surface temperature measurements show that the maximum deposit surface temperature mainly depends on the deposit thickness compared to the *GMR*. The grain size in the as-sprayed materials also increases at higher maximum deposit surface temperatures. Comparison between porosity and the maximum deposit surface temperature reveal that the porosity increases with decreasing maximum deposit surface temperatures below the solidus temperature of the alloy. An empirical prediction model is derived to calculate the maximum deposit surface temperature that is validated with the experimental data for AISI 52100 steel. Furthermore, for transferring the acquired knowledge to other alloying systems a dimensionless parameter DTT (ratio of the maximum deposit surface temperature and solidus temperature) is introduced.

Introduction of hot gas atomization show that smaller particles with high velocity and low temperature can be produced at lower gas consumption by a CCA. With smaller particles sizes and higher velocities, the particles deformation time is lowered. The spray-formed tubes with hot gas atomization show less porosity even at lower deposit surface temperatures with hot gas atomization. The grain sizes also decrease due to lower maximum deposit surface temperatures. However, the microstructures of the as-sprayed materials show hardly any difference. Substrate preheating by the hot process gas lowers the porosity level in the vicinity of the substrate. Larger tube diameter result in additional cooling of the deposit and resulting lower maximum deposit surface temperature and smaller grain size. Comparison between the relative density at the deposit center and the maximum deposit surface temperature depicts that higher density can be achieved by hot gas atomization even well below the solidus temperature, which subsequently extended the process window of the spray forming of tubes. For cold gas a relative density > 0.95 is achieved at $1 < DTT < 1.13$ and for hot gas atomization at $0.85 < DTT < 1.13$.

Spray forming of Al-alloy tubes with CCA show similar materials quality like the steel tubes, suggesting that the knowledge from the spray forming of steel tubes is transferable to other alloy systems. Refined grain structures with nano-meter-sized intermetallic phases are observed. High amount of porosity is found in the vicinity of the substrate (about 20% of the deposit thickness). The DTT of the Al-alloys deposits are calculated with the proposed empirical model. A minimum porosity is found for $1.02 < DTT < 1.05$. However, the model needs to be validated with experimental data for Al-alloys.

Zusammenfassung

Das Sprühkompaktieren ist ein Herstellungsverfahren für metallische Halbzeuge, bei dem ein überhitzter Schmelzestrom mittels hohem Inertgaseintrag (z.B. N₂, Ar oder He) durch eine Düse in feine Tropfen zerstäubt wird. Je nach Anforderung an das zu fertigende Halbzeug, werden die zerstäubten und halberstarrten Partikel in einer endkonturnahen Form, beispielsweise als Bolzen, Scheibe, Ring, Rohr oder Blech, auf ein Trägersubstrat abgeschieden. Durch die hohen Abkühlraten dieses Prozesses ($10^3 - 10^6$ K/s), wird ein feineres Korngefüge als bei konventionellen Blockguss- oder Pulvermetallurgieverfahren erreicht. Die intermetallische Verfeinerung und das makroseigerungsfreie Gefüge verbessern das mechanische Verhalten des Materials und ermöglichen die Herstellung zahlreicher neuer oder angepasster Legierungen mit spezifischen Legierungselementen.

Das Sprühkompaktieren von Rohren ermöglicht eine noch schnellere Abkühlung des aufgetragenen Materials im Vergleich zu anderen Formen wie Bolzen oder Blöcken. Dadurch kann eine höhere Produktionsrate bei der Herstellung von Beschichtungen auf Stäben oder Rohren sowie von plattierten Rohren, gegenüber anderen Produktionsverfahren, erreicht werden. In der Praxis werden sprühgeformte Rohre oder Ringe in der Regel mit Freifallzerstäubern (FFA) hergestellt, die für gewöhnlich eine geringe Ausbeute haben. Darüber hinaus können die größeren Partikel ($d_{50,3} = 100 - 200 \mu\text{m}$) eines FFA-Sprays in der frühen Phase des Materialauftrages zu einer hohen Porosität führen. Eine kürzlich durchgeführte Studie [ELLE14] hat gezeigt, dass mit Close-Coupled Zerstäubern (CCA) eine hohe Ausbeute und geringe Porosität für Rohre mit kleinem Durchmesser erreicht werden kann.

Das Ziel dieser Dissertation ist, die Auswirkungen der Prozessbedingungen zu verstehen um einen geeigneten Prozessweg für die Herstellung von sprühkompaktierten Rohren mittels CCA zu entwickeln. Dabei lautet die zentrale Hypothese, dass eine geringere Porosität und eine höhere Ausbeute durch höhere Aufprallgeschwindigkeiten der zerstäubten Tropfen auf dem Substrat bei der CCA-Zerstäubung erreicht werden können. Ausgehend von der zentralen Hypothese werden vier Arbeitshypothesen abgeleitet: i) die Porosität des kompaktierten Werkstoffs kann aufgrund der kleineren Tropfen durch den CCA verringert werden, ii) die Tropfengeschwindigkeit kann mittels Heißgaszerstäubung weiter erhöht werden, iii) eine verringerte Verformungszeit während des Aufpralls führt zu Werkstoffen mit hoher Dichte und vergrößert das Prozessfenster, und iv) die erworbenen

Erkenntnisse sind auf andere Legierungssysteme übertragbar. Hierfür wird ein CCA für das Spritzgießen von Rohren unter Verwendung von Heißgas entwickelt, um so die Tropfengeschwindigkeiten zu erhöhen. Zum Verständnis und zur Weiterentwicklung des Prozesses sollen während der Zerstäubung In-situ-Messungen der Temperatur und Partikelgeschwindigkeit durchgeführt werden.

Durch die Anpassung des Zerstäubers konnte bei sprühkompaktierten AISI 52100-Rohren eine geringere Porosität durch kleinere Partikel, aufgrund der Nutzung eines CCA im Vergleich zum FFA, erreicht werden. Allerdings ist die Porosität an den Endpositionen des kompaktierten Halbzeugs, aufgrund des geringeren Schmelzmassenstroms und der Abschattung durch die Rückprallpartikel, höher. Mit zunehmendem Verhältnis von Gas- zu Schmelzmassenstrom (GMR) steigt die Porosität in Substratnähe, wo hauptsächlich kalte Porositäten auftreten. In-situ-Messungen der Oberflächentemperatur des Werkstücks zeigen, dass die maximale Temperatur hauptsächlich von der Dicke des aufgetragenen Materials abhängt, verglichen mit dem GMR. Bei einer hohen maximalen Oberflächentemperaturen des Materialauftrages nimmt die Korngröße des sprühkompaktierten Stahls zu. Bei niedrigen maximalen Oberflächentemperaturen des Materialauftrages unterhalb der Solidustemperatur, steigt die Porosität. Es wurde ein empirisches Modell zur Berechnung der maximalen Oberflächentemperaturen des Materialauftrages abgeleitet, welches mit den experimentellen Daten für AISI 52100 Stahl validiert wurde. Zur Übertragung der gewonnenen Erkenntnisse auf andere Legierungssysteme, wurde ein dimensionsloser Parameter DTT (Verhältnis zwischen der maximalen Oberflächentemperaturen des Materialauftrages und der Solidustemperatur) eingeführt.

Die Nutzung von Heißgas bei der CCA-Zerstäubung führt zu kleineren Partikeln mit höheren Geschwindigkeiten und niedrigeren Temperaturen, sowie zu einer Reduktion des Gasverbrauchs. Kleine Partikelgrößen und hohe Geschwindigkeiten verringern die Deformationszeit der Partikel. Die mit heißem Zerstäubergas sprühkompaktierten Rohre weisen, selbst bei niedrigen maximalen Oberflächentemperaturen des Materialauftrages, nur eine geringe Porosität auf. Aufgrund geringerer maximaler Oberflächentemperaturen nimmt auch die Korngröße ab. Allerdings zeigt die Mikrostruktur des kompaktierten Materials kaum einen Unterschied. In Kombination mit dem heißen Zerstäubergas, reduziert das Vorheizen des Substrats die Porosität des aufgetragenen Materials in Substratnähe. Größere Rohrdurchmesser führen zu einer zusätzlichen Abkühlung des

aufgetragenen Materials und damit zu einer niedrigeren maximalen Oberflächentemperatur und einer kleineren Korngröße. Durch die Zerstäubung mittels Heißgas kann auch weit unter der Solidustemperatur eine höhere Dichte des Werkstücks erreicht werden, wodurch sich das Prozessfenster für zum Sprühkompaktieren von Rohren vergrößert. Bei der Zerstäubung mittels Kaltgas wurde eine relative Dichte $> 0,95$ bei $1 < DTT < 1,13$ nachgewiesen und für die Heißgas-Zerstäubung bei $0,85 < DTT < 1,13$.

Die mit der zuvor genutzten Stahllegierung vergleichbare Werkstoffqualität von sprühkompaktierten Aluminiumrohren deutet auf eine Übertragbarkeit auf andere Legierungssysteme hin. Es wurden feine Kornstrukturen mit intermetallischen Phasen in Nanometergröße beobachtet. Weiterhin wurde eine hohe Porosität in der Nähe des Substrats festgestellt (etwa 20 % der Schichtdicke). Die DTT der Al-Legierungen wurden mit dem entwickelten empirischen Modell berechnet und es wurde eine minimale Porosität für $1,02 < DTT < 1,05$ ermittelt. Das Modell muss jedoch noch mit experimentellen Daten für Al-Legierungen validiert werden.

1 Introduction and Motivation

*“All material Things seem to have been composed
of the hard and solid Particles”*

— Sir Isaac Newton¹

The modern civilization has been created by an intelligent technical use of materials from the nature. The human prehistory is divided based on the use of materials by each of the generations (Stone Age, Bronze Age, Iron Age) [McCL06]. The use of metallic materials started at about 3300 BC from the Bronze Age of the human prehistory. The Iron Age is based on use of iron as a fundamental element of the development. The industrial revolution in the early eighteenth century promoted the modern age where metallic materials are being used in multiple technical applications, from tiny mobile devices to larger space-crafts.

In the classical metallurgy, metallic materials are extracted from ores or recycled and processed through conventional casting techniques. In a conventional casting process the molten metals or alloys typically solidify slowly. With the state-of-the-art of modern materials engineering, a spectrum of new alloys has been developed with advanced qualities. Economic reasons also drove the need of new materials for the rapidly growing industries. In addition, the use of potentially health hazardous alloying elements like lead, cadmium or arsenic is increasingly restricted by law, so that other alloy systems are required to meet the desired properties. However, the conventional casting method can not handle the production of numerous newly developed alloys due to its slow solidification kinetics. Macro-segregation in the bulk materials is one of the main drawbacks of conventional casting. In the mid of last century new techniques have been developed in the metal working industry to overcome these challenges, for instance the “rapid solidification” processes [KLEM60].

Solidification means formation of a solid with or without chemical reactions from a gaseous (vapor) or liquid (melt) parent material. The solidification can be either slow or rapid. “Rapid solidification” is normally relevant for fast melt solidification (e.g., metals) [ASHB83]. The term “rapid” can be attributed to as a short-time interval between initiation and completion of solidification and a high velocity of propagation of the advancing solidification front

¹ From Optics (1704, 2nd ed., 1718), 377-378.

[JOHN10]. Such rapid solidification is induced by forcing a high cooling rate (e.g. $> 10^4$ K/s) during solidification [LAVE10]. The commonly practiced rapid solidification techniques for metal melts are melt-atomization, spray forming or spray-deposition, splat-quenching, melt-spinning etc. [SCHM79, ASHB83, LAVE10, JOHN10]. The melt-atomization process is a long-established technology, where a drop or melt-stream tends to break up into droplets by impinging of high velocity jets of a second fluid (e.g., a stream of inert gas or water jet) [SING70, SCHM79]. The spray forming process has been introduced nearly half a century ago in metal forming [SING70], where the melt-atomization technique has been used to form “near-net-shape” deposits with advanced material properties [SING83, GRAN95, LI99].

“Near-net-shape” processing is an established process route of the Materials Science and Engineering community, which may reduce the production steps and subsequent waste of materials and energy. The routes of near-net-shape processing are considered to be green or sustainable process [HENE17]. Usually specific gas atomizers are used for the spray forming process [GRAN95; LI99] that provide the flexibility to move the spray by scanning the nozzle. This option allows the process to achieve different deposit shapes (e.g. billet, plate, ring, tube, strips). The refined grain structure of the as-sprayed materials provides a better mechanical behavior than materials via conventional ingot casting or powder metallurgy techniques [LIU17; SPRI17]. Intermetallic refinement and macro segregation free microstructure allow to produce numerous new or adapted alloys with specific alloying elements [ELLE10b].

Spray forming of tubular deposits provides faster cooling of the as-sprayed materials compared to other forms i.e. billets. The process may open a new approach for flexible production of clad tubes in high temperature applications like heat exchangers [LAWL98; LEE18], wear and corrosion resistant bi-metallic pipes in drilling [ZEPO16], or would provide a faster coating technology. However, spray-formed tubular deposits have been hardly used on an industrial scale up to now due to insufficient deposit quality in terms of porosity and bonding to the substrate. Usually, spray-forming of tubes or rings is achieved by free-fall atomizers (FFA). The FFA sprayed deposits exhibit high porosity in the vicinity of the substrate and at the outer surface area [BUCH03; CUI04; CUI05]. The large droplets size from a free-fall atomizer (typically 100 – 200 μm) [FRIT05] may be the reason for the higher deposit porosities. In contrast, high yields and low porosities for small diameter tubes have been achieved with close-coupled atomizers (CCA) [ELLE14]. Small amounts of sample for research and development applications can be produced (Figure 1-1). CCAs are very robust

and often used under industrial conditions, which makes this process interesting for future developments.



Figure 1-1: Samples from spray-formed steel tube produced by a close-coupled atomizer.

The reason for the higher yield in spray forming with close-coupled atomizers is unclear yet. It is suspected that increased impact particle velocities increase the yield. The finer droplets from a close-coupled atomizer would be suitable for producing high density material. The faster droplet cooling rate achieved by CCA [CIFT19] may affect the deformation mechanism of the impinging droplets in the deposition area, which may provide different material properties, i.e. better splats with lower porosity [CHAN09]. In addition, the spray of a close-coupled atomizer is much tighter compared to a free-fall atomizer [ANDE17], making it more suitable for surface coating and cladding with less overspray. With regard to the smaller particles in a CCA spray, it should be mentioned that the introduction of hot atomization gas further reduces the particle size [ANDE02, ANDE17] at lower energy consumption [DOPL21]. The hot gas atomization has been recently introduced for particle production and needs yet to be used in the spray forming process.

Detailed investigations are needed in spray forming with CCA in order to provide more insight knowledge and better understanding of the process. The aim of this thesis is to introduce close-coupled atomizers utilizing hot gas for the spray forming process in order to produce dense tubes and extend the process window in the spray forming process. Transferability of the achieved knowledge for spray forming alloys based on steel and Al-alloys will be investigated.

2 State of the Art

2.1 Spray forming process

Spray forming is also known as “spray casting” or “spray deposition”, which was first proposed by Singer (Swansea University, Wales, UK) in the early 1970s. Initially the technology had been given the name Osprey Process [SING70]. The process can take into account the solidification conditions of the material between conventional casting and powder metallurgy [GRAN95, LI99, SING83, ELLE10b, LACH11]. In the spray forming process a molten metal or alloy stream is atomized by means of high speed gas jets and the sprayed droplets are collected on a substrate [LI99, LAVE10, LAVE96]. Usually the melting process is carried out in a protective environment, typically achieved by continuously supplying the melting chamber with N₂, Ar or He [CAI97, MI08a, HENE17]. During atomization, in the generated spray a broad spectrum of the generated droplets (size distribution app. 5 – 500 µm) reach the substrate with a velocity in a range of app. 70–140 m/s [TILL99, KHAT17]. The droplets characteristics typically depend on the material, the gas-to-melt-mass flow ratio (GMR), and the velocity of the inert gas in the atomization area. Depending on the droplet size, its thermo-physical properties and trajectory, the droplets in the spray are in three states during deposition; solidified, partially solidified or liquid state [LAVE96, CANT97]. Spray forming is a rapid solidification process, where the cooling process can be divided into three phases, flight phase in the spray, impact and deformation phase at impingement and deposit cooling. During the flight and impact phase the cooling rate of the droplet is in the range $10^3 - 10^6$ K/s [MEYE12], which influences the microstructure formation in the solidification process. In contrast, the cooling rate after deposition has minor effect on the microstructure, which is in a range of $10^0 - 10^1$ K/s [GRAN95, HUSS20a]. A faster cooling leads to products with advanced materials properties [SCHU08, UHLE07]. From a microstructural point of view spray-formed materials show [LIAN93, HENE17, GRAN07]:

- I. refined equiaxed grains (10 – 100 µm)
- II. intermetallic refinements for high alloyed materials
- III. macro segregation free microstructure

The refined grain structure provides a better mechanical behavior than materials that have been produced via conventional ingot casting or powder metallurgy techniques [SIQU10, KIM05, LU16, SPRI17, HANL03]. Recently Lu et al. reported that spray-formed tool steels show better performance (tool life) than the steel manufactured via conventional ingot casting or powder metallurgy techniques [LU16]. Intermetallic refinement and macro segregation free microstructure open the processability of a new spectrum of alloys with advanced alloying elements [PAYN93, GRAN07]. Recently, a high modulus steel (FeTiB_2) was produced by spray forming, which shows microstructural features on a nanometric scale and better mechanical behavior than conventionally casted materials (see Figure 2-1) [SPRI17].

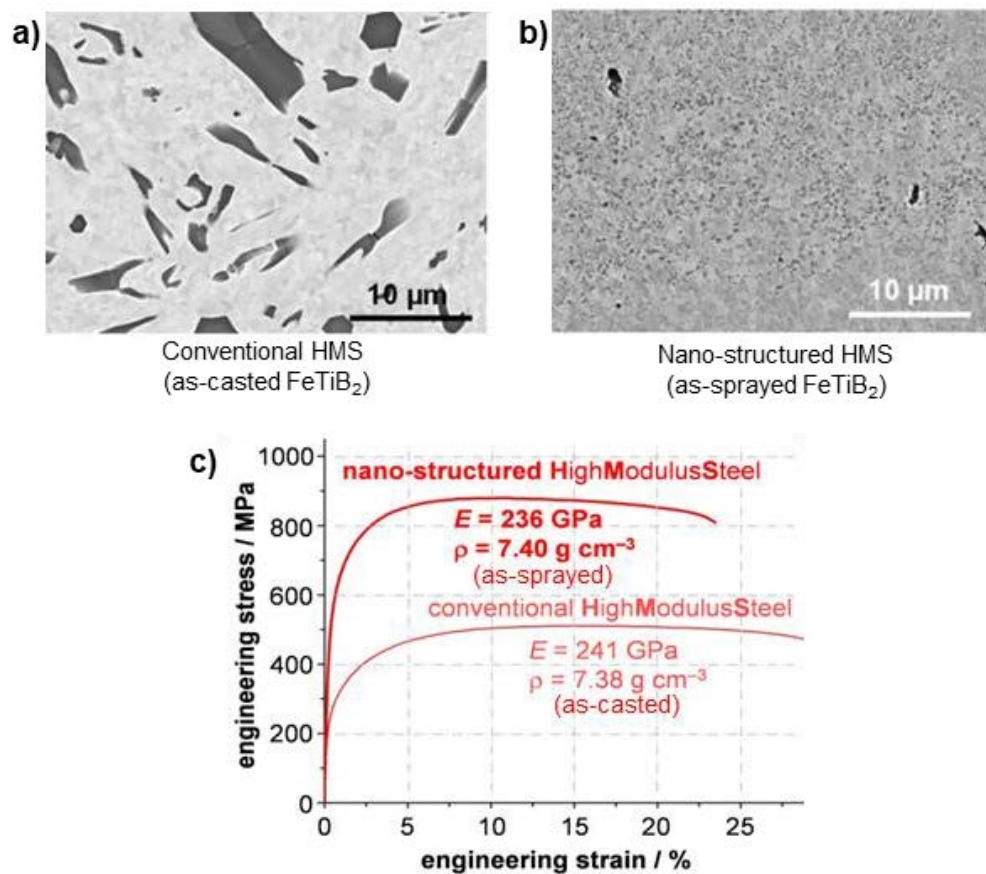


Figure 2-1: Comparison of conventional cast and spray-formed (rapidly solidified) FeTiB_2 (HMS = High Modulus Steel) a) microstructure as-casted, b) microstructure as-sprayed, and c) stress-strain curves. The figure is adopted from [SPRI17].

The cast material showed TiB_2 precipitates (dark gray) with dimensions up to approx. 10 μm . The spray-formed variant had a much finer microstructure with precipitates in the nanometer range. The finely distributed precipitates lead to a substantial improvement in

the mechanical properties. The tensile strength increased by approx. 60%, whereby the elongation at break decreases only insignificantly (Figure 2-1b). In addition, the modulus of elasticity reduced slightly. Spray forming provides better qualities also for other alloys, e.g. Al-alloys [ELLE07a, RAJU08, STEL06, CUI14], Cu-alloys [ELLE14, MÜLL01, MÜLL03, LIAN93].

Along with the better materials quality, spray forming also offer semi-finished or “near-net-shaped” products [LI99, GRAN07, GRAN95, HENE17]. Based on the spray and substrate movement a deposit in several shapes can be produced as for instance billets [MÜLL01, MÜLL03, ELLE04, CUI09, STEL06, YU13, SIQU10, CUI14], plates or strips [BRIN01, SAHU09, ACHE09], and tubes or rings [WARN97, CUI04, WALT05, ELLE14, SPRI17, BUCH03, ZEPO16].

2.1.1 Spray forming of tubular deposits

The spray forming process can be used to produce tubes or ring-shaped deposits [SING83]. Payne et al. first carried out some detailed investigations of spray-formed tubular deposits [PAYN93]. Spray-formed tubes may open a new production technique of clad tubes for heat exchangers [LAWL98]. This technique can also be used to generate thick layers of coatings on rods or tubes [CUI04, CUI05b]. By increasing the interfacial bonding between the substrate and the deposited material spray forming can also be used in surface coating [WAHL93, LEE18]. Recent investigations by Berger et al. have shown how thermal spraying is used for various protective coatings in layers smaller than 1 mm [BERG15]. The thermal spraying process uses a concentrated heat source to melt feedstock materials (powder, wire, rod) and the resulting molten droplets are ejected with high kinetic energies to the substrate surface [VUOR14]. Similar to the thermal spraying route, the spray forming process also allows the deposition of molten droplets onto a substrate. The ability to coat a substrate surface utilizing the melted feedstock materials directly on the coating surface is a major advantage of the spray forming process. The production rates achieved by spray forming are an order of magnitude faster compared to those using thermal spray techniques [MI08a, MI08b]. Figure 2-2 shows an experimental setup for spray forming of tubular deposits.

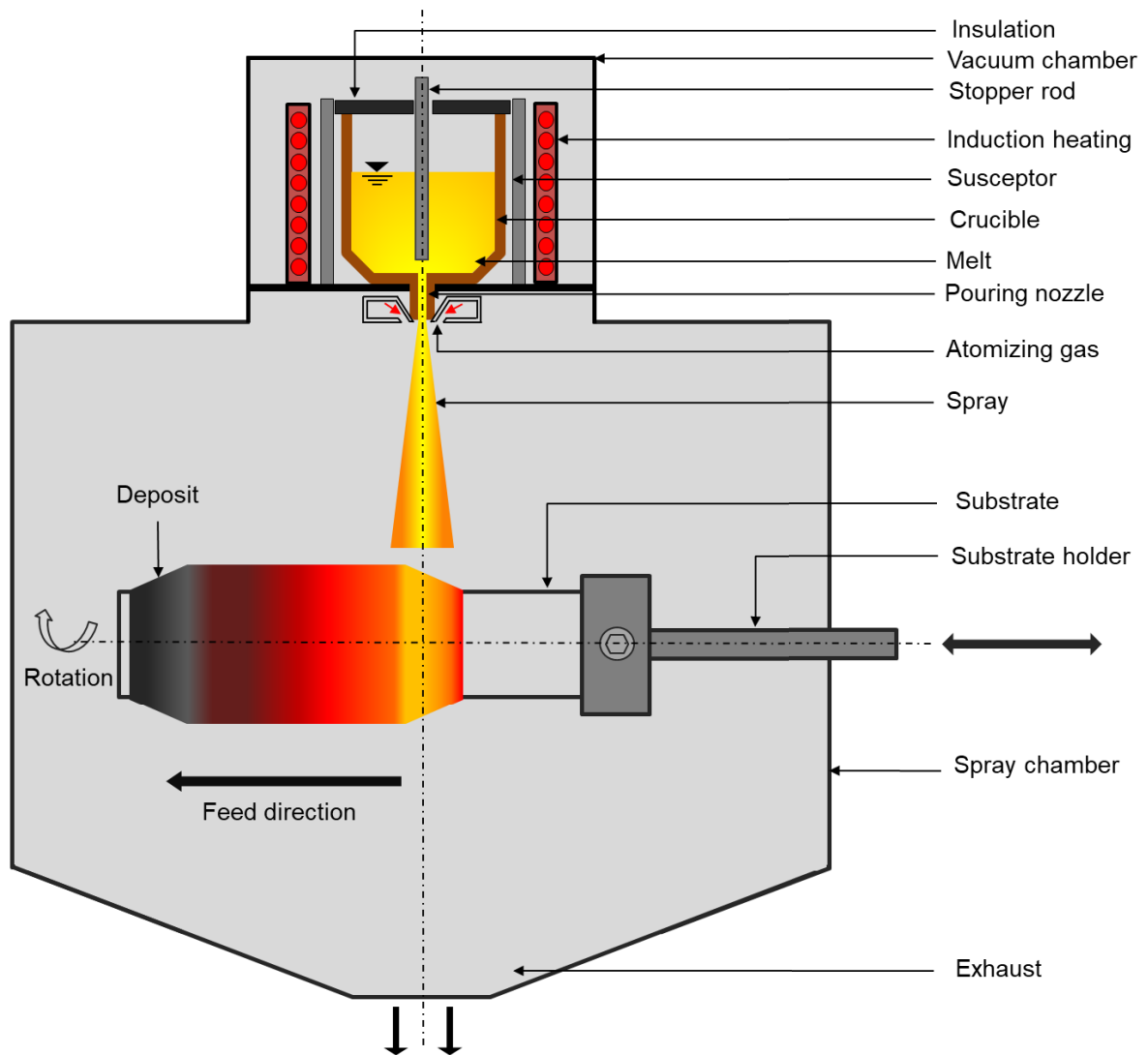


Figure 2-2: Schematic diagram of the spray forming set up (PA7 at University of Bremen) with a close-coupled atomizer for steel. The figure is adopted from [HUSS20a].

In spray forming, the feedstock material is melted and superheated (heated 50 – 250 °C above melting temperature) in a protective environment [SING83, CUI06], then fed into the pouring nozzle and atomized with high pressure jets of process gas by either free-fall atomizer (FFA) or close-coupled atomizer (CCA) (a brief description of the atomizers configuration is presented in the next section). The atomized droplets are collected on a rotating tubular substrate of similar material or dissimilar material, which is usually sandblasted to adhere the initial layers of the droplets [MI08c, CUI04, LEE18]. The thickness of the deposition layer can be controlled by varying the substrate transitional speed v_s or melt mass flow rate \dot{M}_L . Co-spray or twin-nozzle systems are also used for spray forming of thick [ALAN99] and bi-layer tubular deposits [ZEPO16].

In the spray forming process of tubular deposits, several process parameters play a vital role on the quality of the as-sprayed deposits. These process parameters are listed from previous literatures [MATH88, MATH91, GRAN95, HENE17, HENE17, ELLE10b, MEYE13, HUSS20a] and combined with the present study in Table 2-1.

Table 2-1 Process parameters in spray forming process of tubular deposits.

Parameters	Symbol	Unit	Remarks
Pouring temperature of melt	–	°C	Above 50 – 250 °C of melting temperature
Gas temperature	T_G	°C	Temperature of process gas in the atomizer nozzle
Feed stock mass	–	g	–
Pouring nozzle diameter	\varnothing_n	mm	Melt flow rate depends of that
Atomization gas	–	–	Gas mass flow rate varies with different gases (N ₂ , Ar, He)
Atomization gas pressure	p_G	MPa	Define the gas mass flow rate
Spray distance	z	mm	Influence the solid fraction and deposit surface temperature in the impingement zone
Substrate diameter	\varnothing_s	mm	Influence deposit cooling
Substrate wall thickness	S	mm	Influence deposit cooling
Transitional velocity of substrate	v_s	mm/s	Influence deposit thickness and cooling
Rotational speed of substrate	v_r	rps	Influences deposit surface temperature
Gas flow rate	\dot{M}_G	kg/h	–
Mean melt flow rate (feedstock mass/run time)	\dot{M}_L	kg/h	–
Gas-to-melt mass flow ratio	GMR	–	Vital parameter of deposit cooling
Deposit thickness	y	mm	Influence the deposit surface temperature
Deposit surface temperature	T_D	°C	Deposit temperature after droplet impingement
Substrate temperature	T_s	°C	Indicate the deposit cooling rate

2.2 Atomization techniques

Gas atomizers as for instance free-fall atomizers (FFA) are usually used for spray forming of tubes [MI08a, CUI04]. Close-coupled atomizers some times also are used for spray forming but are not common in practice [GRAN95]. As pointed out by Ellendt et al. the impulse atomization technique can also be used for spray forming of tubes and rings [ELLE04]. In this thesis the free-fall atomizer and the close-coupled atomizer have been considered for further investigations. In a gas atomization process the liquid melt stream is disintegrated energetically into micro-meter sized droplets by a second stream of fluid (high pressure process gas) [ZHEN11, ANDE17]. The superheated molten metal stream is forced through an orifice and is subsequently disintegrated into droplets by impingement of gas jets [ANTI13, CZIS08b, CZIS08]. Afterwards the droplets are accelerated and cooled down by the flow of process gas during the flight in the spray chamber. The mechanisms of melt disintegration, the design of the atomization devices, the thermal transport in atomized droplets, the characteristics of droplet/particle size, the size distribution will be discussed briefly next, as they define the material quality in the deposition zone. In the rest of this dissertation, the term droplet(s) or particle(s) will be used interchangeably to mean droplets that are liquid, semi-solid or fully solid. If a distinction is required this will be made clear.

2.2.1 Particle size distribution

The particles/droplets size distribution is an important parameter in the spray forming process, which defines the properties in the as-sprayed deposit such as liquid fraction, deformation behavior, microstructure etc. The principles of droplet formation and the most important empirical contributions to estimate the particle size as well as particle size distribution are presented in this section.

Liquid stream disintegration and droplet formation behavior have been studied experimentally as starting from [BIDO29, SAVA33] and theoretically as initially done in [RAYL78]. A theoretical description of a liquid stream disintegration process was presented by Weber in 1931 [WEBE31]. Weber stated that the disintegration process depends on the liquid stream velocity along with liquid properties such as surface tension, density, and viscosity. Because of this achievement the relationship between inertial force and surface

tension was named after him. The dimensionless liquid Weber number (We_l) is described as:

$$We_l = \frac{\rho_l \cdot u_l^2 \cdot D_l}{\sigma} \quad \text{Eq. 2-1}$$

where, ρ_l is the liquid density, u_l is the liquid stream velocity, D_l is the liquid stream diameter, and σ is the liquid surface tension. In a gaseous medium the gas or aerodynamic Weber number (We_g) is the decisive parameter, which is described as:

$$We_g = \frac{\rho_g \cdot u_{rel}^2 \cdot d_p}{\sigma} \quad \text{Eq. 2-2}$$

here, ρ_g is the gas density, u_{rel} is the relative velocity between the droplet and surrounding fluid, d_p is the droplet/particle diameter, and σ is the surface tension of the liquid melt. During gas atomization process, it is often assumed that $We_g > 10$ results in the disintegration of melt droplets [UHLE91]. Based on the Weber number numerous empirical correlations have been developed to estimate the droplet size during gas atomization. The empirical correlation by Lubanska [LUBA70] is the most commonly used correlation in gas atomization to predict the mass median particle diameter $d_{50.3}$:

$$\frac{d_{50.3}}{D_l} = K \left[\frac{\nu_l}{\nu_g} \frac{1}{We} \left(1 + \frac{\dot{M}_L}{\dot{M}_G} \right) \right]^{0.5} \quad \text{Eq. 2-3}$$

$$We = \frac{\rho_l \cdot u_{gl}^2 \cdot D_l}{\sigma} \quad \text{Eq. 2-4}$$

$$GMR = \frac{\dot{M}_G}{\dot{M}_L}. \quad \text{Eq. 2-5}$$

Eq. 2-3 consists of the ratio of liquid viscosity ν_l to the gas viscosity ν_g , the Weber number We as a function of liquid density ρ_l , liquid stream diameter D_l , gas velocity at impact with the liquid stream u_{gl} , liquid surface tension σ , as well as the mass flow ratio (the ratio of the gas mass flow rate \dot{M}_G and the melt mass flow rate \dot{M}_L , which is often abbreviated as GMR). K is an atomizer geometric constant, which typically ranges from 40 to 50 [LUBA70]. At a given atomizer dependent geometry and a fixed alloy the particle size distribution depends on the GMR, as a higher GMR leads to finer particles. The Lubanska correlation is often used in gas atomization studies. However, Uhlenwinkel reported that deviations between measurements and the Lubanska correlation up to 50 % are commonly found [UHLE91].

According to the Lubanska correlation (Eq. 2-3) the particle size also depends on the liquid stream diameter D_L , and the gas velocity at impact with the liquid stream u_{gl} . These two parameters determine the droplet break-up and influence the initial droplet cooling, dependent on the atomizer configuration. For the gas velocity in the atomization process, the atomizer (gas nozzle) design is of particular importance.

The particle size distribution in sprays may be estimated by a Rosin-Rammler-Sperling-Bennett (RRSB) function [ROSI33]. From a given particle size distribution the particle size distribution can be extrapolated for other atomization conditions with the following correlation [ELKO82]:

$$SMD = 51 \varnothing_n Re^{-0.39} We^{-0.18} \left(\frac{\dot{M}_L}{\dot{M}_G} \right)^{0.29} \quad \text{Eq. 2-6}$$

where, \varnothing_n is the pouring nozzle diameter, Re is the Reynolds number, We is the Weber number, and \dot{M}_L and \dot{M}_G are the melt mass flow rate and the gas mass flow rate, respectively.

2.2.2 Atomizer design

Two subdivisions can be introduced in atomizer design based on the opening of the gas nozzles [CZIS08b, ANDE17, LOHN03].

- a. **Annular or slit jet:** the gas exit is a continuous circular slit.
- b. **Multi or discrete jet:** a ring of circular gas exits are used.

Figure 2-3 illustrates two types of nozzle design in a gas atomizer. In this study a multi jet free-fall atomizer and an annular close-coupled atomizer configuration are used for spray forming of tubes. Figure 2-4 illustrates a schematic of the gas atomization system including two different gas atomizers [CIFT20]. In the following sections the two types of atomizers will be described briefly.

2.2.3 Free-fall atomizer

The design of a conventional free-fall atomizer (FFA) is simple, robust and very reliable [FRIT12]. In free-fall atomizers the melt stream falls through the pouring nozzle via gravity in the disintegration or atomization zone [ANDE17]. Liquid and gas are brought into contact outside (about 10 – 20 cm [NEIK18]) the nozzle [YULE94]. The discrete gas jet meets the

melt stream by an angle of attack as shown in Figure 2-4a. This angle and the impact distance can be adjusted to vary the process parameters. In a typical nozzle design about 5 cm distance is maintained between the melt stream and the gas nozzle to avoid melt splashing or melt film back flow (“lick-back”) due to gas recirculation flow [FRIT12, ANDE17]. The main disadvantage of the free-fall atomizer is a higher gas-to-melt ratio (GMR, Eq. 2-5) that is needed. The larger distance of the atomization zone from the gas nozzle prevents the melt freezing but the gas jet loses some of its velocity before reaching the atomization zone which yields in larger particles [CZIS08b, CZIS08c]. The reduced gas velocity also affects the convective droplet cooling and results in a higher liquid fraction in the deposition zone during spray forming process [LOHN03]. The typical droplet size is 100 to 200 μm by a free-fall atomizer [FRIT05]. The yield (ratio of feedstock and final deposit mass) usually is in the range of 60 to 90% for a FFA spray forming process [ZEPO16].

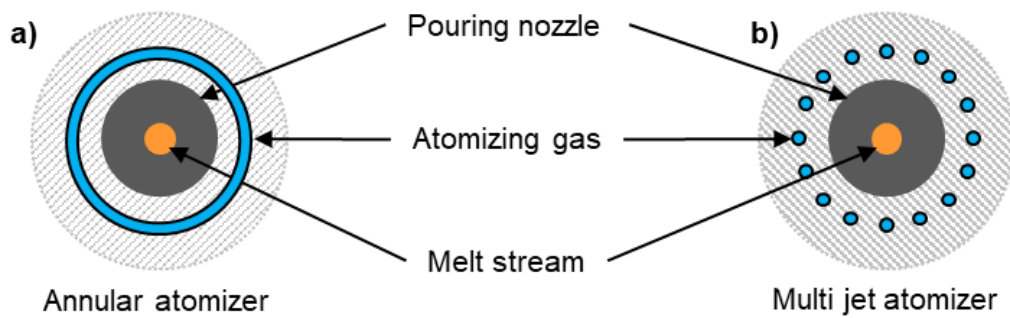


Figure 2-3: Schematic a) annular atomizer b) multi jet atomizer with melt and gas exits.

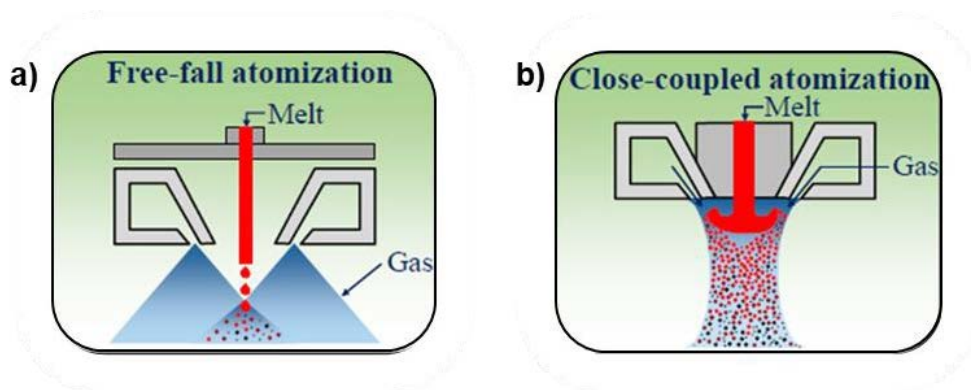


Figure 2-4: Schematic diagram of a) free-fall atomization, b) close-coupled atomization. The figures are adopted from [CIFT20].

2.2.4 Close-coupled atomizer

The close-coupled atomizer (CCA), also known as confined atomizer, is mainly used for producing finer particles in metal powder production [ZHEN11, LI17, MULL08]. The mass median particle diameter of metal powders by close-coupled atomizers is ranging from 20 to 80 μm [CIFT18]. In close-coupled atomization systems, a higher gas pressure results in smaller particles, but at the same time leads to a higher gas consumption. Unlike free-fall atomizer the gas jet impact the liquid melt directly at the opening of the pouring nozzle (see Figure 2-4b) [MULL11, ANDE02]. Due to this close proximity the gas kinetic energy is consequently higher in comparison with the free-fall atomizer and produces a higher yield of fine powders [ANDE17, ZHAO12, GRAN07]. Figure 2-5 shows a typical particle size distribution by a free-fall atomizer and a close-coupled atomizer (two atomization runs performed in the powder production setup at University of Bremen). The spray of the close-coupled atomizer is narrower than that of the free-fall atomizer operated at almost identical conditions and gas pressure [ANTI13, ZHAO09], which leads to lower overspray material during spray forming of tubes [ELLE14]. A comparison between free-fall atomizer and close-couple atomizer is outlined in Table 2-2.

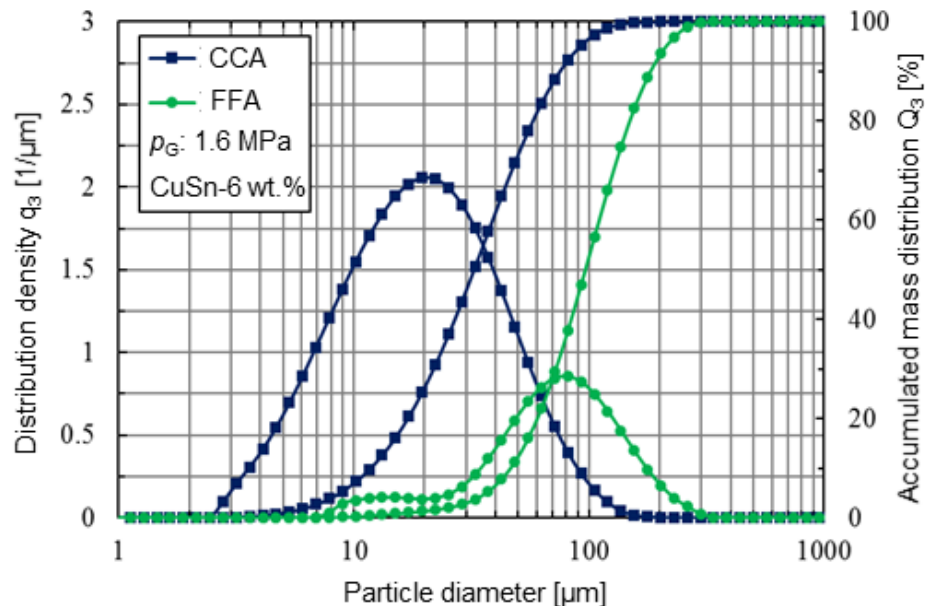


Figure 2-5: Typical particle size distributions with free-fall atomizer (FFA) and close-coupled atomizer (CCA) for CuSn6 for identical gas pressure ($p_G = 1.6 \text{ MPa}$).

Table 2-2 Comparison between free-fall and close-coupled atomizers.

Free-fall atomizer	Close-coupled atomizer
Melt atomized at a distance from the pouring nozzle	Melt atomized at pouring nozzle tip
Higher melt to gas ratio	Lower melt to gas ratio
Gas-to-melt mass flow ratio	Vital parameter of deposit cooling
No melt freeze-off	Prone to melt freeze-off
Larger droplet size ($d_{50.3}$: 100 – 200 μm)	Smaller droplet size ($d_{50.3}$: 40 – 80 μm)
Wide spray cone	Narrow spray cone
Higher overspray material	Lower overspray material

Main disadvantage of a close-coupled atomizer is the possibility of freezing of the melt (freeze-off) in the pouring nozzle. The melt pouring nozzle get chilled by the flow of cool process gas before starting the atomization process [GRAN07, CIFT20]. Previously, the close-coupled atomizer was used in conjunction with low melting point materials where the temperature difference between melt and process gas is relatively small to avoid this problem. A higher superheat temperature is being used to overcome the freeze-off problem (200 – 300 °C) [ANDE17, NEIK18]. However, higher superheat temperatures may lead to vaporization of sensitive alloying elements with low evaporation temperatures and may cause chemical reactions between crucible and feedstock materials. Another drawback is the unavailability of high temperature resistant crucible materials. Previous studies reported that the melt stream of a close-coupled atomizer is distributed as a film, covering the pouring nozzle tip [MULL11]. However, the convergent-divergent close-coupled atomizer (CD-CCA-0.8, this atomizer is used for the spray forming runs) developed by Schwenck et al. shows a falling melt stream without forming a film under the pouring nozzle [SCHW17, CIFT20].

Figure 2-6a shows the melt flow at the nozzle tip of the convergent-divergent close-coupled atomizer (CD-CCA-0.8). The construction details of the atomizer can be found in [SCHW17, BECK20]. Ciftci et al. mentioned that a successful atomization with respect to process stability and droplets size control can be performed without the presence of a melt film underneath the melt film tip with this atomizer [CIFT20].

In close-coupled atomizers the melt flow rate relies on the static pressure upon the melt in the crucible, pouring nozzle diameter and aspiration pressure (in the close-coupled atomizer the local gas recirculation promotes a negative aspiration pressure, which results in suction and stable melt delivery [CIFT20]) at the pouring nozzle tip [SCHW17, JEYA09]. The aspiration pressure depends on the atomization gas pressure. Schwenck et al. reported that the aspiration pressure increases with increasing atomization gas pressure (see Figure 2-7). It is recommended that the aspiration pressure should always be below zero (i.e. 0 kPa) to avoid gas pushing upwards in the pouring nozzle [SCHW17], which may cause freeze-off.

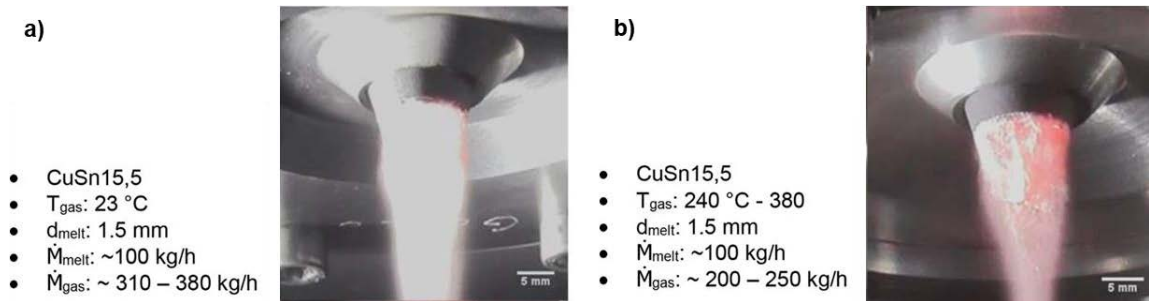


Figure 2-6: Process video images showing the melt building up at the nozzle due to flow separation for the given nozzle geometries as well as for a) cold and b) hot gas conditions. The figure is adopted from [SCHW17].

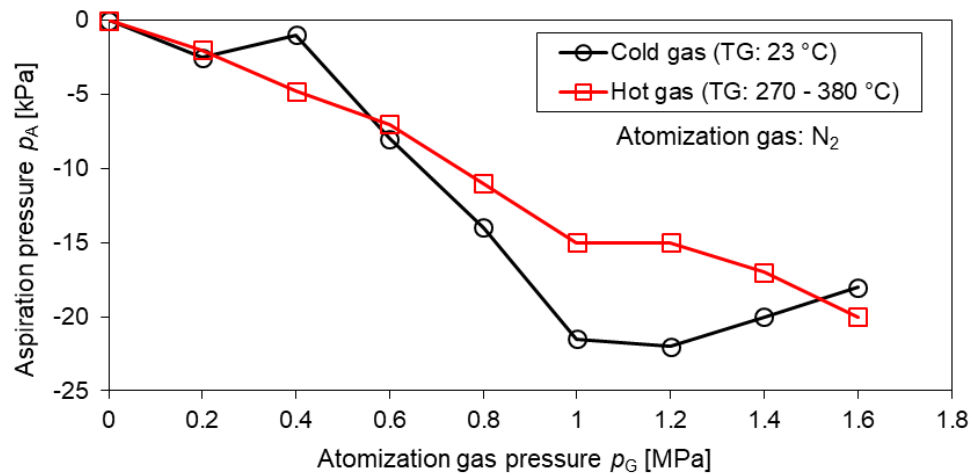


Figure 2-7: Aspiration pressure at the melt pouring nozzle exit (without melt in cold condition) for CCA (CD-CCA-0.8) nozzles at cold gas and hot gas conditions. The figure is adopted from [SCHW17].

2.2.5 Hot gas atomization (CCA)

Hot gas atomization is relatively new in metal powder production [ANDE02, ANDE03, ANDE17]. This technique is used for production of finer particles with decreased gas consumption [CIFT18, HUSS20b]. Ciftci et al. reported that the cooling rate of the droplets strongly depends on the droplet diameter and the gas-to-melt mass flow ratio (GMR); the GMR is also dependent on the initial gas temperature (T_G) [CIFT19, CIFT20]. The lower density of the hot gas reduces the gas volume at same pressure compared to cold gas, which also affects the aspiration pressure of the close-coupled atomizer as reported by Schwenck et al. (see Figure 2-7) [SCHW17].

Ciftci et al. compared the measured gas mass flow rates with theoretically calculated gas mass flow rates in the CD-CCA-0.8 [CIFT20]. Theoretically the gas mass flow rate $\dot{M}_{G,theo}$ is calculated with some assumptions for simplification (i.e. the atomization system is assumed to be a vessel at constant pressure, the orifice cross-section is treated as an annular gas nozzle [CIFT18, CIFT20]). By the following equation the gas mass flow rate can be calculated (considering isentropic condition) [CIFT20]:

$$\dot{M}_{G,theo} = A_n \cdot \psi_{max} \cdot \sqrt{2 \cdot \rho_g \cdot p} \quad \text{for } p_i > p_{crit} \quad \text{Eq. 2-7}$$

where, A_n represents the cross section of the gas exit and the parameters ψ_{max} , ρ_g and p describe the outflow function, gas density, and atomization pressure. The parameter ψ_{max} corresponds to p_{crit} , which is a function of the isentropic exponent κ ($\psi_{max} = 0.514$ for argon and $\psi_{max} = 0.444$ for nitrogen) [CIFT20]. At elevated gas temperatures the gas mass flow rate \dot{M}_G , can be calculated with the following equation [CIFT18]:

$$\dot{M}_G = \dot{M}_{G,0} \cdot \sqrt{T_{G,0}/T_G} \quad \text{Eq. 2-8}$$

where, $\dot{M}_{G,0}$ is the gas mass flow rate at room temperature, $T_{G,0}$ is the gas temperature in cold condition (RT), \dot{M}_G is the gas mass flow rate at elevated atomization gas temperature T_G . Ciftci et al. also proposed a discharge coefficient C_d , which is the ratio of the experimentally determined gas flow rate $\dot{M}_{G,exp}$ and theoretically calculated gas mass flow rate $\dot{M}_{G,theo}$ [CIFT20]:

$$\dot{M}_{G,exp} = C_d \cdot \dot{M}_{G,theo} \quad \text{Eq. 2-9}$$

here, the averaged C_d value at cold gas condition is $C_{d,RT} = 0.88$ and at hot gas atomization is $C_{d,HG} = 0.84$. Figure 2-8 shows the relationship between gas mass flow rate and atomization pressure for the close-coupled atomizer (CD-CCA-0.8). With increasing atomization gas pressure the gas mass flow rate also increases. Hot gas atomization resulted in lower gas consumption than in atomization at ambient temperature (cold condition), caused by the lower gas density (the gas density depends on temperature). For instance, gas consumption decreased by one third for a typical atomization pressure of 1.6 MPa with hot gas atomization, demonstrating that hot gas atomization is a valuable tool to reduce gas consumption. However, atomization at elevated gas temperatures require a higher energy consumption for gas heating that need to be considered for commercial viability [CIFT20].

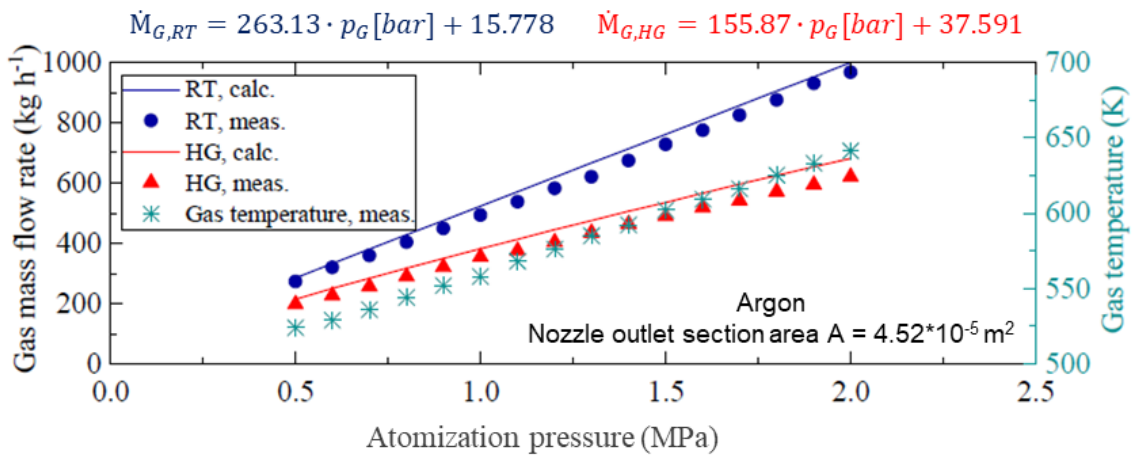


Figure 2-8: Gas mass flow rate for a CCA as a function of atomization gas pressure and temperature. HG ($T_G \sim 300^\circ\text{C}$) and RT ($T_G \sim 20^\circ\text{C}$) stand for hot gas atomization and atomization at ambient temperature. Measured (meas.) and calculated (calc.) gas mass flow rates at ambient temperature are compared with gas mass flow rates at elevated gas temperatures. Argon was used as process gas. The figure is adopted from [CIFT20].

As shown by Ciftci et al. elevated gas temperatures result in significantly smaller mass median particle diameters, demonstrating that hot gas atomization is a promising tool for the production of smaller particles required for various powder consolidation techniques [CIFT18, SCHW17]. Figure 2-9 shows at a constant gas mass flow rate, that for increasing the melt mass flow rate an increased GMR and a decreased mass median particle diameter result. By keeping the melt mass flow rate and GMR constant, hot gas atomization provides smaller mass median particle diameter.

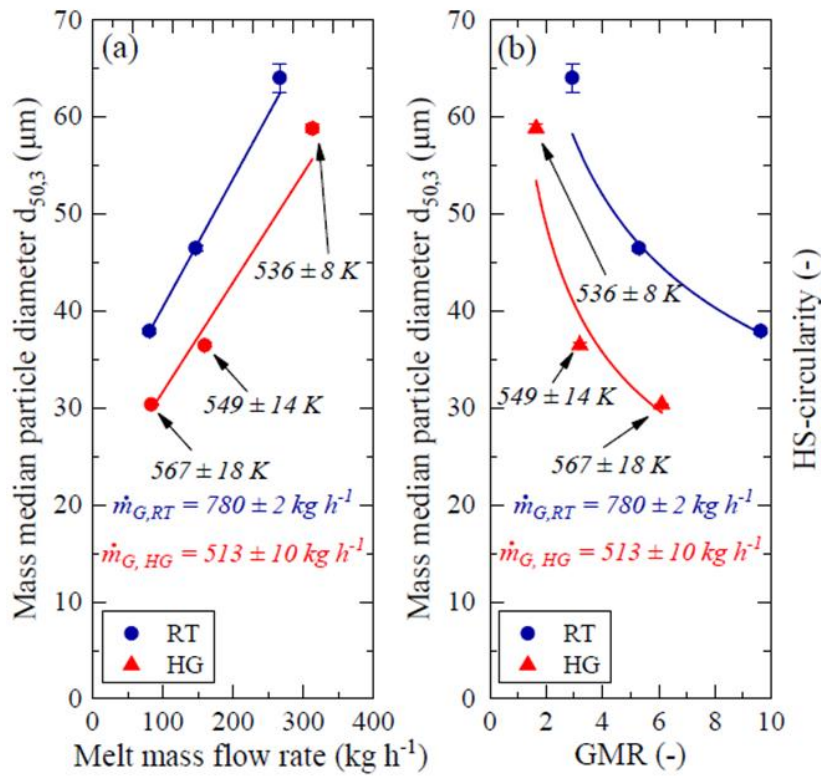


Figure 2-9: The mass median particle diameter $d_{50,3}$ of $\{(\text{Fe}_{0.6}\text{Co}_{0.4})_{0.75}\text{B}_{0.2}\text{Si}_{0.05}\}_{96}\text{Nb}_4$ powders as a function of a) melt mass flow rate, b) gas-to-melt mass flow ratio (GMR). The averaged hot gas temperatures and gas mass flow rates are listed. The lines serve only as visual guides. An increased GMR and gas temperature result in smaller $d_{50,3}$ values [CIFT20].

Thus, in metal melts atomization, the gas atomization technique is well practiced for powder production. The free-fall atomizer (FFA) construction and maintenance are simple and robust. Close-coupled atomizers (CCA) provide finer particles compared to free-fall atomizer. In contrast, close-coupled atomizers show melt freeze-off and higher gas consumption. However, by using hot gas atomization these drawbacks can be overcome. Furthermore, hot gas atomization provides smaller droplets.

2.3 Porosity in spray forming process

Along with promising advantages of the spray forming process e.g. remarkable microstructure and grain refinement, the porosity in the as-sprayed materials is a main drawback of the technology [GRAN95, CAI97, UHLE14]. Regardless the materials (alloys) or deposit geometry, porosity was reported in most of the spray forming processes investigated to date [LAVE10, HENE17]. Porosity reduces the materials quality for the subsequent processes. However, secondary forming processes are suitable to reduce the porosity in the as-sprayed materials, i.e. forging, hot isostatic pressing, hot rolling, extrusion etc. [MEYE13, WALT05, SPRI17].

2.3.1 Types of porosity

In spray forming process the porosity is mainly divided into two types based on their forming mechanism: cold porosity and hot porosity [LAVE88, CAI97, HU00]. The forming mechanisms of cold and hot porosity are presented below.

- **Cold porosity:** Cold porosity in spray forming is mainly observed in the vicinity of the substrate, which is also mentioned as interstitial porosity [HU00]. The particles start to solidify completely in the deposition zone during very cold spray condition [CUI05c]. The second layer of particles impinge onto this already solidified layer and form a deposit layer with high porosity without filling the cavities. With further layers of particles, the deposition zone gathers higher enthalpy to increase the liquid content and decrease the viscosity of the mushy zone. This mushy zone further reduces the porosity in the deposit [CAI97].
- **Hot porosity:** As the temperature of the as-sprayed deposit surface increases in the mushy zone, the liquid fraction continues to increase as well as the viscosity of the droplets. In that hot mushy zone gas bubbles may be entrapped and remain in the deposition layer, which form circular pores in the deposit. As long as there is enough liquid in the mushy zone, these pores may be combined in to larger pores [CUI09]. Hot pores are also called gaseous pores [HU00].

Figure 2-10 shows examples of cold and hot porosity from a spray formed Mg_2Si -containing Al alloy [ELLE07a]. The comparison shows that hot pores are significantly larger than cold pores. However, smaller gas pores are also observed depending on the condition.

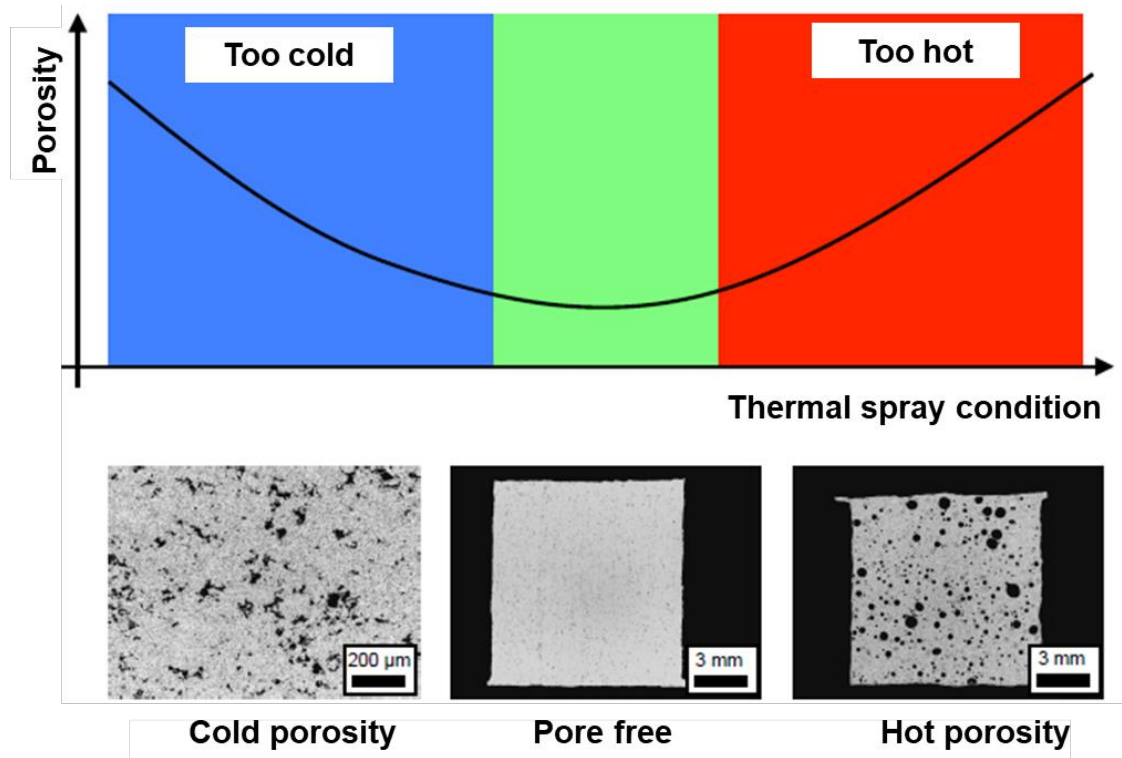


Figure 2-10: Cold and hot porosity in spray-formed deposits. The figure is adopted from [UHLE14].

2.3.2 Influences on porosity in spray forming

Several parameters are decisive for porosity formation in the spray forming process. In the literature influencing factors are categorized as metallurgical, geometric and thermal behavior in porosity formation of as-sprayed deposits.

2.3.2.1 Metallurgical influences

Meyer et al. reported that different porosity levels are detected for different alloys [MEYE14]. Similar to conventional casting the pores can also form in the deposit center due to shrinkage during solidification, in case of higher liquid fraction in the deposit center [UHLE07a]. The shrinkage level depends on the alloy and its alloying elements. In addition, temperature dependent gas solubility may lead to gaseous diffusion, e.g. nitrogen entrapment during melting process [ELLE10b, SCHU04]. For example, nitrogen may dissolve during spray forming of steel with N_2 gas atomization. Alloying elements also influence the porosity of the as-sprayed deposit, such as addition of Ti, Zr, Al [MÜLL04]. Titanium can chemically bind the nitrogen contained in pores and hence reduce porosity.

The authors investigated the effect of small addition of Ti (0.25 wt%) in Cu-based alloys. Ti reacted with nitrogen and formed TiN precipitates, which reduced the overall nitrogen pores (Figure 2-11) without affecting the materials properties [MCHU08a].

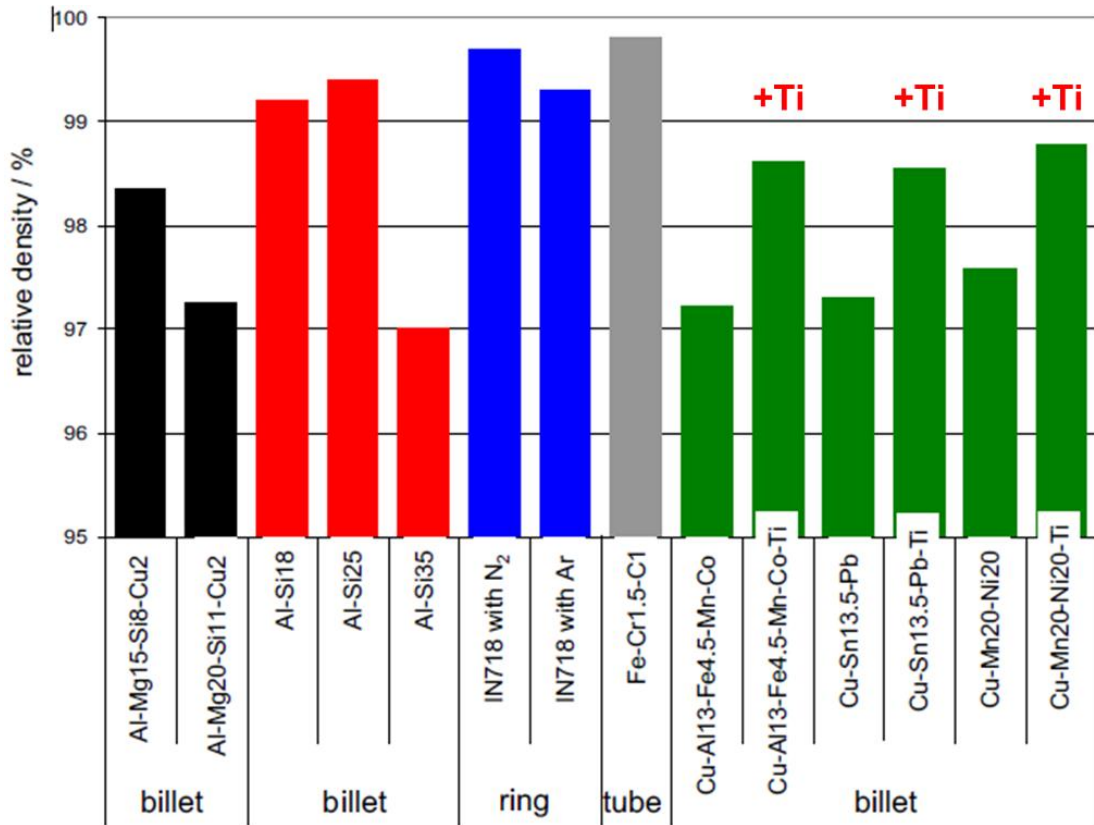


Figure 2-11: Relative density of different alloys in the as-sprayed condition [MCHU08a].

2.3.2.2 Geometric influences

In the deposition zone different aspects are present during the initial droplets impingement. The impinging droplets may change their morphology by adhering onto the surface (substrate or deposit), or by fracturing into further secondary droplets, or may bounce off the surface [HU00]. According to Liu et al. the porosity increases with increasing surface roughness in the deposition zone [LIU95]. For example, the initial clusters of impinging droplets encounter a relatively flat surface, where the porosity remains minimal. However, in the initial layer of deposition cold porosity makes the surface rough and hinders the splashing of the forthcoming droplets. Furthermore, gas entrapment into the solidified layer also creates pore. Hu et al. proposed a model with a combination of impact angle

(deposition angle) and surface roughness for the geometric influence on porosity [HU00]. The impact angle (α) is defined as the angle between the surface tangent and the spray direction of droplets (Figure 2-12a). The droplet spreading is influenced by the impact angle. Larger impact angle causes inhomogeneous droplet splashing and bumps can be formed in the deposition zone. These bumps build up further and intensify the formation of shadows [PASA02]. Therefore, subsequent droplets can no longer reach areas underneath that and pores are formed [HU00, LIU18]. Hu et al. suggested to maintain the impact angle perpendicular to the deposit surface to avoid this kind of porosity [HU00]. However, further experimental investigations by Uhlenwinkel et al. showed that the critical value of impact angle is 26° for spray forming of rings [UHLE07a]. Quantitative evaluations of the porosity showed that at an average impact angle of approximately 25° , there was a sudden increase in the scatter of the porosity from 2% to up to 15% (Figure 2-12b). However, thermal effects have not been taken into account in this investigation.

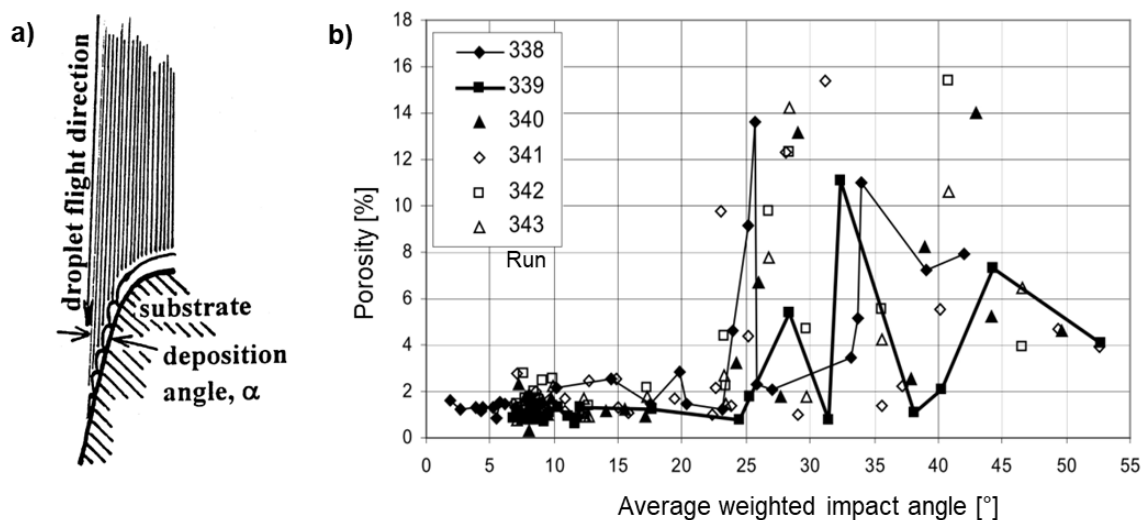


Figure 2-12 a) Schematic formation of rough surface and shadowing effect by higher impact angle (deposition angle) [HU00], b) porosity of spray-formed rings (material: IN718) as a function of impact angle α [UHLE07a].

2.3.2.3 Thermal influences

Thermal influences are reported as a vital parameter for porosity formation in previous studies [MINI02, MEYE03, UHLE07a, ELLE10b, MCHU08a, MEYE14]. The thermal conditions of the droplets (amount of solid or liquid fraction) affect the geometric parameters like deposit surface quality [ELLE10b]. The temperature and solid fraction in the droplets

have a strong influence on the droplet spreading behavior [WAN01]. Due to higher liquid fractions the droplets deform irregularly and are disintegrated in the outer surface after impingement, which prevent the spreading of the droplets and formation of a layer of uniform splat. Furthermore, those irregularly shaped droplets release heat from the disintegrated periphery and form a cold and rough surface for the forthcoming droplets [DHIM09]. This rough and irregular surface hinders the spreading of subsequent droplets and favors the formation of shadow areas (geometric porosity) [HU00].

In many previous studies, the liquid (or solid) fraction of the impinging droplets is correlated with the resulting porosity [LAVE96, WARN97, CAI98]. Warner et al. investigated the relationship between average liquid fraction in the spray and average porosity of spray-formed tubes and billets (Inconel 625/Ni-based and Cu-6wt%Ti) [WARN97]. The average liquid fraction in the spray was calculated from the spray forming process parameters. For both deposit forms, there is a decrease in the average porosity with increasing liquid fraction to a minimum with a liquid content of approx. 0.55 - 0.6 which indicates cold porosity (Figure 2-13). It should be noted that in [WARN97] the cooling rate of single droplets is overestimated. Therefore, the calculated liquid fraction in the droplet is generally too low.

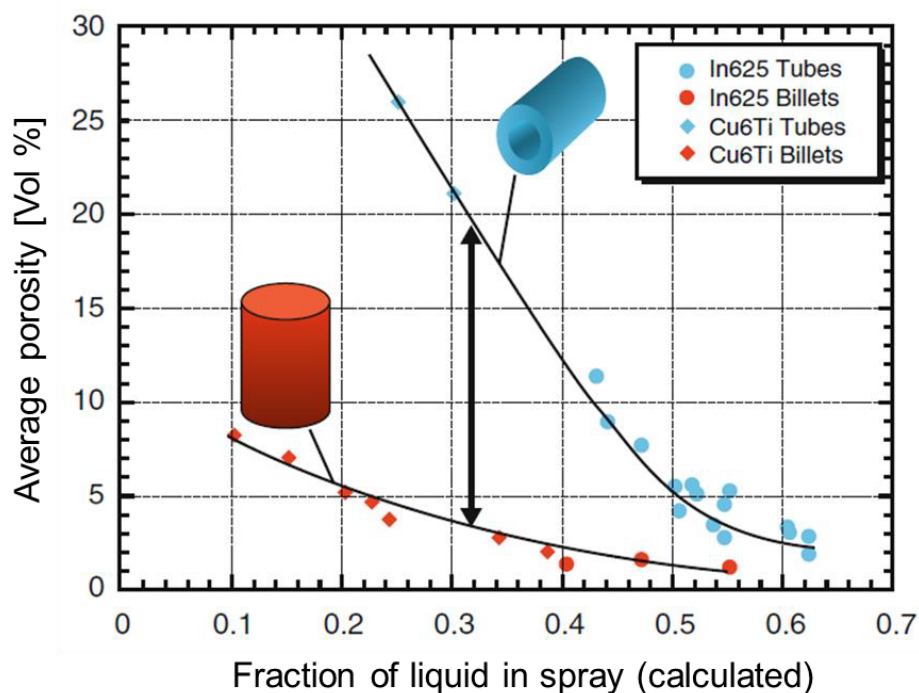


Figure 2-13

Influence of the average liquid fraction in the spray on the average porosity in the spray-formed tubes and billets [WARN97]. The figure is adopted from [HENE17].

However, the investigations revealed different porosities for tubes and billets with the same calculated liquid fraction, which is due to different cooling conditions of the two deposit forms. The surface to volume ratio is different for these two forms, which result in different deposit surface temperatures. This behaviour shows that the relationship between porosity and liquid fraction in the droplets depend on the deposit geometry (deposit form, deposit diameter and length etc.) [WARN97]. With increasing deposit surface temperature, the porosity in the deposit decreases.

Since the droplet size distribution, the droplet velocity, the mass flow density distribution (MSD) and the convective heat emission of the droplets depend on the gas-to-melt ratio [FRIT12, CIFT18, CIFT20], the deposit thermal profile is also related to the gas-to-melt ratio (*GMR*) [UHLE14]. Ultimately, the *GMR* determines the liquid fraction in the spray, hence, the thermal profile of the deposit. However, it must be noted that the *GMR* also depends on the atomization system used. Therefore, Ellendt et al. proposed the concept of EGR (ratio of enthalpy flow to gas mass flow) to determine the temperature difference (overheating) of the melt to link liquidus temperature with the *GMR* [ELLE10b].

The substrate surface temperature also influences the droplets spreading behaviour [DHIM05]. A colder substrate surface means a higher temperature difference at the contact surface, which promotes the heat release of the droplet and thus its prompt solidification. The influence of the substrate temperature on the propagation behaviour of single drops during impact was investigated by Dhiman et al. [DHIM05] (Figure 2-14). With increasing substrate temperature, the droplet can spread further and more evenly, since its spreading phase was less hampered by the simultaneous solidification. For higher substrate temperatures, more uniform spreads were achieved with almost no splitting of the droplet. In addition, the impact velocity also influences the deformation behaviour, with higher impact velocity the droplet spreading was more uniform.

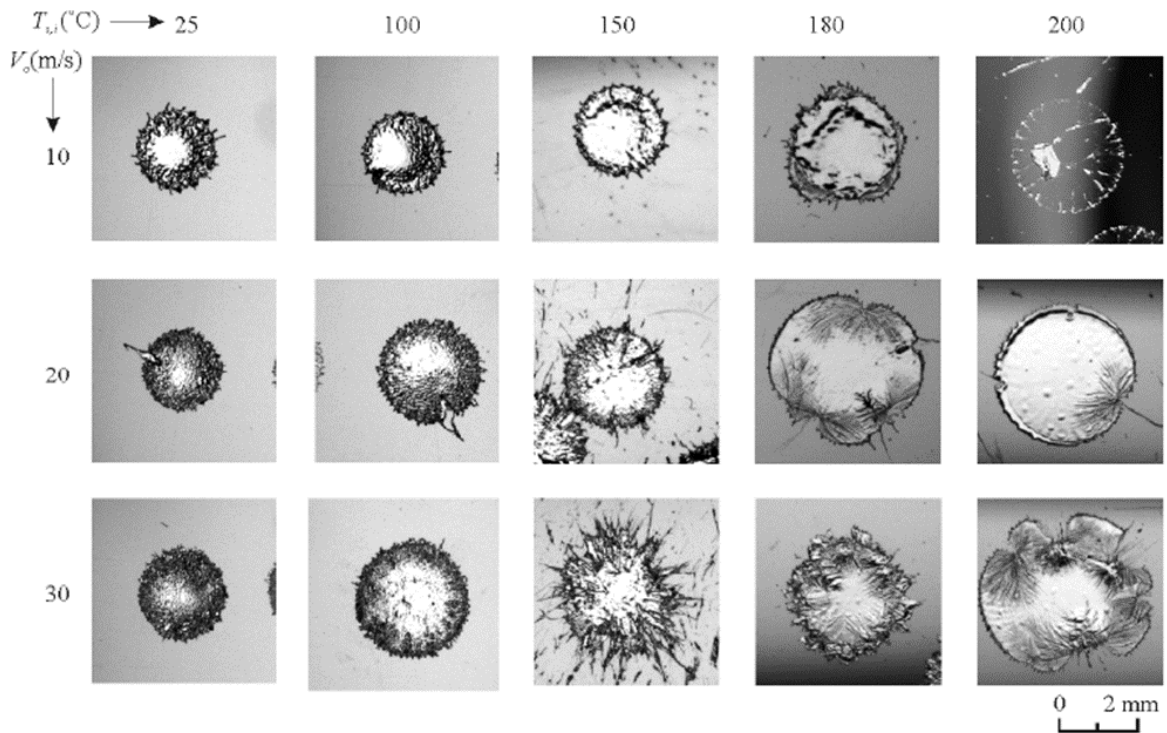


Figure 2-14 Influence of substrate temperature and impact speed on the deformation behaviour of droplets during impact (tin on stainless steel substrates [DHIM05]).

The deformation kinetics of droplets in rapid solidification processes depends on the droplet deformation time [CHAN09]. During rapid solidification process the impacting droplets breakup based on their velocity and solidification kinetics. An impacting droplet forms a solid layer around its edges, obstructing liquid flow from the center and triggering uniform splashing. In contrast, when a droplet does not solidify during impact, it disintegrates and ruptures internally. During slow deformation nonuniformly distributed splats are formed. The faster deformation time facilitates a solid layer around its edges, which prevent further droplet breakup. McHugh et al. reported that the deformation time t_d depends on the droplet velocity v_d and the droplet diameter d_d for a specific droplet temperature [MCHU08a]:

$$t_d \propto d_d / v_d. \quad \text{.Eq. 2-10}$$

A shorter deformation time can be achieved with smaller droplet size d_d and higher droplet velocity v_d .

However, during the spray forming process the deposit surface act as a substrate for the upcoming droplets, which means the surface temperature of the deposit affects the porosity. Grant reported that in-situ measurement of the deposit temperature may be helpful to gain

insight of the spray forming process and the influence of process conditions on the porosity and microstructure of the spray-formed deposits [GRAN95]. Similarly, Walter et al. reported that the deposit surface temperature is the most important parameter for porosity control [WALT05]. Uhlenwinkel et al. were able to demonstrate experimentally that the deposit surface temperature has a strong influence on the porosity [UHLE07a]. Figure 2-15 shows the influence of the deposit surface temperature on the porosity of spray-formed rings (Ni based alloy). With low deposit surface temperatures high porosity was observed (over 10%), which mainly has been identified as cold porosity. The porosity decreased in the deposit with increasing deposit surface temperature. The porosity was about 1% at deposit surface temperature of 1260°C. As the deposit surface temperature continued to rise, the porosity increased further due to hot porosity. The deposit surface temperatures were measured at the deposit center region of the spray-formed ring with a two-color pyrometer. Further investigations are necessary here for better understanding and transferability to other product geometries and materials.

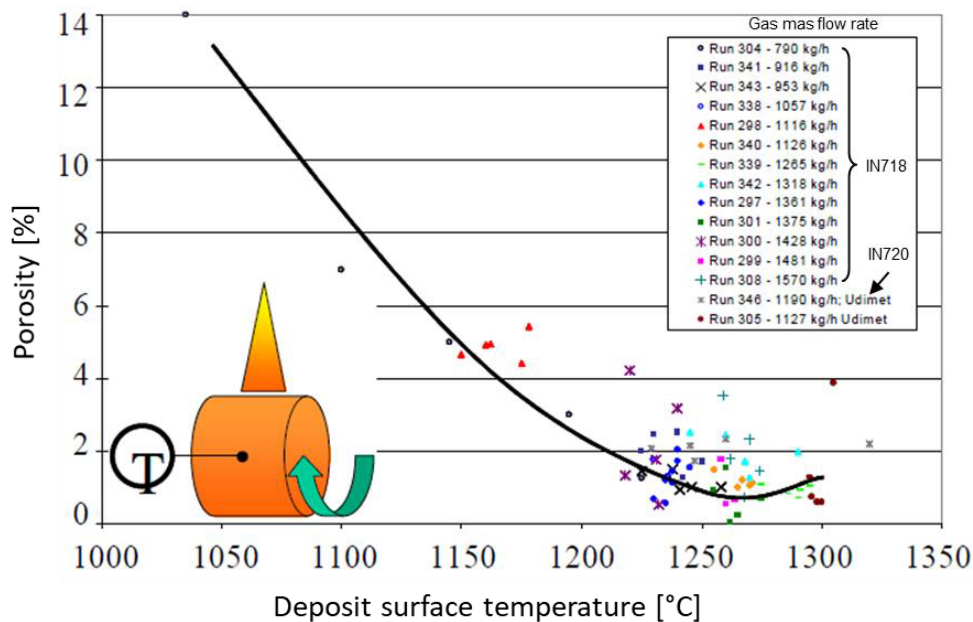


Figure 2-15 Influence of the deposit surface temperature on the porosity of spray-formed rings (Ni based alloy). The figure is adopted from [UHLE07a].

Meyer et al. have shown that the same relationship between the porosity level and the deposit surface temperature can be observed in spray-formed sheets for different materials such as Cu alloys (Al-bronze and Sn-bronze) and nitriding steel [MEYE14]. The authors reported that the deposit surface temperature itself is unsuitable to transfer results to other alloys. For example, a deposit surface temperature of 1260 °C would lead to the complete

melting of the aluminum alloys. Therefore, a concept of dimensionless enthalpy of deposit surface (h_{surf}^*) was proposed [MEYE13] and it has been shown that the optimum porosity levels are always obtained when the deposit surface temperature was close to the alloy's solidus temperature (Figure 2-16). The authors also showed that cold porosity in the vicinity of the substrate can be considerably reduced by preheating the substrate at temperatures close to the alloy's solidus temperature. However, the magnitude of the minimum porosity level was strongly dependent to the material.

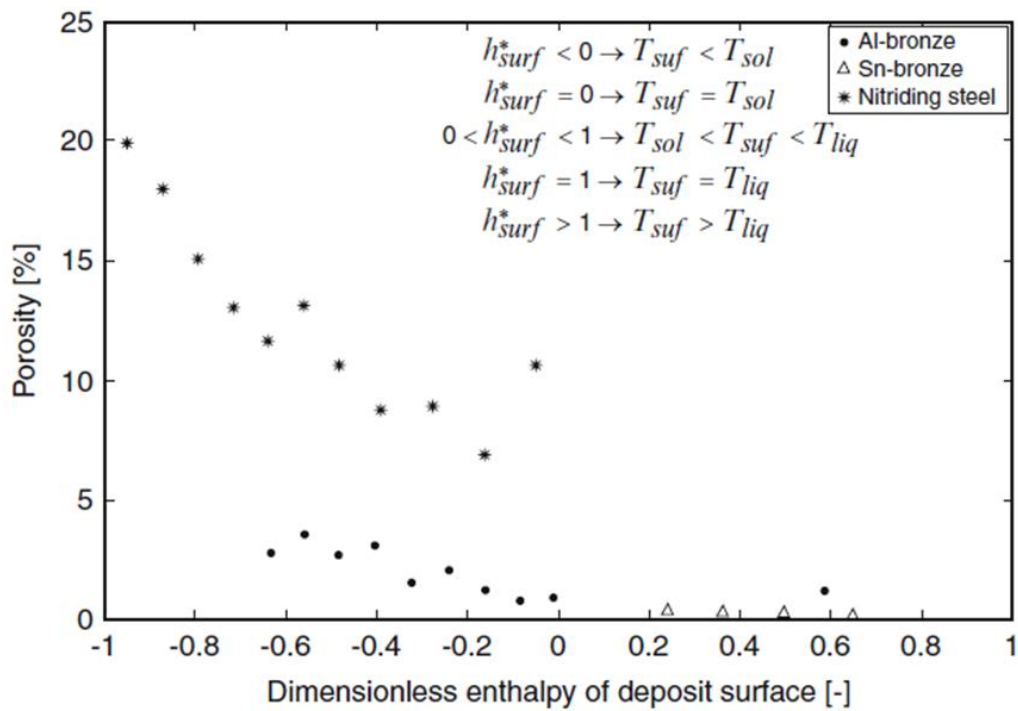


Figure 2-16 Effect of the dimensionless enthalpy of deposit surface on porosity of Al-bronze, Sn-bronze and nitriding steel (adapted from [MEYE14]).

Within the spray forming process a model for the distribution of the non-dimensional specific enthalpy (h_0^*) in the spray was developed based on an existing mass flux model by Ellendt et al. [ELLE07b]. The non-dimensional enthalpy at the nozzle distance z can be determined by the following equation [ELLE07b]:

$$h_0^*(z) = \exp(a_2 \cdot z^{b_2} \cdot d_{50,3}^{c_2}) \quad \text{Eq. 2-11}$$

where, a_2 , b_2 and c_2 are constants and $d_{50,3}$ is the mass median droplet diameter in the spray. The constants depend on the atomizer geometry and the alloys.

According to Eq. 2-10 smaller droplets reduce the enthalpy transfer into the deposit. The deposit surface temperature T_D depends on the specific enthalpy in the deposition zone. The following equation can be derived from Eq. 2-11:

$$\Delta T_D \propto \Delta h = f(a_2 \cdot z^{b_2} \cdot d_{50,3}^{c_2}) \quad \text{Eq. 2-12}$$

where, ΔT_D is the change of deposit surface temperature, Δh is the change of specific enthalpy in the deposition zone and $d_{50,3}$ is the mass median droplet diameter in the spray.

2.3.3 Porosity and thermal behaviour of tubular deposits

The thermal behaviour and porosity of spray-formed tubes and rings have been studied in several previous investigations [LAWL98, CUI04, CUI05a, CUI05b, MI08a, MI08b, UHLE07a, MEYE13a, BUCH03, ZEPO16, LEE18]. Tubular deposits typically show similar porosity behaviour like other deposit geometries. Figure 2-17 shows a spray-formed AISI 52100 (100Cr6) tool steel tube, spray formed using a free-fall atomizer. From the porosity analysis higher porosities in the vicinity of the substrate and at the outer surface are observed. In contrast, high relative density materials have been found in the deposit center. Figure 2-17c shows a ring segment from the as-sprayed deposit. In the vicinity of the substrate the porosities were mainly cold porosities and in the deposit center about 100 μm large circular hot (gas) pores are found.

Cui et al. investigated the thermal behavior of a tubular preform numerically. A three-dimensional heat transfer model [CUI05b] of a spray-formed tube has been established to predict the thermal profiles of a growing tubular deposit in spray forming. The model was constructed based on a three-dimensional shape model [CUI05a]. The model showed that the temperature gradient of the deposit in the vicinity of the substrate was higher than that in the center or surface region (see Figure 2-18). In the center of the deposit a mushy zone is formed while the complete solid layers at the base and the top surface of the deposit promote cold porosity.

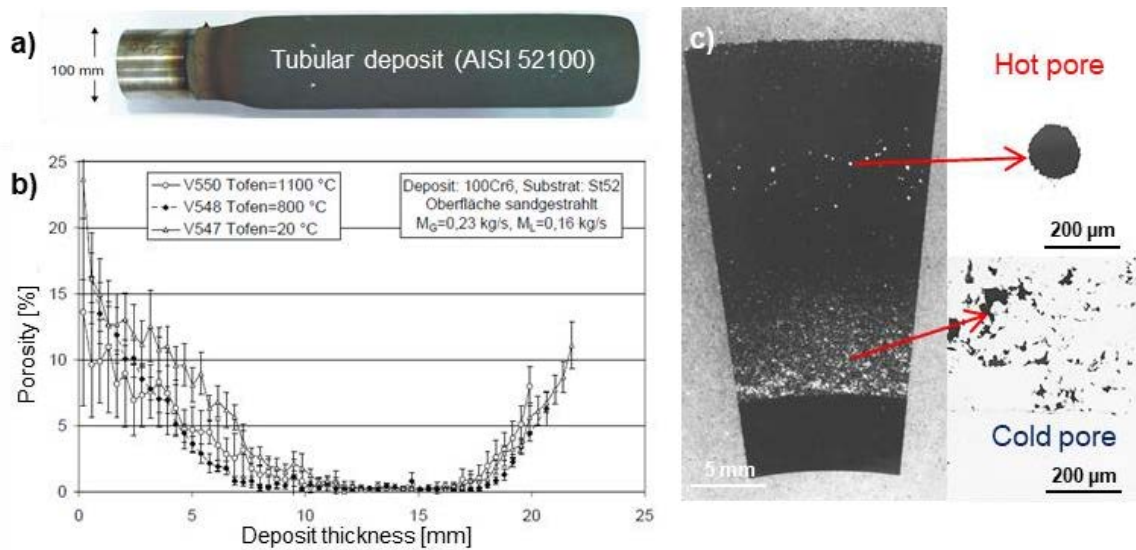


Figure 2-17 Spray-formed **a)** tubular deposit of AISI 52100 (100Cr6) tool steel, **b)** porosity distribution in deposit thickness, **c)** cross-section of the ring segment with hot porosity (gaseous) in the deposit center and cold porosity in the vicinity of the substrate. The figure is adopted from [BUCH03, GRAN17].

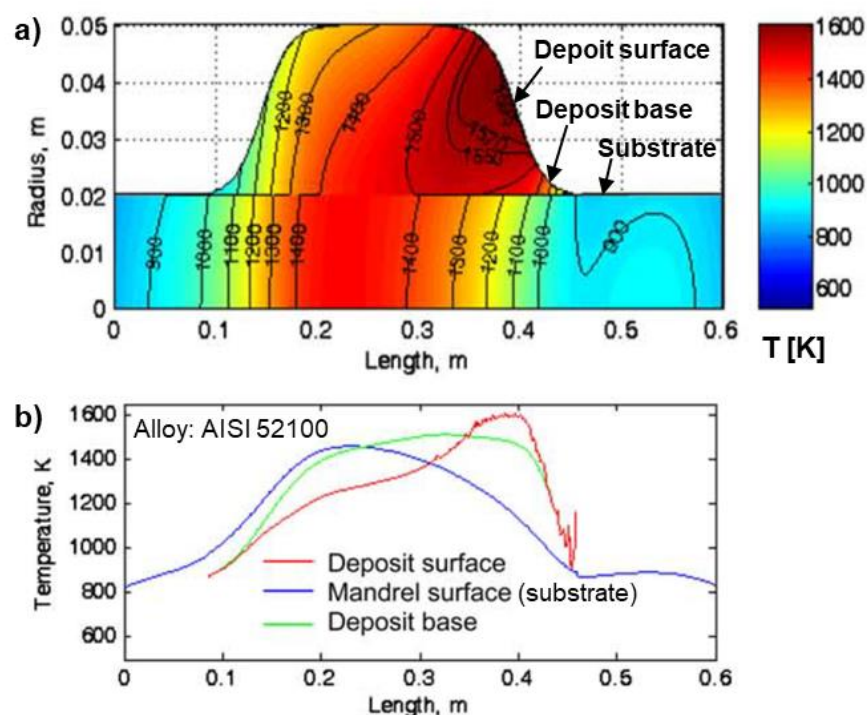


Figure 2-18 **a)** Temperature distribution through the longitudinal section of a tubular preform (AISI 52100), **b)** cooling behaviour at different regions in the deposit. The figure is adopted from [CUI05b].

Mi et al. reported a similar cooling behaviour in a tubular deposit. In addition, the authors compared the grain size of the spray-formed IN718 deposit in different regions with changing temperatures [MI08b]. The center of the deposit with higher temperature (higher residual liquid fraction) showed relatively uniform and equiaxed grains with average size of 42 μm and an average residual porosity of 1.5%.

The thermal behaviour of the deposit depends on the liquid fraction in the spray. At constant process parameters, the liquid fraction in the spray forming can be varied by changing the spray distance [ELLE14]. However, moving the deposit distance may affect the geometric yield of the deposit. In spray forming, yield is defined as the ratio of feedstock mass and final deposit mass. Figure 2-19 shows that the distance of the deposit also affects the deposit temperature by changing the liquid fraction. During spray forming of tubular deposits an optimum spray distance should be determined according to the substrate diameter and the atomization conditions.

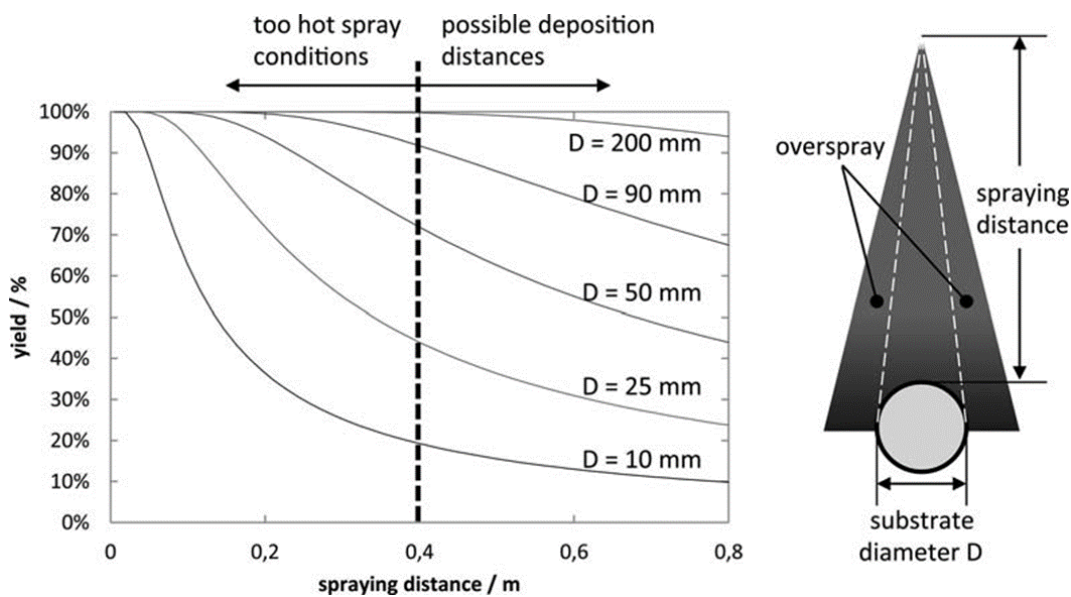


Figure 2-19 Calculated fraction of overspray for coating of thin tubes with a conventional free-fall-atomizer [ELLE14].

Ellendt et al. reported that high yield during spray forming of tubular deposits is achievable at shorter spray distances with a close-coupled atomizer [ELLE14]. Figure 2-20 shows the materials yield as a function of spray distance in a close-coupled atomizer. However, the too short spray distance (64 mm) leads to a hot deposit with uneven surface and high hot porosity in the deposit. The hot deposit surface can be avoided by higher *GMR* by

increasing the gas mass flow rate (the gas pressure). At larger distance (144 mm) the deposit was colder with lower porosity.

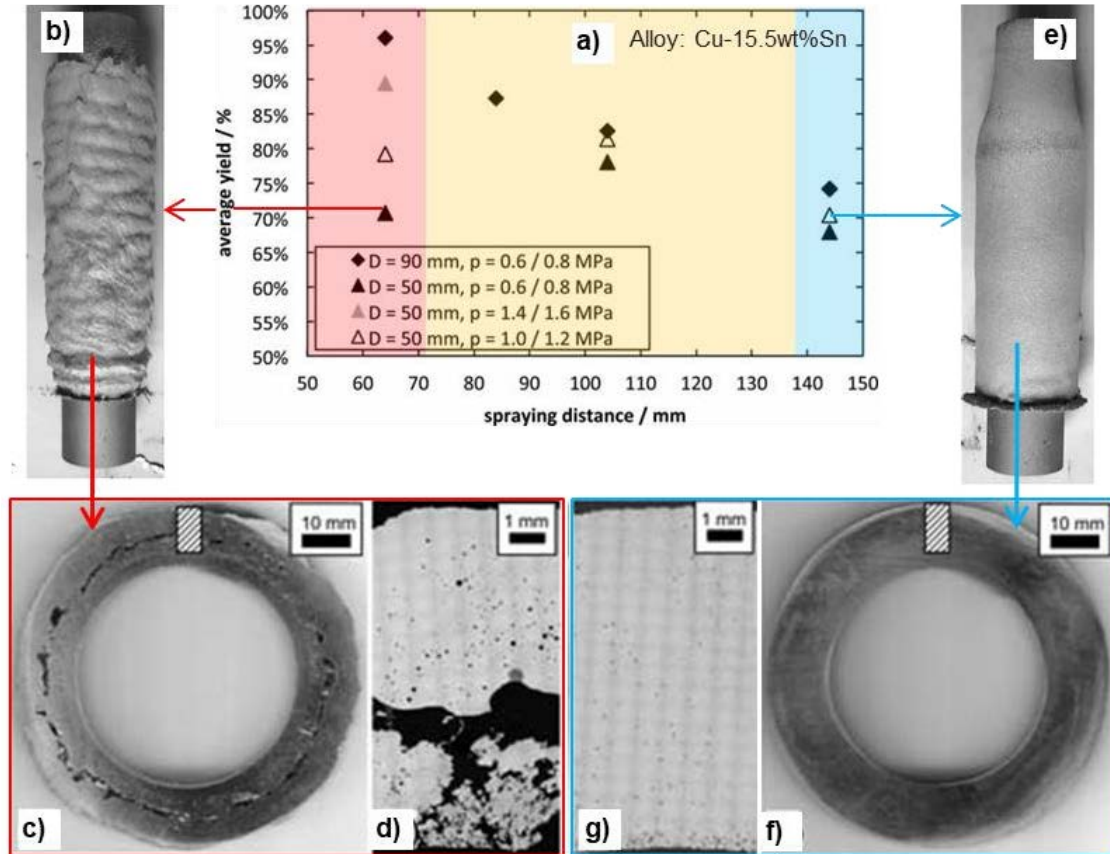


Figure 2-20 a) Effect of spray distance on yield of tubular deposits by close-coupled atomizer (alloy: Cu-15.5wt%Sn), b) rough deposit surface at short spray distance; c) and d) higher porosity in the vicinity of the substrate. e) better surface at long spray distance, f) and g) lower porosity in the vicinity of the substrate. D – substrate diameter, p – atomization gas pressure. The figures are adopted from [ELLE14].

In a recent study, Zepoen showed that twin nozzle systems can be used for spray forming of wear resistant bimetallic tubes (Figure 2-21a) [ZEPO16]. The first layer of the deposit was approximately 8 mm thick and showed a high relative density of more than 99% due to preheating of the substrate. The second layer possessed a low relative density in the vicinity of the interface. About 70% of the second layer (approx. 25 mm thick) had a high relative density as well (Figure 2-21). The preheating of the substrate reduces the porosity near the substrate. Recently, Lee et al. reported that the preheating of the substrate also may not remove the near substrate porosity (see Figure 2-21b) due to different materials in cladding

of two dissimilar steels [LEE18]. However, the authors suggested that the preheating up to a temperature range of 70% - 85% of the spray formed alloy solidus temperature may increase the interfacial shear strength up to 90% compared to cold condition.

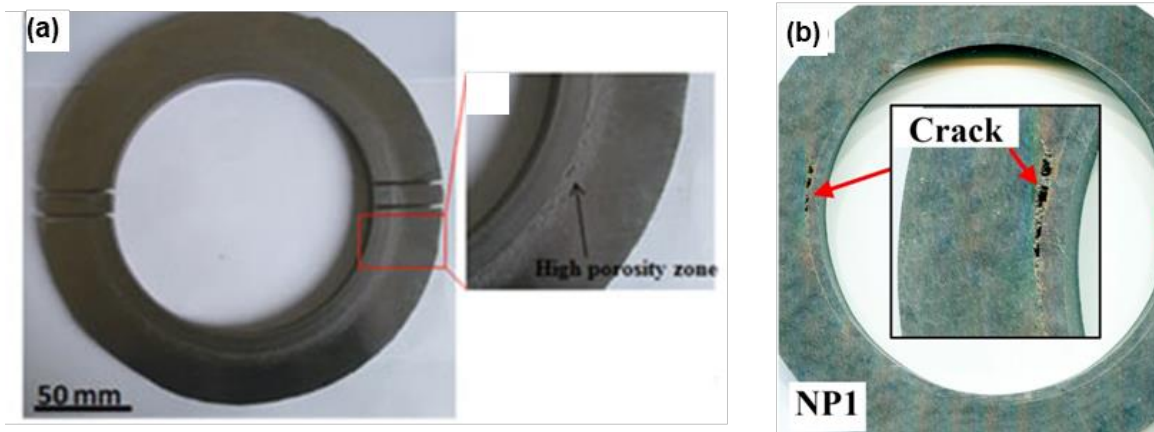


Figure 2-21 Porosity in tubular deposit a) interfacial porosity in bimetallic spray-formed tube [ZEPO16], b) interfacial crack in cladding of two dissimilar steels [LEE18]. The figures are adopted from [ZEPO16] and [LEE18].

2.4 In-situ measurement in the spray forming process

In the previous section it has been described that the deposit profile (structure and material properties) depends directly on the thermal character of the partially solid/liquid droplets during impact. According to Khatibi et al., monitoring specific droplet properties as, i.e. droplet temperature, velocity and size as well as mass and enthalpy fluxes provide a unique tool for optimizing the material properties as well as controlling the spraying conditions during deposition [KHAT17]. However, real time measurements of the melt atomization process and subsequent spray deposition process is challenging task due to high temperature in the atomization chamber. In this section the available in-situ measurement techniques will be presented.

2.4.1 In-situ measurement techniques

Since spray-formed deposits are substantially a collection of impinging droplets/particles on the substrate in a molten or partially molten state (also fully solid), the diameter, the velocity and especially the temperature of those particles have been studied to understand the

process [HENE92, GRAN95, TILL99, BREN00, KRAU02, ZIES02, BERG04]. Numerous studies at University of Bremen have been performed to measure in-situ the droplet characteristics (e.g. size, mass flux or flow rate, velocity and temperature) in the spray based on following principles [KHAT17]²:

- **Optical based techniques:** PIV (particle image velocimetry) is a high-speed imaging with shadowgraphy. The Particle Master (LaVision GmbH in Göttingen, Germany) is a high-magnification shadow imaging system [LAVI17], has been used for visualizing particles. However, high temperature melt radiation (i.e. molten steel) may hamper the shadowing, hence, the particle detection.
- **Thermal radiation techniques:** Based on pyrometry and infrared imaging Krauss et al. adopted DPV-2000 from Tecnar/Canada for the spray forming process and detected the particle impact velocity and size in the different process conditions [KRAU02].
- **Laser based techniques:** A number of laser-based sensors are available to carry out in-situ measurements of droplets and are adaptable even to hostile environments. PCSV-P (particle counting, size and velocity) is a forward laser scattering technique based on the focusing of a laser beam into a measuring volume through which particles flow. This technique was used in [HENE92]. EPSV works based on laser diffraction technique and an adapted version was used in [BOYK93]. PDA/LDA (Phase/Laser-Doppler-Anemometry) is commonly used for measuring droplets/particles size and velocity in sprays [TILL99, ZIES02]. The basic principles of this technique have been described in Chapter 4 of [HENE17].

2.4.2 Previous droplet studies in molten metal sprays

Ziesenis et al. demonstrated by PDA-based analysis that the atomization gas pressure has an influence on the mean particle diameter and velocity [ZIES03]. Figure 2-22 shows that the particle velocity increases at higher gas pressure and decreases with smaller particle diameter.

² These measurement techniques are also used in particle characterization of other processes. For a better description of each of the techniques the reader is referred to Chapter 6 of Metal Sprays and Spray Deposition, published by Springer (2017) [HENE17].

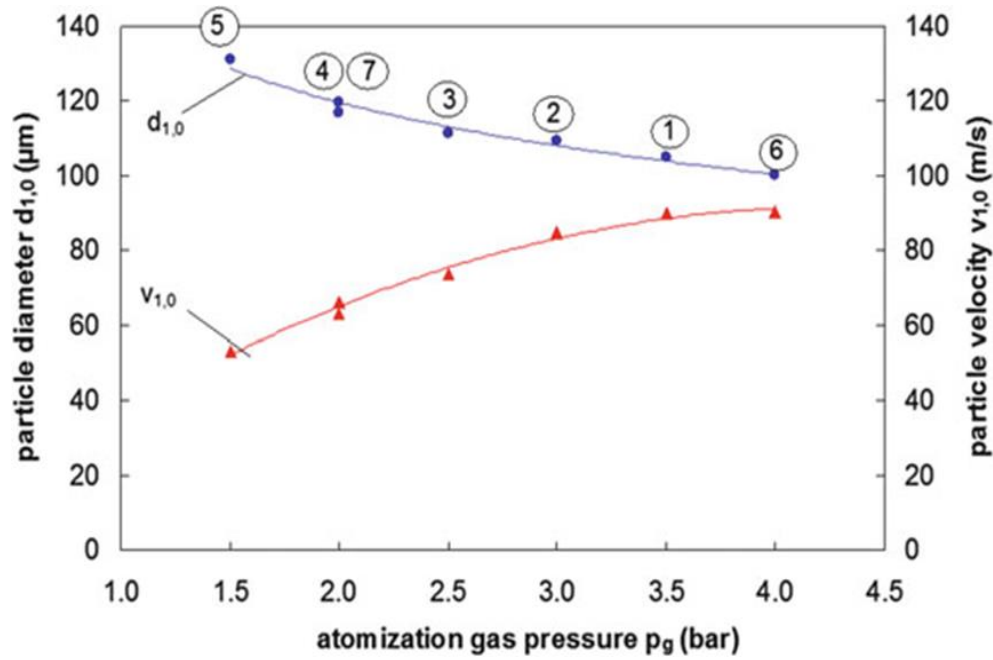


Figure 2-22 PDA results in copper (Cu) spray with a free-fall atomizer in the deposition zone. The figure is adopted from [ZIES03] in [KHAT17].

Tillwick et al. reported similar characteristics for copper and copper alloys, low carbon steel, aluminium alloys and tin in the radial direction of the spray cone [TILL99]. Krauss et al. compared the results between the DPV high-speed-pyrometer and PDA in the atomization of low carbon steel with constant process condition (melt super heat 150 K, gas pressure 0.35 MPa, spray distance 420 mm, radial distance 20 mm, pouring nozzle diameter 4 mm) [KRAU02]. Figure 2-23a shows that the values determined by PDA and the pyrometer are similar and the measured particle velocity decreases with increasing particle diameter. In addition, the authors compared three different melt materials (low carbon steel Ck35, tool steel X20Cr13, copper alloy CuNi) by pyrometer (DPV-2000) measurement [KRAU02]. Figure 2-23b demonstrates the influence of different materials at constant atomization pressure (0.5 MPa).

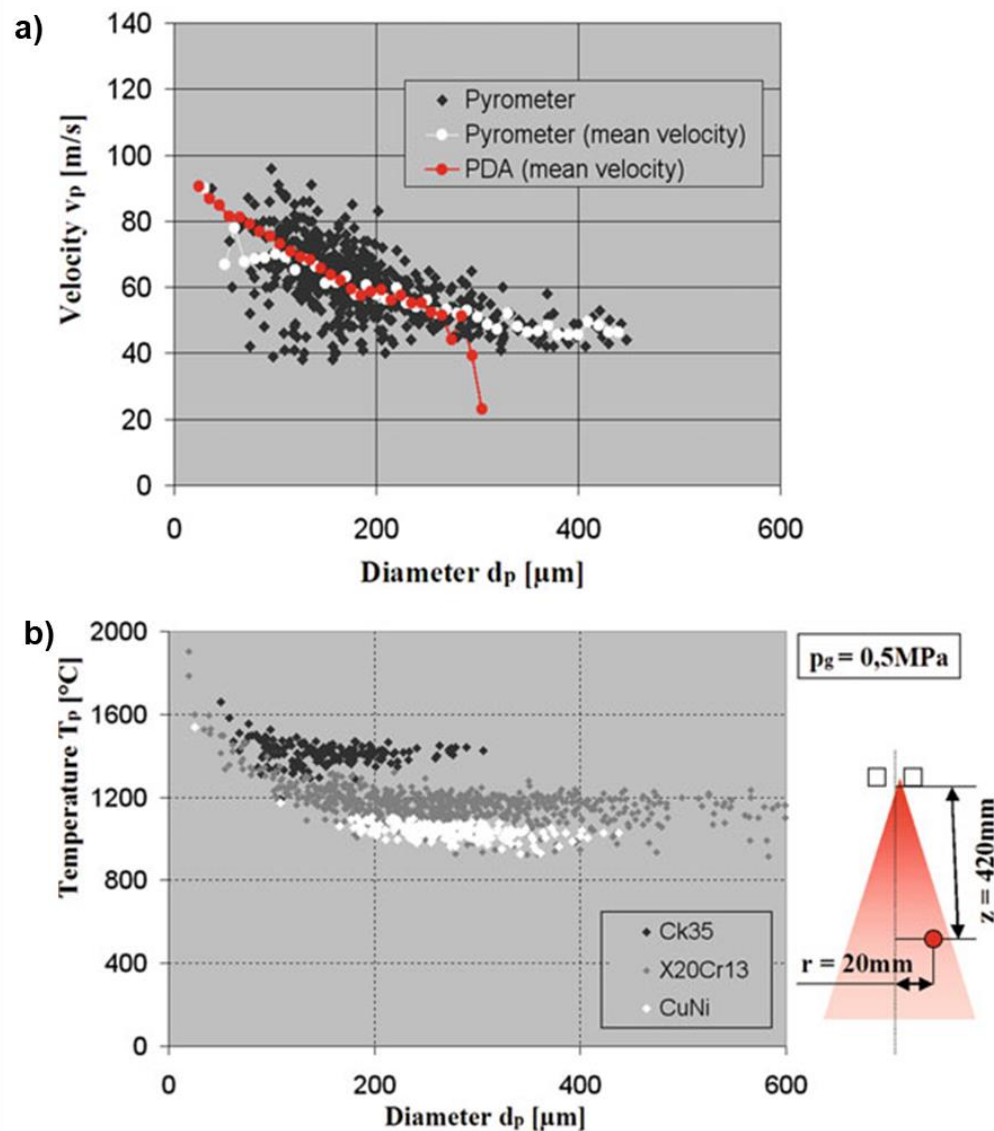


Figure 2-23 Particle size, velocity and temperature measurement in metal droplet spray **a)** comparison of pyrometer (DPV-2000) and PDA, **b)** influence of the different alloys. The figures are adopted from [KRAU02].

Besides in-situ measurements in the spray, numerical modeling and simulation is common to determine the spray conditions. Fritsching performed a multiphase flow simulation in the spray forming process and reported similar relations between the particle size and velocity [FRIT05]. In addition, the author reported how the particle velocity varies with flight distance in the spray.

2.5 Summary of the State of the Art

The spray forming technology is an established process as a rapid solidification method in the metal forming industry since about half a century. Near-net-shaped, semi-finished metal products with desirable geometries can be produced with the spray forming process. The main advantage of the process is the refined microstructure of the as-sprayed materials, which allows production of high alloyed materials. Usually, gas atomization is used for atomizing the superheated melt in spray forming. Free-fall atomizers (FFA) or close-coupled atomizers (CCA) are adopted for spray deposition. Free-fall atomizers provide more flexibility for producing larger products. However, higher porosity in the as-sprayed materials with FFA is one of the drawbacks of the spray forming process. Close-coupled atomizers spray with finer particles are also used in spray forming. In recent years, hot gas atomization has been introduced in metal powder production for producing finer particles with lower gas consumption.

Since porosity is the main concern of the as-sprayed materials in spray forming, therefore, numerous investigations have been carried out to understand the porosity formation. In the spray forming process porosities occur mainly in two types, cold porosity and hot or gaseous porosity. These porosities and final microstructure in the as-sprayed deposits are evolved based on different criteria like metallurgical, geometrical and thermal. Apart from these influencing principles, the droplets in the spray play as a decisive factor in spray forming. The droplets characteristics in the spray, i.e. droplets size, thermal behaviour, liquid fraction, velocity significantly define the properties of the final products. Therefore, in-situ measurement in metal sprays have been carried out to understand the process with different mechanisms in-situ spray diagnosis system. Among them pyrometry and laser based LDA/PDA techniques have shown suitable results in spray forming conditions.

Spray forming of tubular deposits has been already carried out mainly with free-fall atomizers, where porosity in the vicinity of the substrate was the main drawback. High yields and low porosities for small diameter tubes have been achieved with close-coupled atomizers, which makes this atomizer interesting for future developments. Investigations are needed to understand the process elaborately. Furthermore, investigation of the effect of hot gas atomization may open a new process window in spray forming. Based on these fundamental findings from earlier investigations, in the next chapter the objective and solution approaches of the thesis will be presented.

3 Objectives and Outline of Thesis

With recent technological advancements, the spray forming process has made it possible to produce high quality materials in near-net-shape. However, porosity formation in the produced deposits till is one of the main deficits of the spray forming process. Through the state of the art the main reasons for porosity formation have been depicted. The characteristics of the droplets and droplets deformation kinetics define the level of porosity in the as-sprayed materials. In spray forming of tubular deposits with free-fall atomizers, porosity especially in the vicinity of the substrate has been detected. Using close-coupled atomizers result in lower porosity for Cu alloy. However, the reason behind the lower porosity and higher yield are yet not understood. Higher droplets velocities of the close-coupled atomizer may affect the droplet kinetics. Introduction of hot gas in the process may further increase the droplet velocity, which may open a new process window for the process itself. Further understanding the mechanisms in the spray forming process would provide guidelines for future research and application in the industry. Therefore, the aim of this PhD thesis is to push understanding of the role and influence of droplet size and velocity in the spray forming process. The following central research hypothesis of this thesis is derived from the motivation and objective:

“In the spray forming process of tubular deposit higher spray droplet impact velocities lead to less porosity and increased yield.”

The larger droplets from a free-fall atomizer with comparatively longer deformation time and lower solid fraction during impact result in higher porosity in the deposit due to disintegration and the internal rupture during the impact. The smaller droplets from close-coupled atomization and the faster droplet velocity with hot gas will reduce the deformation time and result in high density deposits. The following working hypotheses are derived from the central research hypothesis:

Hypothesis 1: The porosity of a tubular deposit can be reduced by the smaller droplets sprayed by a close-coupled atomizer.

Hypothesis 2: The particle velocity in the spray can be increased by using hot gas in atomization even at similar droplet size.

Hypothesis 3: Decreased deformation times during droplet impact will result in high density materials and will extend the process window.

Hypothesis 4: The developed knowledge of improving production of spray formed tubes with advanced properties is transferable to other alloy systems.

Thesis outline and solution approach

Based on the working hypotheses, the solution approaches will be presented in this chapter.

Figure 3-1 illustrates the outline of the thesis working process.

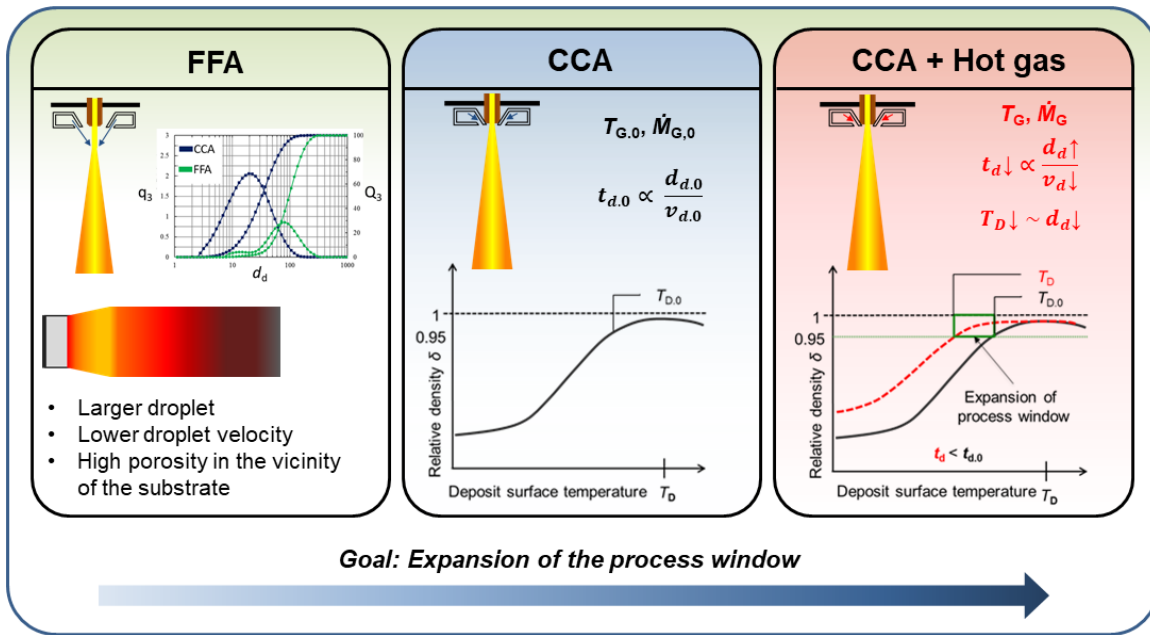


Figure 3-1: Graphical outline of the course of the thesis. In the PhD dissertation a close-coupled atomizer is adopted to spray form tubular deposits. The smaller droplet size by a close-coupled atomizer influence the porosity. Hot gas introduction reduces the droplet size and increase the droplet velocity, which further reduce the deposit surface temperature and the droplet deformation time. With faster droplet deformation highly dense materials can be produced at lower temperatures. (T_G – gas temperature, \dot{M}_G – gas mass flow rate, d_d – droplet diameter at hot gas, v_d – droplet velocity at hot gas, t_d – droplet deformation time at hot gas, T_D – deposit surface temperature at hot gas, Δh – specific enthalpy change, subscript 0 means cold gas atomization condition).

i) Adapting a close-coupled atomizer for spray forming of tubular deposits and finding optimal process parameters

- **Adapting close-coupled atomizer:** A close-coupled atomizer with provision of hot gas application is adapted for spray forming of tubular deposits. The expected smaller droplet sizes by CCA lead to higher solid fractions compared to FFA spray at impact, which may result in shorter droplet deformation time during impact (the deformation time t_d is proportional to the droplet diameter d_d Eq. 2-9). The porosity of the spray-formed tubular deposit with CCA is to be compared with deposits from FFA.
- **Optimizing process parameters for CCA:** In the spray forming process several parameters are vital for the material quality, e.g. substrate thickness, flight distance, gas-to-melt ratio (*GMR*). The process parameters are optimized for spray forming of tubes by CCA.

ii) In-situ temperature measurement: To gain insight into the spray forming process and the influence of process conditions on the porosity and microstructure of the deposits, in-situ measurement of temperatures (deposit surface and substrate) are to be carried out. The deposit surface temperature is measured by optical method and substrate temperature is measured by thermo-couples at different positions. The temperature measurement can be further used to validate the numerical model of the spray forming process.

iii) Particle velocity measurement at different gas flow rates

The droplet deformation time t_d depends on the particle velocity v_d during spray impingement in the deposition zone. The particle velocity is measured in the spray chamber at the position of impingement by Laser Doppler Anemometry (LDA). The effect of atomization gas temperature is analysed by measuring the particle velocity at identical gas pressures for the same particle size.

iv) Introduction of hot gas atomization in the spray forming process

Hot gas atomization is to be used in the spray forming process. Application of hot gas atomization may change the cooling behaviour of the spray-formed deposits and the faster particles produced by hot gas atomization may influence the droplet deformation in the deposition zone. Furthermore, hot gas may affect the initial substrate temperature T_s , which improves interfacial bonding and allows the process to be used to manufacture clad tubes to be implemented in surface coating. In addition, the influence of larger substrate diameter

on cooling behaviour of the deposit is to be investigated. The goal is to extend the spray forming process window.

v) Spray forming of Aluminium alloys

The acquired knowledge from the spray forming of steel tubes by a close-coupled atomizer is transferred to other alloys. For example, Aluminium alloys are spray formed to investigate the processability of the materials with CCA in tubular form. The porosity and microstructure of spray formed Al-deposits are compared with literature data with FFA and conventionally processed materials (casted).

4 Methodology and Experiments

In this chapter the selected methodology and experimental procedure will be discussed. Figure 4-1 illustrates an overview of the used methodology and experimental setups in this PhD thesis.

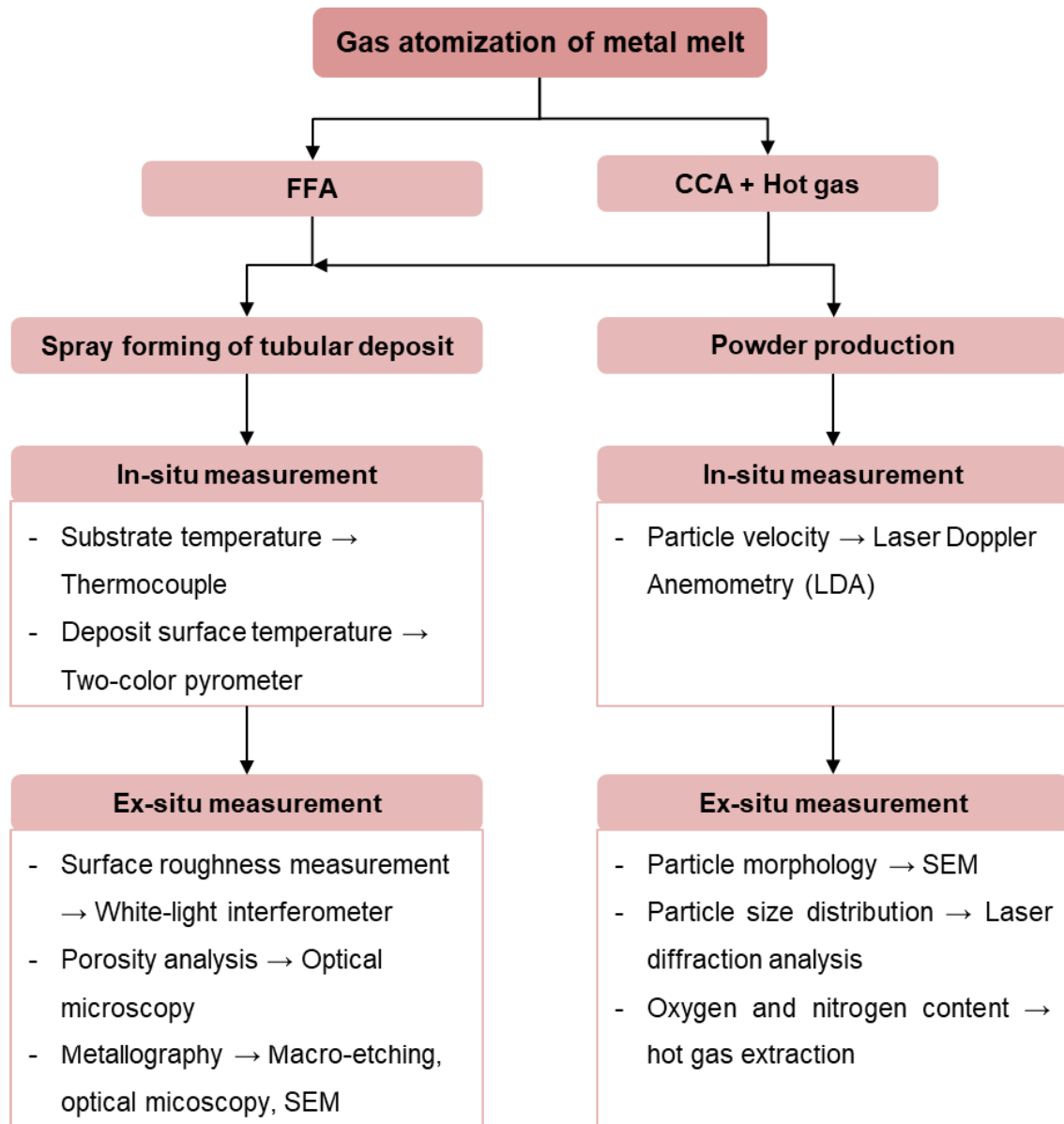


Figure 4-1: Overview of the used methodology and experimental procedure in this PhD thesis.

4.1 Close-coupled atomizer for spray forming

A close-coupled gas atomizer has been adopted for spray forming of tubular deposit. The gas atomizer is used to produce sprays and droplets with different cooling conditions that vary with particle size. The gas nozzle section can be changed from close-coupled atomization to free-fall atomization, which has been used to compare the deposit quality. The schematic layout of the spray forming system is shown in Figure 2-2. The spray forming setup system consist of four main components:

- i. A vacuum melting chamber with melt temperature up to 1750 °C
- ii. A spray chamber with a maximum particle falling distance of 4.8 m (which is also used for powder production)
- iii. A gas atomizer (which is changeable to free-fall atomizer)
- iv. A substrate holder with rotating and axial movement

In the melt chamber either Al_2O_3 (CA97-GK80/20, MiTec Middeldorf) or graphite crucibles are used. About 2 to 5 kg of feed stock material are melted in a protective environment consisting of N_2 or Ar. For spray forming of steel, the feed stock is heated up to 1000°C in a N_2 environment (N_2 supplied from the main process gas tank) and above 1000°C the N_2 environment is changed to an Ar environment (Ar supplied from a gas cylinder) to avoid N_2 diffusion to the steel. The melt temperature is held constant for 5 minutes at superheat temperature (about 200 K above the liquidus temperature) before atomization. In the crucible a stopper rod is placed to prevent the melt flow into the nozzle during the heating process. The stopper rod is removed mechanically by a pneumatic system a few milli seconds before the atomization process starts. The melt temperature is measured by a type B thermocouple placed in the stopper rod. A second type K thermocouple is placed inside the graphite susceptor, which is located in between the induction coil and crucible. The atomization gas pressure, melting chamber pressure, and differential pressure between the spray chamber and the vacuum vessel are also recorded. The gas flow rate is calculated based on the empirical model by [CIFT18].

The pouring nozzles are made of ceramic material (HeBoSint O120), Al_2O_3 (CA97-GK80/20, MiTec Middeldorf) or graphite (in case of Al-alloys and Cu-alloys). The ceramic material (HeBoSint O120) showed erosion by the running melt from the crucible to the atomization zone. Therefore, Al_2O_3 nozzles have been used for all the experiments (section 5.3). Graphite nozzles are used for graphite crucibles. 2 – 2.5 mm pouring nozzle diameters are used for the spray forming runs.

The melt chamber is constructed by several electrically polished ring segments and a conical collector to capture the solidified particles. A cyclone is connected with the spray tower to separate particles from the gas.

A slit jet type (slit of 0.8 mm) convergent-divergent close-coupled atomizer (CD-CCA-0.8) and a multi jet free-fall atomizer (20 holes with 1.1 mm diameter) are used as gas atomizer.

The substrate holder is fixed in the spray chamber. The substrate rotation and axial velocity can be controlled remotely by a control box. Sand blasted low carbon steel tubes with different diameters (90 mm, 110 mm and 133 mm) and wall thickness (3 – 6 mm) have been used as substrates.

4.1.1 Hot gas atomization

Hot gas atomization is performed by preheating the process gas by an electrical heat exchanger (Elmess – HG/SE – 56). The heated gas is brought into the atomization zone through an insulated piping system. The gas temperature is measured by a K-type thermocouple in the gas nozzle opening. The maximum gas temperature can reach up to 350 °C (623 K) by the system. The gas mass flow rate for hot gas atomization is calculated by the empirical model presented in Eq. 2-7.

4.1.2 Powder production for particle size analysis

In addition to the spray forming experiments, several melt atomization runs with the same equipment are performed to produce powder. The powders are produced both under the cold gas and hot gas condition. The produced powders are further sieved and analysed to investigate the effect of atomization conditions on the particle size distribution.

4.2 Materials selection

A bearing steel AISI 52100 (100Cr6) has been used for spray forming of tubes within the scope of this dissertation. The nominal chemical composition of the AISI is listed in Table 4-1. The selected steel is considered for different spray forming conditions: a) spray forming with a free-fall atomizer, b) spray forming with a close-coupled atomizer and c) spray

forming in hot gas atomization. Stainless steel AISI 316L was taken for verifying the effect of hot gas atomization on particle size, particle morphology, and N₂ pickup at elevated gas temperature.

Table 4-1 Nominal chemical composition of AISI 52100 (100Cr6).

Elements	C	Si	Mn	Cr	Fe
wt. %	0.93 – 1.05	0.15 – 0.35	0.25 – 0.45	1.35 – 1.60	balance

Table 4-2 Nominal chemical composition of AISI 316L (Fe – balance)

Elements	C	Si	Mn	Cr	Ni	Mo	S	P
wt. %	0.3	0.44	1.84	17.5	12.3	2.5	0.001	0.21

To verify the transferability of the knowledge to other alloying system, two commercial aluminium alloys Al-5083 and Al-6082 have been spray-formed. The nominal chemical composition of the selected aluminium alloys are listed in Table 4-3.

Table 4-3 Nominal chemical composition of spray-formed Al alloys in wt.% (Al – balance).

Alloy	Si	Mg	Mn	Fe	Cr	Cu	Zn
5083	0 – 0.4	4 – 4.9	0.4 – 1	0 – 0.4	0.05 – 0.25	0 – 0.1	0 – 0.25
6082	0.7 – 1.3	0.6 – 1.2	0.4 – 1	0 – 0.5	0 – 0.25	0 – 0.1	0 – 0.1

4.3 In-situ spray and deposit analysis

4.3.1 Deposit surface temperature

The deposit surface temperature is measured by means of 2-color pyrometer (Galaxy SC 12 model from Sensor Therm). The pyrometer is placed parallel to the deposit (Figure 4-2). The temperature is measured in a line scan. The length of the pyrometer line-scan is 180 mm to 210 mm.

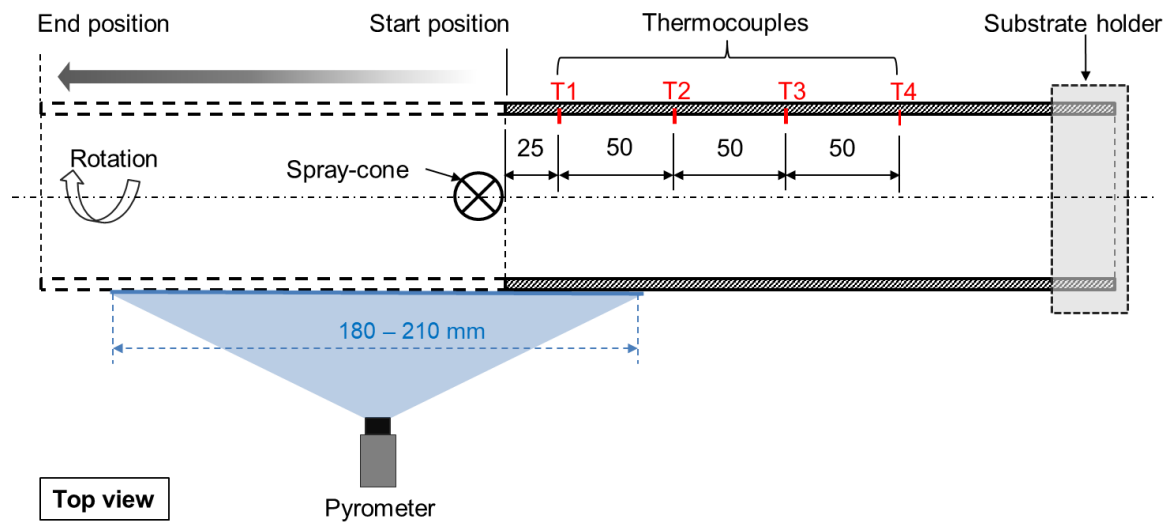


Figure 4-2: Line-scan range of the pyrometer and position of thermocouples in the substrate. The figure is adapted from [HUSS20a].

4.3.2 Substrate temperature

The substrate temperatures at four different positions in the longitudinal direction are measured by thermocouples (Figure 4-2). The thermocouples positions are 0.5 mm below the substrate surface. The first thermocouple, T1, is located 25 mm from the substrate end and the subsequent thermocouples (T2, T3, and T4) are placed in 50 mm distances along the substrate following T1. The substrate is positioned adjacent to the spray cone at start position.

4.3.3 Particle velocity (LDA)

The LDA anemometer working principle is based on the Doppler shift of a radiated laser source scattered by a moving object. The frequency change of the scattered radiation is related to the velocity of the moving object [ABBI74]. The Laser Doppler Anemometry (LDA) device basically consists of two crossing laser beams and an optical detector (transmitting and receiving optics). The measurement is conducted at the measuring volume, which is the intersection area of the two laser beams. The structure in the measuring volume can be characterized by parallel planes of alternating light intensity (fringe pattern). When a particle passes through the measuring volume the scattered light creates a corresponding signal voltage in the photodetector, which is the Doppler bursts (see Figure 4-3). The frequency of the Doppler burst is proportional to the particle velocity. At smaller distances to the atomizer, LDA measurements in the spray typically are not possible owing to the high particle concentration, thus leading to crossover signals of multiple particles in the measurement volume [ZIES02].

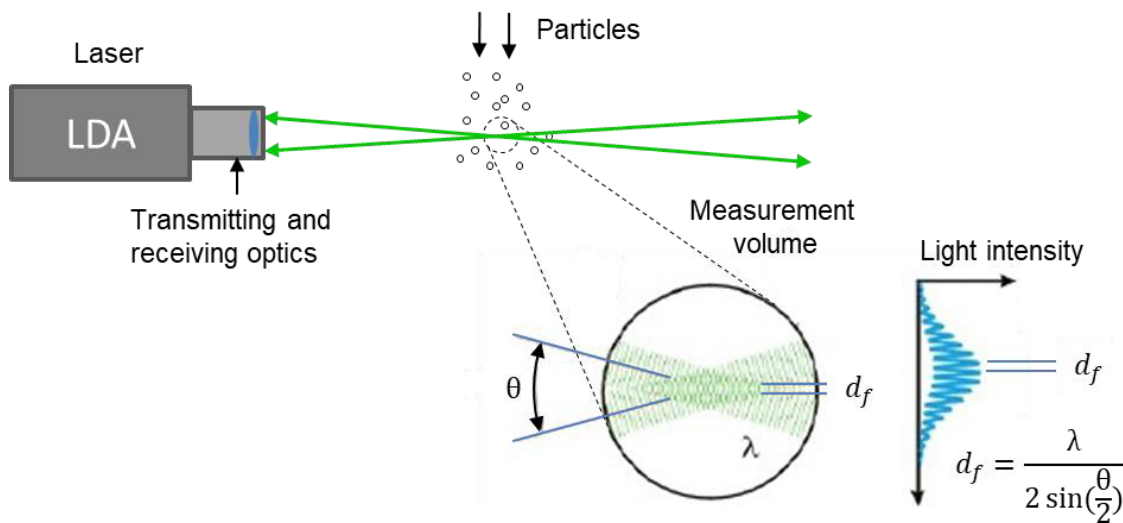


Figure 4-3: Arrangement and measuring principle of Laser Doppler Anemometer (LDA) in back scattering arrangement. The figure is adopted from [DANT20].

In this study, the velocity of the particle has been measured at the center of the spray at the flight distance of 130 mm (at the position of the substrate in spray forming) by the Laser Doppler anemometry (LDA) technique with a Laser Doppler System (from TSI, TR – SS – 2D) in back scattering arrangement. Figure 4-4 illustrates the LDA measurement setup and the parameters used for the measurement. Instead of measurement in a spray of molten

metal droplets, a cold metal powder (AISI 52100 steel powder, size fraction of 63 – 90 μm) is injected through the pouring nozzle. The gas from the atomizing nozzle was flown in the atomization chamber.

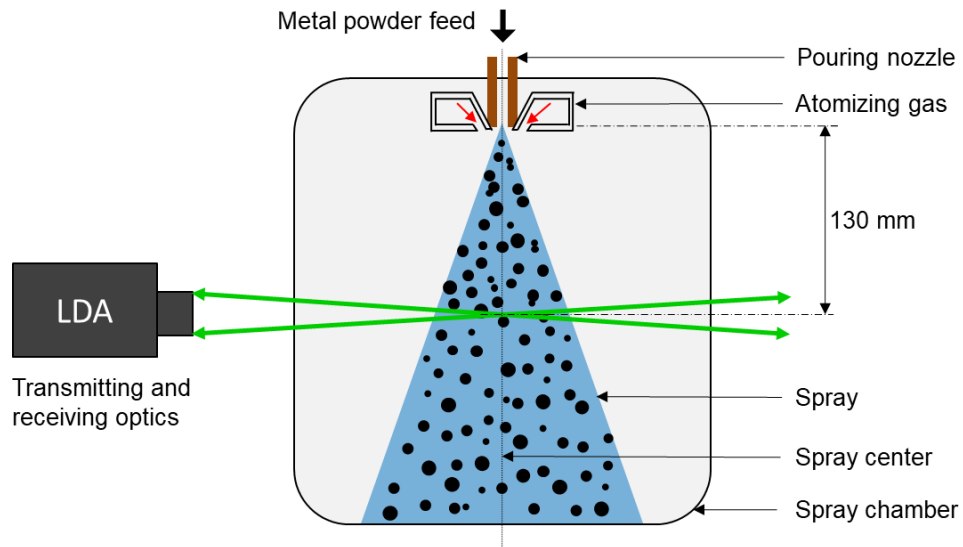


Figure 4-4: Schematic diagram of LDA particle velocity measurement (back scattering arrangement) in the spray chamber. The figure is adopted from [HUSS20b].

4.4 Ex-situ materials characterization

Figure 4-5 shows a representative deposit and deposit contour as sprayed. At the beginning of the spray forming process the edge of the substrate is placed directly below the spray and then moved axially with time. At the end of the deposit the deposit thickness decreases due to lower mass flow rate with reduced melt pressure in the nozzle at the end of the process.

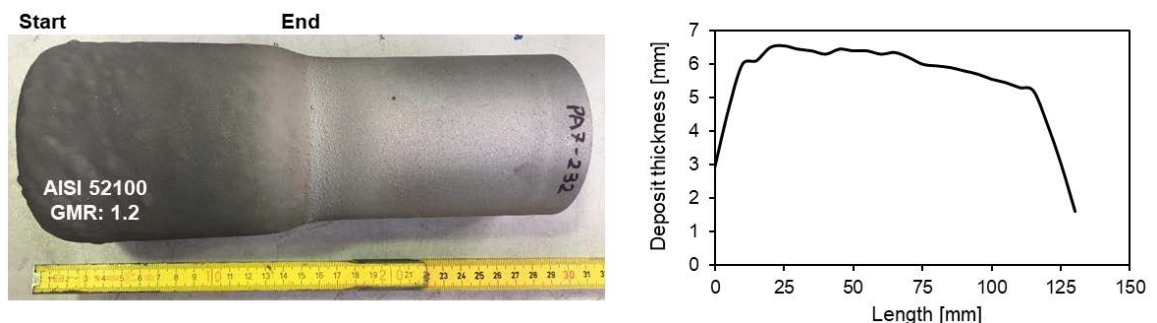


Figure 4-5: a) Photo and (b) contour of a spray-formed tubular AISI 52100 steel deposit (PA7-230).

Ring segments have been taken from the as-sprayed tubes by electric discharge machining (EDM) due to the high hardness of the as-sprayed deposit. The taken samples are ground and polished for the investigation of the resulting microstructure and porosity. Figure 4-6 shows a ring segment of spray-formed tubular deposit. P1 is close to the outer surface (about 2 mm below the surface), P2 is at the deposit center/core, and P3 is near the inner surface (about 2 mm above the substrate).

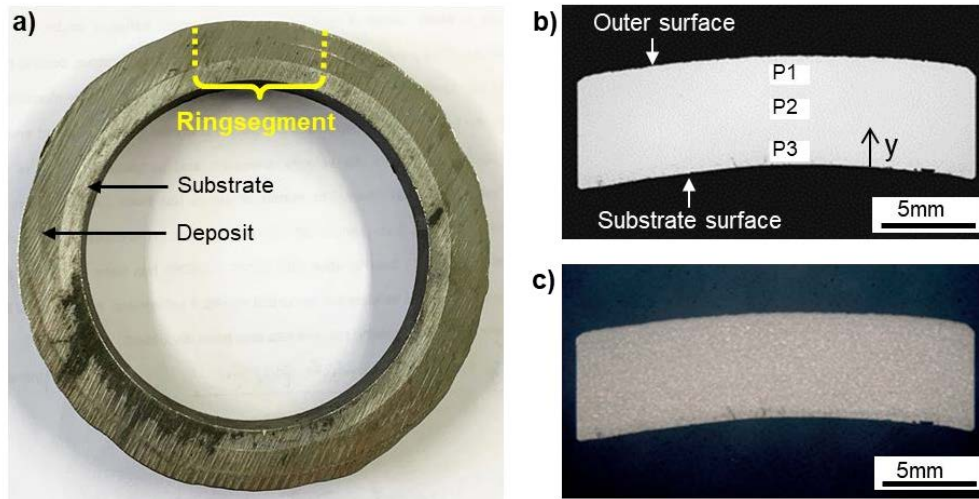


Figure 4-6: a) Ring of a spray-formed tubular deposit (GMR: 1.6, atomization gas temperture: RT, PA7-170); b) ring segment before macro-etching; c) after macro-etching. Micrographs are taken at three positions (P1, P2 and P3). P1 is near the outer surface, P2 is at the deposit core and P3 is near the inner surface. The figures are adopted from [HUSS20a].

4.4.1 Surface roughness

The deposit surface roughness was measured by white light interferometry (Taylor Hobson – Taylsurf CCI HD). The white light interferometry is a non-contact and rapid optical method for surface height measurement on 3-D structures with surface profiles varying between tens of nanometers and a few centimeters [ADI08]. The measuring principle includes scanning the object through Z axis in noncontact mode, using white light and measuring the visibility of the interference fringes (degree of coherence) at each pixel in the image [KUWA97]. Figure 4-7 illustrates a scheme of the instrument for this technique. The light beam is emitted from an illumination source, which is further divided into two paths by a beamsplitter. One beam goes directly to the measuring surface and the other beam to the white light interferometer (Mirau interferometer) consisting of a microscopic object, a semi-transparent mirror, and a reference mirror. Afterwards, both beams are reflected back and

combined in the beamsplitter to create interference fringes. These interference fringes are recorded by a charge-coupled device (CCD) camera. From the interference pattern the surface profile can be obtained, the resulting constructive fringes along the scanning axis give the height of the surface at that point, and their variation along the surface gives information about the variation on the surface roughness [ADI08]. The surface roughness of the deposit segments, S_a (arithmetical mean height, ISO 25178) values were measured in a measurement area of $335\ \mu\text{m} \times 335\ \mu\text{m}$.

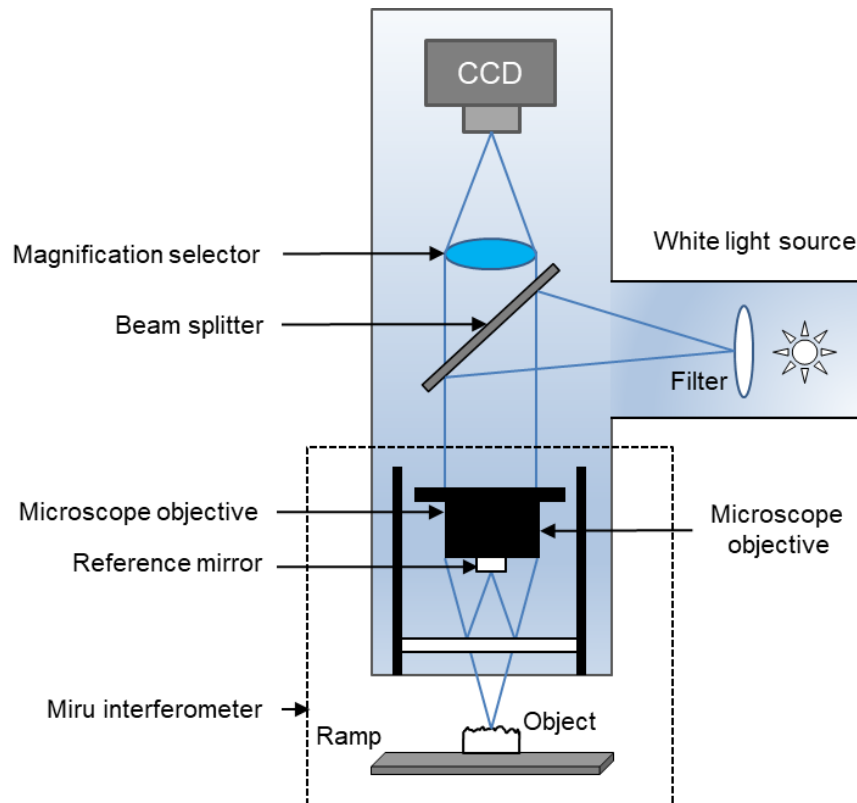


Figure 4-7: Schematic diagram of scanning white-light interferometer.

4.4.2 Porosity analysis

The porosity is measured from a polished ring section by image analysis (Leica Qwin 2.4). The pore content is determined as a percentage of the pore area present within each measurement field ($\sim 370\ \mu\text{m} \times 370\ \mu\text{m}$). The mean porosity percentage is plotted against the deposit thickness from the near substrate region to the outer surface region. Figure 4-8 shows an example of porosity measurement from a spray-formed deposit (PA7-170, GMR = 1.6, cold gas atomization with CCA) ring segment.

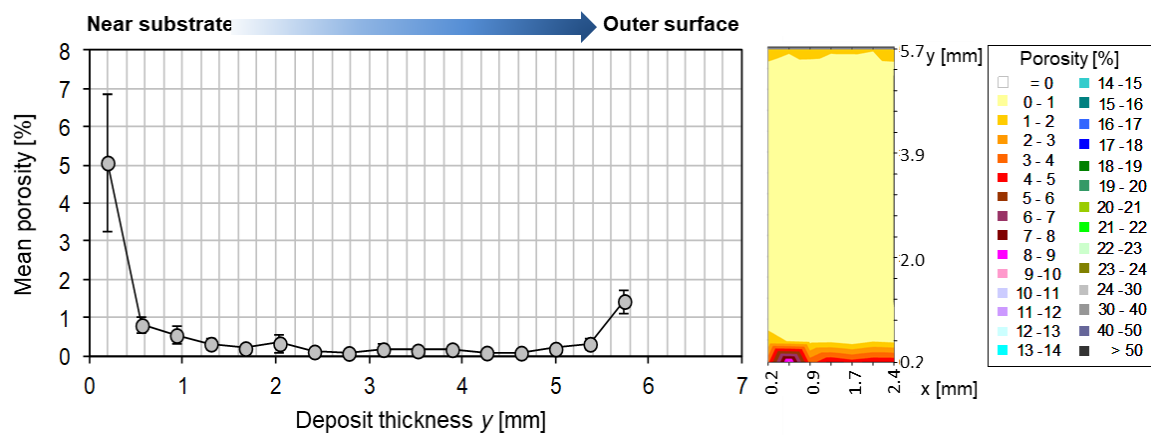


Figure 4-8: Porosity in terms of surface area in deposit thickness direction from substrate to outer surface ($GMR = 1.6$, PA7-170). The figure is adapted from [HUSS20a].

4.4.3 Metallography

For microstructure studies, ring segments were taken from the tubular deposit, metallographic samples and have been ground, polished and etched. The etching mediums for different alloys are listed in Table 4-4.

Table 4-4 List of etching solutions and conditions for different materials.

Material	Etching 1	Etching 2
AISI 52100	Nital solution	Picric acid at 50 °C
Al-5083	Sulfuric acid and hydrofluoric acid solution	Potassium permanganate and solidum hydroxide solution
Al-6082	Sulfuric acid and hydrofluoric acid solution	Potassium permanganate and solidum hydroxide solution at 30 °C

4.4.3.1 Optical microscopy

The etched samples have been analyzed with optical microscopy. The grain size is measured from the optical microscopy images, using the intercept method (DIN EN ISO 643).

4.4.3.2 SEM

The ground, polished and etched as-sprayed samples and particles are analyzed with an SEM device to determine the particle morphology and surface quality (Carl Zeiss, SUPRA 40 equipped with a Bruker XFlash 6/30 EDX detector).

4.4.4 Powder characterization

The atomized powders have been sieved below 200 μm (CCA) to remove the unwanted chips and flakes. Afterwards, the powders are divided with a vibratory feeder (DR100, Retsch) and rotating powder divider (PT100, Retsch). The divided powders are collected in 8 glass bottles. A representative sample fraction (1/8 of the entire powder) is taken for further analysis.

4.4.4.1 Laser diffraction analysis

The particle size distribution has been measured by a laser diffraction system (Mastersizer 2000, Malvern; ISO 13320). The sieved powders are dispersed with water and delivered to the optical bench, where the scattering patterns of the particles are detected. A detector array made up of several individual detectors within the optical bench collects the light scatter from a range of angles (Figure 4-9). All the detected information from each individual detector are accumulated in one measurement and analyzed by the Malvern software using Fraunhofer or Mie theory. Despite the high accuracy and resolution, the system considers ideal spherical particles and can only be used to measure particle sizes (no shape measurement is possible). Nine measurements for each powder have been conducted and averaged.

4.4.4.2 Oxygen and Nitrogen analysis

The oxygen, nitrogen content in the atomized powders have been measured by hot gas extraction method (An ELTRA ONH-2000). Five measurements were performed for each of the powder and average of the measured value is taken.

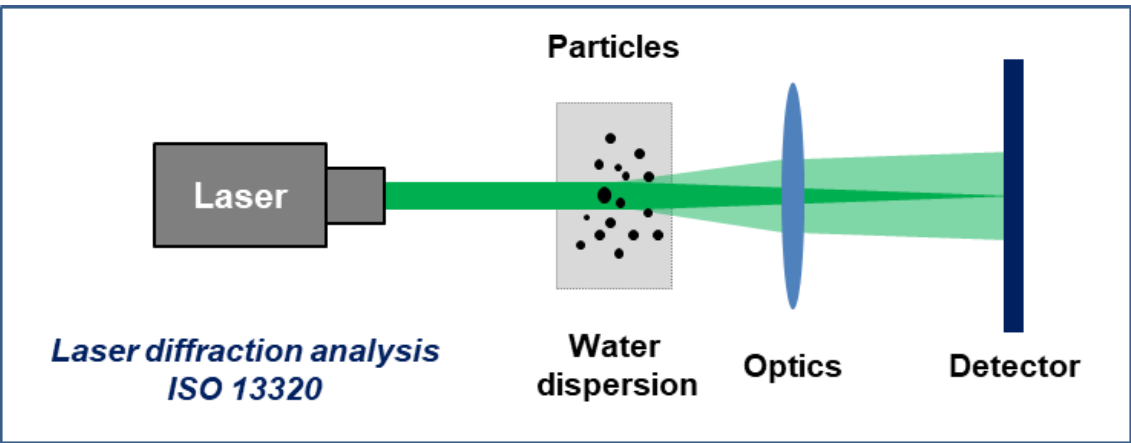


Figure 4-9: Measuring principle of laser diffraction analysis of metal powders.

4.4.4.3 Error in measurement techniques

Several errors are observed during the experimental procedures. For example, the contact point of the thermocouples could vary. The thermocouple also shows a slight deviation in the temperature measurement. The two-color pyrometers used in this work also have deviations from the actual temperature, since the absorptivity of the medium and the environment can be different for each atomization process. During the Laser Doppler Anemometry (LDA) measurement, the spray center also fluctuates depending on the gas pressure. Possible errors during the measurement are listed in Table 4-5.

Table 4-5 Error in adopted measurement techniques.

Measurement technique	Error
Type K thermocouple	$\pm 2.2\text{ }^{\circ}\text{C}$ or 0.75%.
Two-color pyrometer	May differ $\pm 50\text{ }^{\circ}\text{C}$ from the actual temperature due to absorptivity of a medium. Reproducible for a constant medium.
Laser Doppler Anemometry (LDA)	The adjustment of the laser at the spray center may differ $\pm 2\text{ mm}$.

5 Results and Discussion

5.1 Comparison of CCA with FFA

The mean particle size in a spray from a close-coupled atomizer (CCA) is reduced compared to a free-fall atomizer (FFA) (see Figure 2-5). Based on that observation a ***hypothesis 1: “the porosity of a tubular deposit can be reduced by the smaller droplets sprayed by a close-coupled atomizer”*** has been proposed. In this section the hypothesis 1 is investigated and discussed in detail. Several spray forming experiments are performed with AISI 52100 steel. The key parameters varied in the experiment series are listed in Table 5-1. All the process parameters of spray forming runs can be found in Appendix (Table A-1).

Table 5-1 Key process parameters varied in section 5.1.

Atomizer	Substrate $\varnothing_s \times l_s$ [mm]	Substrate thickness [mm]	Gas temperature T_G [°C]	Gas pressure [MPa]	GMR [-]
CCA/FFA	90 x 270	2.9 – 6.3	20 (RT)	0.8 – 2.0	1.4 – 2.9

The microstructure of the spray-formed AISI 52100 steel in the three regions of the as-sprayed representative deposits are shown in Figure 5-1. The deposit segments are taken 20 mm away from the deposit starting end. The microstructure exhibits equiaxed pearlite with fine carbides at the primary austenite grain boundaries. The grain size at the outer surface is smaller while the grain size in the deposit center region of the deposit is larger at the deposit with close-coupled atomizer (Figure 5-1a). This variation is due to differing rates of cooling and solidification. Particularly, the microstructure in the vicinity of the substrate shows smaller grain sizes, which indicates more intensive cooling in the vicinity of the substrate. The pearlite spacing depends on the cooling rate of the steel [BLEC11]. The interlamellar pearlite spacing is also different at the outer surfaces of the deposit and in the center of the deposit, confirming that the cooling conditions in the various regions are different. The deposit with free-fall atomizer shows a similar trend of the grain structure (Figure 5-1b). In comparison with the AISI 52100 tubes spray-formed using a free-fall atomizer (as shown in Figure 5-1), the microstructure of the tubular deposit using a close-coupled atomizer is at least one order of magnitude finer.

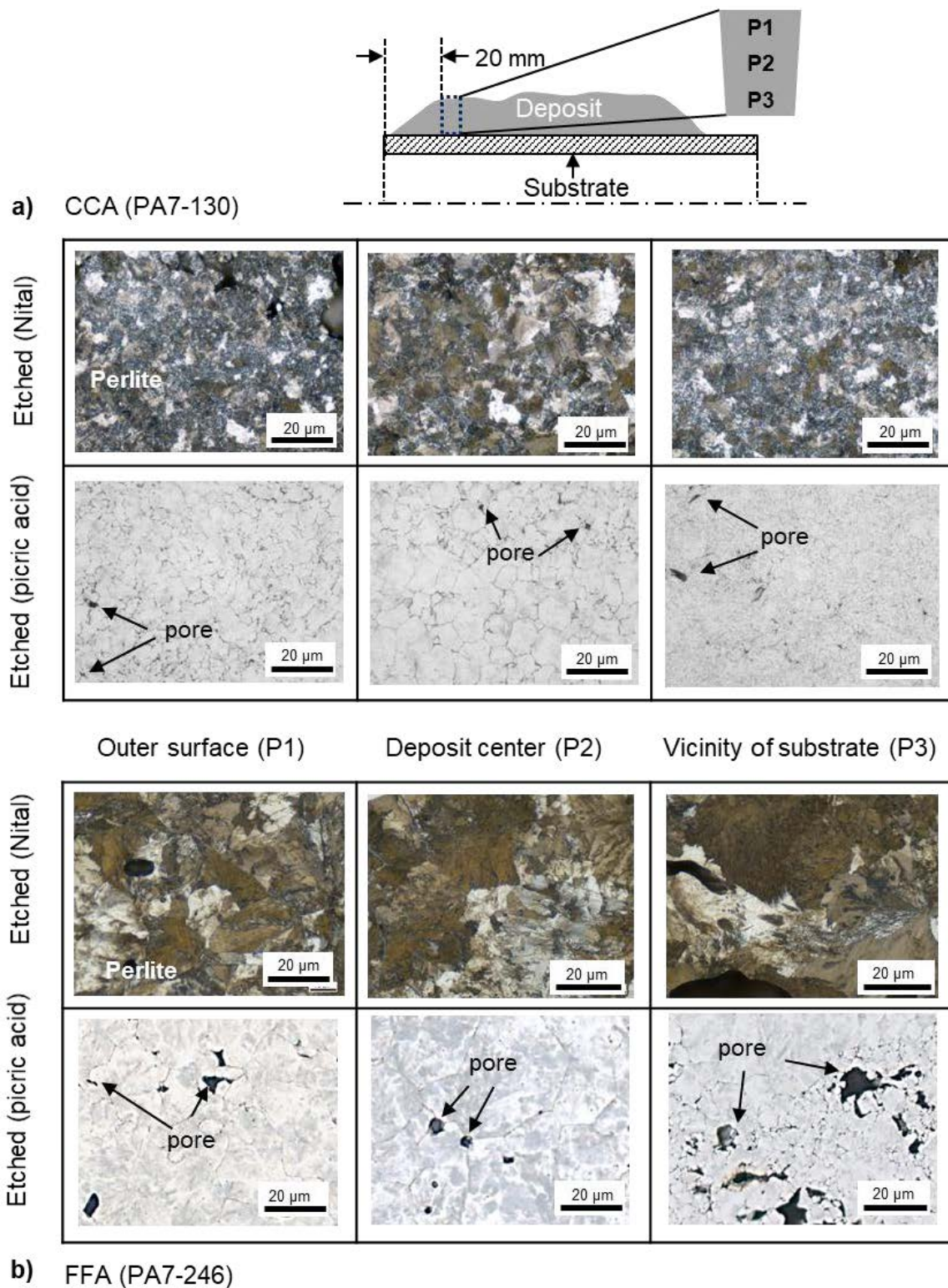


Figure 5-1: Micrographs of the representative tubular AISI 52100 deposit spray-formed with a) close-coupled atomizer (CCA) and b) free-fall atomizer (FFA). Here, PA7 is the atomization setup name and the three digit number is designated for individual run number.

The porosity profiles of tubular deposit spray-formed using a free-fall atomizer alongside porosity profiles achieved using a close-coupled atomizer are shown in Figure 5-2. The deposits spray-formed using a close-coupled atomizer result in a much better porosity profiles compared to the deposits spray-formed with a free-fall atomizer. It can be seen that the variation of process parameters (GMR, deposit thickness, substrate thickness) hardly showed any significant differences in the porosity profiles, except in the inner surface region of the deposits for spray forming with close-coupled atomizer. Therefore, the substrate thickness of 5 mm is used as standard for later experiments. The microstructure refinement in the tubular deposit can be attributed to high cooling and solidification rates due to the high surface area-to-volume ratio of the droplets generated by close-coupled atomizers (see Section 2.2.3). The intensive cooling in this study rarely shows high amount of cold porosity, as presented in the tubular deposits via free-fall atomizer. This indicates that the faster droplet velocity and the smaller droplet size related to the use of close-coupled atomizers may have reduced the cold porosity.

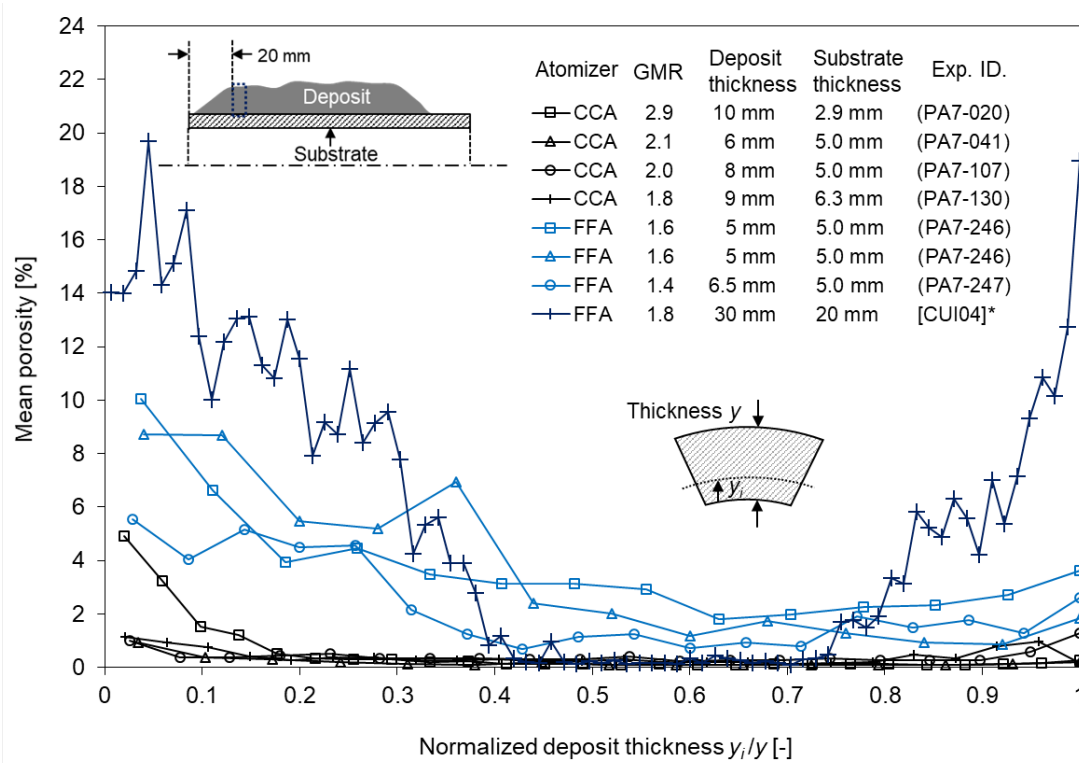


Figure 5-2: Porosity distribution of tubular AISI 52100 steel deposits spray-formed with close-coupled atomizer (CCA) and free-fall atomizer (FFA). Deposit section taken from deposit start position measured by image analysis (measurement field: $\sim 370 \mu\text{m} \times 370 \mu\text{m}$). The process parameters with Exp. ID is listed in the Appendix (Table A1). * Data from Cui et al. [CUI04] for comparison.

5.2 Optimizing process parameters for CCA

In the previous section (5.1) it is shown that spray forming with close-coupled atomizer reduces the porosity for similar geometries of steel tubes compared to a free-fall atomizer. However, the process conditions also may influence the porosity profiles among the deposits. To further understand the influence of process parameters on the as-sprayed tubular deposit several investigations have been conducted. In the spray forming runs the atomization gas pressure was changed after half of the spray forming time to vary the gas-to-melt ratio (*GMR*) in a single experiment, except one run (Run-3/PA7-170, representative deposit). The varied process parameter in this section is listed in Table 5-2. The process parameters of spray forming runs can be found in Appendix (Table A-2) in details.

Table 5-2 Key process parameters varied in section 5.2.

Atomizer	Substrate thickness [mm]	Substrate velocity [mm/s]	Gas temperature [°C]	Gas pressure [MPa]	GMR [-]
CCA	5	2 – 3	20 (RT)	0.8 – 1.2	1.1 – 1.9

5.2.1 Microstructure and porosity analysis

5.2.1.1 Microstructure

The microstructure and the grain size of the as-sprayed material depict the information about the cooling condition. Figure 4-6 show the ring segments of the representative tubular deposit from deposit start position. The ring segment was taken at 20 mm distance from the deposit starting edge (close to the position of Thermocouple T1 (see Figure 4-2). For further microstructure analysis the ring segment has been divided into three areas in deposit thickness direction (Figure 4-6). All the deposits show equiaxed pearlitic microstructure with fine carbides at the primary grain boundaries as mentioned in the previous section (5.1). The average grain sizes for different spray forming conditions (*GMR* of 1.1 – 1.9) are listed in Table 5-3. The average grain size in the deposit center (P2) is larger than at the deposit surface region (P1) and in the vicinity of the substrate areas (P3), due to different cooling conditions and solidification rates. The average grain size in the outer surface region and in the vicinity of the substrate region are about 64 μm and 60 μm , respectively (Figure 5-3). The average grain size in the deposit center is about 81 μm . A difference in interlamellar

perlite spacing is also observed close to the substrate region and at the deposit surface, which depicts the variation of cooling and solidification conditions in the different region in deposit thickness direction (Figure 5-3).

Table 5-3 Grain size at different spray forming condition in spray-formed tubular AISI 52100 deposits.

Experiment (ID)	GMR	Avg. grain size at P1 [μm] (Outer surface)	Avg. grain size at P2 [μm] (Deposit center)	Avg. grain size at P3 [μm] (Vicinity of substrate)
Run 2 (PA7-169)	1.1	74.8	101.4	70.9
Run 2 (PA7-169)	1.3	61.9	66.9	42
Run 3 (PA7-170)	1.6	63.8	81.4	60.1
Run 4 (PA7-173)	1.3	60.1	79.5	64.3
Run 4 (PA7-173)	1.9	52.1	62.8	- *
Run 5 (PA7-174)	1.2	84.3	81.4	54.2
Run 5 (PA7-174)	1.5	72.3	54	- *

*Grain size cannot be measured due to high amount of porosity.

5.2.1.2 Porosity

Porosity in spray formed materials is one of the main drawbacks of the spray forming process. The spray forming technique can be used to generate thick layers of coating on rods and tubes if the porosity can be minimized. In industrial practice the thermal spraying process is used for various protective coatings in layers smaller than 1 mm [BERG15]. In thermal spraying a concentrated heat source is used to melt the feedstock materials (powder, wire, rods) and the resulting molten droplets are ejected with high kinetic energies to the surface of the substrate [VUOR14]. Similar to thermal spraying, the spray forming process also allows for the deposition of molten droplets onto a substrate. The ability to coat a substrate surface utilizing the melted feedstock materials directly is a major advantage of the spray forming process [HUSS20a]. The production rates in the spray forming process are much higher compared to thermal spray techniques. Therefore, the porosity of the as-sprayed deposits is studied in detail.

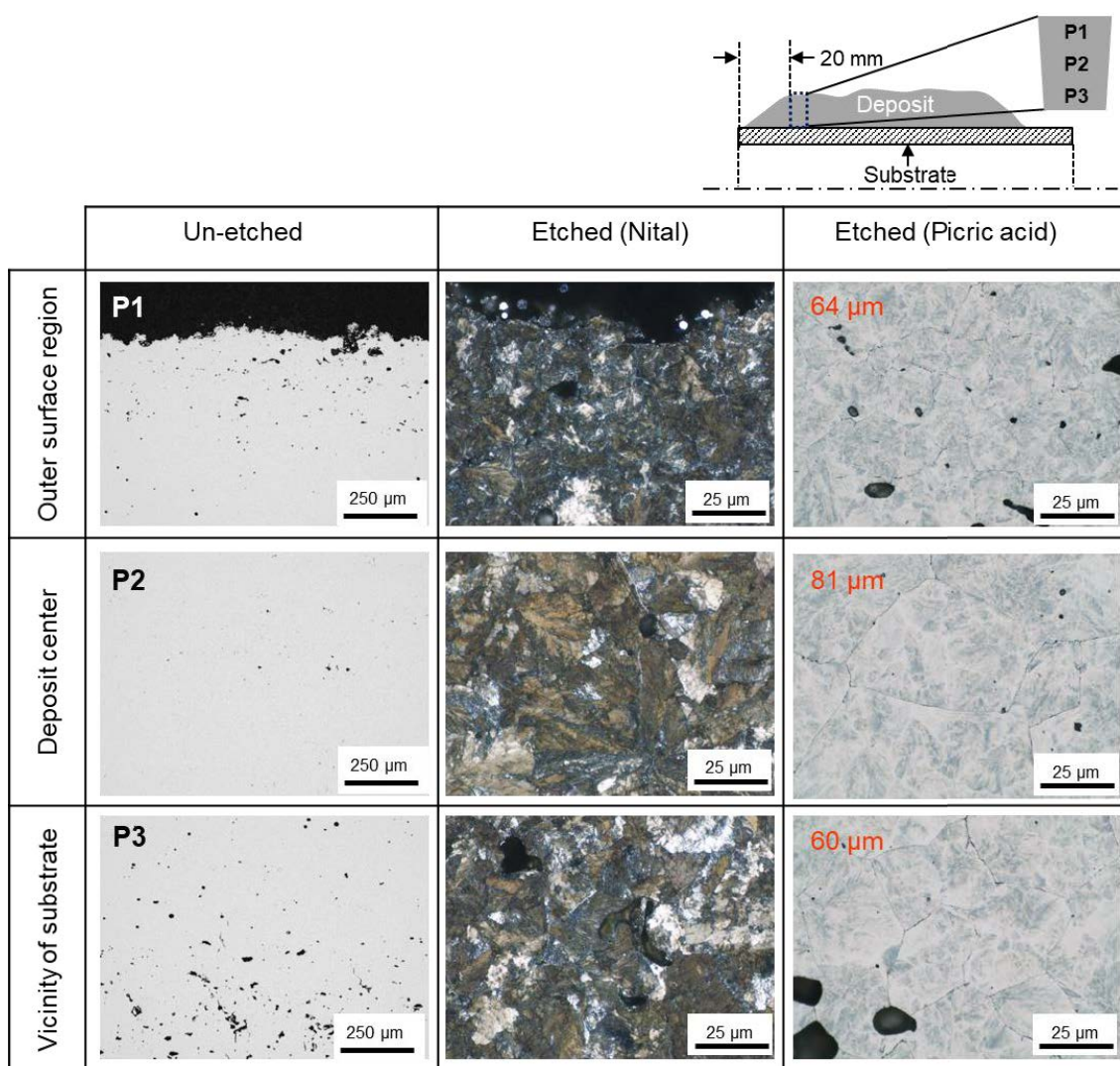


Figure 5-3: Micrographs of the spray-formed tubular AISI 52100 deposit (Run 3 (PA7-170)/ GMR: 1.6) with a close-coupled atomizer, before and after etching. The positions are same as Figure 4-6. The figure is adopted from [HUSS20a].

The images of the un-etched samples in Figure 5-3 show the pore structure in three (P1, P2, and P3) different regions (Run 3 (PA7-170) / GMR: 1.6). In the vicinity of the substrate region (P3) irregularly shaped interstitial pores (named cold porosity [HU00]) are observed. In the deposit center (P2) the smaller circular pores are found, mainly at the interior of the grains or at the grain boundaries. Near the outer surface region higher amounts of interstitial pores are found in the grain interior, mainly gas pores (circular shaped larger pores). The position of the deposit segment also plays an important role in the amount of porosity. Figure 5-4 shows that a high amount of porosity is found in the vicinity of the substrate at the end of the deposit. Two ring segments were taken from each of the spray-formed

deposits, one from the deposit start position (near T1 region) and another from the deposit end position (near T3 region). The porosity in the vicinity of the substrate increases with increasing *GMR* and gas mass flow rate \dot{M}_G in all the deposits. For example, for Run 2 (PA7-169) at a *GMR* of 1.1 and at gas mass flow rate \dot{M}_G of 316 kg/h the porosity in the vicinity of the substrate region is about 2% and at a *GMR* of 1.3 and at gas mass flow rate \dot{M}_G of 385 kg/h the porosity is about 22%. Similarly, at Run 1 (PA7-168) and Run 4 (PA7-169) the porosity in the vicinity of the substrate region increases with increasing *GMR* and gas mass flow rate \dot{M}_G . For Run 3 (PA7-170), the *GMR* and the gas mass flow rate \dot{M}_G were constant and porosity profiles are similar along the deposit length.

For a better understanding of the influence of the deposit length on porosity, several samples were taken in longitudinal direction of the tubular deposit from Run 2 (PA7-169) (Figure 5-5). Each sample is approximately 10 mm distance from the next sample. The first half of the deposit was sprayed at a *GMR* of 1.1 (represented by the black points in Figure 5-5a) and the second half of the deposit was sprayed with a *GMR* of 1.3 (represented by blue crosses in Figure 5-5a). It is observed that the porosity increases in the vicinity of the substrate from deposit start position to the deposit end position. Along with the increasing mean porosity in the vicinity of the substrate (from 2% to 23%), the thickness of the porous layer (mean porosity above 0.5 %) also increases by 2%. The porous layer thickness is about 0.5 mm at the start and about 4 mm at the end for a deposit length of 180 mm (Figure 5-5b). The reason for the increased porosity in the vicinity of the substrate is that previously solidified droplets impinge on the substrate, which re-bounce from the nearby sprayed deposit. These pre-solidified droplets also increase the roughness of the surface and increase the porosity. In addition, overspray particles (solid or semi-solid) are circulating in the spray chamber and may adhere to the substrate surface outside the spray zone (primary deposition zone Figure 5-6). Similarly, some particles from the periphery of the spray cone adhere on the adjacent substrate surface. These particles may create a porous layer on the substrate surface. With time, more over-sprayed particles are deposited on the substrate surface outside of the primary deposition zone, which facilitate shadowing [HU00] by increasing the surface roughness of the substrate. The increasing surface roughness in the deposition zone further promotes void formation. Usually two conditions may arise on the rough surface deposition: i) separation between the deposit surface and the spreading droplets; ii) splashing of the liquid on an irregular deposition surface. Both conditions contribute to void formation and entrapment of atomizing gas. The pre-deposited rough surface also changes the impact angle of the upcoming droplets, which leads to higher porosity [UHLE07a].

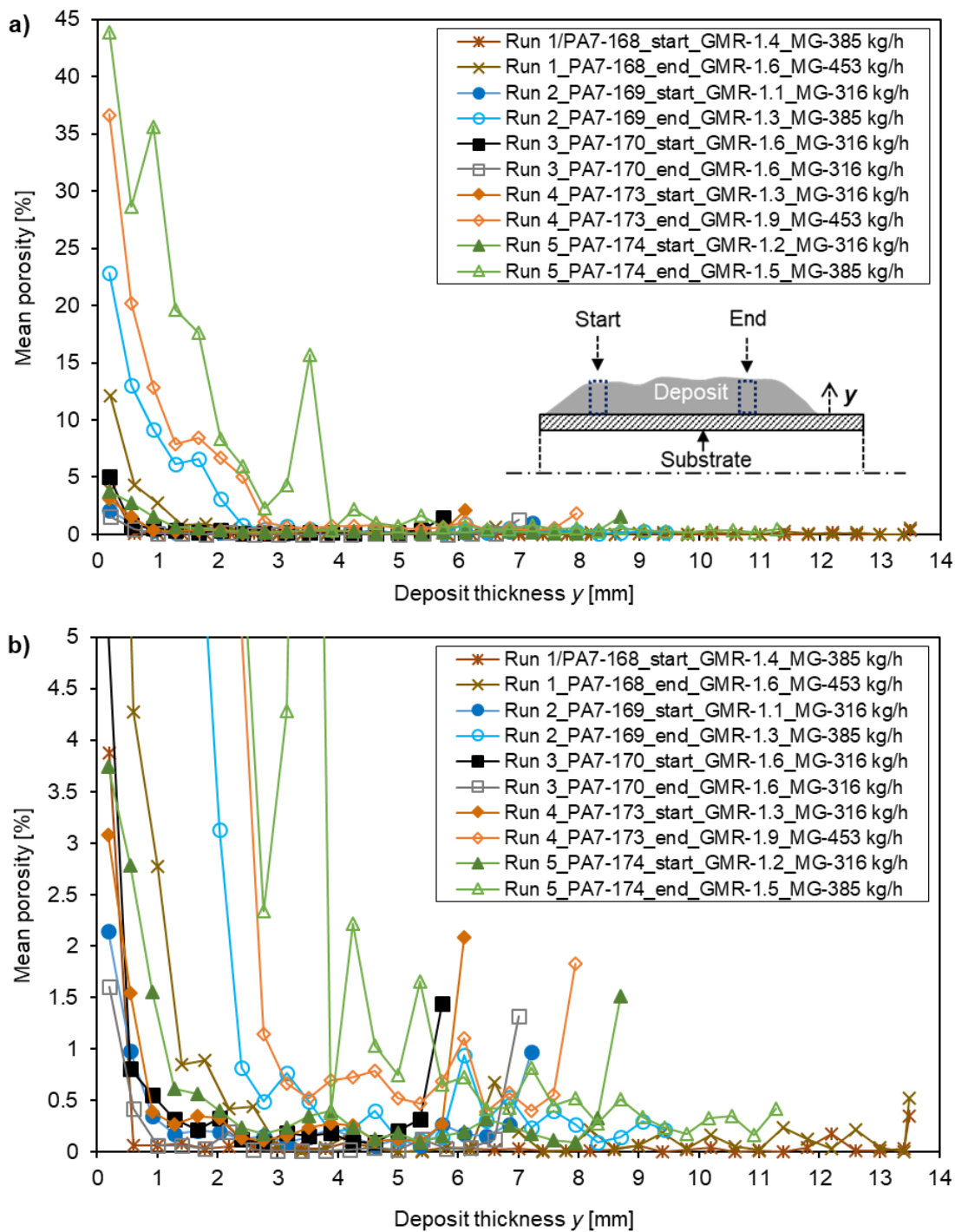


Figure 5-4: a) Porosity distribution of tubular AISI 52100 (100Cr6) steel deposits spray-formed under different process conditions with a close-coupled atomizer; b) enlarged area of the porosity profile 0% - 5%. Two samples were taken from each run. The first one is from deposit start position and the second one is from deposit end position. The figure is adopted from [HUSS20a].

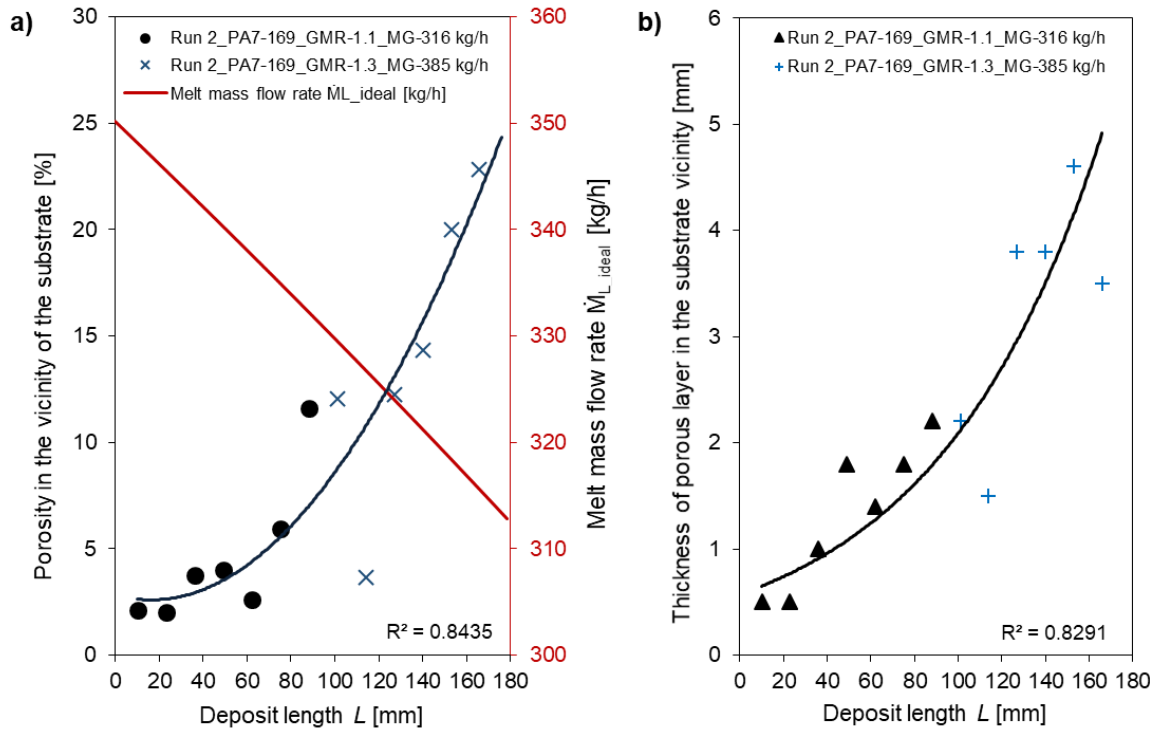


Figure 5-5: Porosity versus deposit longitudinal distance at Run 2 (PA7-169, GMR of 1.1 at deposit start and GMR of 1.3 at deposit end). a) mean porosity in the vicinity of the substrate and melt mass flow rate (calculated); b) thickness of the porous layer (with porosity > 0.5%) in the vicinity of the substrate. The figure is modified and reprinted from [HUSS20a].

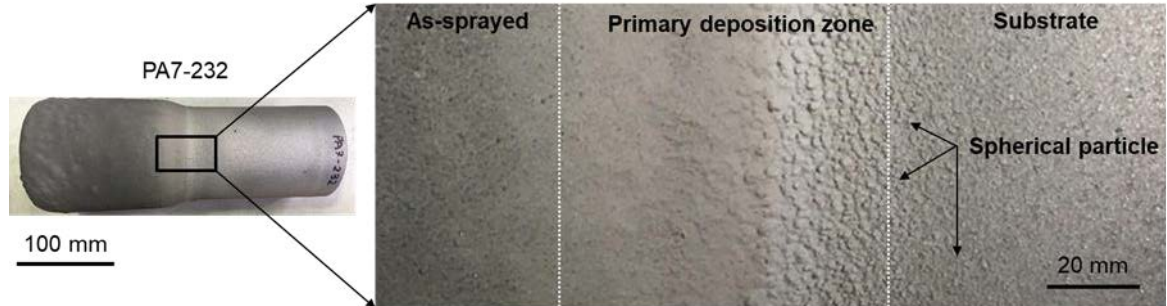


Figure 5-6: Adhered spherical particles on the substrate near deposition zone (PA7-232).

Higher gas mass flow rates \dot{M}_G also influence the porosity in the vicinity of the substrate [HU00]. Furthermore, the liquid fraction in the spray changes with *GMR* and affects local porosity [LAVE96, WARN97, CAI98]. Since the melting chamber pressure was not varied, with time the melt mass flow rate \dot{M}_L decreases due to decreasing metal-static height in the crucible (lower potential energy of liquid mass). The melt mass flow rate $(\dot{M}_L)_t$ can be calculated from the melt velocity in the pouring nozzle:

$$(\dot{M}_L)_t = (v_{melt} \cdot A_{Nozzle} \cdot \rho)_t \quad \text{Eq. 5-1}$$

where, \dot{M}_L is melt mass flow rate, v_{melt} is the velocity of melt at the pouring nozzle tip, A_{Nozzle} cross section area of pouring nozzle, ρ is density of the melt, and t is time. The melt velocity v_{melt} can be calculated by the simplified Bernoulli's equation [JAYW00]:

$$p_{chamber} + \rho g h_{melt} = p_{Asp.} + \frac{1}{2} \rho v_{melt}^2$$

$$\Rightarrow v_{melt} = \sqrt{2 \frac{(\Delta p + \rho g h_{melt})}{\rho}} \quad \text{Eq. 5-2}$$

where, $p_{chamber}$ is the over pressure on the melt, ρ is the density of the melt, g is gravitational acceleration, $p_{Asp.}$ is aspiration pressure at the pouring nozzle tip (the aspiration pressure is taken from [SCHW17]), v_{melt} is the velocity of melt at the pouring nozzle tip, Δp is pressure difference of melt surface and nozzle tip. The aspiration pressure is the downward force observed in the pouring nozzle tip for close-coupled atomizers (Figure 5-7). The values for the melt mass flow rate calculation are listed in the Appendix (Table A-8).

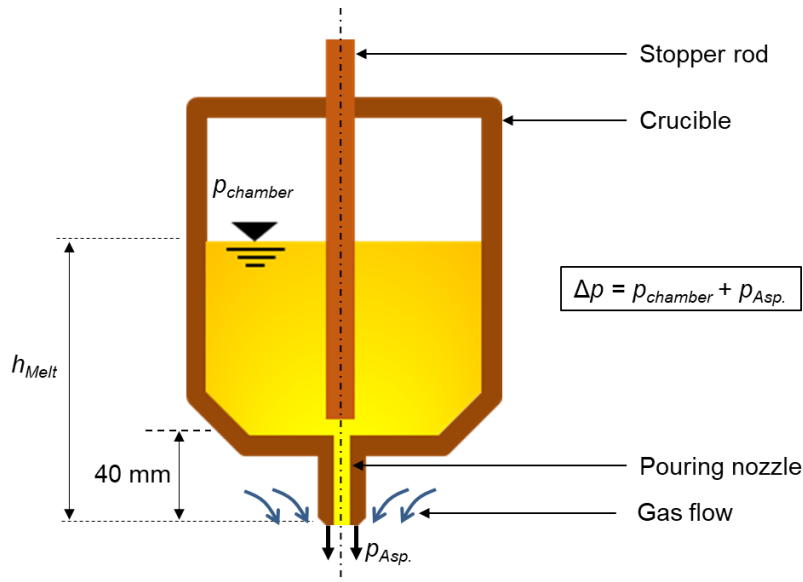


Figure 5-7: Pressure difference in the melt during atomization by close-coupled atomizer.

From Figure 5-5a it can be seen that the melt mass flow rate \dot{M}_L decreases with increasing deposition length (or time). At a constant gas mass flow rate \dot{M}_G the GMR increases with decreasing melt mass flow rate (Eq. 2-5), which subsequently increases the solid fraction

in the atomized melts and forms interstitial porosity in the vicinity of the substrate. It can be summarized that denser tubular deposits can be achieved at the starting areas of deposition compared to the end areas. Introduction of protecting cover on the substrate outside the primary deposition zone may reduce this pre-deposition of colder porous layer by preventing deposition of recirculating particles. This influence should be considered during spray forming of long tubular deposits, as well as during surface coating via close-coupled atomization.

Figure 5-8 shows that the porosity in the vicinity of the substrate increases with increasing *GMR* for tubular deposits at the deposit start position (T1 region). The deposit end positions are not considered here to avoid the shadowing effect by overspray particles. At a *GMR* of 1.1 the porosity is about 2% and at a *GMR* of 1.6 the porosity is about 5%. This effect can be attributed to the elevated cooling rate with higher *GMR* form colder layers in the vicinity of the substrate where interstitial pores are formed.

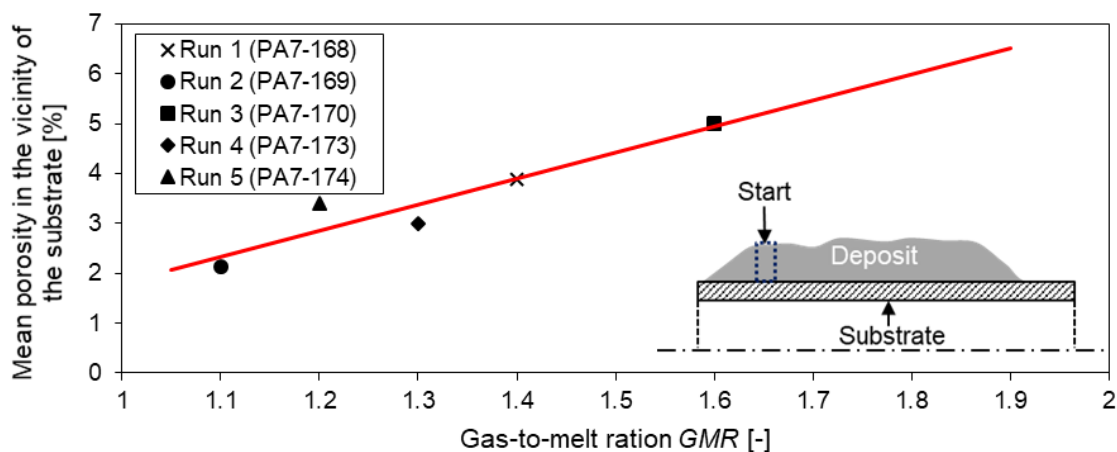


Figure 5-8: Relationship between the gas-to-melt ratio (*GMR*) and the mean porosity in the vicinity of the substrate at deposit start positions of spray-formed tubular 52100 deposits with close-coupled atomizer. The figure is adopted from [HUSS20a].

5.2.2 In-situ temperature measurement

The deposit surface temperature further reveals the insight of the deposition process and influences of other process conditions. It provides the actual cooling rate of the deposit after deposition. The deposit surface temperature is also an important parameter for porosity control. The in-situ deposit surface temperature has been measured in tubular deposits produced by close-coupled atomizer with a 2-color pyrometer and the substrate

temperatures (T_s) were measured with thermocouples at four different positions (see Figure 4-2).

5.2.2.1 Substrate temperature measurement

Figure 5-9 shows the in-situ substrate temperature measurement with time. At the beginning of the deposition the substrate temperature is at room temperature ($RT - 20^\circ\text{C}$). No preheating was performed in the spray forming runs (Run 1 to Run 5). With the impingement of the atomized droplets the substrate temperature near T1 position increases initially at rate of about 13.2 K/s. Gradually the substrate temperature increases at positions T2, T3, and T4 due to heat conduction in the deposit. The substrate temperature reaches a maximum ($T_{s,max}$) after the deposition is completed at that position (Figure 5-9a). Despite different positions at the substrate the temperature increases at a rate of about 13 K/s (Figure 5-9b). The substrate cools down in two separate steps. The initial cooling step is due to the atomization gas flow. The atomizing gas flow was reduced from atomizing gas pressure (p_G) to 0.01 MPa (e.g. from 0.8 MPa to 0.01 MPa in Run 3/PA7-170) after the atomization is completed. After reducing the gas pressure, the substrate temperature remains stable for a short time, suggesting that heat energy is coming from the hot deposit. Afterwards, the substrate continues to cool down in the second step with a cooling rate of 1.0 K/s – 1.3 K/s.

5.2.2.2 Deposit surface temperature measurement

The measured deposit surface temperatures T_D differ significantly from the single point substrate temperature T_s . The deposit surface temperature T_D was measured near to the thermocouples position (e.g. T1, T2, and T3) from a pyrometer line scan. Figure 5-10 shows the deposit surface temperature (T_D) against spray time for the corresponding run (Run 3/PA7-170) at the positions T1, T2, and T3. For comparison with different deposition positions, the time at the maximum deposit surface temperature $T_{D,max}$ is set to zero. From Figure 5-10 it can be seen that at the position T1 the deposition surface temperature increases from about 850 °C to the maximum deposit surface temperature ($T_{D,max}$) of about 1350°C. Cui et al. mentioned that the maximum deposit surface temperature is found at the center of the spray for tubes [CUI05b]. From the maximum deposit surface temperature $T_{D,max}$ the deposit cools down rapidly by the atomizing gas. In this case the cooling rate is 13.0 K/s. However, the substrate temperature increases at that time (e.g. at position T1 the temperatures increases from 205 °C to 705 °C (Figure 5-9). In the deposit length direction

similar thermal profiles are observed at the T2 and T3 positions. At the beginning of the spray impingement at position T2 and T3 the substrate temperatures ($T_{S2} = 320^\circ\text{C}$ and $T_{S3} = 305^\circ\text{C}$) are higher than the substrate temperature at position T1 ($T_{S1} = 205^\circ\text{C}$), which is due to conduction of heat from the nearby deposited materials. In this case the deposit surface cooling rates at T2 and T3 are 13 K/s and 11.3 K/s respectively.

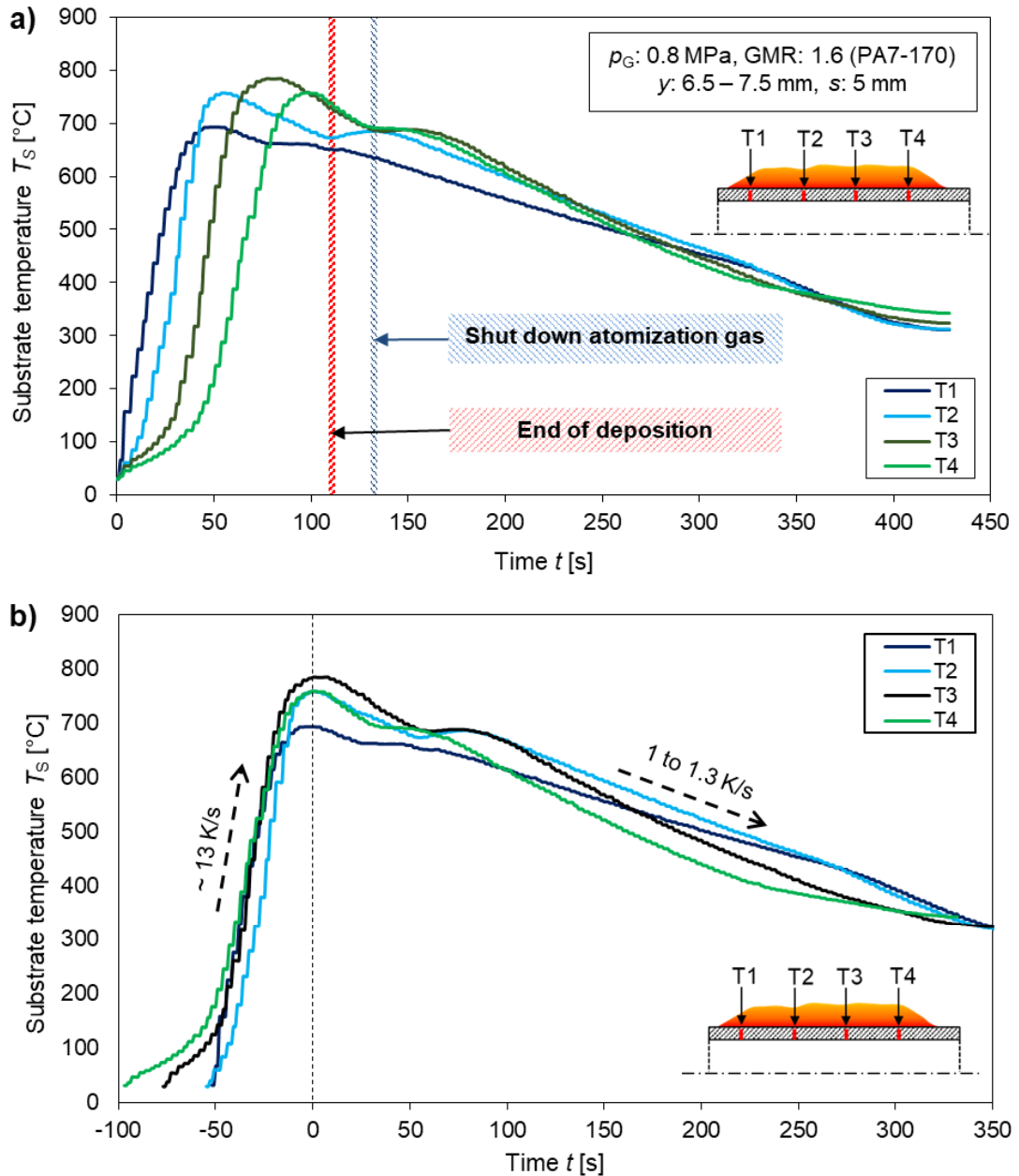


Figure 5-9: a) Substrate temperature at position T1, T2, T3, and T4 (Run 3/PA7-170). The end of deposition means end of melt flow. b) For comparison of the temperature profiles, the time at the maximum substrate temperature is set to zero ($T_{S,\max} = 0$ s). The figures are adopted and modified from [HUSS20a].

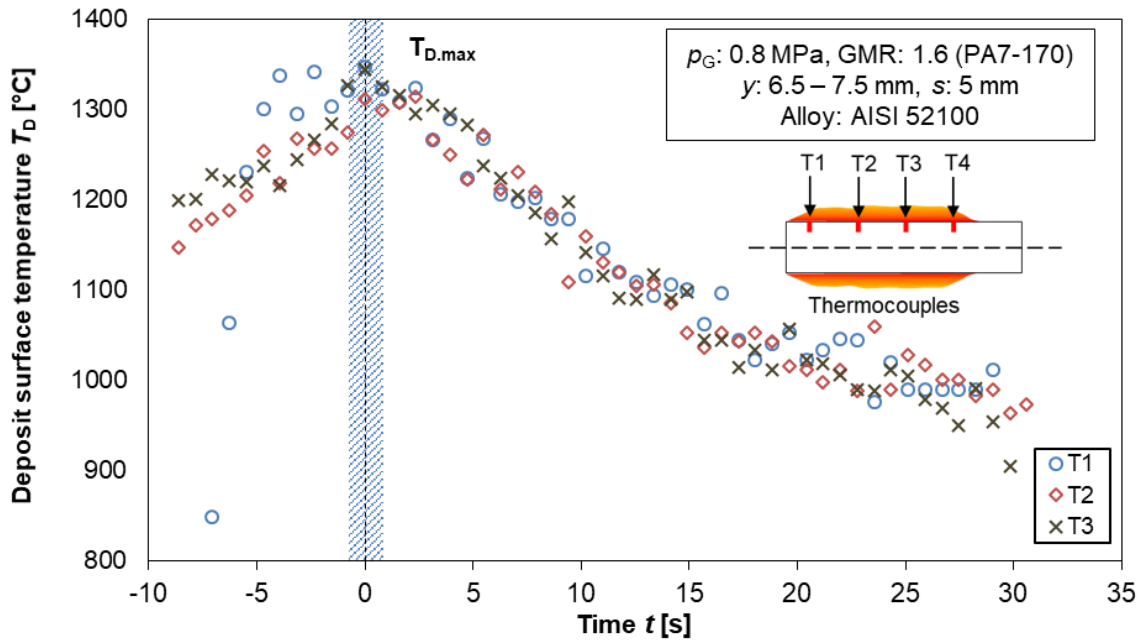


Figure 5-10: Deposit surface temperature at position T1, T2, and T3 (Run 3/PA7-170). For comparison of the temperature profiles, the time at the maximum deposit surface temperature is set to zero ($T_{D,max} = 0$ s). The figure is adopted from [HUSS20a].

5.2.3 Temperature and process parameters

To understand the influence of the process parameters on the deposition process a comparative study with the in-situ measured temperatures is performed in this section.

In the spray forming process the deposit surface temperature T_D depends on the process parameters like: i) deposit wall thickness y , ii) the melt temperature T_{melt} (super heat), iii) spray distance z , iii) gas-to-melt ratio GMR , iv) substrate transitional velocity v_s , and v) substrate thickness s [GRAN95, CUI05a, UHLE07a]. The melt temperature T_{melt} (1730 °C) and spray distance z (130 mm) were kept constant for the present series of spray forming runs (Run 1 to Run 5, see Table A-2). The substrate transitional velocity v_s (from 2 mm/s to 3 mm/s) was changed to achieve variation in the deposit thickness y . Figure 5-11 shows the relationship between the deposit thickness y and the maximum deposit surface temperature $T_{D,max}$. The deposit surface temperature T_D increases with increasing deposit thickness y . With varying deposit thickness the enthalpy on the deposition zone differs and this subsequently affects the cooling rate of the deposit. At higher deposit thickness a high amount of enthalpy comes from the spray and increases the deposit surface temperature T_D (deposit surface temperature is related to change of enthalpy in the deposition zone Eq.

3-2). At smaller deposit wall thickness y (about 6.5 mm) the maximum deposit surface temperature $T_{D,max}$ is found to be about 1315 °C, which is just above the solidus temperature (for AISI 52100 steel $T_{sol} = 1300$ °C). At larger deposit thickness y (about 14 mm) the maximum deposit surface temperature $T_{D,max}$ is found to be about 1425 °C, which is below the liquidus temperature of AISI 52100 steel ($T_{liq} = 1458$ °C).

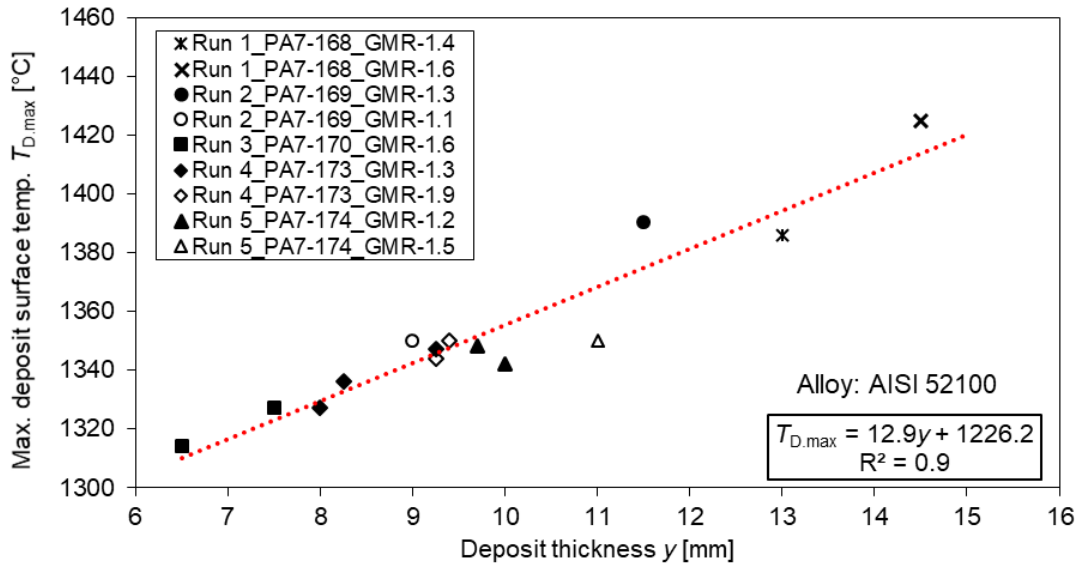


Figure 5-11: Maximum deposit surface temperature $T_{D,max}$ versus deposit thickness y for spray forming of tubes with a close-coupled atomizer. The figure is adopted from [HUSS20a].

Figure 5-12 shows the relationship between maximum deposit surface temperature $T_{D,max}$ and gas-to-melt ratio GMR of the spray formed tubular deposits by close-coupled atomization. The maximum deposit surface temperature $T_{D,max}$ decreases with increasing GMR (the GMR was changed at constant melt mass flow rate by changing the gas flow rate) at similar deposit wall thickness y . For example, at a deposit thickness y of about 9 mm, higher maximum deposit surface temperatures $T_{D,max}$ have been observed at $GMR = 1.1$ (Run 2/PA7-169) than that observed at $GMR = 1.9$ (Run 4/PA7-173). At higher GMR more gas flow impinges on the deposit surface, which increases the cooling of the surface layers. Furthermore, at a constant GMR higher maximum deposit surface temperature $T_{D,max}$ are observed with increasing deposit thickness (except at a GMR of 1.1). At a GMR of 1.9 the maximum deposit surface temperature $T_{D,max}$ slightly increases due to increase of deposit thickness y (Run 4/PA7-173). Similarly, at $GMR = 1.3$ a higher maximum deposit surface temperature $T_{D,max}$ is observed than at $GMR = 1.1$ due to higher deposit wall thickness y (deposit wall thickness y of about 11.5 mm at a GMR of 1.3 and deposit wall thickness y of about 9 mm at a GMR of 1.1). Such observations indicate that the deposit

wall thickness y has a more significant influence on the maximum deposit surface temperature than the gas-to-melt flow rate GMR , which is mainly related to the amount of melt flow in the deposition zone [HUSS20a].

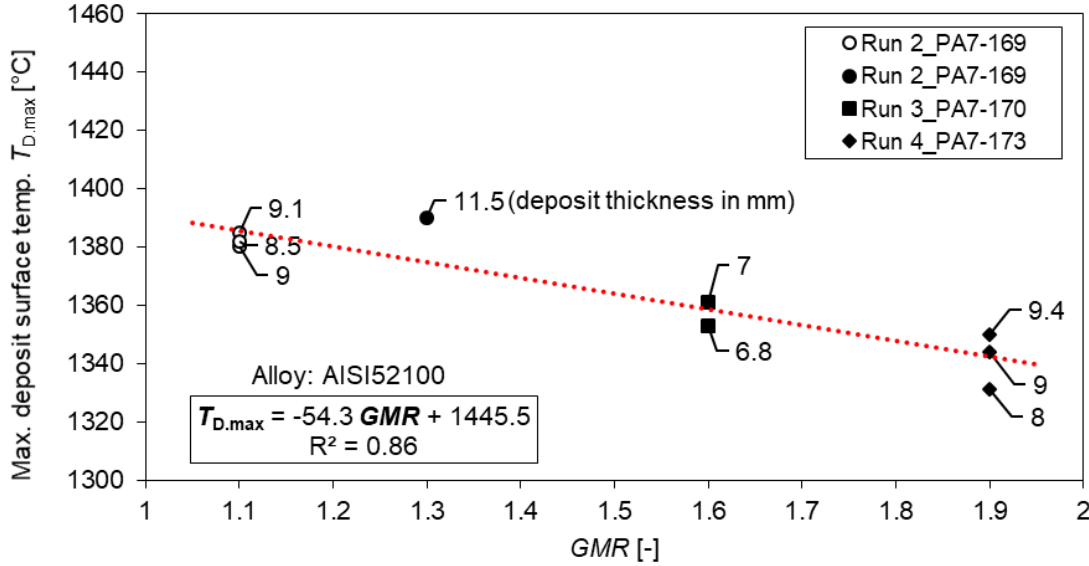


Figure 5-12: Maximum deposit surface temperature $T_{D,max}$ versus gas-to-melt ratio GMR at similar wall thickness y . In this figure the data from Figure 5-11 with similar wall thickness y is plotted. The figure is adopted from [HUSS20a].

Further influence of the process parameters on the deposit surface temperature T_D and the substrate temperatures T_S are presented in Figure 5-13. The maximum deposit surface cooling rate decreases with increasing deposit thickness y (Figure 5-13a) because thicker deposits accumulate more heat in the deposit and the time necessary to release the heat to the surrounding increases. In contrast, the GMR has an inverse effect on the deposit cooling rate. At higher GMR the deposit surface cooling rates are faster due to the increased amount of gas passing through the as-sprayed deposit at similar thickness (Figure 5-13b). With increasing deposit wall thickness the substrate cooling rate also decreases linearly (Figure 5-13c). Higher deposit surface temperatures T_D are detected for thicker deposits due to the increased amount of deposited material (higher enthalpy). Therefore, an increasing amount of heat is transferred to the substrate, which leads to higher maximum substrate temperatures. However, the atomizing gas has a limited effect on the cooling of the substrate after deposition (Figure 5-13d). From Figure 5-13e it can be seen that with an increasing ratio of the deposit to substrate thickness y/s the ratio of the deposit to substrate temperature $T_{D,max}/T_{S,max}$ (as Eq. 5-3) decreases. Suggesting that with increasing deposit substrate thickness, more heat is released through the substrate.

$$\frac{T_{D,max}}{T_{s,max}} = (-0.68 \cdot \frac{y}{s}) + 3.51. \quad \text{Eq. 5-3}$$

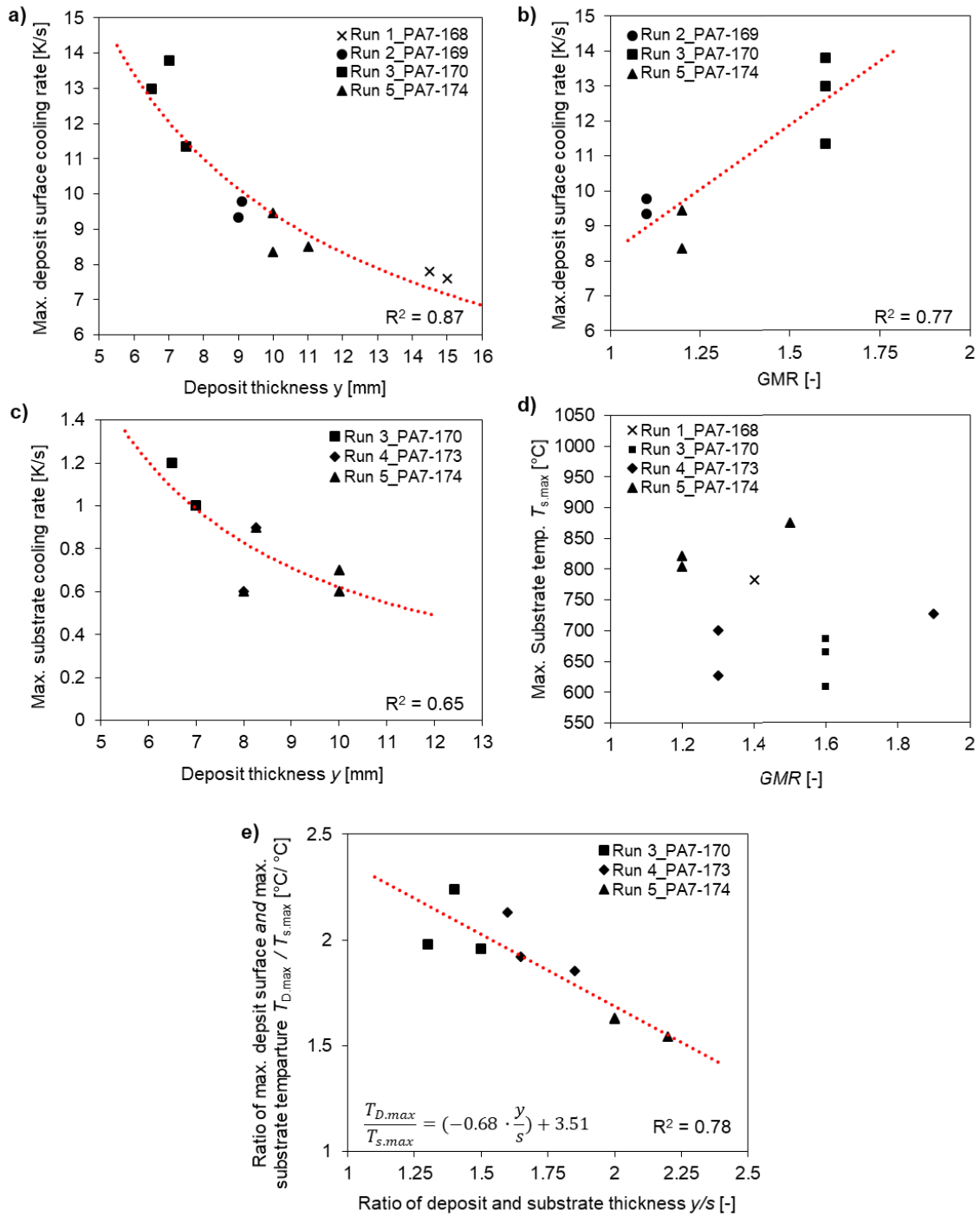


Figure 5-13: a) Deposit surface cooling rate versus deposit thickness; b) deposit surface cooling rate versus *GMR* (at similar wall thickness); c) maximum substrate temperature versus deposit thickness; d) maximum substrate temperature versus *GMR*; e) ratio of maximum deposit surface temperature versus ratio of deposit thickness and substrate thickness. The figures are adopted from [HUSS20a].

5.2.4 Grain size, deposit surface temperature, and GMR

The influence of the deposit surface temperature and *GMR* on the grain size is outlined in Figure 5-14a. At a higher local average deposit surface temperature $T_{D,avg}$, the grain size is larger due to slower cooling rates. In the vicinity of the substrate the local average deposit surface temperature $T_{D,avg}$ is lower compared to the deposit center regions and the deposit surface regions. Therefore, the grain size is smaller in the vicinity of the substrate than in the other two regions, which indicates faster cooling of the deposit through the substrate. Larger grains are observed in the deposit center with higher local average deposit surface temperature $T_{D,avg}$.

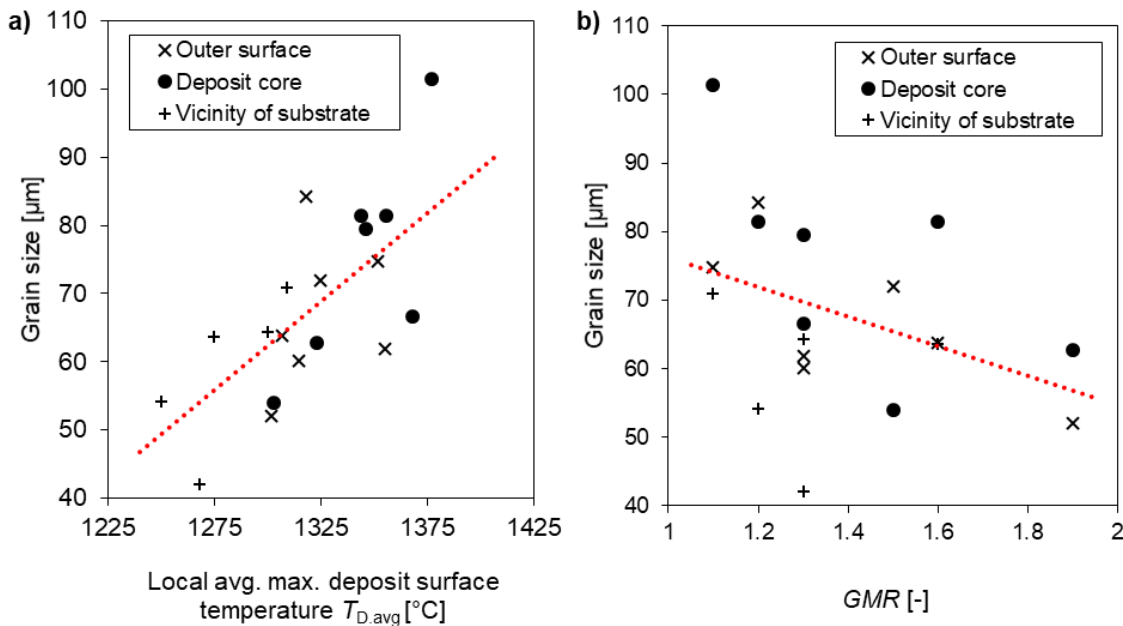


Figure 5-14: Grain size versus a) local average deposit surface temperature, b) GMR of spray-formed tubular AISI 52100 deposits with close-coupled atomizer. The figure (a) is adopted from [HUSS20a].

According to the model presented by Srivastava et al. for Al-18% Si alloy, the grain size near the substrate is much smaller than that in the deposit center [SRIV04]. However, the difference of the grain size in the deposit center and in the vicinity of the substrate is not large as presented by Cui et al. for AISI 52100 steel tubes generated by free-fall atomizer [CUI04]. The main reason is that the deposit thickness y in the present study (deposit thickness y is about 6.5 to 11.5 mm in Run 1 to Run 5) is thinner than that of the tubular deposits (deposit thickness y is about 30 mm) by Cui et al. generated with a free-fall atomizer [CUI04]. Thinner deposit thickness leads to uniform cooling of the as-sprayed materials, subsequently resulting in a more uniform grain size through the deposit

thickness. From Table 5-3 it can be seen that slightly thicker deposits (thickness of about 8.5 mm to 11.5 mm) result in a larger difference in the grain size at the deposit center than the grain size near the substrate. Figure 5-14b shows the influence of *GMR* on grain size. As expected, with increasing *GMR* the grain size decreases because of faster cooling of the deposit with higher gas flow.

5.2.5 Porosity and deposit surface temperature

According to Walter et al., the deposit surface temperature provides important information about the porosity in the as-sprayed deposit [WALT05]. The authors showed that with increasing deposit surface temperature the porosity in the deposit decreases for different steel grades generated with a free-fall atomizer. In Figure 5-15 the local deposit surface temperature T_D is plotted against the mean local porosity of the deposits, where the position of the deposition has been also considered (i.e. start of the deposition and end of the deposition). At lower deposit surface temperatures T_D the porosity in the deposit is higher due to cold porosity [WALT05, HUSS20a]. In the present study with close-coupled atomizer, similar characteristics are observed. In addition, at similar deposit temperatures the porosity is higher at the deposit end position than at the deposit start position. For example, at a local deposit surface temperature T_D of 1250 °C the mean local porosity is about 0.5% to 1.5% at the deposit start position. In contrast, a mean local porosity of about 0.5% to 20% is observed at the deposit end position (Figure 5-15a). Highly dense materials are found above the solidus temperature ($T_{sol} = 1300$ °C for AISI 52100 steel) for both at the deposit start and end positions. In addition, a temperature range of 1275 °C to 1375 °C is found to be suitable for spray forming of AISI 52100 steel with the close-coupled atomization system in cold gas condition. Within this temperature range porosity below 1% is desirable, which would be suitable for surface coating. However, the deposit surface temperature is not transferable to other alloying systems (i.e. Al-alloys). The ratio of deposit surface temperature T_D and solidus temperature T_{sol} is independent to the alloy. For transferability of the results within different alloys a dimensionless parameter DTT (ratio of Deposit surface Temperature and solidus Temperature) can be used as:

$$DTT = T_{D,max}/T_{sol} \text{ (}^{\circ}\text{C/}^{\circ}\text{C)} \quad \text{Eq. 5-4}$$

It is observed that at DTT values $0.95 < DTT < 1.1$ the porosity is below 1% for AISI 52100 steel (Figure 5-15b).

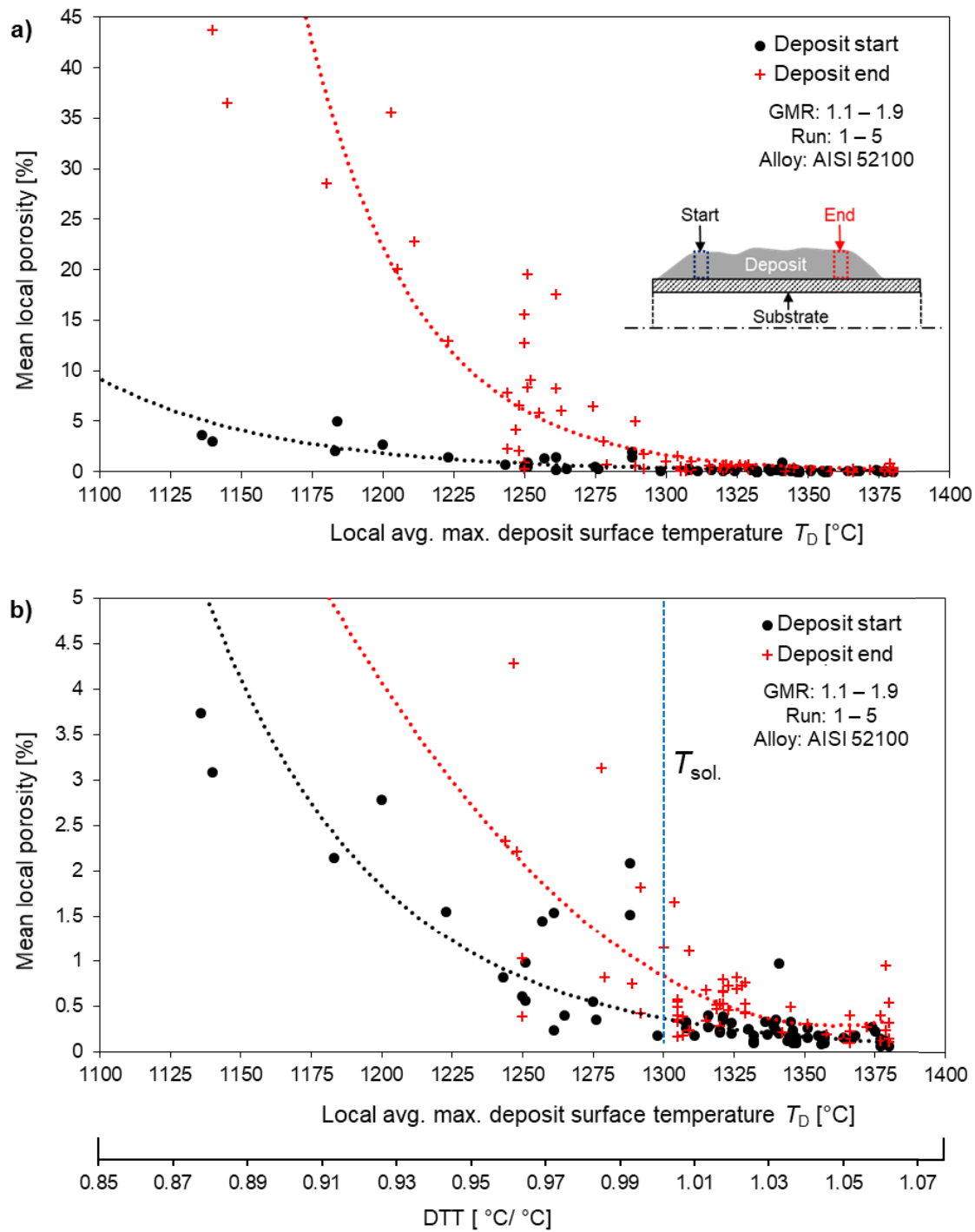


Figure 5-15: a) Porosity in relation to the deposit surface temperature during spray forming (GMR: 1.1 – 1.9, Run 1 – Run 5); b) enlarged area of the porosity profile. The black dots are taken from the deposit start positions and the red pluses are taken from the deposit end positions. The figure is adapted from [HUSS20a].

5.2.6 Empirical model for maximum deposit surface temperature

In the previous sections (5.2.2 to 5.2.5) it is discussed that the maximum deposit surface temperature $T_{D,max}$ is a vital parameter in spray forming of tubular deposit. In this section an empirical correlation is to be constructed based on the experimental results. The maximum deposit surface temperature $T_{D,max}$ depends on several process parameters as listed in Table 5-4.

Table 5-4 Process parameters related to the maximum deposit surface temperature.

Parameter	Effects
Deposit thickness (y)	$y \uparrow - T_{D,max} \uparrow$
Substrate thickness (s)	Substrate thickness controls the heat loss to the surroundings
<i>GMR</i>	$GMR \uparrow - T_{D,max} \uparrow$
Substrate distance (z)	$z \uparrow - T_{D,max} \downarrow$
Deposit and substrate materials	The heat loss (heat flux) to the surroundings depends on the materials properties like, specific heat capacity (c_p), density (ρ), solidus temperature ($T_{sol.}$)
Atomizing gas temperature (T_G)	The gas temperature will change the gas density and heat conductivity
Atomizing gas type	N_2 has different thermal properties than Ar

In subchapter (5.2), the substrate distance z , atomizing gas temperature T_G , atomizing gas and have not been varied. Therefore, these parameters are not considered for the correlation. The maximum deposit surface temperature $T_{D,max}$ can be predicted as follows:

$$T_{D,max} = T_{sol} + a^* \cdot GMR^{b^*} \cdot \left(\frac{y}{s}\right)^{c^*} \cdot \left(\frac{\Delta H_D}{\Delta H_S}\right)^{d^*} [^{\circ}C]$$

$$\Rightarrow T_{D,max} = T_{sol} + a^* \cdot GMR^{b^*} \cdot \left(\frac{y}{s}\right)^{c^*} \cdot \left(\frac{\rho_D \cdot c_{pD}}{\rho_S \cdot c_{pS}}\right)^{d^*} [^{\circ}C]$$

Eq. 5-5

$$(T_{sol} \leq T_{D,max} \leq T_{liq} \text{ at } y < 15 \text{ mm})$$

a^*	b^*	c^*	d^*
20	- 0.7	1.8	0.5

where, $T_{D,max}$ is the deposit surface temperature, T_{sol} is the solidus temperature of the deposited material, GMR is the gas-to-melt ratio, y is the deposit thickness, s is the substrate thickness, ΔH_D is the heat loss of the deposit to surrounding environment, ΔH_s is the heat loss of the substrate to surrounding environment, ρ_D is density of the deposit, ρ_S is density of the substrate, c_{pD} is specific heat capacity of the deposit, c_{pS} is specific heat capacity of the substrate, and a^* , b^* , c^* and d^* are constants found to be 20, - 0.7, 1.8 and 0.5 respectively. The empirical equation is valid in the range of solidus and liquidus temperatures of the deposited material and deposit thickness below 15 mm for cold N_2 gas atomization. Figure 5-16 shows the comparison between experimental maximum deposit surface temperature and the model for AISI 52100 steel deposit (Run 1 to Run 5).

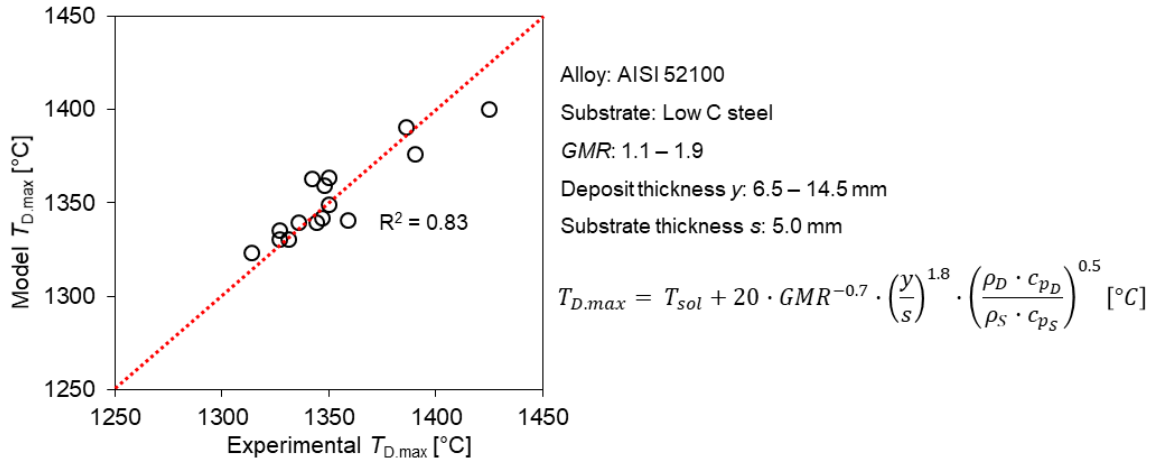


Figure 5-16: Comparison of the experimental and the model maximum deposit surface temperatures for AISI 52100 steel.

The dimensionless DTT equation (Eq. 5-4) can be rewritten with the empirical maximum deposit surface temperature as.

$$DTT = T_{D,max}/T_{sol} = (T_{sol} + a^* \cdot GMR^{b^*} \cdot \left(\frac{y}{s}\right)^{c^*} \cdot \left(\frac{\rho_D \cdot c_{pD}}{\rho_S \cdot c_{pS}}\right)^{d^*} [°C])/T_{sol} \quad \text{Eq. 5-6}$$

Eq. 5-6 may be used for the prediction of DTT for other alloy system. In the later section 5.4 it will be discussed further.

In summary of the sub-chapters 5.1 and 5.2: the spray forming of tubular deposits with CCA shows better quality than deposits with FFA in terms of porosity (Figure 5-2). The experimental results show that porosity of a tubular deposit can be reduced by the smaller droplets sprayed by a CCA as proposed in the ***hypothesis 1: the porosity of a tubular deposit can be reduced by the smaller droplets sprayed by a close-coupled atomizer.*** The equiaxed pearlitic microstructure with fine carbides at the primary austenite grain boundaries are observed for the deposits with CCA at deposit thickness of 6.5 mm to 11.5 mm (Figure 5-3). In the deposit center the grain size is larger than the grains in the outer and inner surface regions due to slower cooling rate. High amount of porosity and thicker porous layer have been observed at the deposit end position than the deposit start position due to change of the melt flow rate and also the shadowing effect by rebounding droplets from the spray (Figure 5-5 and Figure 5-6). The porosity in the vicinity of the substrate increases with increasing *GMR* due to faster cooling of the as-sprayed material (Figure 5-8). The in-situ temperature measurement shows that the deposit thickness has a significant influence on the deposit surface temperature than the gas-to-melt ratio (*GMR*) (Figure 5-11 and Figure 5-12). The *GMR* has an influence on the thermal profile of the deposit surface but not on the substrate temperature after deposition (Figure 5-13). With increasing deposit surface temperature, the grain size increases as well in the deposits (Figure 5-14). The porosity is high at a deposition surface temperature below solidus temperature of the alloy (Figure 5-15). A dimensionless parameter DTT (ratio of Deposit surface Temperature and solidus Temperature can be used) has been proposed to predict the porosity in the deposit. For AISI 52100 alloy at a DTTs value of 0.95 to 1.1 the porosity is below 1% in cold gas atomization condition. Based on the experimental result an empirical correlation has been constructed to predict the maximum deposit surface temperature for tubular deposits (Figure 5-16). Since only one substrate material (low carbon steel) and deposit material (AISI 52100 steel) has been used during the spray forming runs (Run 1 to Run 5). The value of the constants in Eq 5-5 remain to be optimized in future works.

5.3 Hot gas atomization

The working hypotheses 2 and 3 have been proposed based on the hot gas (HG) atomization by a close-coupled atomizer (see Chapter 3). According to the ***hypothesis 2: the particle velocity in the spray can be increased by using hot gas in atomization even at similar droplet size***, which means with the hot gas atomization will reduce the particle size d_d and will increase the particle impact velocity v_d in the spray. And the ***hypothesis 3: decreased deformation times during droplet impact will result in high density materials and will extend the process window***, which means the particle deformation time t_d during impact can be reduced with faster particle velocity v_d , which will produce dense materials at lower deposit surface temperature T_D . Hence, the process window can be extended for a broader temperature range. In this section the hypothesis 2 and 3 are to be discussed. The influences of the hot gas (up to 1000 °C) on the atomizing process conditions has been analysed by a CFD model. A series of spray forming runs have been performed with hot gas ($T_G = 290 \pm 40$ °C) and cold gas (RT) with the same CCA system. The varied key process parameters in this section are listed in Table 5-5. The process parameters can be found in Appendix (Table A-3 to Table A-7) in detail.

Table 5-5 Key process parameters varied in section 5.3.

Atomizer	Gas temperature [°C]	Gas pressure [MPa]	GMR [-]
CCA-HG	20 – 1000	0.6 – 1.6	0.8 – 1.9

5.3.1 Spray condition

It is assumed that a higher gas temperature T_G introduces an increased kinetic energy as a result of the higher sound velocity $c = \sqrt{\kappa \cdot R_s \cdot T_G}$, where κ is the isentropic exponent, R_s is the specific gas constant, and T_G is the gas temperature [CIFT20]. During hot gas atomization the gas mass flow rate \dot{M}_G is calculated as [CIFT18]:

$$\dot{M}_G = \dot{M}_{G,0} \cdot \sqrt{T_{G,0}/T_G} \quad \text{Eq. 5-7}$$

where, $\dot{M}_{G,0}$ is the gas mass flow rate in cold condition (RT), $T_{G,0}$ is the gas temperature in cold condition (RT), \dot{M}_G is the gas mass flow rate at elevated atomization gas temperature T_G . It should be noted that the Eq. 5-7 is valid in ideal gas condition.

For the simulation of the spray process a CFD model is used (the CFD model has been developed by L. Buss as described in [HUSS22]), where the droplets/particles are characterized as a dispersed phase in a Lagrangian approach with two-way coupling between the phases under steady-state conditions and turbulent, compressible flow. The details of the numerical model can be found in. Figure 5-17 illustrates the simulation results for gas only flow.

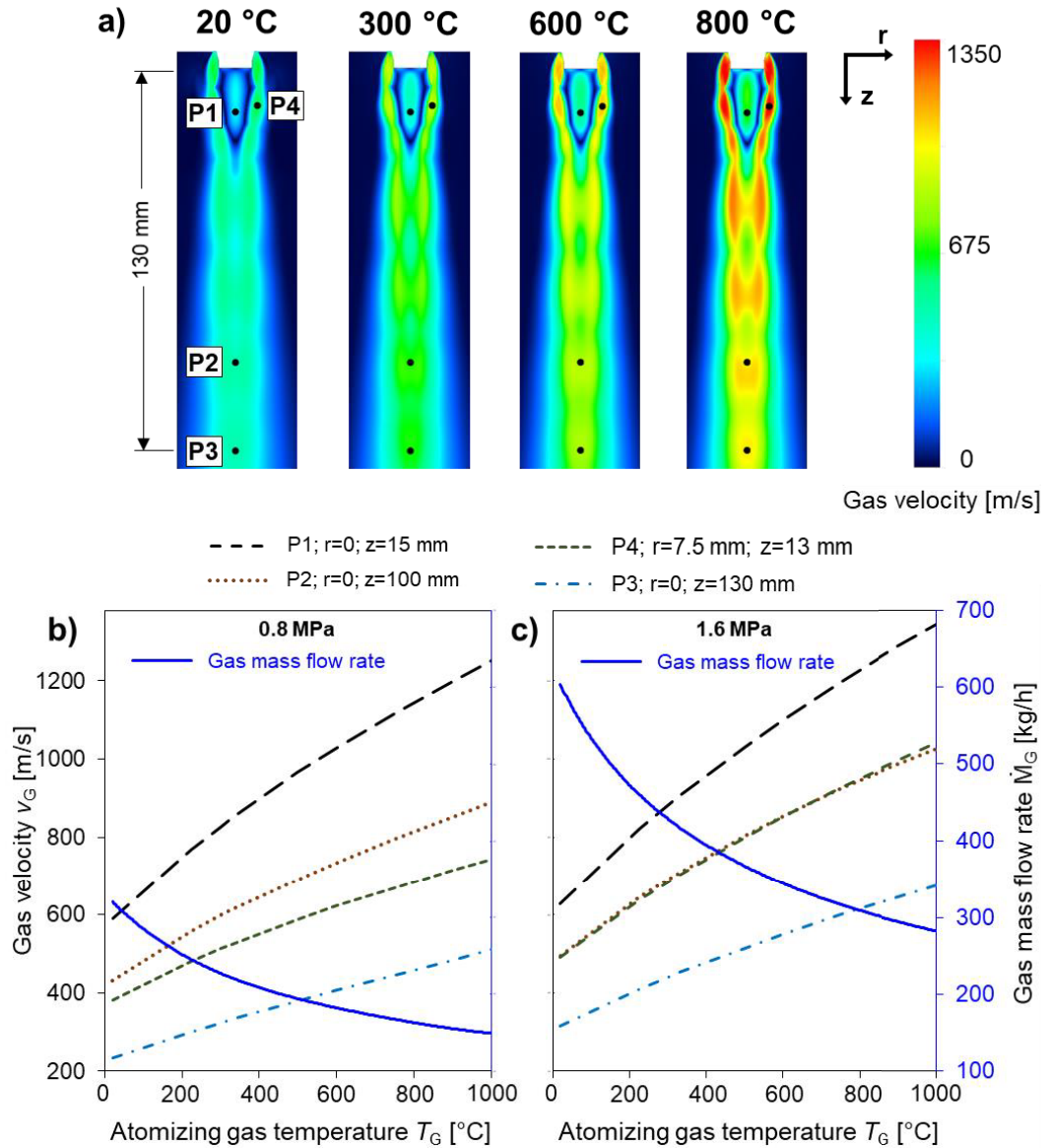


Figure 5-17: Numerical results of gas velocity at different atomization gas temperatures. a) Image of gas velocity distribution in spray chamber with atomization gas pressure of 1.6 MPa; and gas velocity and gas mass flow rate as a function of atomizing gas temperature with atomization gas pressure of 0.8 MPa (b) and 1.6 MPa (c). Simulation data from [HUSS22] performed by L. Buss.

During hot gas atomization with a close-coupled atomizer the gas velocity v_G increases as the sound velocity increases at elevated gas temperature T_G (Figure 5-17). The gas velocity v_G is plotted in four different positions in the gas jet without any droplet. The gas velocity v_G is minimum below the melt pouring nozzle opening (P1, Figure 5-17). The gas velocity v_G is higher at 100 mm and 130 mm (P2 and P3, Figure 5-17) below the melt pouring nozzle than at the P1 position. At the atomization zone (P4, Figure 5-17) the maximum gas velocity v_G is observed. However, the sound velocity can be varied by using different atomization gases. It can also be seen that with increasing atomization gas temperature T_G the gas mass flow rate \dot{M}_G is decreasing at a constant gas pressure p_G (Figure 5-17b and c). For example, at $p_G = 1.6$ MPa the gas mass flow rate \dot{M}_G at 20 °C (RT, cold gas condition) is about 600 kg/h and at 300 °C is about 430 kg/h and at gas temperature T_G (1000 °C) the gas mass flow rate is about 280 kg/h. Suggesting that hot gas atomization introduces lower gas consumption.

Figure 5-18 illustrates that the melt mass flow rate \dot{M}_L increases with increasing gas mass flow rate \dot{M}_G . Based on the experimental results a correlation is formulated between the gas mass flow rate \dot{M}_G and melt mass flow rate \dot{M}_L :

$$\dot{M}_L = m \dot{M}_G + n$$

m	n
0.63	59.31

Eq. 5-8

where, \dot{M}_L is the melt mass flow rate, \dot{M}_G is the gas mass flow rate, m and n are constant with a value of 0.634 and 59.31, respectively. Eq. 5-8 is valid for the used nozzle configuration (CD-CCA-0.8). The calculated melt mass flow rates have been used in the numerical simulations according to Eq. 5-8.

5.3.2 Particle size

The particle size in the spray is an important parameter during the spray forming process. For example, larger particles possess higher liquid fractions at the same deposition distance than smaller particles.

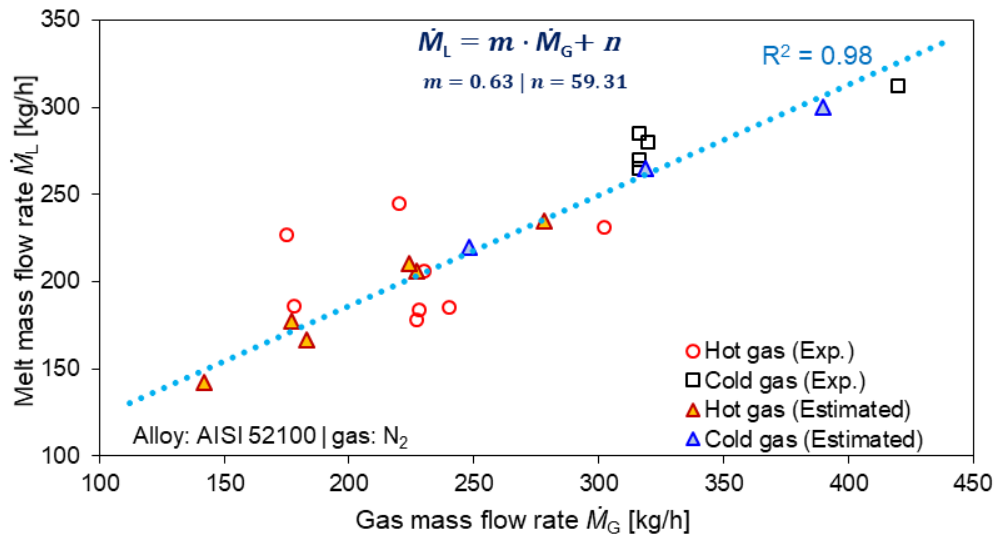


Figure 5-18: Correlation between the gas mass flow rate and the melt mass flow rate at different atomization gas temperature. A linear model is estimated based on the experimental results (Run H1 to H13).

Three powder producing atomization runs have been performed to investigate the effect of hot gas atomization on the spray particle size with a close-coupled atomizer. The process parameters for the powder production runs are listed in Appendix (Table A-4). The stainless steel AISI 316L was atomized with 1.6 MPa N_2 pressure at three different gas temperatures (RT/20 °C, 225 °C and, 330 °C). Figure 5-19 shows the particle size distribution of the AISI 316L powders for size fraction of 0 to 200 μm (powder size distribution performed by laser diffraction analysis). Higher atomization gas temperature T_G leads to smaller particle size (at RT the value of $d_{50.3} = 62 \mu m$ and at $T_G = 330^\circ$ the value of $d_{50.3} = 48 \mu m$). At the same atomizing gas pressure p_G (1.6 MPa) the gas mass flow rate \dot{M}_G also decreases with increasing gas temperature T_G (from about 600 kg/h at RT to about 400 kg/h at 330 °C), suggesting that smaller particles can be produced at lower gas consumption at elevated gas temperature T_G .

Figure 5-19b shows that the nitrogen content in the atomized powders increases with increasing gas temperature T_G . In the atomized powders (size fraction of 20 – 63 μm) the nitrogen content is found about 560 ppm at $T_G = RT$, about 700 ppm at $T_G = 225^\circ C$, and about 880 ppm at $T_G = 330^\circ C$. Typically, the nitrogen content in AISI 316L steel is 200 – 300 ppm [CUI19], which indicates that during atomization process the molten stream picks nitrogen from the process gas even at cold gas condition. At higher gas temperature the pickup further increases (Figure 5-19b). From RT to $T_G = 225^\circ C$ the particle size decreases, which would provide larger surface area and facilitate higher nitrogen diffusion. However,

there is hardly any difference of the particle size between $T_G = 225\text{ }^{\circ}\text{C}$ and $T_G = 330\text{ }^{\circ}\text{C}$. The nitrogen pickup may be related to other process conditions. Furthermore, the nitrogen diffusion increases with high nitrogen partial pressure in molten high Cr steel like AISI 316L steel [JIAN05]. At high nitrogen partial pressure nitrogen is defused in the alloy and form CrN [BERN18]. At higher gas temperature the sound velocity ($c = \sqrt{\kappa \cdot R_s \cdot T_G}$) of the atomizing gas increases, which may cause nitrogen diffusion in the atomization zone by higher nitrogen partial pressure. This nitrogen diffusion would affect the material properties (corrosion resistance, strength, creep strength and toughness [JIAN05]). If argon is used as atomizing gas, this problem may be avoided in the atomized powders. The oxygen content remains fairly consistent at different atomizing gas temperatures.

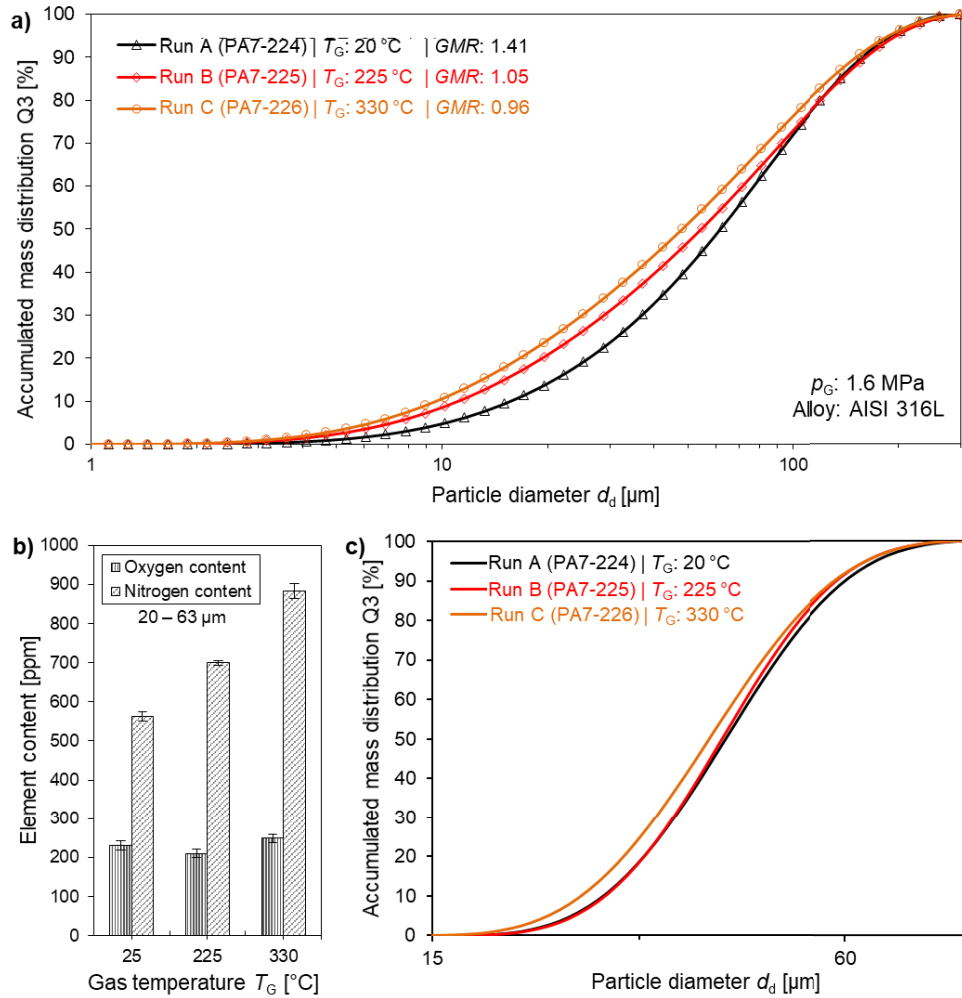


Figure 5-19: a) Particle (size fraction 0 – 200 μm) size distribution as accumulated mass percentage distribution, b) oxygen and nitrogen content at different atomizing gas temperature T_G of 316L stainless steel (size fraction of 20 – 63 μm), c) particle size distribution of size fraction 20 – 63 μm . The figures are adopted from [HUSS20b].

Figure 5-20 shows SEM (scanning electron microscopy) images of the atomized AISI 316L powders at RT and 330 °C. The particles produced at 330 °C show rough surfaces. Different cooling conditions may affect this change of surface roughness on the atomized powder surface. Further investigations are needed to bring more insights in this context.

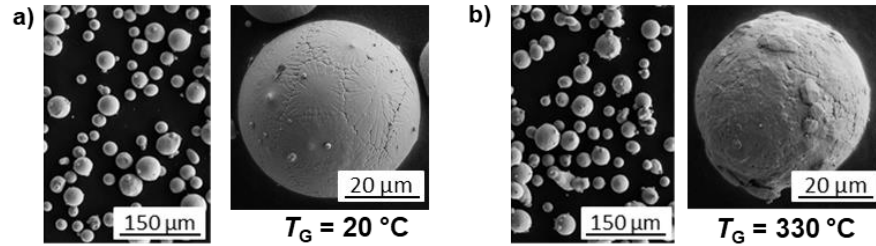


Figure 5-20: SEM images of the atomized AISI 316L stainless steel particles (size fraction 20 – 63 μm), a) at atomization gas temperature T_G of 20 °C; b) at atomization gas temperature T_G of 330 °C with close-coupled atomizer.

Figure 5-21 shows the correlation between the mean particle size $d_{m,RRSB}$ for different atomization gas temperatures T_G and varying gas pressure p_G . The particle size distributions for AISI 52100 steel are estimated to follow a Rosin-Rammler-Sperling-Bennett (RRSB) function by Eq. 2-7. It can be seen that the mean particle size decreases with increasing atomizing gas pressure p_G and gas temperatures T_G . These estimated particle size distributions are utilized in the simulation runs for corresponding atomization conditions (see Appendix Table A-6 for the considered RRSB parameters).

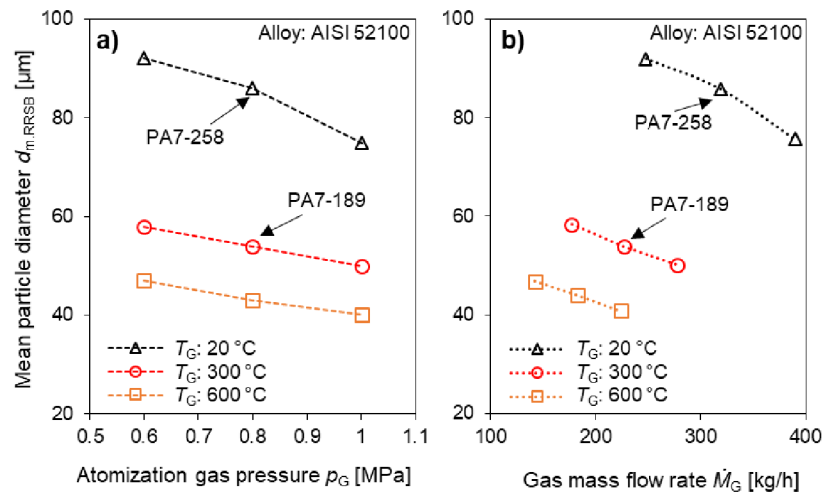


Figure 5-21: Mean particle size $d_{m,RRSB}$ at different atomizing gas temperatures (T_G – 20 °C, 300 °C, and 600 °C) a) at different gas pressures; b) at different gas mass flow rates. The particle size distributions are estimated by RRSB-functions from the experimental results (PA7-258 and PA7-189). Particle size distribution calculated by L. Buss.

5.3.3 Particle velocity and thermal conditions

5.3.3.1 Particle velocity in cold condition

In the previous section (simulation of gas velocity v_G) it has been shown that increasing gas temperatures T_G lead to higher gas velocities v_G . To observe the particle velocity v_d in the spray chamber the mean velocity $v_{d,m}$ of cold particles accelerated in the atomization gas jet has been measured by Laser Doppler Anemometry (LDA) for different gas temperatures T_G (the experimental setup is described in section 4.3.3). The parameters for the LDA measurement are listed in Appendix (Table A-3). Figure 5-22 shows the mean particle velocities $v_{d,m}$ of AISI 52100 steel powders (size fraction of 63 – 90 μm powders is injected through the melt pouring nozzle) at RT (293 K) and at about 300 °C (573 K). The mean particle velocity $v_{d,m}$ increases at elevated atomizing gas pressures p_G and gas temperatures T_G . Even at very low gas mass flow rates \dot{M}_G , higher mean particle velocities $v_{d,m}$ can be achieved with hot gas atomization. As an example, the mean particle velocity $v_{d,m}$ is about 125 m/s for gas mass flow rate \dot{M}_G of about 150 kg/h with cold gas and gas mass flow rate \dot{M}_G of about 75 kg/h with hot gas ($T_G \sim 300$ °C). This suggests that the same mean particle velocity $v_{d,m}$ can be achieved at 50% of the gas flow rate \dot{M}_G with hot gas atomization [HUSS20b].

In addition, a CFD simulation (in house study by L. Buss) with single particles has been performed to observe the effect of particle velocity in the spray chamber. Figure 5-22a shows a typical particle trajectory in the gas jet for single particle simulation. The initial particle velocity of the single particle is considered as 15 m/s and three different simulations are performed with particle sizes of 65 μm , 75 μm , and 85 μm (in a range of 63 – 90 μm , similar to the experiment by LDA). The average of the three simulation runs are plotted (Figure 5-22b and c). A certain difference is found between the simulation and the experimental results. In the experiment, a particle size fraction of 63 – 90 μm was taken, but only three representative particles are considered in the numerical simulations. At room temperature, the particle velocities with the simulation are closer to the experimental result and a higher difference is observed at hot gas conditions. However, the trends are quite similar of the experimental and simulated results.

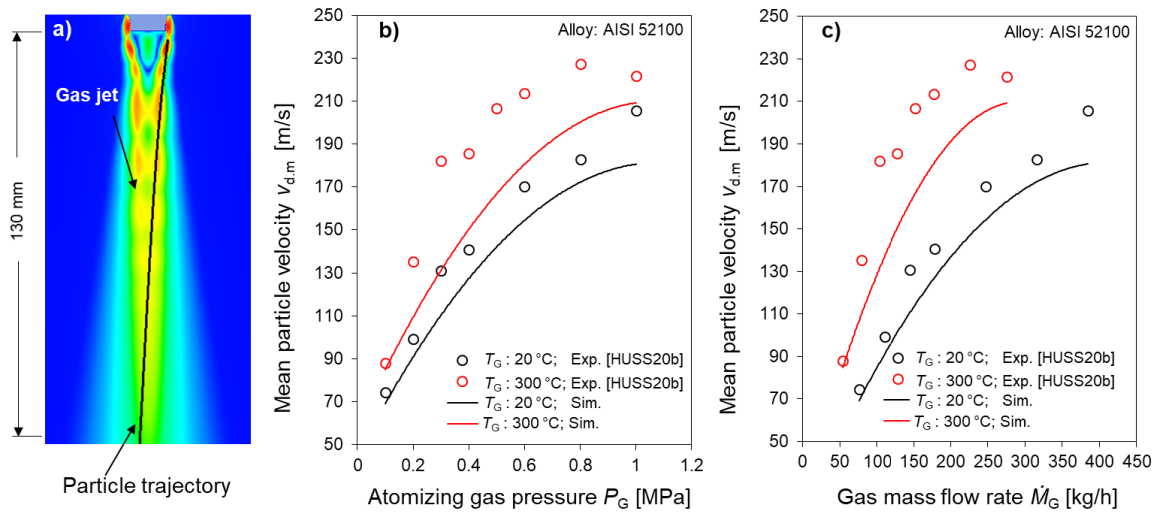


Figure 5-22: a) Particle trajectory in the gas jet (CFD simulation). Mean particle velocity measured with LDA and simulation of single particle b) as a function of atomizing gas pressure p_G , c) as a function of gas mass flow rate \dot{M}_G with cold gas at RT (293 K) and with hot gas at $\sim 300^\circ\text{C}$ (573 K) (AISI 52100 steel powders, size fraction of 63 to 90 μm) at $z = 130$ mm. The figures are adopted from [HUSS20b] simulation data by L. Buss.

5.3.3.2 Particle velocity in spray condition (simulation)

Figure 5-23 shows the mean particle velocities (for the mean particle size $d_{m,RRSB}$) at different atomization gas temperatures T_G (20 $^\circ\text{C}$, 300 $^\circ\text{C}$, and 600 $^\circ\text{C}$) and gas pressures p_G (0.6 MPa, 0.8 MPa, and 1.0 MPa) at the deposition zone for the actual melt atomization conditions. The estimated values of the process parameter for simulation runs are listed in Appendix (Table A-7). The particle velocity v_d increases with increasing gas pressure p_G for a constant gas temperature T_G and also increases at a constant gas pressure p_G with increasing atomization gas temperature T_G due to the higher kinetic energy of the atomizing gas. Since, the mean diameter of the particle size distributions decreases more drastically with increasing atomization gas temperature T_G . Therefore, the particle velocity v_d in the deposition zone is more sensitive to the changes of the atomization gas temperature T_G than the modifications in the atomization gas pressure p_G . In few cases deceleration of the particles near the nozzle ($z < 50$ mm) have been observed, which can be due to the transonic flow condition (as can be observed in Figure 5-22a) and in these cases, the particles that pass through such regions are more affected by the behavior of the gas phase.

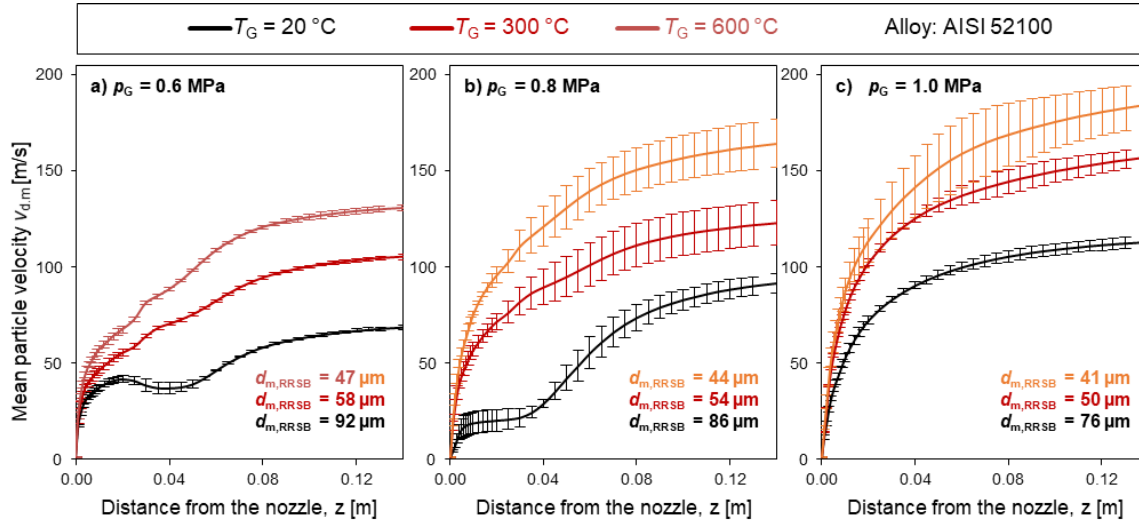


Figure 5-23: Calculated mean velocity of the AISI 52100 particles at different atomizing gas temperatures T_G (20 °C, 300 °C, and 600 °C); a) at $p_G = 0.6$ MPa, b) at $p_G = 0.8$ MPa, and c) at $p_G = 1.0$ MPa in the spray forming zone of the atomization chamber. Simulation by L. Buss.

5.3.3.3 Particle impact velocity and deformation time (simulation)

Figure 5-24a shows that the particles which are impacting at the deposition zone ($z = 130$ mm) possess higher impact velocities v_d at elevated atomization gas temperatures T_G . In addition, the particle impact velocity v_d also increases at higher atomization gas pressure p_G , i.e., from 0.6 MPa to 0.8 MPa. The impact velocities v_d show similar trends at different gas temperatures T_G (20 °C, 300 °C, and 600 °C).

In section 5.3.2 it has been shown that the mean particle size d_m decreases with increasing atomization gas temperature T_G (Figure 5-21). According to Eq. 2-10, the particle deformation time t_d after impact will reduce at a higher mean particle impact velocity $v_{d,m}$ and at a smaller mean particle size d_m ($d_{m,RRSB}$). A relative particle deformation time t_d is calculated to understand the influence of the atomization gas temperature T_G based on Eq. 2-11. The mean particle diameter $d_{m,RRSB}$ and the mean particle velocity $v_{d,m}$ are considered as:

$$t_d \propto \frac{d_{m,RRSB}}{v_{d,m}}$$

$$\text{or, } t_d = a_{def} \cdot \frac{d_{m,RRSB}}{v_{d,m}}$$

Eq. 5-9

where, t_d is the particle deformation time, $d_{m.RRSB}$ is the mean particle size from RRSB distribution, $v_{d.m}$ mean particle impact velocity and a_{def} is a proportional constant, which has been considered as 1 in a first approach.

It can be seen in Figure 5-24b that the particle deformation time t_d decreases with increasing atomization gas temperature T_G at the deposition zone $z = 130$ mm. The particle deformation time t_d also decreases with increasing atomization gas pressure p_G , since a higher atomization gas pressure p_G also reduces the mean particle size d_m and increases the mean impact particle velocity $v_{d.m}$. A sharp drop of the particle deformation time t_d has been observed from $T_G = 20$ °C to $T_G = 300$ °C. However, the particle deformation time drops slowly from $T_G = 300$ °C to $T_G = 600$ °C. It can be said that, at lower atomization temperature, the atomization gas pressure p_G has a considerable impact on particle deformation time t_d than at elevated atomization gas temperature.

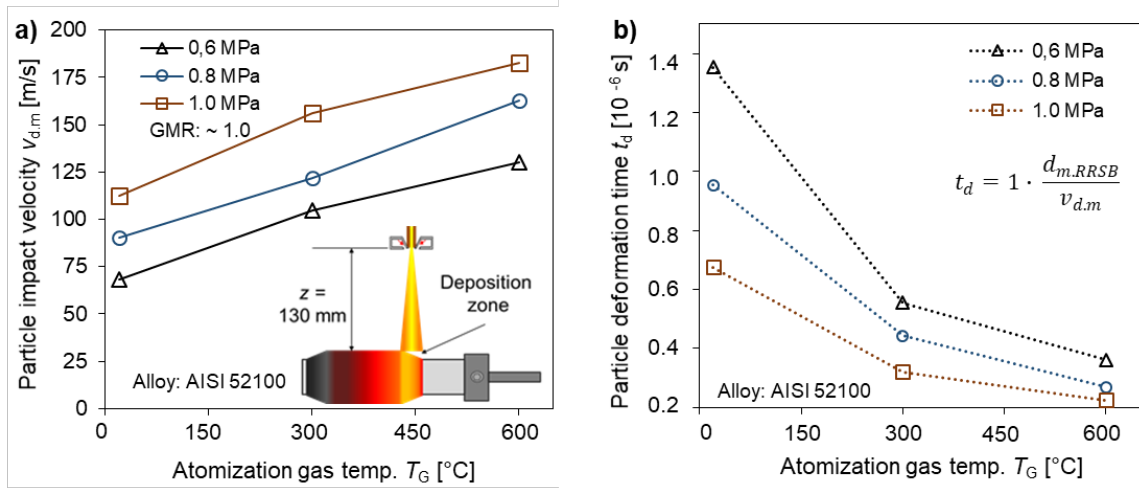


Figure 5-24: a) Calculated mean particle velocity $v_{d.m}$ versus the atomization gas temperature T_G (20 °C, 300 °C, and 600 °C) at different gas pressures p_G (0.6 MPa, 0.8 MPa, and 1.0 MPa) at a distance $z = 130$ mm from the nozzle (deposition zone); b) particle deformation time t_d at different atomization gas temperatures T_G (20 °C, 300 °C, and 600 °C) and gas pressures p_G (0.6 MPa, 0.8 MPa, and 1.0 MPa) at the deposition zone. Simulation by L. Buss.

5.3.3.4 Particle temperature and cooling rate (simulation)

Figure 5-25 shows the mean particle temperatures at different atomization gas temperatures T_G (20 °C, 300 °C, and 600 °C) and atomization gas pressures p_G (0.6 MPa, 0.8 MPa, and 1.0 MPa) at the solidification region ($T_d \leq T_{sol}$). It can be seen that the particles temperatures decrease rapidly up to the liquidus temperature T_{liq} , and the temperature

change is slow between the liquidus and solidus region. At a certain atomization gas pressure p_G , the mean particle temperature decreases with increasing atomization gas temperature T_G . Thus, by increasing the pressure of the atomization gas p_G , the axial position where the mean particle temperature reaches the liquidus and solidus temperatures moves towards the nozzle and the particles with lower temperatures would impact on the substrate at elevated gas temperatures. For example, the axial distance from the nozzle where the mean particle temperature reaches the solidus temperature ranges from ~ 0.8 to ~ 1.15 m for the cases with atomization gas pressure of 0.6 MPa, and between ~ 0.55 and ~ 0.7 m for the cases with inlet gas pressure of 1.0 MPa.

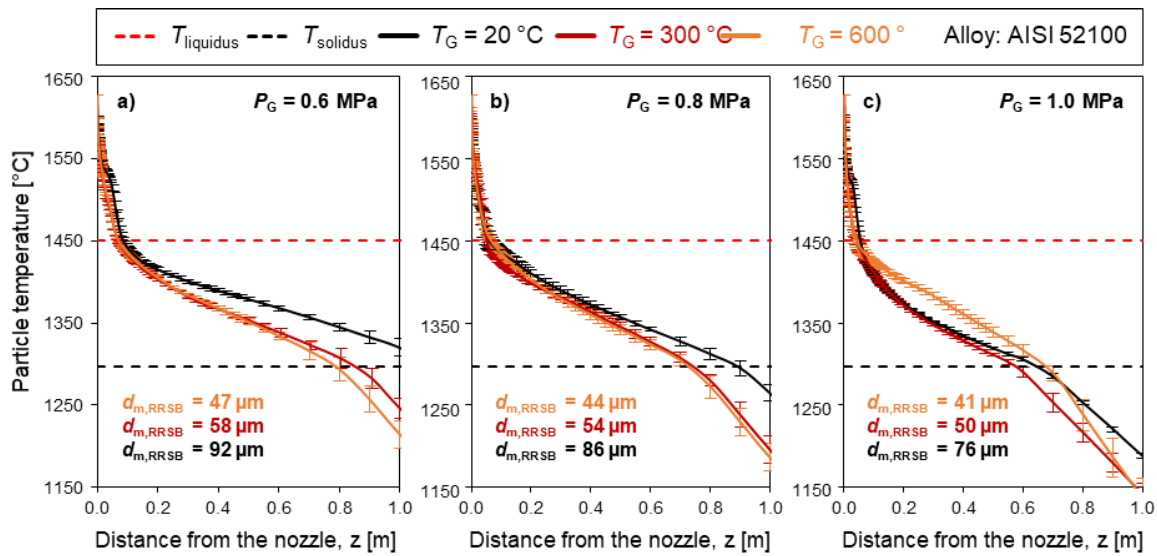


Figure 5-25: Calculated mean particle temperatures of the AISI 52100 particles at different atomizing gas temperatures T_G (20 °C, 300 °C, and 600 °C); **a)** at $P_G = 0.6$ MPa, **b)** at $P_G = 0.8$ MPa, and **c)** at $P_G = 1.0$ MPa in the spray forming zone of the atomization chamber. Simulation by L. Buss.

The calculated mean particle cooling rate is maximum in the region $0 \leq z \leq 20$ mm (Figure 5-26a). Beyond $z > 20$ mm the cooling rate is slower. At a higher atomization gas temperature T_G , the mean particle cooling rate is higher (Figure 5-26d). The mean particle size $d_{m,RRSB}$ also plays an important role in the particle cooling rate. The smaller mean particle size induces higher surface area, which further increases the cooling rate at the deposition zone. Therefore, the cooling rate of the mean particles ($d_{m,RRSB}$) is fast at higher gas inlet temperatures / atomization gas temperature T_G . Hence, the mean particle size is smaller under these operating conditions. However, an anomaly is observed at $T_G = 20$ °C and $p_G = 0.6$ MPa, which could be due to lack of simulation data.

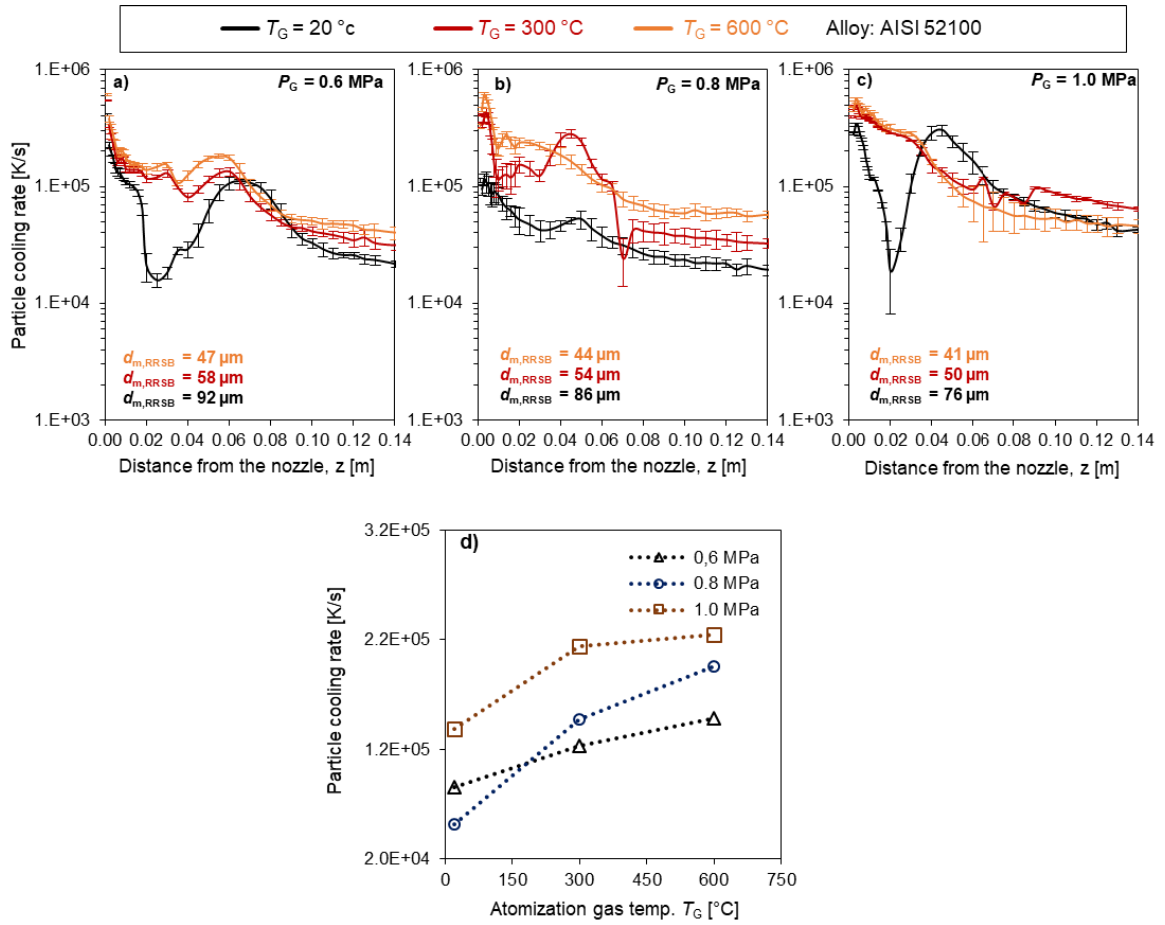


Figure 5-26: Calculated mean particle cooling rates of the AISI 52100 particles at different atomizing gas temperatures T_G (20 °C, 300 °C, and 600 °C); **a)** at $P_G = 0.6\text{ MPa}$, **b)** at $P_G = 0.8\text{ MPa}$, and **c)** at $P_G = 1.0\text{ MPa}$ in the spray forming zone of the atomization chamber, and **d)** relationship between particle cooling rate and atomization gas temperature. Simulation by L. Buss.

5.3.3.5 Enthalpy change (simulation)

Figure 5-27 shows the calculated enthalpy change of the spray from the atomization zone to the deposition area ($z = 130\text{ mm}$). The enthalpy-change increases with increasing atomization gas temperature T_G for a certain gas pressure p_G . For example, at a atomization gas pressure $p_G = 0.6\text{ MPa}$ the enthalpy change of the spray ΔH is about 16%, at a atomization gas temperature $T_G = 20\text{ °C}$ and ΔH is about 33% at $T_G = 600\text{ °C}$, which is about twice as high. The increased gas velocity v_G and smaller particle size d_d at elevated atomization gas temperature T_G facilitate more heat loss from the spray. In addition, at a

certain gas temperature T_G the enthalpy change is also higher at higher atomization gas pressure p_G due to higher gas flow.

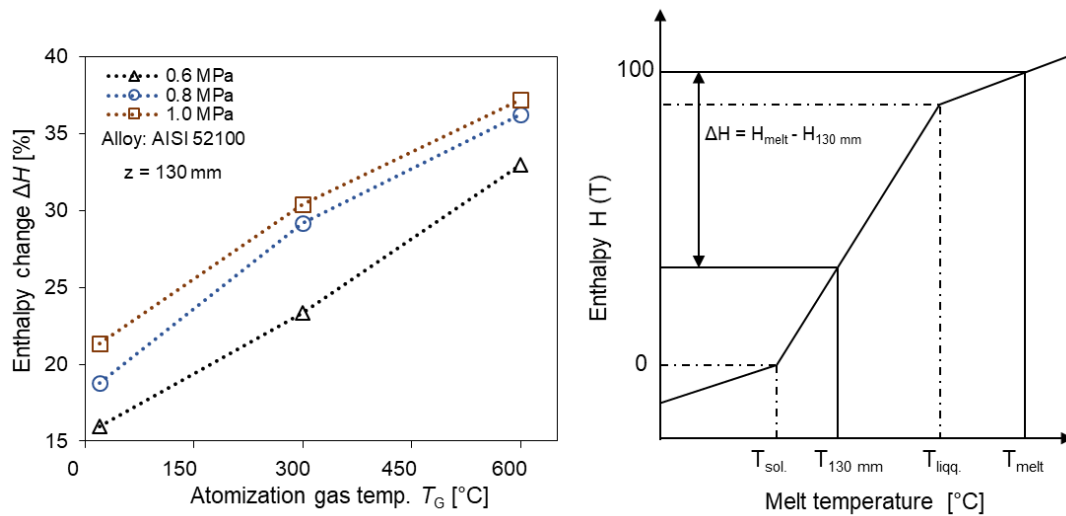


Figure 5-27: Calculated mean enthalpy change of the AISI 52100 spray at different atomization gas temperatures T_G (20 °C, 300 °C, and 600 °C) and atomization gas pressures ($P_G = 0.6, 0.8$, and 1.0 MPa) in the spray forming zone ($z = 130$ mm) of the spray chamber. Simulation by L. Buss.

In summary of the sub-chapters 5.3.1 to 5.3.3 (hot gas atomization): the gas velocity increases and gas mass flow rate decreases with increasing atomization gas temperature (Figure 5-17). At elevated gas temperature the melt mass flow also decreases with decreasing gas mass flow rate (Figure 5-18). The higher gas velocity results in smaller particles with lower gas consumptions at elevated atomizing gas temperatures (Figure 5-19 and Figure 5-21), as proposed in the ***hypothesis 2: the particle velocity in the spray can be increased by using hot gas in atomization even at similar droplet size***. The elevated atomization gas temperatures further increase the particle impact velocity (Figure 5-23), which subsequently reduces the particle deformation time (Figure 5-24). Furthermore, the smaller particles cool faster with hot gas atomization (Figure 5-26), i.e. the mean particle temperature is lower (Figure 5-25) and enthalpy change of the spray is higher (Figure 5-27) at the deposition zone. The particle with decreased deformation time and colder at the deposition zone with hot gas atomization are achievable as proposed in the ***hypothesis 3: decreased deformation times during droplet impact will result in high density materials and will extend the process window***. In the next section the effect of the decreased deformation time and colder particles on the as-sprayed deposits will be presented.

5.3.4 Spray-formed deposits with hot gas atomization

In this section the *hypothesis 3: decreased deformation times during droplet impact will result in high density materials and will extend the process window*, will be discussed. The spray-formed deposits with different gas temperatures (RT/ 20 °C and HG/ 290 ± 40) will be investigated and compared to understand the effect of the atomization gas temperature. In particular, the deposit surface temperature, microstructure, porosity, grain size, and relative density are investigated. Furthermore, the extension of the process window via hot gas atomization will be discussed. The varied key process parameters in this section are listed in Table 5-6. The process parameters can be found in Appendix (Table A-4 to A-5b) in details.

Table 5-6 Key process parameters varied in section 5.3.4.

Atomizer	Substrate $\varnothing_s \times l_s$ [mm]	Substrate thickness [mm]	Gas temperature T_G [°C]	Gas pressure [MPa]	GMR [-]
CCA-HG	90 x 270 130 x 180	3.5 – 5	20 – 330	0.6 – 1.6	0.8 – 1.5

5.3.4.1 Deposit surface temperature and surface roughness

Figure 5-28a shows the relationship between the deposit thickness y and the maximum deposit surface temperature $T_{D,max}$ at a spray distance $z = 130$ mm. Similar to the previous section (5.2), the maximum deposit surface temperature $T_{D,max}$ increases with increasing deposit thickness y for both cold gas (RT) atomization and hot gas ($T_G = 280 \pm 30$ °C) atomization [HUSS20b]. For similar deposit thickness y the maximum deposit surface temperature $T_{D,max}$ is higher in cold gas atomization than in hot gas atomization. It suggests that the smaller droplets during hot gas atomization cool faster and lower heat energy (enthalpy, ΔH) is brought into the deposition zone by hot gas atomization. Similar observations are found in the simulation results.

However, the melt mass flow rate \dot{M}_L also decreases with decreasing gas mass flow rate \dot{M}_G for the close-coupled atomizer (see Figure 5-18), which is due to the lower aspiration pressure on the melt pouring-nozzle opening area [SCHW17, CIFT20] with hot gas. A lower melt mass flow rate \dot{M}_L also contributes to the enthalpy input in the deposition zone [HUSS20b].

In addition, the surface roughness is also affected by the deposit surface temperature T_D (Figure 5-29a). The deposit surface roughness measurements show that the deposit with higher maximum deposit surface temperature $T_{D,max}$ possesses higher surface roughness (S_a is the arithmetical mean height). However, the higher surface roughness can be avoided by increasing the deposition distance z [Eq. 2-12]. Higher deposition distance z increases the solid fraction in the deposition zone by releasing more heat to the surrounding [ELLE14].

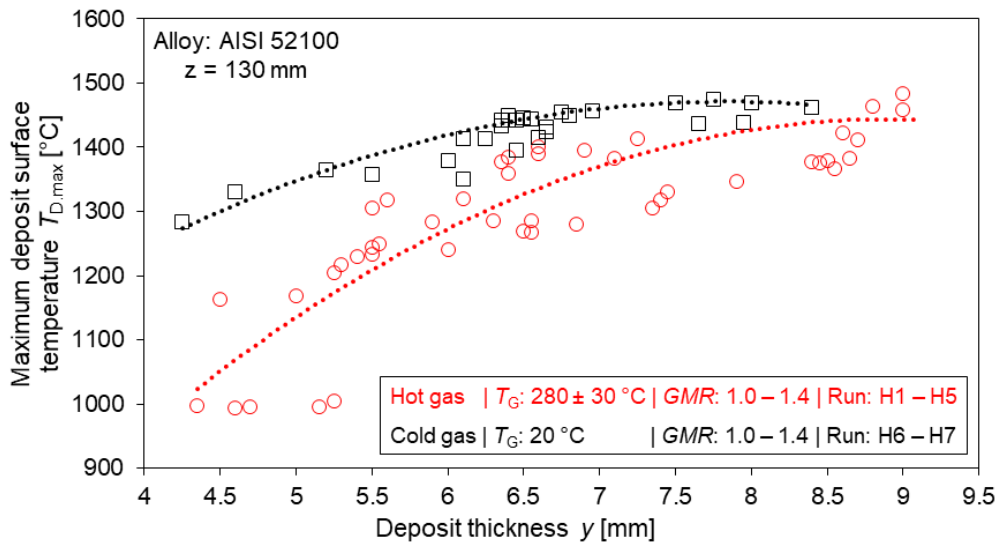


Figure 5-28: a) Deposit thickness y versus maximum deposit surface temperature $T_{D,max}$, b) gas mass flow rate \dot{M}_G versus melt flow rate \dot{M}_L in spray forming with a CCA in cold gas atomization ($T_G = RT$, GMR: 1.2 – 1.5) and hot gas atomization ($T_G = 280 \pm 30$ °C, GMR: 1.0 – 1.4). The figures are adopted from [HUSS20b].

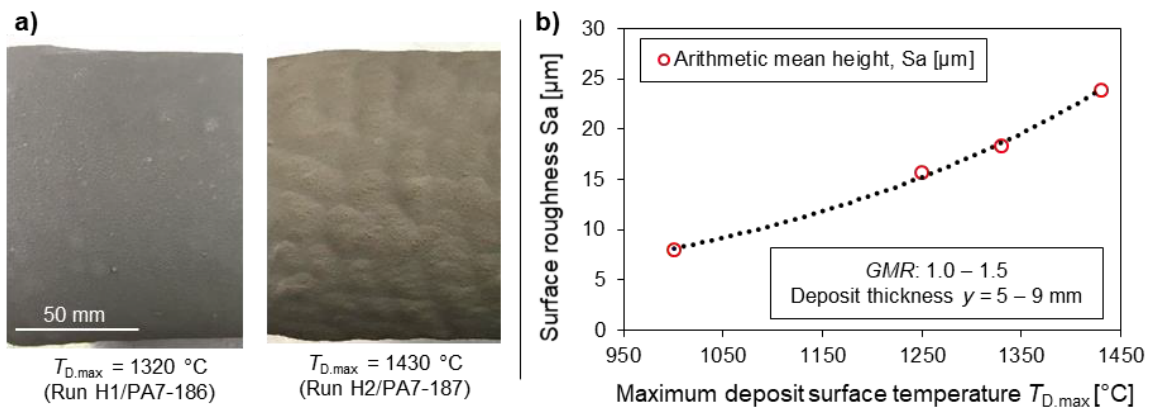


Figure 5-29: a) Deposit surface at two different deposit surface temperatures for different atomizing conditions; b) relationship between the maximum deposit surface temperature $T_{D,max}$ with the deposit surface roughness (S_a). Surface roughness measured by white light interferometry. The figures are reprinted from [HUSS20b].

5.3.4.2 Microstructure and porosity

The microstructure and the porosity of the spray-formed deposit at similar *GMR* have been compared for hot gas and cold gas atomization conditions to understand the influence of the process parameters. Figure 5-30a shows two deposit segments from Run H5 (PA7-232, $T_G = 300\text{ }^\circ\text{C}$ and $GMR = 1.2$) and Run H6 (PA7-228, $T_G = 20\text{ }^\circ\text{C}$ and $GMR = 1.2$). Both the ring-segments have been taken from 20 mm distance of the deposit start position. The etched (see Table 4-4 for etching solutions and conditions) samples show a pearlitic microstructure (Figure 5-30b). The microstructure shows hardly any significant change at different atomizing gas temperatures [HUSS20b].

From the polished unetched samples, magnified images in three different areas are shown in Figure 5-30c, where P1 is near the outer surface, P2 is at the deposit center and P3 is in the vicinity of the substrate. In the vicinity of the substrate the porosity is higher, the pores are mainly cold pores as mentioned in section 5.1. The deposit center shows the least porosity, with mainly smaller circular hot or gas pores. However, the deposit spray-formed via cold gas atomization shows larger hot pores in the deposit center due to higher deposit temperatures.

Figure 5-31 shows the porosity profile of the deposit segments from Run H5/PA7-232 and Run H6/PA7-228 from near the substrate region to the outer surface. The deposit via cold gas atomization (Run H6/PA7-228) shows higher porosity than the deposit via hot gas atomization (Run H5/ PA7-232). In the deposit center of Run H6 the larger pores can be attributed to be hot porosity, which are formed by gas entrapment [HUSS20b]. At a relatively higher deposit temperature, a higher liquid fraction in the deposition zone is developed and the gas bubbles are trapped in the mushy zone [HU00, LIU18].

Figure 5-32 shows the relationship between the average grain size (grain diameter) and the local average deposit surface temperature $T_{D,avg}$ (the average of the deposit surface temperatures from pyrometer line-scan is taken at the same position as the grain size measurement). The grain size distribution shows a similar trend as the model proposed by [SRIV04], where the grains are smaller in the vicinity of the substrate (chilled zone) and the grain size is maximum at the deposit center (mushy zone). The deposits produced with hot gas atomization ($T_G = 280 \pm 30\text{ }^\circ\text{C}$, $GMR: 1 - 1.4$) show smaller grain sizes compared to the deposits produced with cold gas atomization ($T_G = 20\text{ }^\circ\text{C}$, $GMR: 1.2 - 1.5$), suggesting faster cooling of the deposit with hot gas atomization. The reduced particle size and higher

cooling rate of the particles by hot gas atomization further increase the solid fraction in the deposition zone. This faster solidification in the deposition zone hinders the coalescence of the deposited droplets through re-melting

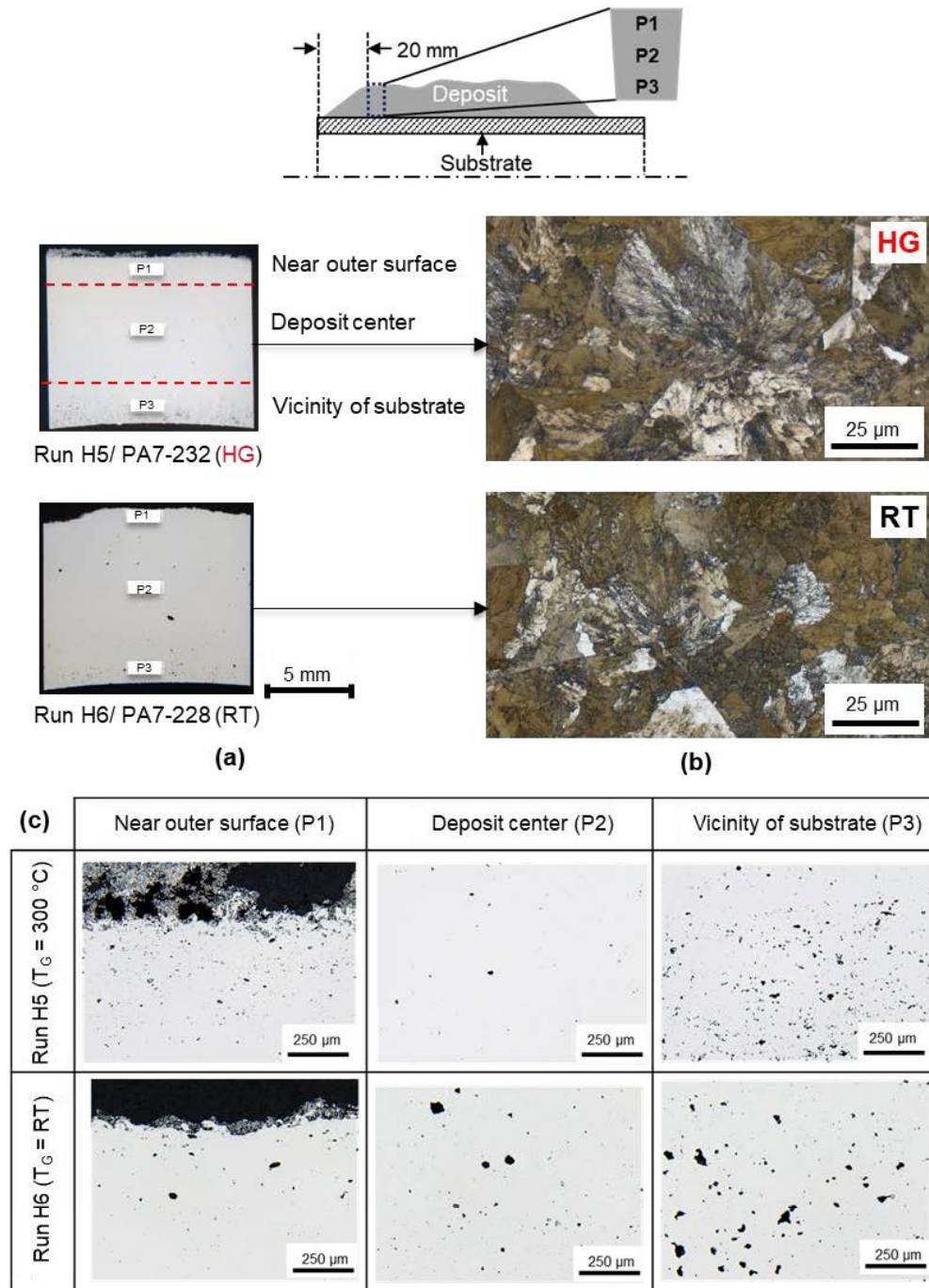


Figure 5-30: Ring segment of the deposit a) polished un-etched (P1 is near the outer surface, P2 is at the deposit center and P3 is neat to the substrate), b) etched at P2 region (pearlitic microstructure); c) magnified image at P1, P2 and P3 areas of the deposits (Run H5/PA7-232 at HG and Run H6/PA7-228 at RT). The figures are adopted from [HUSS20b].

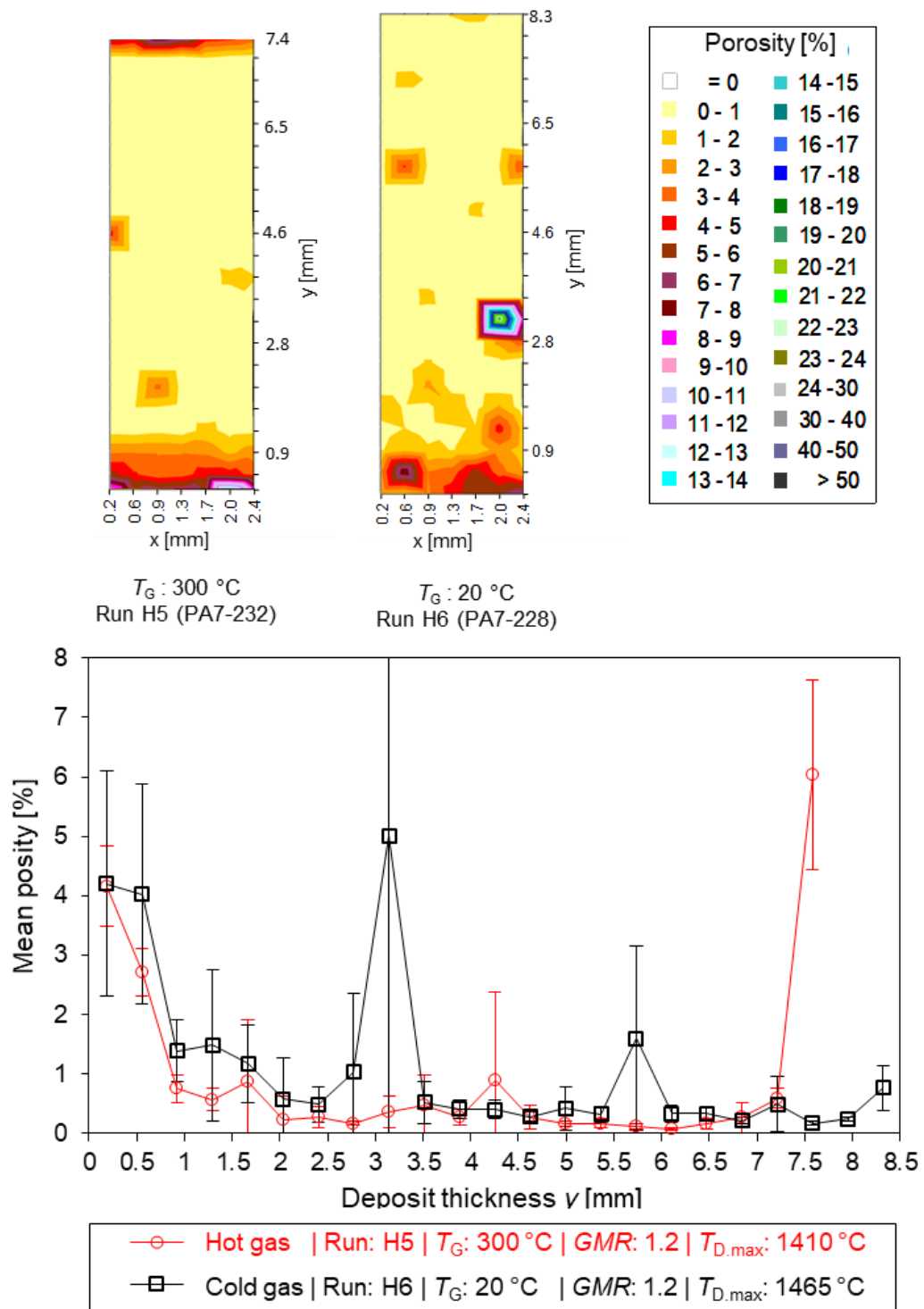


Figure 5-31: Mean porosity of deposit sections from the vicinity of the substrate to the outer surface. Two samples are taken from Run H5/PA7-232 and Run H6/PA7-228 (Run H5 at $T_G = 300$ °C and Run H6 at $T_G = RT$). The figures are adopted from [HUSS20b].

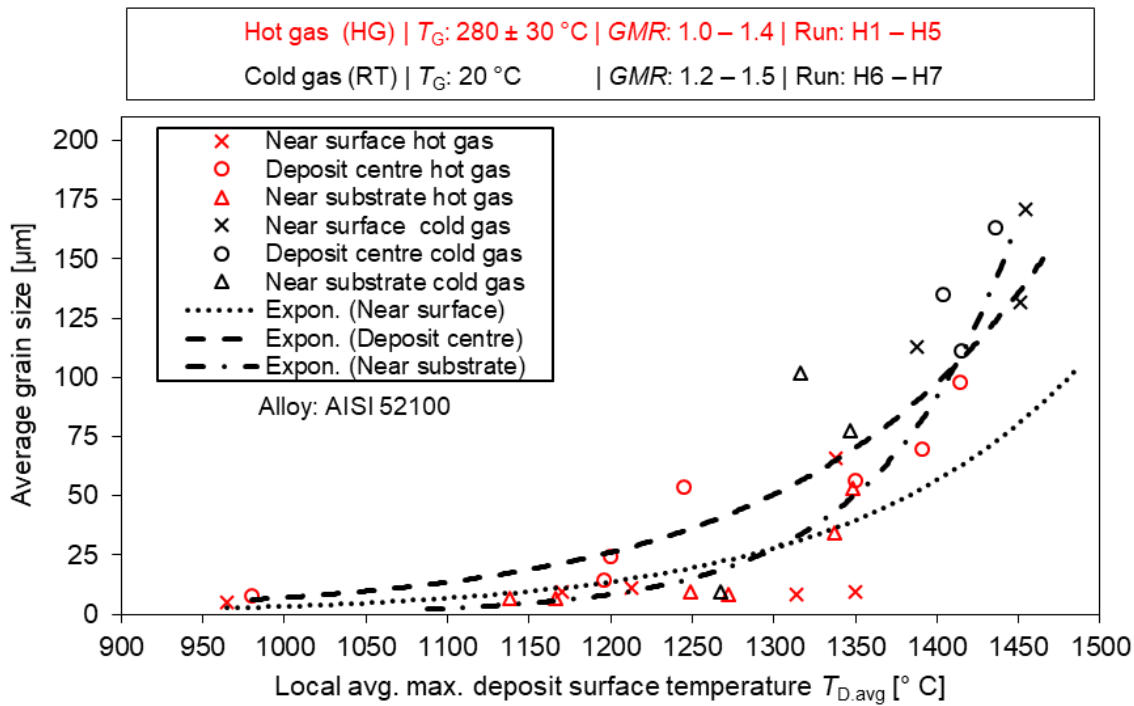


Figure 5-32: Relationship between average grain size and local average deposit surface temperature (Run H1 to Run H7). At hot gas (HG) atomization $T_G = 280 \pm 30^\circ\text{C}$, GMR: 1 to 1.4 and at cold gas atomization $T_G = 20^\circ\text{C}$, GMR: 1.2 to 1.5. The figure is modified reprinted from [HUSS20b].

Figure 5-33 shows the relationship between the mean porosity and the grain size in hot gas and cold gas atomization conditions (at hot gas (HG) atomization $T_G = 250 - 310^\circ\text{C}$, GMR: 1 to 1.4 and at cold gas atomization $T_G = 20^\circ\text{C}$, GMR: 1.2 to 1.5). The grain size and the porosity were measured at similar positions in the deposit segments. The porosity increases with decreasing grain size for both hot gas and cold gas atomization conditions. The deposits produced with hot gas atomization show lower porosity even at smaller grain sizes (porosity is below 2% for grain sizes of 10 – 75 μm). The deposits produced with cold gas atomization show larger grain sizes due to the slow cooling of the deposit with higher deposit surface temperature. At below 2% porosity level the mean average grain size is about 110 to 175 μm for cold gas condition. The finer grains in the hot gas atomization suggests better mechanical properties of the as-sprayed deposits [HUSS20b].

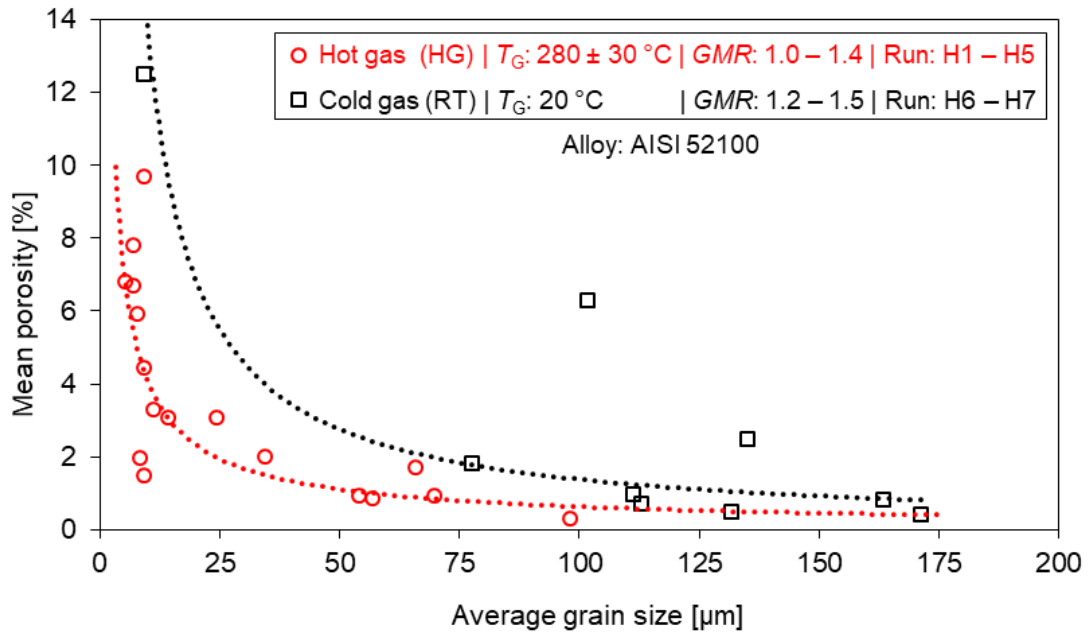


Figure 5-33: Mean porosity of deposit sections as a function of average grain size from the vicinity of the substrate to the outer surface. At hot gas (HG) atomization $T_G = 250 - 310\text{ }^{\circ}\text{C}$, $GMR: 1$ to 1.4 and at cold gas atomization $T_G = 20\text{ }^{\circ}\text{C}$, $GMR: 1.2$ to 1.5 . The figure is reprinted from [HUSS20b].

5.3.4.3 Extension of the process window

According to Eq. 3-1 at smaller droplet sizes d_d and at higher impact velocities v_d the droplet deformation time t_d is expected to be reduced. At shorter droplet deformation time the impacting particle may provide much denser deposits by better compaction of the droplets in the deposition zone. Furthermore, higher droplet velocity also increases the spreading after impingement [DHIM05]. It has been shown that smaller droplets with higher impact velocities v_d can be produced by a close-coupled atomizer with elevated gas temperature T_G . In addition, the deposit surface temperature with hot gas atomization is lower at a similar deposit thickness compared to cold gas atomization (Figure 5-28), which is due to lower specific enthalpy input into the deposit by smaller droplets (Eq. 2-12). The smaller grain sizes with hot gas atomization also suggests a colder deposit due to a higher amount of solid fraction in the impinging droplets [HUSS20b]. It has been shown that the porosity increases with decreasing deposit surface temperature T_D (Figure 5-15). The deposit surface temperature T_D is also related to the melt mass flow rate \dot{M}_L , higher melt mass flow rate brings more heat in to the deposition area. The porosity increases at lower melt mass

flow rate \dot{M}_L [CAI97]. The effect of hot gas atomization on the relationship between the deposit surface temperature and relative density in the deposit center is outlined in Figure 5-34.

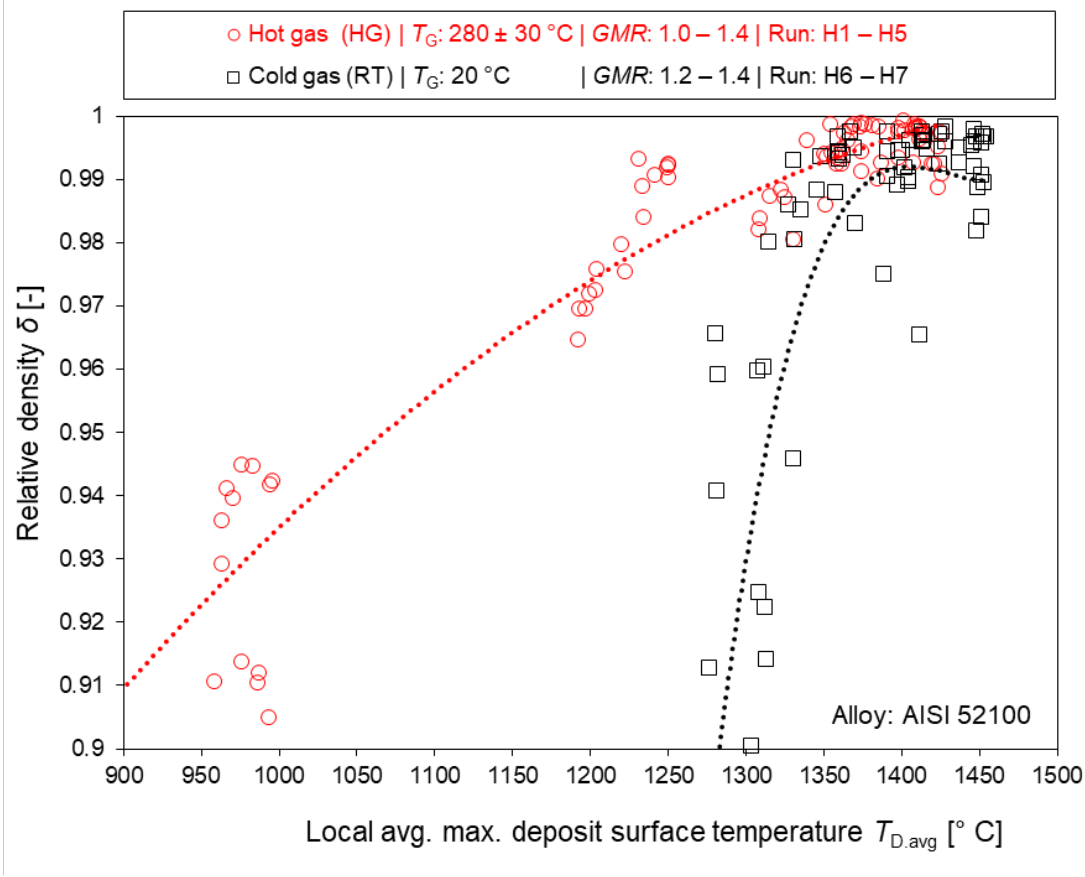


Figure 5-34: Relative density δ of the spray-formed deposits in relationship to the local deposit surface temperature $T_{D,avg}$ for cold gas ($T_G = 20$ °C, $GMR: 1.2$ to 1.5) and hot gas atomization ($T_G = 280 \pm 30$ °C, $GMR: 1$ to 1.4) in the deposit center areas. The porous regions in the vicinity of the the substrate and in the deposit surface zone are excluded. The process parameters can be found in Table A-5. The figure is reprinted from [HUSS20b].

Three groups of data points are to be observed for the hot gas atomization runs due to the variation of the deposit thickness y (the deposit thickness varies by changing the substrate transitional velocity v_s). Above the solidus temperature T_{sol} (for AISI 52100 solidus temperature $T_{sol} \sim 1300$ °C; solidus temperature calculated by *ThermoCalc* software using Fe-database), the deposits show high relative density δ (above 0.95) in the deposit center for both cold gas atomization and hot gas atomization. The deposits produced with cold gas atomization ($T_G = 20$ °C, $GMR: 1.2$ to 1.5) show lower relative density δ (below 0.95) at the local deposit surface temperatures $T_{D,avg}$ below solidus temperature T_{sol} . In contrast, the

deposits produced with hot gas atomization show higher relative density δ at lower local deposit surface temperature $T_{D,avg}$ even below the solidus temperature T_{sol} . For example, the relative density is approx. 0.99 at a local deposit surface temperature $T_{D,avg} \sim 1230$ °C for the deposits produced with hot gas atomization. The obtained outcome supports the proposed hypothesis that at lower deposit surface temperatures T_D , a deposit with a high relative density δ can be spray-formed with hot gas atomization utilizing the better deformation of the impinged droplets. However, low relative densities δ are found in the local deposit surface temperature range of 950 °C to 1000 °C with hot gas atomization (corresponding deposit thickness $y \sim 5$ mm, Run H3/PA7-188). This suggests that a minimum deposit surface temperature T_D must be achieved to obtain high relative densities in the deposit, even with the use of hot gas atomization [HUSS20b]. The deposit surface temperature is also related to the deposit thickness, which suggests that a minimum deposit thickness y also must be achieved to obtain a high relative density.

5.3.4.4 Effect of substrate heating and larger substrate diameter

The effect of substrate pre-heating up to 300 °C (573K) with hot process gas from the atomizer is investigated. Here different substrate geometry (substrate diameter $\varnothing_s = 130$ mm x thickness $s = 3.5$ mm) is used for the spray forming runs. With a larger substrate diameter, the effect of substrate diameter in cooling behaviour of the deposit is investigated. The surface area increases for $\varnothing_s = 130$ mm than $\varnothing_s = 90$ mm. The process parameters are listed in Appendix (Table A-5b).

Figure 5-35 shows the relationship between normalized deposit thickness and mean porosity in the deposit start position (all the samples are taken 20 mm away from the deposit starting end). With increasing substrate pre-heating (substrate temperature T_s before starting melt atomization) the mean porosity in the vicinity of the substrate decreases significantly. The mean porosity in the vicinity of the substrate is maximum (about 35%, Run H8/PA7-268) without any substrate pre-heating for cold gas atomization. However, in the previous sections (5.2.1.2 and 5.3.4.2) the porosity is much lower in the vicinity of the substrate with CCA (for substrate diameter $\varnothing_s = 90$ mm). In this case the larger surface area facilitates higher and faster cooling of the initial layers of the deposit and form cold porosity. At a substrate pre-heating temperature $T_s = 150$ °C (Run H10/PA7-270) the porosity in the vicinity of the substrate is lower than cold condition (Run H8/PA7-268). For substrate pre-heating temperature $T_s = 300$ °C the porosity in the vicinity of the substrate is

minimum (about 5%, Run H11/PA7-271). At higher pre-heating temperatures less porosity can be achieved. Further pre-heating of the substrate would provide less porosity in the vicinity of the substrate. For example, using of higher atomization gas temperature T_G (up to 1000°C) will provide substrate pre-heating without any additional substrate heating arrangement [BUCH04].

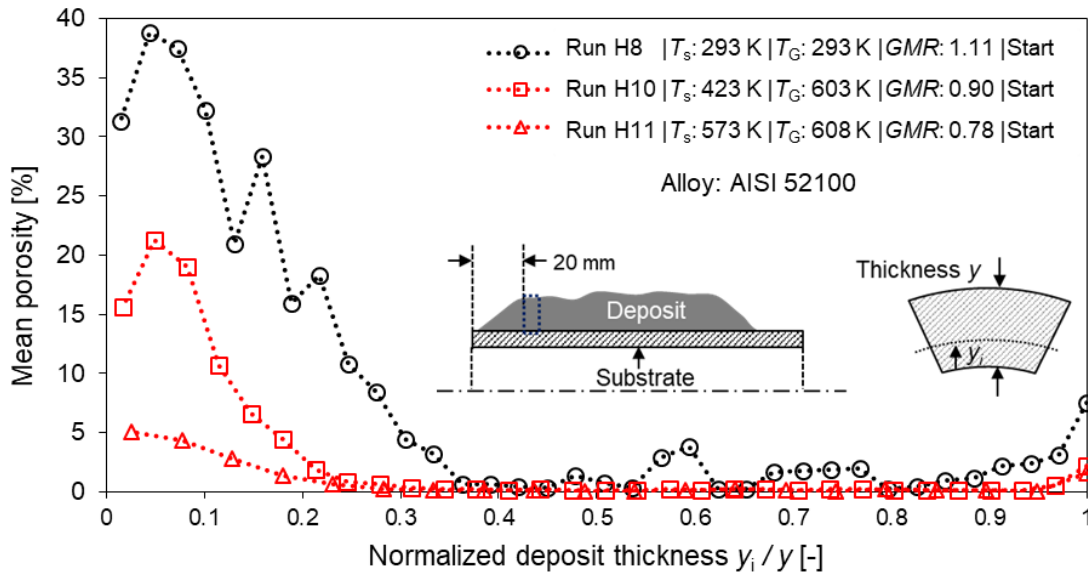


Figure 5-35: Effect of substrate pre-heating on the porosity in the vicinity of the substrate. Substrate heating with hot N_2 gas from the atomizer. Samples taken 20 mm away from the deposit starting end (start position).

In the previous section (5.3.4.2) it has been shown that the porosity increases with smaller grain size and that a lesser porosity is achievable with hot gas atomization (Figure 5-33). For larger substrate diameters, further smaller grain sizes are found at lesser porosity level. Figure 5-36 shows the effect of the substrate diameter on the relationship between the mean porosity and the grain size for both hot gas ($T_G = 290 \pm 40$ °C, GMR : 0.8 to 0.9) and cold gas ($T_G = 20$ °C, GMR : 1.1 to 1.2) conditions. During hot gas atomization condition the grain sizes in the deposits are smaller at substrate diameter $\varnothing_s = 130$ mm than the substrate diameter $\varnothing_s = 90$ mm. The larger substrate introduces more surface area to the surroundings and facilitate faster cooling of the deposit. Therefore, smaller grain sizes can be achieved at similar atomizing conditions. For cold gas atomization the same behaviour is observed, the grain size goes down without affecting the porosity. These observations indicate that with larger substrate diameter the process window of the tubular deposit production also can be influenced. Deposits with higher densities can be produced at lower deposit surface temperature and with better mechanical qualities.

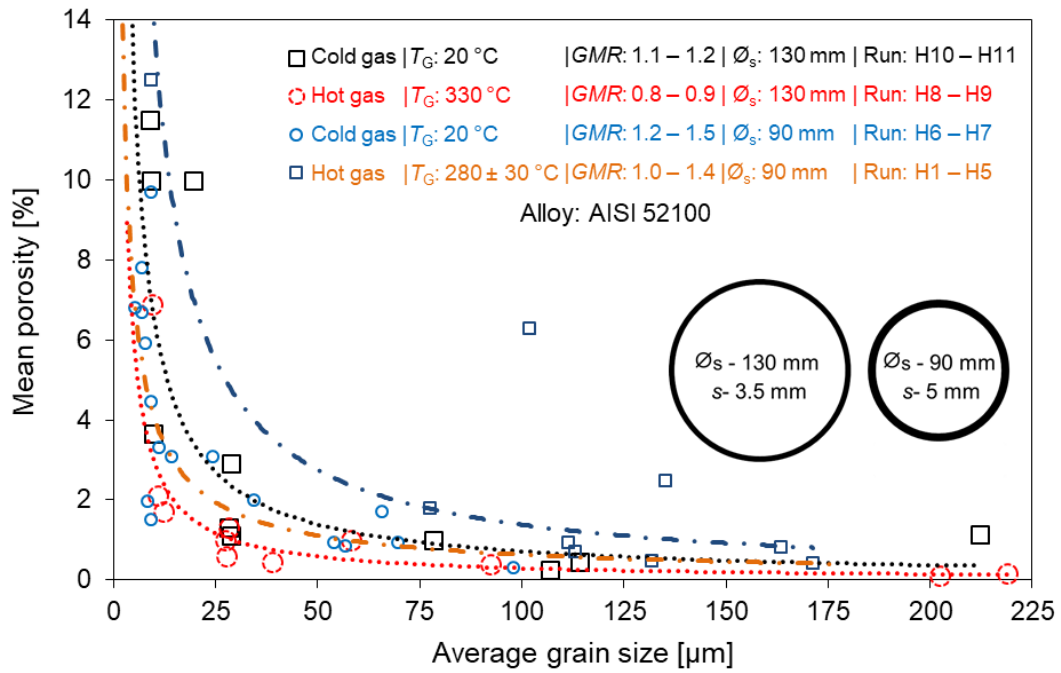


Figure 5-36: Mean porosity of deposit sections as a function of average grain size from the vicinity of the substrate to the outer surface for hot gas (HG) $T_G = 290 \pm 40$ °C, GMR : 0.8 to 1.4 and cold gas atomization $T_G = 20$ °C, GMR : 1.1 to 1.5. Process parameters in Appendix (Table A-5a and 5b).

Figure 5-37 shows the relationship between the local average deposit surface temperature $T_{D,avg}$ and the relative density δ in the deposit center for two different substrate diameters ($\varnothing_s = 130$ mm and $\varnothing_s = 90$ mm). It can be seen that a much higher relative density can be achieved with larger substrate diameters for both cold gas and hot gas atomization. The curves shift toward the left, which indicates that with larger substrate diameter denser deposits can be spray-formed even at lower deposit surface temperatures. With combination of larger substrate diameter ($\varnothing_s = 130$ mm) and hot gas atomization, about 0.99 relative density is achieved at a DTT (ratio of Deposit surface Temperature and solidus Temperature) of 0.85. In contrast, with smaller substrate diameter ($\varnothing_s = 90$ mm) about 0.99 relative density is achieved at $DTT = 0.95$ with hot gas atomization. Above $DTT > 0.95$ a higher density deposit is desirable with hot gas atomization. However, with cold gas atomization lower relative densities are observed even at $DTT = 1.0$. It can be concluded that hot gas atomization leads to better material quality and higher yield even at a lower deposit surface temperature, which subsequently extends the process window and provides more flexibility during the production of tubular deposits.

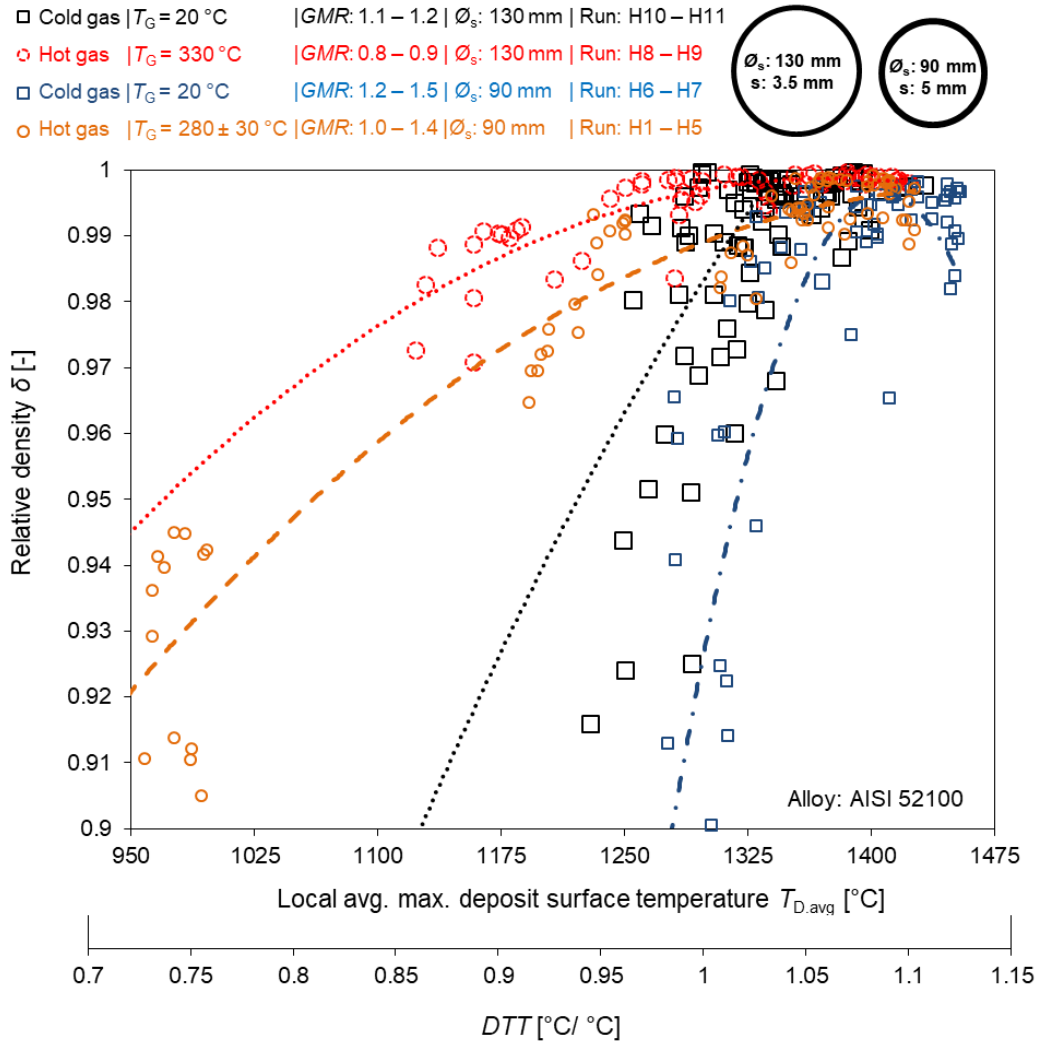


Figure 5-37: Relationship between relative density δ and local deposit surface temperature $T_{D,avg}$ of the spray-formed deposits via cold gas ($T_G = 20\text{ °C}$, $GMR: 1.1$ to 1.2) and hot gas atomization ($T_G = 330\text{ °C}$, $GMR: 0.8$ to 0.9) in the deposit center areas. Process parameters are listed in the Appendix (Table A-5). The porous regions near the substrate and in the deposit surface zone are excluded.

5.3.4.5 Prediction of density

The density in the tubular deposit are mainly affected by the process parameters like GMR , position of the sample (e.g. end position shows lower density), maximum deposit surface temperature. The GMR has more effect on the density in the vicinity of the substrate (Figure 5-8) and deposit surface region, as faster cooling rate result in cold porosity in those regions. Only the denser ($\delta > 0.90$) deposit center has been considered for the prediction

of the density of the tubular deposits. In addition, the tubular deposit with hot gas atomization show better relative density than the deposit with cold gas atomization. Therefore, two different prediction models for hot and cold gas are presented in Figure 5-38. The prediction models show more packed distribution at higher relative densities ($0.96 < \delta < 1$) for both hot gas and cold gas atomization conditions. For hot gas condition the predicted relative density also comparable to the experimental data and the $R^2_{Hot\ gas} = 0.87$ for the hot gas model. In contrast, at lower densities ($0.90 < \delta < 0.96$) the predicted relative densities are more deviated from the experimental data. The $R^2_{Cold\ gas} = 0.35$ for the cold gas model.

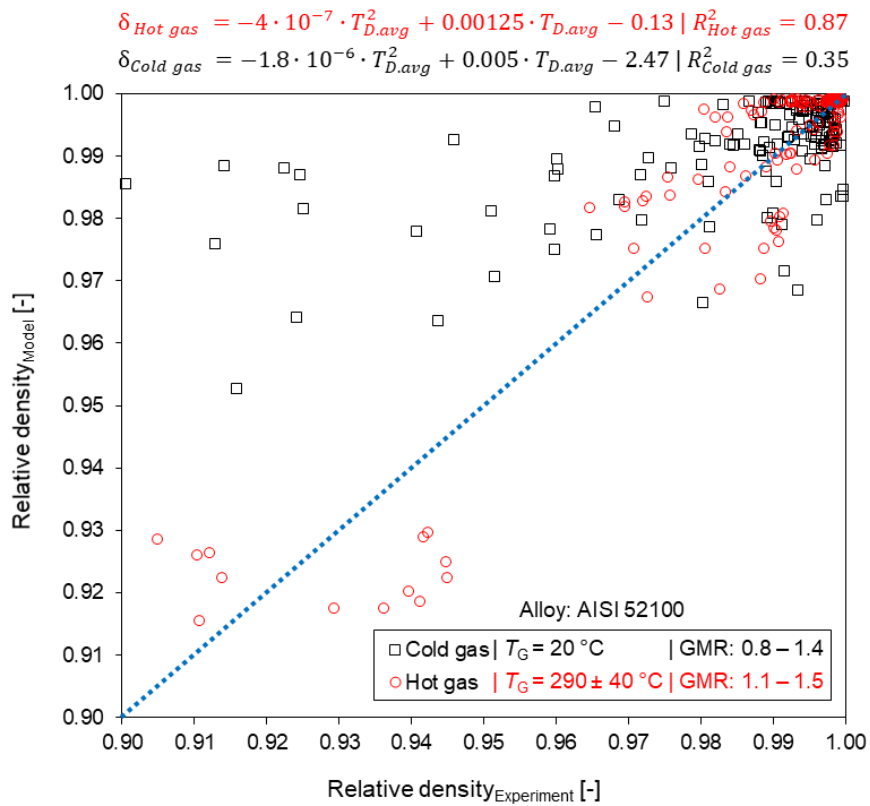


Figure 5-38: Comparison of the experimental and the model relative density in the deposit center for AISI 52100 steel. Process parameters can be found in Appendix (Table A-5). The porous regions near the substrate and in the deposit surface zone are excluded.

In summary of 5.3.4 spray forming of tubular deposit with hot gas atomization: the smaller particles bring lower heat energy in the deposition zone due to the higher solid fraction in the droplets by hot gas atomization. Therefore, the deposits with hot gas atomization show lower deposit surface temperatures than the deposits with cold gas atomization at a similar deposit wall thickness (Figure 5-28). At a higher deposit surface temperature, the surface roughness of the deposit also increases (Figure 5-29), which is also vital for the final product

quality. However, the microstructure of the spray-formed deposit (AISI 52100) by hot gas atomization is same as the deposit by cold gas atomization (Figure 5-30). The porosity level decreases at a constant *GMR* during hot gas atomization (Figure 5-31) due to higher impact velocity and shorter deformation time as proposed in the ***hypothesis 3: decreased deformation times during droplet impact will result in high density materials and will extend the process window***. At lower deposit surface temperatures, the grain size of the spray-formed deposit decreases (Figure 5-32) and less porosity is observed even at lower grain sizes for hot gas atomization conditions (Figure 5-33). Higher relative densities can be achieved even at lower deposit surface temperatures even below solidus temperature by hot gas (Figure 5-34), suggesting the denser tubular deposit can be produced for an extended temperature window as proposed in the ***hypothesis 3***. However, a certain level of deposit surface temperature should be reached for higher density. Substrate pre-heating up to 300 °C shows that the porosity level in the vicinity of the substrate decreases with increasing pre-heating (Figure 5-35). Larger substrate diameter also affects the cooling behaviour of the spray-formed deposits. The faster cooling of the deposits introduces smaller grain sizes (Figure 5-36) and lower deposit surface temperature even at higher density (Figure 5-37). The prediction model for the density in the tubular deposit with hot gas atomization shows comparable data as the experiments (Figure 5-38). However, for cold gas condition the prediction model differs in the lower density region. The derived knowledge for spray forming with a CCA are summarized in Table 5-7.

Table 5-7 Effect of hot gas atomization on key parameters/factors by CCA compared to FFA.

Parameters/Factor	Cold gas	Hot gas	Note
Gas velocity	↑	↑↑	At same gas pressure
Gas consumption	↑	↓↓	At same gas pressure
Melt mass flow rate		↓	At same gas pressure
Particle diameter	↓	↓↓	At same gas pressure
Particle velocity		↑↑	At same spray distance
Particle cooling rate		↓	At same gas pressure
Particle temperature		↓	At same spray distance
Enthalpy change of spray		↓	At same spray distance
Deposit surface temp.		↓	At same spray distance and deposit thickness
Surface roughness	↓	↓	At same deposit thickness
Porosity	↓	↓↓	At same surface temperature
Grain size		↓	At same deposit porosity

5.4 Spray forming of Al alloys tubes

In section 5.1, tubular steel (AISI 52100) deposits spray-formed with a close-coupled atomizer showed better material qualities in terms of porosity and yield. In this section, the ***hypothesis 4: the developed knowledge of improving production of spray formed tubes with advanced properties is transferable to other alloy systems***, will be discussed. To investigate that, two Al-alloys: Al-5083 (AlMg4.5Mn0.7) and Al-6082 (AlMgSi1) have been spray-formed with a close-coupled atomizer in cold gas condition. The varied process parameters in this section are listed in Table 5-8. Process parameters for spray forming runs with Al-alloys can be found in the Appendix (Table A-9) in detail.

Table 5-8 Key process parameters varied in section 5.4.

Atomizer	Substrate thickness [mm]	Substrate velocity [mm/s]	Gas temperature [°C]	Gas pressure [MPa]	GMR [-]
CCA	3.5	2	20	0.5 – .7	1.5 – 1.9

5.4.1 Spray forming setup and deposit

For spray forming of aluminium tubes a atomizing facility (tilting crucible technique, SK-2/PA9 at University of Bremen, FB 04) was used, which is facilitated with an explosion protection system. Figure 5-39 shows a schematic of the Al-spray forming setup with the close-coupled atomizer (CD-CCA-0.8). The feed stock material is melted in a separate ceramic crucible with an induction system in N₂ environment. During atomization the melt is poured into a graphite tundish and passes through a graphite pouring nozzle. The tundish and pouring nozzle are preheated to melt temperature (e.g. 800 °C for Al-5083 alloy). Sand blasted low carbon steel tubes are used as substrate (substrate diameter \varnothing_s – 130 mm x substrate thickness s – 3.5 mm). The same substrate movement mechanism system as steel deposits is used for substrate rotation and transitional velocity.

Figure 5-40a shows a tubular Al-5083 spray-formed deposit produced with a close-coupled atomizer (Run A2/PA9-824). Some extra melt in the tundish is sprayed (layer 2) on the initial layer (layer 1) of the deposit, as shown in Figure 5-40b. However, the ring segments are taken from initial layer (Figure 5-40c) of the deposit similar to the steel deposit. Two ring segments are taken from deposit start and end positions (as shown in Figure 5-40c). Porosity and microstructure measurements of the ring segments are done in three areas

(P1 – near surface, P2 – in the deposit center, and P3 – in the vicinity of the substrate; Figure 5-40c).

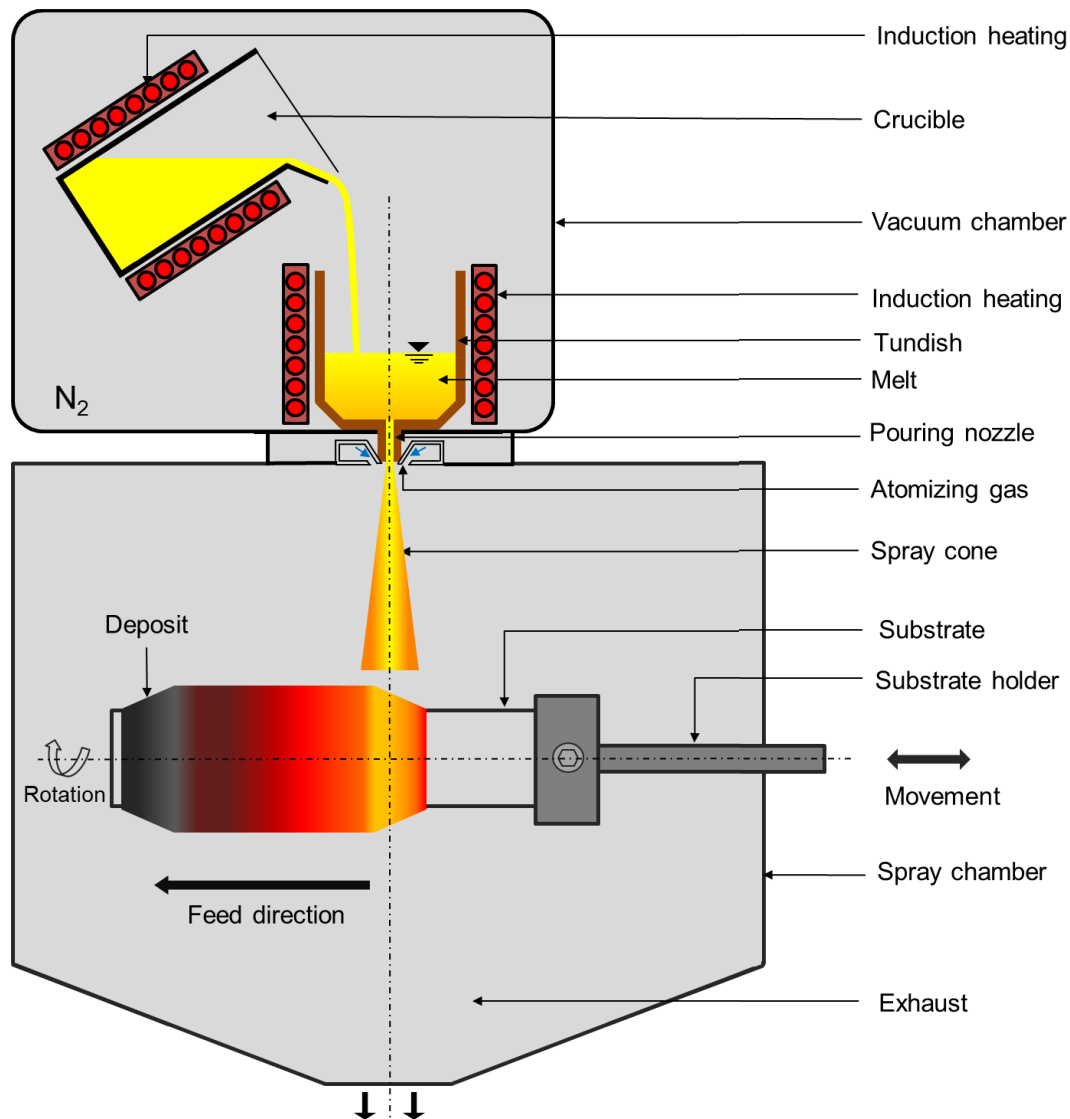


Figure 5-39: Schematic diagram of the spray forming set up (tilting crucible technique, SK-2/PA9 at University of Bremen) of tubular deposit with a close-coupled atomizer for Al-alloys.

From the polished and un-etched sample (Figure 5-41), in the vicinity of the substrate cold porosity is observed and the cold pores form a network similar to the steel deposits [HUSS20a]. The deposit center is almost pore free and circular gas pores are observed near the outer surface, also similar to the steel deposits (Figure 5-1).

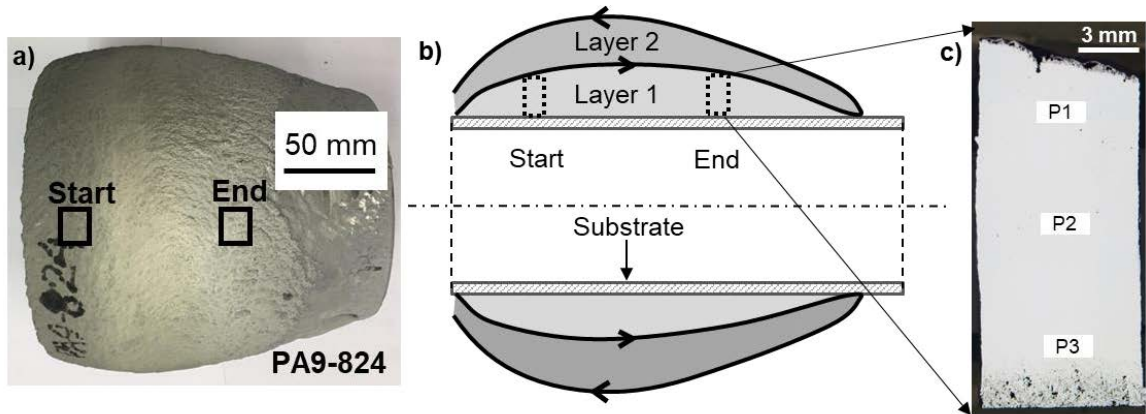
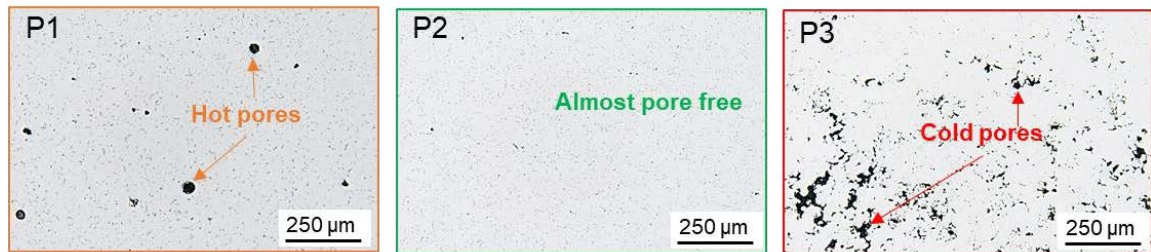


Figure 5-40: a) spray-formed deposit, b) deposit segment at the deposit end (Run A2/PA9-824). P1 is in the vicinity of the substrate, P2 is at the deposit center, and P3 is near the outer surface.



Run A2 | PA9-824 | GMR: 1.9 | Alloy: AlMg4.5Mn0.7 (5083)

Figure 5-41: Magnified images of the un-etched polished deposit segment in P1, P2 and P3 areas (Run A2_End_PA9-824). In the vicinity of the substrate (P3 area) the pores are irregular shape (mainly cold porosity), the deposit center (P2 area) is almost pore free. At the surface region (P1 area) circular hot pores are observed.

The etched samples show uniform grain structures for both the Al-5083 and Al-6082 alloys (Figure 5-42). Similar to the steel deposits, in the vicinity of the substrate the grains are smaller compared to the deposit center due to faster cooling through the substrate. For Al-5083 alloy (Run A1/PA9-826 and Run A2/PA9-824) the intermetallic phases (dark black spots) are equally distributed in the matrix, mainly in the grain boundaries. In case of Al-6082 alloy the intermetallic phases are also found inside the grains and larger intermetallics are seen at the grain boundaries (Run A3/PA9-825). The distribution of the intermetallic phases and uniform grain structure in the spray formed deposit suggest that the smaller and faster droplets of the close-coupled atomizer reduces the porosity and also refines the grain structure.

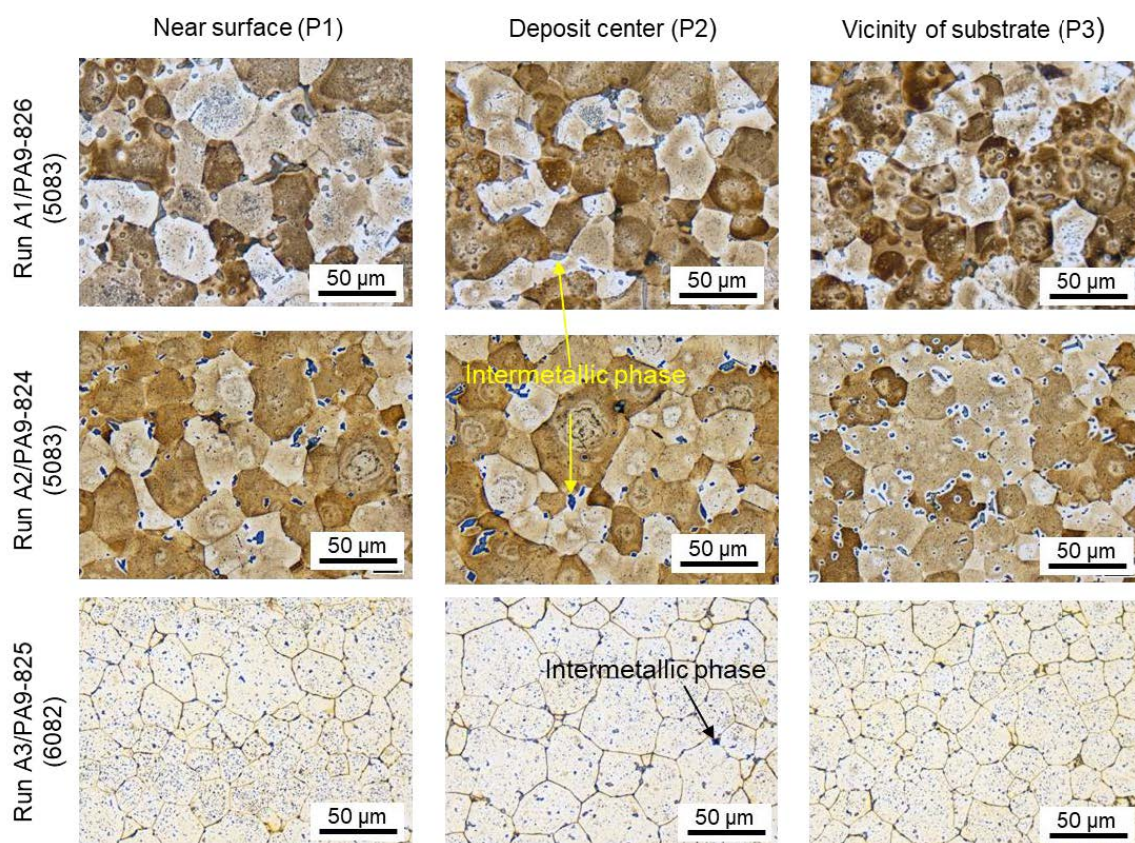


Figure 5-42: Optical micrograph of etched (see Table 4-4) samples in different positions. All the samples show equiaxed uniform grain structure.

Previously, grain and intermetallic refinement of the Al-5083 alloy of spray formed material with a FFA have been compared with conventionally casted materials in [KIM05]. The spray-formed material showed better material properties in terms of microstructure (refined and uniform) and mechanical properties (higher yield strength). In the present study the Al-6082 alloy is compared with conventionally casted material from [MROW09]. The conventionally casted materials show micrometer sized and complex (“Chinese script” as mentioned by [MROW07]) intermetallic phases (Figure 5-43). In contrast, the as-sprayed sample (Run A3/PA9-825) show equally distributed small size (nanometer scale) intermetallic phases (Figure 5-43b and c). Figure 5-43d shows that the intermetallics are distributed in the entire grain equally and larger intermetallics are found at the grain boundaries.

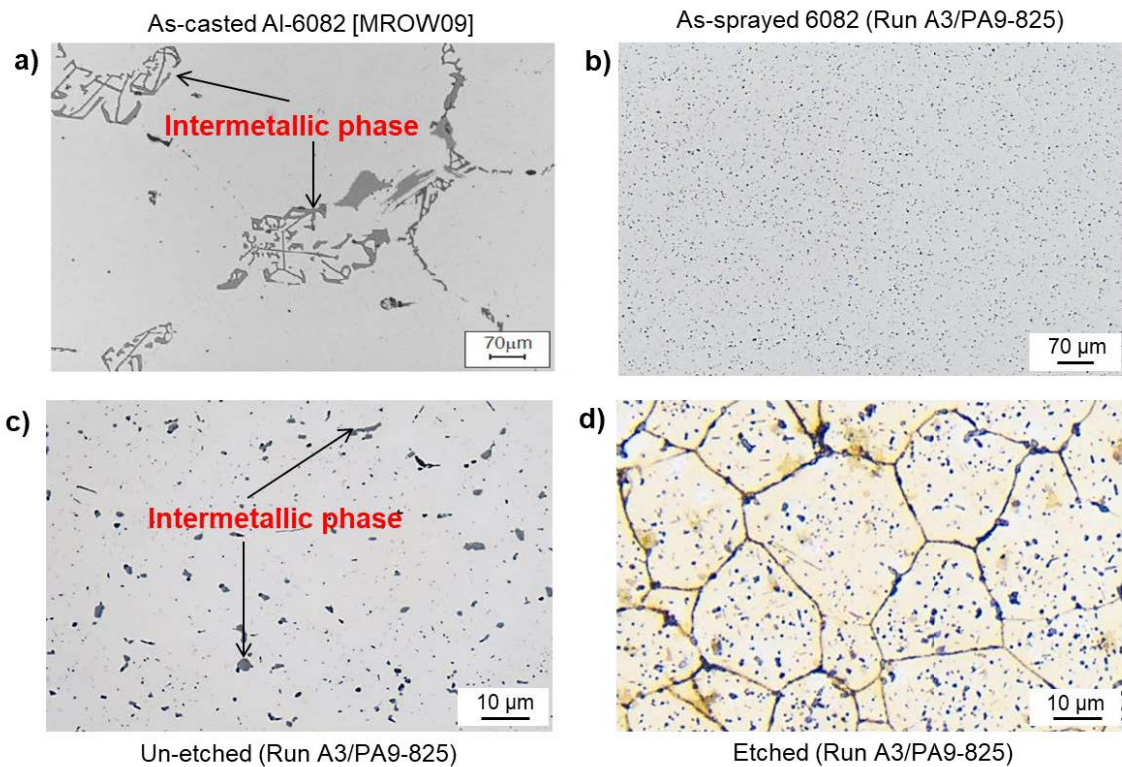


Figure 5-43: Intermetallic phases of Al-6082 alloy a) as-casted material shows complex-shaped larger intermetallic phases [MROW09]; b) and c) as-sprayed materials shows uniformly distributed smaller intermetallic phases; d) etched microstructure show larger intermetallic phases are at grain boundaries and smaller intermetallic phases are dispersed within the grain.

5.4.2 Porosity and process parameters

The porosity measurement of the aluminium deposits shows high amount of porosity in the vicinity of the substrate, mainly cold pores (Figure 5-44). About 20% of the deposit thickness (~3 mm) is covered with a porous layer (porosity above 5%) in the vicinity of the substrate. Except that, the center of the deposit is mostly pore free. In the porosity profile a few random peaks are observed, which are mainly gas pores. Compared to the previous study from Kim et al. (for billets with free-fall atomizer [KIM05]) the porosity in the as-sprayed deposits with the close-coupled atomizer is much lower. Moreover, the mean porosity in the deposit center is less than 0.5% (except Run A3/PA9-825 at the start position). Higher porosity in that position can be due to an uneven melt flow from the pouring nozzle at the beginning of the spray run. At the deposit end for the same run (Run A3/PA9-825) the porosity profile shows a similar trend as other spray forming runs with aluminium alloy. Ellendt et al.

reported that higher *GMR* is required to lower the porosity with a free-fall atomizer for production of billets [ELLE10a]. The author suggested a *GMR* of 5.42 for a minimum porosity level for Al-30%MgSi alloy. However, by close-coupled atomizer tubular deposits with lower porosity are achieved even at a much lower *GMR* = 1.5.

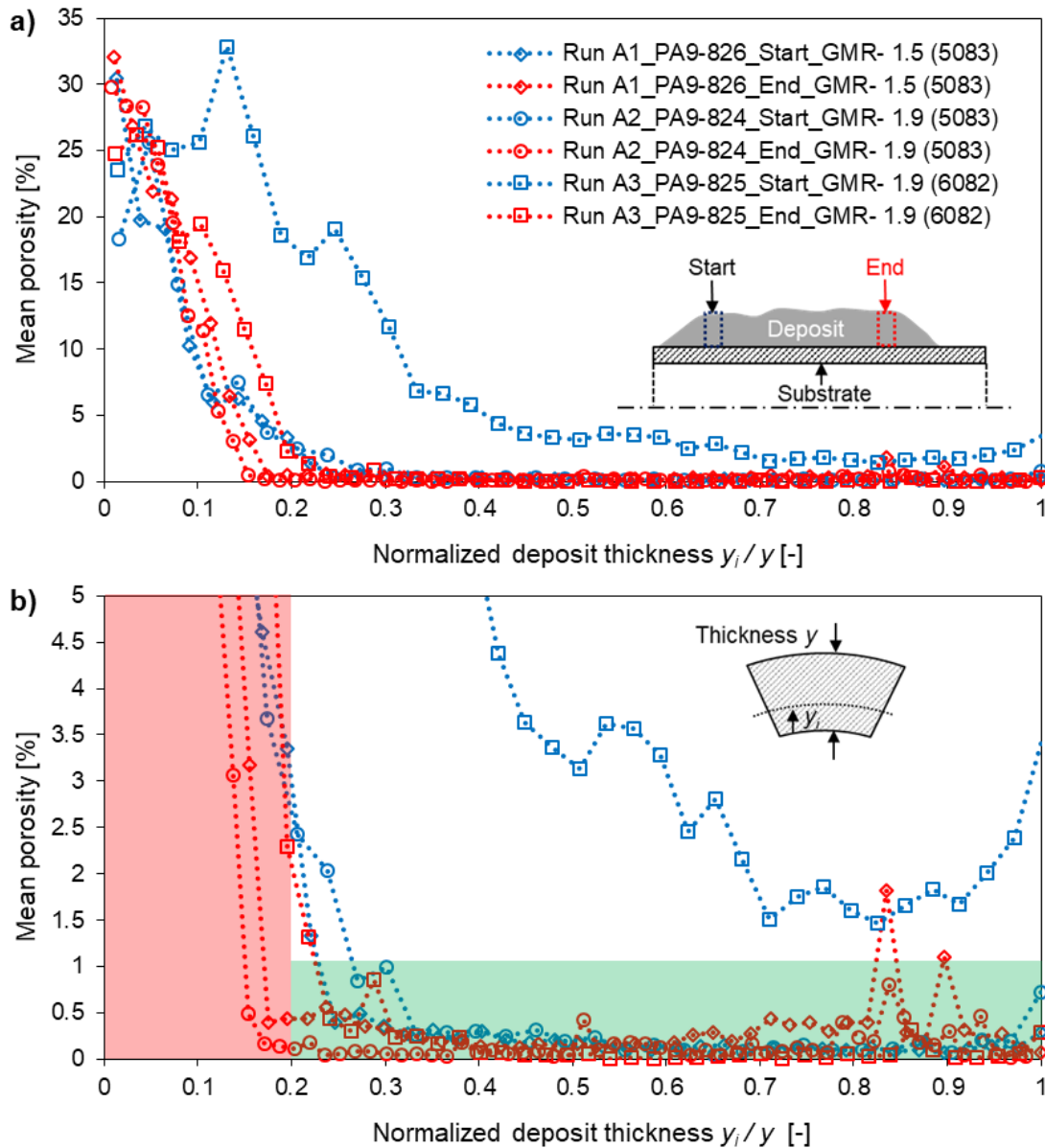


Figure 5-44: **a)** Porosity distribution of tubular deposits (Al-5083 and Al-6082) spray-formed under different process conditions using a close-coupled atomizer; **b)** enlarged area of the porosity profile 0% – 5%. Two samples are taken from each run. The first sample is taken from the deposit start position and the second one is taken from the deposit end position (Figure 5-40).

Figure 5-45a shows that with increasing *GMR* the grain size decreases (similar to the AISI 52100 steel deposits Figure 5-14b). At Run A1/PA9-826 the *GMR* = 1.5 and the average grain size is about 35 μm and at Run A2/PA9-824 the *GMR* = 1.9 and the average grain size is about 30 μm . With increasing *GMR* the gas mass flow rate increases, which implements faster cooling of the deposit surface and hinders grain growth.

However, along with the *GMR* the deposit thickness also affects the maximum deposit surface temperature $T_{D,max}$ [HUSS20a]. With increasing maximum deposit surface temperature $T_{D,max}$ the cooling rate of the deposit will be slower at a given *GMR*, which will also affect the grain size in the as-sprayed deposit. Figure 5-45b shows the relationship between deposit thickness y and average grain size at a constant *GMR*. At deposit center the grain size is larger than near substrate and outer surface areas. Increasing *GMR* also reduces grain size in Run 2 due to higher cooling rate by more gas flow. At a deposit thickness y of about 11 mm the average grain size is about 20 μm and at deposit thickness y of about 22 mm the grain size is about 35 μm (the deposit thickness y was varied by changing the substrate transitional velocity v_s). If the deposit is twice as thick, the grain size increases by approx. 90%.

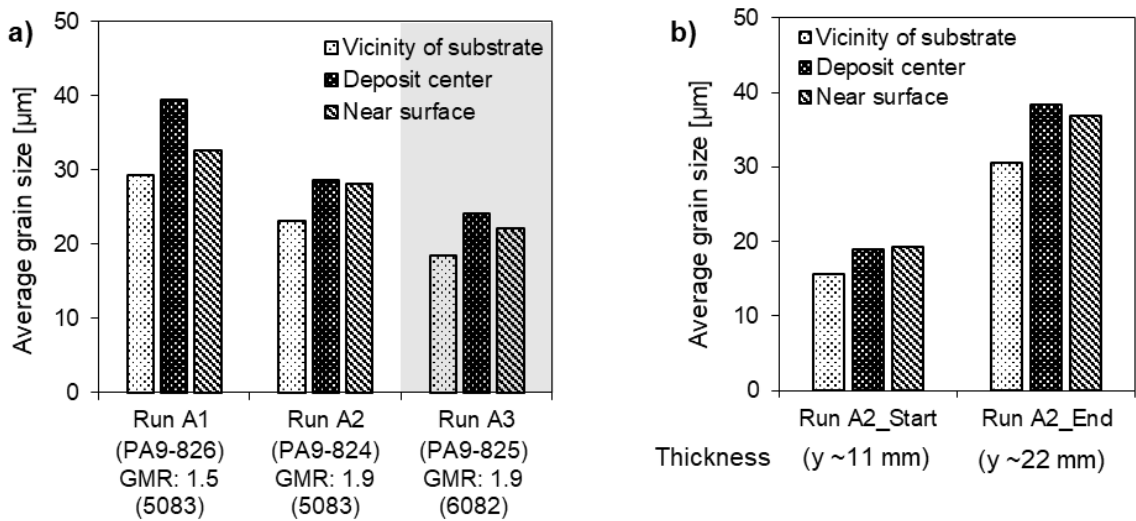


Figure 5-45: a) Average grain size of the spray-formed deposit at near substrate region, center region and near surface region, b) relationship between deposit thickness and average grain size.

In section 5.2.6 an empirical model (Eq. 5.5) has been proposed to calculate the maximum deposit surface temperature $T_{D,max}$ for tubular deposit via close-coupled atomizer in cold gas condition. According to Eq. 5.5 the maximum deposit surface temperatures are to be calculated for the Al-alloy deposits for $y < 15$ mm. Figure 5-46a shows the relationship

between calculated maximum deposit surface temperature $T_{D,max(calc)}$ and deposit thickness y . Run A1/PA9-826 and Run A2/PA9-824 show a trend with increasing deposit thickness y . Run A3/PA9-825 also illustrates a similar trend but differs from the trend line of the Run A1 and Run A2, which is due to different alloys (i.e. Al-5083 and Al-6082). However, the DTT (calculated by Eq. 5-6) is independent to the alloy (Figure 5-46b), thus amphasizing that the moel in principle can be transferred to different alloy systems.

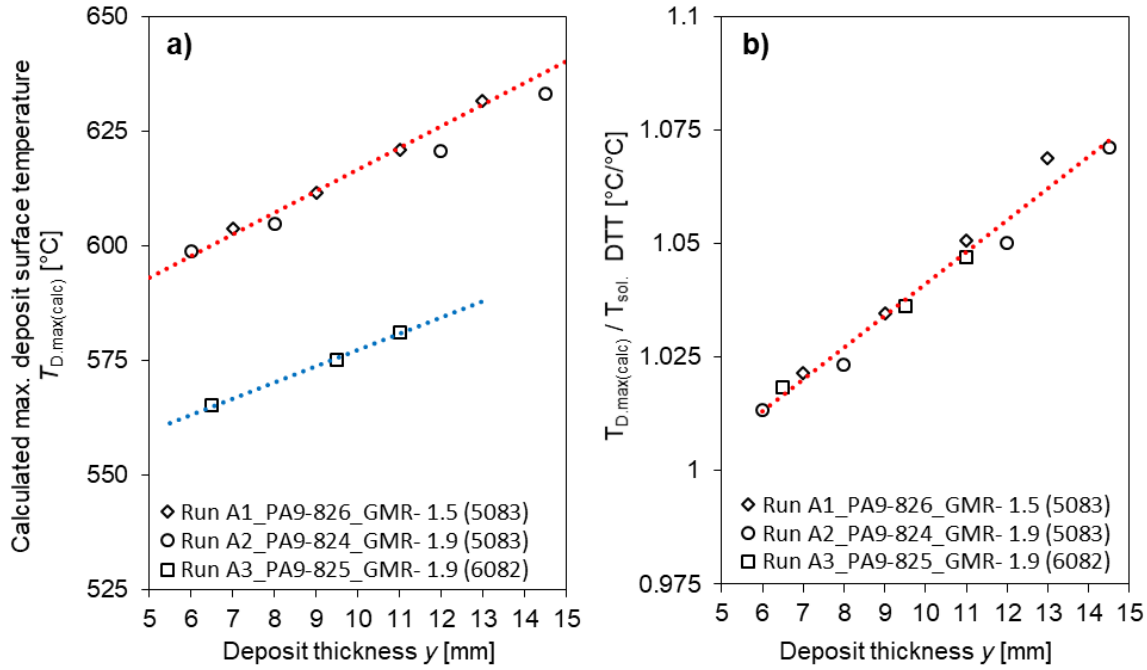


Figure 5-46: Deposit thickness versus a) calculated maximum deposit surface temperature and b) DTT for Al-alloys tubular deposits.

With increasing deposit surface temperature the porosity decreases as reported by [WALT05, HUSS20a]. However, the deposit surface temperatures T_D are different in different alloys (for AISI 52100 steel $T_{sol.} = 1300$ °C and for Al-5083 $T_{sol.} = 591$ °C). Therefore, DTT could be suitable to compare the porosity of different alloys. According to Eq. 5-6 the dimensionless parameter DTT is calculated for the spray-formed deposits (Al-5083 and Al-6082). With increasing DTT the porosity decrease up to $DTT < 1.05$ (Figure 5-47). Beyond ($1.05 < DTT < 1.1$) that the porosity further increases, which can be attributed as hot porosity. The value of the calculated DTT by Eq. 5-6 may differ from the actual value. The calculated deposit surface temperature is always above solidus temperature. However, in the actual case the measured maximum deposit surface temperature in the vicinity of the substrate is found below solidus temperature for AISI 52100 steel. Therefore,

DTT values are also found below 1.0 for steel deposits experimentally (Figure 5-15). However, the calculated maximum DTT = 1.1 for Al-alloys is comparable with the experimentally determined DTT = 1.07 for steel deposits, suggesting that the calculated DTT by Eq. 5-6 can provide a prediction or at least of the porosity for Al-alloys. However, further experimental validation of the empirical model for Al-alloys is needed.

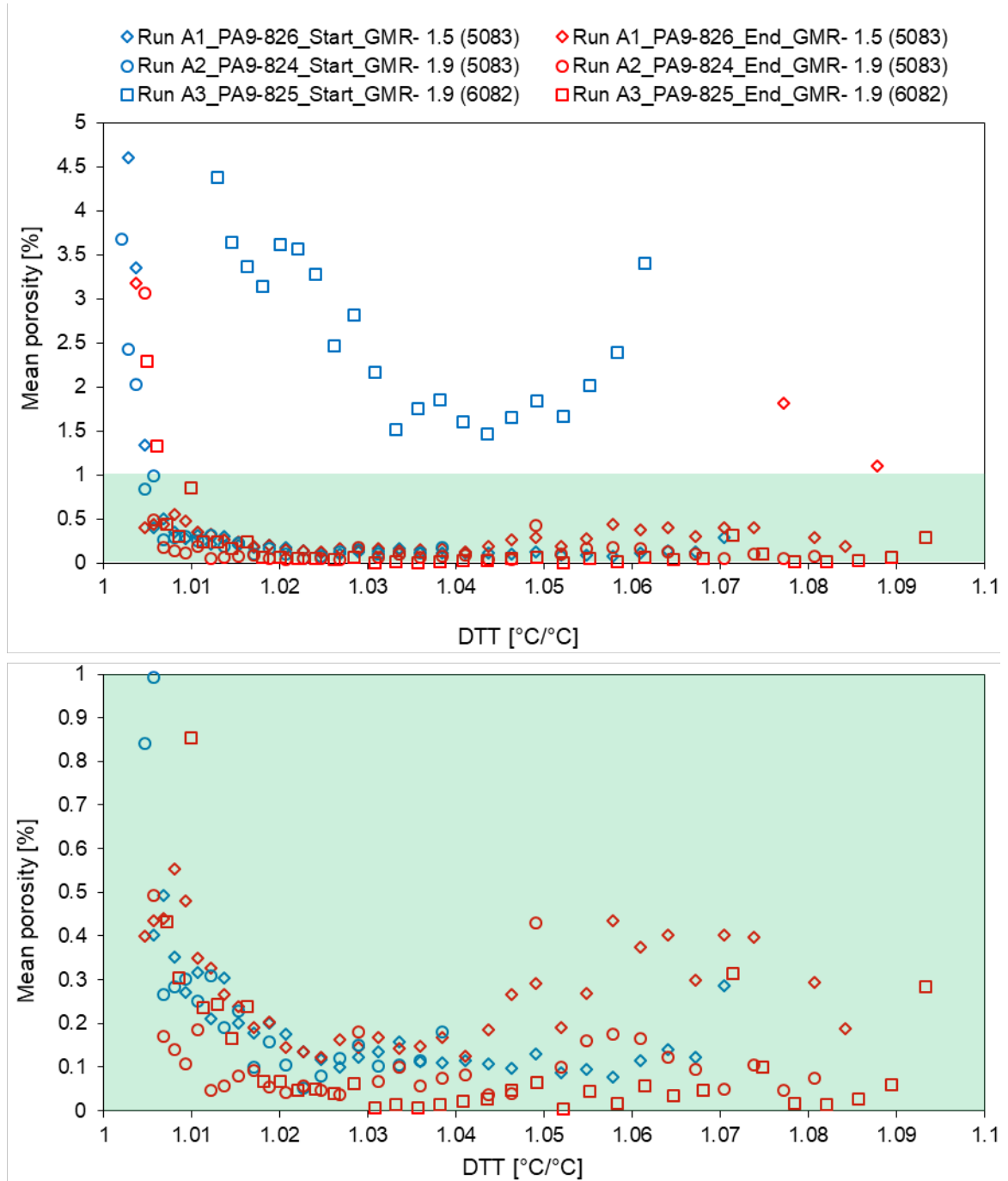


Figure 5-47: Mean porosity versus calculated DTT for Al-alloys (Al-5083 and Al-6082).

In summary of chapter 5.4: the tubular Al-alloys deposits produced by CCA show similar characteristic as steel deposits. Denser deposit centers and a cold porous layer in the vicinity of the substrate is found (Figure 5-41). The microstructure analysis reveals uniformly distributed grain structures (Figure 5-42). Additionally, the rapid solidification process of the spray forming refine the intermetallic phases compared to the conventionally casted Al-6082 alloy (Figure 5-43), which will further improve the mechanical properties of the materials. About 20% of the deposit thickness (in the vicinity of the substrate) has a higher porosity and beyond that the porosity $< 1\%$ (Figure 5-44). The *GMR* affects the grain size for the same alloying system, as smaller grain sizes are found at lower *GMR* (Figure 5-45). Furthermore, larger deposit thickness results in larger grains due to higher maximum deposit surface temperature. The maximum deposit surface temperatures and the DTT are calculated by the empirical model proposed previously (Figure 5-46). It can be seen that the porosity is minimum in a range of $1.02 < \text{DTT} < 1.05$ (Figure 5-47). The trend obtained by the empirical model seems feasible, however, the model needs experimental validation. Finally, it can be said that the knowledge from the steel deposits can be transferred to Al-alloys as proposed in the ***hypothesis 4: the developed knowledge of improving production of spray formed tubes with advanced properties is transferable to other alloy systems.***

6 Conclusions and Outlook

A new approach for the production of dense tubular deposits via the spray forming process, which may be used as guideline for the further development of the spray forming process in industry and academia has been proposed. Previous studies in spray forming mostly focused on free-fall atomizers mainly for economic reasons, ignoring the effect of particle size and particle velocities in the spray. In the present study, hot gas atomization with a close-coupled atomizer is developed and used for the first time in the spray forming process. The impact of the atomization and spray conditions is investigated to gain more insight into the process.

6.1 Conclusion

The spray forming process is used as rapid solidification process in industrial and laboratory scale. The process enables production of materials with higher alloying contents, which are not possible to produce with conventional casting methods. Recent studies showed that with close-coupled atomizer high modulus steel can be produced with nano-structured intermetallic phases [SPRI17]. However, the porosity in the as-sprayed materials is always an issue in the spray forming process. With free-fall atomizers the materials can be produced with lower gas consumption but the larger spray droplets may cause higher porosities [CUI04]. Larger droplets transport more heat energy into the deposition zone, since the larger droplets contain more liquid fraction. Therefore, the process window with a free-fall atomizer is very narrow. In addition, the droplet velocities in the spray of a free-fall atomizer are lower, which also may have an impact on the materials quality. To overcome these drawbacks in the production of tubular deposits, the following approaches have been considered,

- i. Adoption of a close-coupled atomizer (CCA) to spray forming, providing smaller particle sizes in the spray and better cooling of the deposits.
- ii. Introduction of hot gas atomization in spray forming for further decreasing the spray particle size and increasing the particle velocity during impingement.

Adoption of close-coupled atomizer

A convergent-divergent close-coupled atomizer (CD-CCA-08) is adopted for the production of tubular deposits in laboratory scale. In this study the commercial AISI 52100 steel is used for the process parameters studies. The porosity profile of spray formed tubes shows that for similar geometries with close-coupled atomizer exhibit lower porosities than the spray-formed deposits with free-fall atomizer as proposed in the ***hypothesis 1: the porosity of a tubular deposit can be reduced by the smaller droplets sprayed by a close-coupled atomizer***. In both cases high porosities are found in the vicinity of the substrate. The deposits produced by free-fall atomizer show larger gas pores in the deposit center regions. In contrast, the deposits produced by close-coupled atomizer show almost pore free center region. The change of the substrate thickness hardly shows any difference in the porosity in deposits with close-coupled atomizer. The microstructure of the as-sprayed materials is also refined, the grain size is at least one order of magnitude finer by close-coupled atomizer. The etched samples of the as-sprayed AISI 52100 steel show equiaxed pearlitic microstructure. In the deposit center the grain size is larger than the grain size in the outer surface region and in the vicinity of the substrate.

In-situ measurements of the deposit surface temperatures and substrate temperatures obtain more insight into the process. The deposit surface temperature increases with increasing deposit wall thickness and decreasing gas-to-melt ratio (*GMR*). In between the deposit wall thickness and the *GMR*, the deposit wall thickness has a more significant influence on the deposit surface temperature. The deposit wall thickness subsequently also influences the substrate temperature but the influence of *GMR* is small for the production of tubular deposits (the substrate acts as a heat sink during cooling of the as-sprayed deposit). With increasing deposit surface temperatures, the grain size in the deposits also increases due to the slow cooling of the deposit. The results show that the deposit position also has an impact on the porosity. The porosity and the porous layer thickness in the vicinity of the substrate increase at the deposit end position as opposed to the deposit start position. The porosity in the vicinity of the substrate also increases with increasing *GMR*.

Since the deposit surface temperature plays a vital role on the other process parameters, an empirical model is developed to calculate the deposit surface temperature for any given alloy and substrate material. The model is valid in a deposit temperature range of T_{sol} to T_{liq} and below deposit thicknesses of 15 mm. The relationship between the deposit surface temperature and the porosity shows that with decreasing deposit surface temperature the porosity increases. However, the deposit surface temperature is not directly comparable

with other alloys. Therefore, a dimensionless term DTT (ratio of **D**eposit surface **T**emperature and solidus **T**emperature) is introduced. The porosity is above 0.5% above the solidus temperature ($T_{sol} = 1300\text{ °C}$ for AISI 52100 steel) or $DDT < 1.0$.

Hot gas atomization

Numerical simulations show that introduction of hot gas atomization increases the gas velocity in the spray. The gas velocity can be doubled by heating the process gas from ambient temperature (RT) to 1000 °C at the same gas pressure. In contrast, the gas mass flow rate is reduced, which reduces the gas consumption. The particle velocity (experimentally by LDA and numerical simulation) in the spray shows that hot gas atomization also increases the particle velocity as proposed in the ***hypothesis 2: the particle velocity in the spray can be increased by using hot gas in atomization even at similar droplet size***. An identical particle velocity can be achieved at a 50% gas consumption during hot gas atomization. The elevated gas temperature also leads to smaller particles. For example, at RT the mean particle size is $d_{50.3} = 62\text{ }\mu\text{m}$ and at $T_G = 330^\circ$ the value $d_{50.3} = 48\text{ }\mu\text{m}$ for atomization of AISI 316L steel at 1.6 MPa pressure is achieved. The deposit surface temperature measurement shows that lower deposit surface temperatures and faster cooling can be achieved by hot gas atomization ($T_G = 280 \pm 30\text{ °C}$). The deposit surface temperature also influences the deposit surface roughness. With increasing deposit surface temperatures (by cold gas atomization) the surface roughness also increases.

In this dissertation the central hypothesis has been made that the higher impact velocity of the droplet may result in better material qualities and higher yield. With hot gas atomization high relative material densities up to 0.99 in the deposit are achieved even below the solidus temperature ($DDT < 1.0$). This phenomenon extends the process window for production of tubular deposits with higher flexibility as proposed in the ***hypothesis 3: decreased deformation times during droplet impact will result in high density materials and will extend the process window***. However, a minimum deposit surface temperature is required for a sufficiently high density in the deposit. In addition, the hot gas atomization further refines the grain size in the deposit without compromising the material quality.

Substrate pre-heating by the process gas up to 300 °C (573K) reduces the porosity in the vicinity of the substrate. A larger substrate diameter increases the deposit cooling behaviour and further extends the process window. With substrate diameter 130 mm relative density of about 0.99 is achieved at $DDT = 0.88$ by hot gas atomization ($T_G = 330\text{ °C}$). The higher

limit of the DTT is found for both hot gas and cold gas atomization at $DTT = 1.15$. The relative density in the deposit center can be predicted in terms of the maximum deposit surface temperature. However, the model with cold gas atomization shows higher deviation at lower density level.

Spray forming of aluminium alloys

It has been proposed as the ***hypothesis 4: the developed knowledge of improving production of spray formed tubes with advanced properties is transferable to other alloy systems***. Spray forming of aluminium alloys (Al-5053 and Al-6082) shows that high density tubular deposits can be produced with close-coupled atomization. The microstructure investigation shows similar trends and results as for steel deposits. The grain size is larger in the deposit center and smaller in the outer surface region and in the vicinity of the substrate. A comparison of the microstructure shows that spray-formed Al-6082 materials possess more uniformly distributed micro-scale level intermetallic phases than the conventionally casted materials (MORT09).

Porosity analysis shows that about 20% of the deposit thickness in the vicinity of the substrate is highly porous, beyond that the porosity is below 0.5%. In the deposit center the porosity is lower compared to the steel deposits. For both aluminium alloys the DTT values shows that there is an increment of the porosity at $DTT > 1.05$, which is due to a hotter deposit surface.

6.2 Outlook

In-situ measurements of the deposit surface temperature and the substrate temperature may provide more information for validation of the numerical modelling of the spray forming process. Validation of the thermal model of the process can be performed based on the experimental data. The constructed empirical model to calculate the maximum deposit surface temperature is limited to certain deposit thicknesses due to a lack-off in experiments. The model is needed to be further improved and optimized.

The effect of deposit length on the porosity in the vicinity of the substrate should be considered during production of longer products and especially during surface coating. A protective shield on the substrate may reduce sedimentation of circulating particles and overspray droplets from the periphery of the spray.

Numerical simulations show that hot gas atomization increases the mean particle velocity in the spray. However, due to limitations of the experimental setup (heat exchanger temperature ~ 825 K and isolation of the connecting pipe issue) the hot gas temperature in the present study is limited to 335°C (605 K). Atomization gas temperatures up to 1000°C may provide much higher impact velocities and smaller particles, which may further reduce the porosity and the deposit surface temperature. In this direction extended process windows may be found. In addition, pre-heating of the substrate by the hot process gas may further improve the interfacial bonding and decrease the porosity in the vicinity of the substrate.

Introduction of a larger substrate diameter is one of the approaches to cool the deposit faster. Further cooling strategies can be implemented for deposit cooling. For example, using of hydrogen (2-3%) and argon mixtures through a secondary jet as cooling medium. This approach may provide more control on the deposit surface temperature and desired microstructures can be achieved.

In spray-forming of aluminium alloys only cold gas atomization has been considered yet. Hot gas atomization may further improve the materials quality in terms of porosity and microstructure. In-situ temperatures measurements for other alloys may be helpful to validate the empirical model for utilization in a wider range.

The overspray particles and powders from hot gas atomization with close-coupled atomizer show smaller mean particle diameters. Future investigation and characterization on the overspray powder may open a process window for utilizing these powders into the additive manufacturing process chain. In this context, rough particle surfaces affect the flowability of the metal powder, which defines the quality of the powder in additive manufacturing. The flowability of the metal powder increases with increasing surface roughness [GAER21]. This effect opens a new window for using of overspray powder from spray forming with hot gas atomization.

Bibliography

- [ABBI74] ABBISS, J. B.; CHUBB, T. W.; PIKE, E. R.: Laser Doppler anemometry. *Optics & Laser Technology*, (6)6, 1974, S. 249–261
- [ACHE09] ACHELIS, L., UHLENWINKEL, V., RISTAU, R., KRUG, P.: Transient temperatures and microstructure of spray formed aluminium alloy AlSi sheets. *Proc. ICSF VII/SDMA 2009*, Sep. 7th-9th, Bremen, Germany, 2009
- [ADI08] ADI, S.; ADI, H.; CHAN, H.-K.; YOUNG, P. M.; TRAINI, D.; YANG, R.; YU, A.: Scanning white-light interferometry as a novel technique to quantify the surface roughness of micron-sized particles for inhalation. *Langmuir: the ACS journal of surfaces and colloids*, (24)19, 2008, S. 11307–11312
- [ALAN99] LEATHAM, A.: Spray Forming – Alloys, Products, and Markets. *JOM*, (51)4, 1999
- [ANDE02] ANDERSON, I. E.; TERPSTRA, R. L.: Progress toward gas atomization processing with increased uniformity and control. *Materials Science and Engineering: A*, (326)1, 2002, S. 101–109
- [ANDE03] ANDERSON, J. E.; BOOL, L. E.; ARNOLD, A. G.; LEGER, C. B.: Hot gas atomization, 2003
- [ANDE17] ANDERSON, I. E.; ACHELIS, L.: Metal Sprays and Spray Deposition, chapter 2: Fluid Atomization Fundamentals – pp. 49-88. Springer International Publishing AG, Basel, Switzerland, 2017
- [ANTI13] ANTIPAS, G. S. E.: Review of gas atomisation and spray forming phenomenology. *Powder Metallurgy*, (56)4, 2013, S. 317–330
- [ASHB83] ASHBROOK, R. L.: Rapid solidification technology: sourcebook. American Society for Materials International, Metals Park, Ohio, 1983
- [BECK20] BECKERS, D.; ELLENDT, N.; FRITSCHING, U.; UHLENWINKEL, V.: Impact of process flow conditions on particle morphology in metal powder production via gas atomization. *Advanced Powder Technology*, (31)1, 2020, S. 300–311
- [BERG04] BERGMANN, D.; FRITSCHING, U.: Sequential thermal modelling of the spray-forming process. *International Journal of Thermal Sciences*, (43)4, 2004, S. 403–415

- [BERG15] BERGER, L.-M.: Application of hardmetals as thermal spray coatings. *International Journal of Refractory Metals and Hard Materials*, (49), 2015, S. 350–364
- [BIDO29] BIDONE, G.: Experiences sur la forme et sur la direction des veines et des courants d'eau lances par diverses ouvertures. *Imprimerie Royale, Turin*, (6), 1829, S. 1–136
- [BOYK93] BOYKO, C. M.; LE, T. H.; HENEIN, H.: Ensemble and Single Particle Laser probe sizing results for gas atomized zinc powders. *Particle & Particle Systems Characterization*, (10)5, 1993, S. 266–270
- [BREN00] BRENN, G., RAIMANN, J., WOLF, G., DOMNICK, J., DURST, F.: Molten Metal Atomization by Inert Gases: Off-Line and On-Line Metal Powder Characterization by PDA. In: Adrian, R.J., Durão, D.F.G., Durst, F., Heitor, M.V., Maeda, M., Whitelaw, J.H. (eds) *Laser Techniques Applied to Fluid Mechanics*. Springer, Berlin, Heidelberg, 2000
- [BRIN01] BRINKSMEIER, E.; SCHÜNEMANN, M.: Generation and forming of spray-formed flat products. *Journal of Materials Processing Technology*, (115)1, 2001, S. 55–60
- [BUCH03] BUCHHOLZ, M.; UHLENWINKEL, V.; SCHULZ, A.: Kontrollierte Wärmezufuhr zur Beeinflussung von Homogenität und Haftung sprühkompaktierter Rohre aus Stahl. Abschlussbericht des Projekts AiF 12727N, 2003
- [CAI97] CAI, W. D.; LAVERNIA, E. J.: Modeling of porosity during spray forming. *Materials Science and Engineering*, (A226-228), 1997, S. 8–12
- [CAI98] CAI, W.; LAVERNIA, E. J.: Modeling of porosity during spray forming – Part I. Effects of processing parameters. *Metallurgical and Materials Transactions B*, (29)5, 1998, S. 1085–1096
- [CANT97] CANTOR, B.; BAIK, K. H.; GRANT, P. S.: Development of microstructure in spray formed alloys. *Progress in Materials Science*, (42)1-4, 1997, S. 373–392
- [CHAN09] CHANDRA, S.; FAUCHAIS, P.: Formation of Solid Splats During Thermal Spray Deposition. *Journal of Thermal Spray Technology*, (18)2, 2009, S. 148–180
- [CIFT18] CIFTCI, N.; ELLENDT, N.; SOARES BARRETO, E.; MÄDLER, L.; UHLENWINKEL, V.: Increasing the amorphous yield of $\{(Fe\ 0.6\ Co\ 0.4)\ 0.75\ B\ 0.2\ Si\ 0.05\}$ 96 Nb 4 powders by hot gas atomization. *Advanced Powder Technology*, (29)2, 2018, S. 380–385

- [CIFT19] CIFTCI, N.; ELLENDT, N.; COULTHARD, G.; SOARES BARRETO, E.; MÄDLER, L.; UHLENWINKEL, V.: Novel Cooling Rate Correlations in Molten Metal Gas Atomization. *Metallurgical and Materials Transactions B*, (50)2, 2019, S. 666–677
- [CIFT20] CIFTCI, N.: Cooling strategies for the atomization of glass-forming alloys. PhD, Universität Bremen, 2020
- [CUI04] CUI, C.; FRITSCHING, U.; SCHULZ, A.; BAUCKHAGE, K.; MAYR, P.: Spray forming of tubular bearing steel preforms. *Int. J. Powder Metall.*, (40)5, 2004, S. 49–53
- [CUI05a] CUI, C.; FRITSCHING, U.; SCHULZ, A.; LI, Q.: Mathematical modeling of spray forming process of tubular preforms. Part 1: Shape evolution. *Acta Materialia*, (53)9, 2005, S. 2765–2774
- [CUI05b] CUI, C.; FRITSCHING, U.; SCHULZ, A.; LI, Q.: Mathematical modeling of spray forming process of tubular preforms. Part 2: Heat transfer. *Acta Materialia*, (53)9, 2005, S. 2775–2784
- [CUI05c] CUI, C.; FRITSCHING, U.; SCHULZ, A.; TINSCHER, R.; BAUCKHAGE, K.; MAYR, P.: Spray forming of homogeneous 100Cr6 bearing steel billets. *Journal of Materials Processing Technology*, (168)3, 2005, S. 496–504
- [CUI06] CUI, C.; SCHULZ, A.; FRITSCHING, U.; KOHLMANN, R.: Spray Forming of Homogeneous 20MnCr5 Steel of Low Distortion Potential. *Materialwissenschaft und Werkstofftechnik*, (37)1, 2006, S. 34–39
- [CUI09] CUI, C.; SCHULZ, A.; SCHIMANSKI, K.; ZOCH, H.-W.: Spray forming of hypereutectic Al–Si alloys. *Journal of Materials Processing Technology*, (209)11, 2009, S. 5220–5228
- [CUI14] CUI, C.; SCHULZ, A.; ACHELIS, L.; UHLENWINKEL, V.; LEOPOLD, H.; PIWEK, V.; TANG, Z.; SEEFELD, T.: Development of low-melting-point filler materials for laser beam brazing of aluminum alloys. *Materialwissenschaft und Werkstofftechnik*, (45)8, 2014, S. 717–726
- [CZIS08] CZISCH, C.; FRITSCHING, U.: Atomizer design for viscous-melt atomization. *Materials Science and Engineering: A*, (477)1-2, 2008, S. 21–25
- [CZIS08b] CZISCH, C.: Effektive Pulvergengerierung aus hochviskosen mineralischen Schmelzen. PhD thesis, Fachbereich Produktionstechnik, Universität Bremen, 2008

- [CZIS08c] CZISCH, C.; FRITSCHING, U.: Flow-adapted design option for free-fall atomizers. *Atomization and Sprays*, (18)6, 2008, S. 511–522
- [DANT20] DANTEC DYNAMICS: Measurement Principles of LDA. Unter: <https://www.dantecdynamics.com/solutions-applications/solutions/fluid-mechanics/laser-doppler-anemometry-lda/measurement-principles-of-lda/>, 13. Juli 2020
- [DHIM05] DHIMAN, R.; CHANDRA, S.: Freezing-induced splashing during impact of molten metal droplets with high Weber numbers. *International Journal of Heat and Mass Transfer*, (48)25-26, 2005, S. 5625–5638
- [DHIM09] DHIMAN, R.: Splashing and breakup of droplets impacting on a solid surface. PhD thesis, University of Toronto, 2009
- [DOPL05] DOPLER, M.; WEISS, C.: Energy Consumption in Metal Powder Production. *BHM Berg- und Hüttenmännische Monatshefte*, (166)1, 2021, S. 2–8
- [ELLE04] ELLENDT, N.; SCHMIDT, R.; KNABE, J.; HENEIN, H.; UHLENWINKEL, V.: Spray deposition using impulse atomization technique. *Materials Science and Engineering: A*, (383)1, 2004, S. 107–113
- [ELLE07a] ELLENDT, N.; UHLENWINKEL, V.; STELLING, O.; IRRETIER, A.; KESSLER, O.: Spray Forming of Mg₂Si Rich Aluminum Alloys. *Materials Science Forum*, (534-536), 2007, S. 437–440
- [ELLE07b] ELLENDT, N.; UHLENWINKEL, V.: Experimental Investigation and Modeling of the Specific Enthalpy Distribution in a Spray Cone. *Materials Science Forum*, (534-536), 2007, S. 417–420
- [ELLE10a] ELLENDT, N.; STELLING, O.; UHLENWINKEL, V.; HEHL, A. VON; KRUG, P.: Influence of spray forming process parameters on the microstructure and porosity of Mg₂Si rich aluminum alloys. *Einfluss der Prozessparameter auf Mikrostruktur und Porosität beim Sprühkompaktieren von Aluminium-Legierungen mit hohen Mg₂Si-Gehalten. Materialwissenschaft und Werkstofftechnik*, (41)7, 2010, S. 532–540
- [ELLE10b] ELLENDT, N.: Einfluss der Prozessparameter auf Porosität und Mikrostruktur. Dissertation, Universität Bremen, 2010
- [ELLE14] ELLENDT, N.; UHLENWINKEL, V.; MÄDLER, L.: High yield spray forming of small diameter tubes using pressure-gas-atomization. *Materialwissenschaft und Werkstofftechnik*, (45)8, 2014, S. 699–707

- [FRIT05] FRITSCHING, U.: Droplets and particles in sprays – Tailoring particle properties within spray processes. *China Particuology*, (3)1-2, 2005, S. 125–133
- [FRIT12] FRITSCHING, U.; UHLENWINKEL, V.: Hybrid Gas Atomization for Powder Production. In: Kennedy, A. (Ed.): *Porous Metals and Metal Foams Made from Powders*. INTECH Open Access Publisher, 2012
- [GAER21] GÄRTNER, E.; JUNG, H. Y.; PETER, N. J.; DEHM, G.; JÄGLE, E. A.; UHLENWINKEL, V.; MÄDLER, L.: Reducing cohesion of metal powders for additive manufacturing by nanoparticle dry-coating. *Powder Technology*, (379) 2012, S. 585–595
- [GRAN07] GRANT, P. S.: Solidification in Spray Forming. *Metallurgical and Materials Transactions A*, (38)7, 2007, S. 1520–1529
- [GRAN17] GRANT, P. S.; ZEPON, G.; ELLENDT, N.; UHLENWINKEL, V.: Metal Sprays and Spray Deposition, Chapter Seven: Microstructural Evolution in Spray Forming – pp. 265-296. Springer International Publishing AG, Basel, Switzerland, 2017
- [GRAN95] GRANT, P. S.: Spray forming. *Progress in Materials Science*, (39), 1995, S. 497–545
- [HANL03] HANLON, D. N.; RAINFORTH, W. M.: The rolling sliding wear response of conventionally processed and spray formed high speed steel at ambient and elevated temperature. *Wear*, (255)7-12, 2003, S. 956–966
- [HENE17] HENEIN, H.; UHLENWINKEL, V.; FRITSCHING, U.: Metal Sprays and Spray Deposition. Springer International Publishing Cham, 2017
- [HENE92] HENEIN, H.; MEYER, P. L.; HOLVE, D. J.; KUHN, M. A.: On-line measurement of particle size distribution in zinc atomization. *International Journal of Powder Metallurgy*, (28), 1992, S. 149–159
- [HU00] HU, H.; LAVERNIA, E. J.; LEE, Z. H.; WHITE, D. R.: On the evolution of porosity in spray-deposited tool steels. *Metallurgical and Materials Transactions A*, (31)3, 2000, S. 725–735
- [HUSS20a] HUSSAIN, S.; CUI, C.; TEMPLE, N.; UHLENWINKEL, V.; MÄDLER, L.: Porosity and microstructure of steel tubes spray-formed by close-coupled atomizer. *Journal of Materials Processing Technology*, (276), 2020, S. 116407

- [HUSS20b] HUSSAIN, S.; CUI, C.; HE, L.; MÄDLER, L.; UHLENWINKEL, V.: Effect of hot gas atomization on spray forming of steel tubes using a close-coupled atomizer (CCA). *Journal of Materials Processing Technology*, (282), 2020, S. 116677
- [HUSS22] HUSSAIN, S.; BUSS, L.; YAO, D.; FRITSCHING, U.; UHLENWINKEL, V.: Droplet velocity and thermal state from hot gas atomization of steel melt: Impact on the quality of the spray-formed tubular deposit. *Advanced Powder Technology*, (33)7, 2022, S. 103640
- [JEYA09] JEYAKUMAR, M.; KUMAR, S.; GUPTA, G. S.: The Influence of Processing Parameters on Characteristics of an Aluminum Alloy Spray Deposition. *Materials and Manufacturing Processes*, (24)6, 2009, S. 693–699
- [JOHN10] JONES, H.: Chapter 3 Rapid solidification. In: Suryanarayana, C. (Ed.): *Non-equilibrium processing of materials*. Pergamon Materials Series, v. 2, Pergamon, Amsterdam, 2010, S. 23–45
- [KHAT17] KHATIBI, P. D.; HENEIN, H.; FRITSCHING, U.: Metal Sprays and Spray Deposition, Chapter Six: In-Situ, Real Time Diagnostics in the Spray Forming Process – pp. 221-263. Springer International Publishing AG, Basel, Switzerland, 2017
- [KIM05] KIM, W. Y.; YEO, I. D.; RA, T. Y.; KIM, M. S.: Microstructure and Mechanical Property of Al 5083 Alloy Produced by Spray Forming and Hot Extrusion. *Materials Science Forum*, (475-479), 2005, S. 2827–2830
- [KLEM60] KLEMENT, W.; WILLENS, R. H.; DUWEZ, P. O.L.: Non-crystalline Structure in Solidified Gold–Silicon Alloys. *Nature*, (187)4740, 1960, S. 869–870
- [KRAU02] KRAUSS, M.; BERGMANN, D.; FRITSCHING, U.; BAUCKHAGE, K.: In-situ particle temperature, velocity and size measurements in the spray forming process. *Materials Science and Engineering: A*, (326)1, 2002, S. 154–164
- [KUWA97] KUWAMURA, S.; YAMAGUCHI, I.: Wavelength scanning profilometry for real-time surface shape measurement. *Applied optics*, (36)19, 1997, S. 4473–4482
- [LACH11] LACHENICHT, V.; SCHARF, G.; ZEBROWSKI, D.; SHALIMOV, A.: Spray forming – a promising process for making high-quality steels and alloys. *Metallurgist*, (54)9-10, 2011, S. 656–668
- [LAVE10] LAVERNIA, E. J.; SRIVATSAN, T. S.: The rapid solidification processing of materials: science, principles, technology, advances, and applications. *Journal of Materials Science*, (45)2, 2010, S. 287–325

- [LAVE88] LAVERNIA, E. J.; GRANT, N. J.: Spray deposition of metals: A review. *Materials Science and Engineering*, (98), 1988, S. 381–394
- [LAVE96] LAVERNIA, E. J.; WU, Y.: *Spray atomization and deposition*. Wiley, Chichester, 1996
- [LAVI17] ParticleMaster Manual, LaVision GmbH, Göttingen, Germany, 2018
- [LAWL98] LAWLEY, A.; LEATHAM, A. G.: Spray Forming Commercial Products – Principles and Practice. *Materials Science Forum*, (299-300), 1998, S. 407–415
- [LEE18] LEE, T. L.; MI, J.; REN, S.; ZHAO, S.; FAN, J.; KABRA, S.; ZHANG, S.; GRANT, P. S.: Modelling and neutron diffraction characterization of the interfacial bonding of spray formed dissimilar steels. *Acta Materialia*, (155), 2018, S. 318–330
- [LI17] LI, X.-G.; FRITSCHING, U.: *Metal Sprays and Spray Deposition*, chapter Spray Transport Fundamentals – pp. 89-176. Springer International Publishing AG, Basel, Switzerland, 2017
- [LI99] LI, B.; LAVERNIA, E. J.: Chapter 7 Spray-forming: Non-equilibrium Processing of Materials. *Pergamon Materials Series*, Elsevier, 1999, S. 153–193
- [LIAN93] LIANG, X.; LAVERNIA, E. J.: Solidification and microstructure evolution during spray atomization and deposition of Ni3Al. *Materials Science and Engineering: A*, (161)2, 1993, S. 221–235
- [LIU18] LIU, M.; CUI, Z.; SUI, S.: Microstructure and porosity formation of spray-formed GCr15 steel billets. *Procedia Manufacturing*, (15), 2018, S. 1671–1677
- [LIU95] LIU, H.; LAVERNIA, E. J.; RANGEL, R. H.: Modeling of molten droplet impingement on a non-flat surface. *Acta Metallurgica et Materialia*, (43)5, 1995, S. 2053–2072
- [LOHN03] LOHNER, H.; CZISCH, C.; FRITSCHING, U.: Impact of the gas nozzle arrangement on the flow field of a Twin Fluid Atomizer with External Mixing. *Int. Conf. on Liquid Atomization and Spray Systems*, Sorrento, Sep. 2003 (Italien), 2003
- [LU16] LU, L.; HOU, L. G.; ZHANG, J. X.; WANG, H. B.; CUI, H.; HUANG, J. F.; ZHANG, Y. A.; ZHANG, J. S.: Improved the microstructures and properties of M3 – 2 high-speed steel by spray forming and niobium alloying. *Materials Characterization*, (117), 2016, S. 1–8

- [LUBA70] LUBANSKA, H.: Correlation of Spray Ring Data for Gas Atomization of Liquid Metals. *JOM*, (22)2, 1970, S. 45–49
- [MATH88] MATHUR, P.: Analysis of the spray deposition process. PhD thesis, Department of Materials, Drexel University, 1988
- [MATH91] MATHUR, P.; ANNAVARAPU, S.; APELIAN, D.; LAWLEY, A.: Spray casting: an integral model for process understanding and control. *Materials Science and Engineering: A*, (142)2, 1991, S. 261–276
- [McCL06] MCCLELLAN, J. E.; DORN, H.: Science and technology in world history – An introduction / James E. McClellan III and Harold Dorn. 2. Auflage, Johns Hopkins University Press, Baltimore, 2006
- [MCHU08a] MCHUGH, K.M.; UHLENWINKEL, V.; ELLENDT, N.: Density of Spray-Formed Materials. 2008 World Congress on Powder Metallurgy & Particulate Materials, Washington, 2008
- [MEYE03] MEYER, O.; FRITSCHING, U.; BAUCKHAGE, K.: Numerical investigation of alternative process conditions for influencing the thermal history of spray deposited billets. *International Journal of Thermal Sciences*, (42)2, 2003, S. 153–168
- [MEYE12] MEYER, C.; ELLENDT, N.; SRIVASTAVA, V. C.; UHLENWINKEL, V.: Cooling conditions for the generation of bulk metallic glasses by droplet deposition. *International Journal of Materials Research*, (103)9, 2012, S. 1090–1095
- [MEYE13] MEYER, C.: Sprühkompaktieren von Mehrlagenwerkstoffen. PhD thesis, IWT, Universität Bremen, 2013
- [MEYE13a] MEYER, C.; ELLENDT, N.; MÄDLER, L.; CARTER, W. T.; UHLENWINKEL, V.: Spray forming of rings with twin atomizer: SDMA 2013 - 5th Int. Conf. on Spray Deposition and Melt Atomization, Bremen, 2013
- [MEYE14] MEYER, C.; ELLENDT, N.; MÄDLER, L.; MÜLLER, H. R.; REIMER, F.; UHLENWINKEL, V.: Spray forming of high-density sheets. *Materialwissenschaft und Werkstofftechnik*, (45)8, 2014, S. 642–651
- [MI08a] MI, J.; GRANT, P. S.: Modelling the shape and thermal dynamics of Ni superalloy rings during spray forming Part 1 – Shape modelling – Droplet deposition, splashing and redeposition. *Acta Materialia*, (56)7, 2008, S. 1588–1596

- [MI08b] MI, J.; GRANT, P. S.: Modelling the shape and thermal dynamics of Ni superalloy rings during spray forming. Part 2 – Thermal modelling – Heat flow and solidification. *Acta Materialia*, (56)7, 2008, S. 1597–1608
- [MI08c] MI, J.; GRANT, P. S.; FRITSCHING, U.; BELKESSAM, O.; GARMENDIA, I.; LANDABEREA, A.: Multiphysics modelling of the spray forming process. *Materials Science and Engineering: A*, (477)1-2, 2008, S. 2–8
- [MINI02] MINISANDRAM, R. S.; JONES, R. M. F.; KELKAR, K. M.; PATANKAR, S. V.; CARTER, W. T.: Prediction of thermal history of preforms produced by the clean metal spray forming process. *Materials Science and Engineering: A*, (326)1, 2002, S. 184–193
- [MROW07] G. MRÓWKA-NOWOTNIK, J. SIENIAWSKI, M. WIERZBIŃSKA: Intermetallic phase particles in 6082 aluminium alloy. *Archives of Materials Science and Engineering*, (28)2, 2007, S. 69–79
- [MROW09] G. MRÓWKA-NOWOTNIK, J. SIENIAWSKI, A. NOWOTNIK: Effect of heat treatment on tensile and fracture toughness properties of 6082 alloy. *Journal of Achievements in Materials and Manufacturing Engineering*, (32)2, 2009, S. 162–170
- [MÜLL01] MÜLLER, H. R.; KEPPELER, M.; OHLA, K.: Spray Forming of Copper Alloys – Process and Materials. Intern. Conf. “New Developments in Forging Technology” At: Fellbach / Stuttgart - Germany, (ISBN 3-88355-298-4), 2001, S. 79–96
- [MÜLL03] MÜLLER, H. R.; ZAUTER, R.: Spray-formed Copper Alloys – Process and Industrial Applications. *ERZMETALL*, (56)11, 2003, S. 641–648
- [MÜLL04] MÜLLER, H. R.; OHLA, K.; ZAUTER, R.; EBNER, M.: Effect of reactive elements on porosity in spray-formed copper-alloy billets. *Materials Science and Engineering: A*, (383)1, 2004, S. 78–86
- [MULL08] MULLIS, A. M.; ADKINS, N. J. E.; ASLAM, Z.; MCCARTHY, I. N.; COCHRANE, R. F.: Close-coupled gas atomization: High-frame-rate analysis of spray-cone geometry. *International Journal of Powder Metallurgy*, (44)1, 2008, S. 55–64
- [MULL11] MULLIS, A. M.; MCCARTHY, I. N.; COCHRANE, R. F.: High speed imaging of the flow during close-coupled gas atomisation – Effect of melt delivery nozzle geometry. *Journal of Materials Processing Technology*, (211)9, 2011, S. 1471–1477

- [NEIK18] NEIKOV, O. D.; NABOYCHENKO, S.; YEFIMOV, N. V.: Handbook of non-ferrous metals powders – Technologies and applications / edited by Oleg D. Neikov, Stanislav Naboychenko, N.V. Yefimov. Elsevier, Amsterdam, 2018
- [PASA02] PASANDIDEH-FARD, M.; CHANDRA, S.; MOSTAGHIMI, J.: A three-dimensional model of droplet impact and solidification. *International Journal of Heat and Mass Transfer*, (45)11, 2002, S. 2229–2242
- [PAYN93] PAYNE, R. D.; MORAN, A. L.; CAMMARATA, R. C.: Relating porosity and mechanical properties in spray formed tubulars. *Scripta Metallurgica et Materialia*, (29)7, 1993, S. 907–912
- [RAJU08] RAJU, K.; OJHA, S. N.; HARSHA, A. P.: Spray forming of aluminum alloys and its composites – An overview. *Journal of Materials Science*, (43)8, 2008, S. 2509–2521
- [RAYL78] RAYLEIGH: On the Instability Of Jets. *Proceedings of the London Mathematical Society*, (s1-10)1, 1878, S. 4–13
- [SAHU09] SAHU, K. K.; DUBE, R. K.; KORJA, S. C.: Aspects of porosity formation in spray deposited thin aluminium strip. *Powder Metallurgy*, (52)2, 2009, S. 135–144
- [SAVA33] SAVART, F.: Memoire sur la constitution des veines liquides lancées par des orifices. *Annales de Chimie et de Physique*, (53), 1833, S. 337–386
- [SCHM79] SCHMITT, H.: Mathematical-physical consideration regarding the production of metal powders for powder metallurgy. *Powder Met. Internat.*, (11), 1979, S. 17
- [SCHU04] SCHULZ, A.; UHLENWINKEL, V.; BERTRAND, C.; KOHLMANN, R.; KULMBURG, A.; OLDEWURTEL, A.; SCHNEIDER, R.; VIALE, D.: Nitrogen pick-up during spray forming of high-alloyed steels and its influence on microstructure and properties of the final products. *Materials Science and Engineering: A*, (383)1, 2004, S. 58–68
- [SCHU08] SCHULZ, A.; UHLENWINKEL, V.; ESCHER, C.; KOHLMANN, R.; KULMBURG, A.; MONTERO, M. C.; RABITSCH, R.; SCHÜTZENHÖFER, W.; STOCCHI, D.; VIALE, D.: Opportunities and challenges of spray forming high-alloyed steels. *Materials Science and Engineering: A*, (477)1-2, 2008, S. 69–79
- [SCHW17] SCHWENCK, D.; ELLENDT, N.; FISCHER-BÜHNER, J.; HOFMANN, P.; UHLENWINKEL, V.: A novel convergent–divergent annular nozzle design for close-coupled atomisation. *Powder Metallurgy*, (60)3, 2017, S. 198–207

- [SING70] SINGER, A.R.E.: The Principles of Spray Rolling of Metals. *Met. & Mat*, (4), 1970, S. 246–250
- [SING83] SINGER, A.R.E.; ALEXANDER, J. M.: Spray Forming of Metals for Engineering Applications. *CIRP Annals*, (32)1, 1983, S. 145–149
- [SIQU10] SIQUEIRA, G.; SAFRA, L.C.P.G.; MUCSI, C. S.; FERNANDES, M. G.; ROSSI, J. L.: Mechanical Properties Evaluation of a Spray Formed AA-6082 Aluminum Alloy. *Materials Science Forum*, (660-661), 2010, S. 503–509
- [SPRI17] SPRINGER, H.; BARON, C.; SZCZEPANIAK, A.; UHLENWINKEL, V.; RAABE, D.: Stiff, light, strong and ductile – Nano-structured High Modulus Steel. *Scientific reports*, (7)1, 2017, S. 2757
- [SRIV04] SRIVASTAVA, V. C.; MANDAL, R. K.; OJHA, S. N.: Evolution of microstructure in spray formed Al–18%Si alloy. *Materials Science and Engineering: A*, (383)1, 2004, S. 14–20
- [STEL06] STELLING, O.; IRRETIER, A.; KESSLER, O.; KRUG, P.; COMMANDEUR, B.: New Light-Weight Aluminium Alloys with High Mg₂Si-Content by Spray Forming. *Materials Science Forum*, (519-521), 2006, S. 1245–1250
- [TILL99] TILLWICK, J.; UHLENWINKEL, V.; BAUCKHAGE, K.: Analysis of the spray forming process using backscattering phase-Doppler anemometry. *International Journal of Heat and Fluid Flow*, (20)5, 1999, S. 530–537
- [UHLE07] UHLENWINKEL, V., ELLENDT, N., SCHULZ, A., STELLING, O., ZOCH, H.-W.: Optimierung der Dichte sprühkompaktierter Werkstoffe. *Pulvermetallurgie in Wissenschaft und Praxis*, (23), 2007
- [UHLE07a] UHLENWINKEL, V.; ELLENDT, N.: Porosity in Spray-Formed Materials. *Materials Science Forum*, (534-536), 2007, S. 429–432
- [UHLE14] UHLENWINKEL, V.: Wirtschaftliche Herstellung bzw. Beschichtung von Rohren mit kleinen Durchmessern (kleiner 100 mm) durch Sprühkompaktieren unter Anwendung alternativer Zerstäubungstechniken am Beispiel von Gleitlagerwerkstoffen, Project Report, 2014
- [UHLE91] UHLENWINKEL, V.: Zum Ausbreitungsverhalten der Partikeln bei der Sprühkompaktierung von Metallen, PhD thesis, Universität Bremen, 1991
- [VUOR14] VUORISTO, P.: Thermal Spray Coating Processes. In: Vuoristo, P. (Hrsg.): *Comprehensive Materials Processing*. Elsevier, 2014, S. 229–276

- [WAHL93] WAHLROOS, J.; LIIMATAINEN, T.: Interface adherence of spray formed compound tube. J. Wood (Ed.), Proceedings of the Second International Conference on Spray Forming, Woodhead Pub., Swansea, U.K., 1993, S. 225–234
- [WALT05] WALTER, M.; STOCKINGER, M.; TOCKNER, J.; ELLENDT, N.; UHLENWINKEL, V.: Spray Forming and Post Processing of Superalloy Rings. In: Loria, E. A. (Hrsg.): Spray Forming and Post Processing of Superalloy Rings. Superalloys, 02.10.2005 - 05.10.2005, TMS, 2005, S. 429–440
- [WAN01] WAN, Y. P.; ZHANG, H.; JIANG, X. Y.; SAMPATH, S.; PRASAD, V.: Role of Solidification, Substrate Temperature and Reynolds Number on Droplet Spreading in Thermal Spray Deposition: Measurements and Modeling. Journal of Heat Transfer, (123)2, 2001, S. 382–389
- [WARN97] WARNER, L.; CAI, C.; ANNAVARAPU, S.; DOHERTY, R.: Modelling Microstructural Development in Spray Forming: Experimental Verification. Powder Metallurgy, (40)2, 1997, S. 121–125
- [WEBE31] WEBER, C.: Zum Zerfall eines Flüssigkeitsstrahles. ZAMM - Zeitschrift für Angewandte Mathematik und Mechanik, (11)2, 1931, S. 136–154
- [YU13] YU, H.; WANG, M.; SHENG, X.; LI, Z.; CHEN, L.; LEI, Q.; CHEN, C.; JIA, Y.; XIAO, Z.; CHEN, W.; WEI, H.; ZHANG, H.; FAN, X.; WANG, Y.: Microstructure and tensile properties of large-size 7055 aluminum billets fabricated by spray forming rapid solidification technology. Journal of Alloys and Compounds, (578), 2013, S. 208–214
- [YULE94] YULE, A. J.; DUNKLEY, J. J.: Atomization of melts – For powder production and spray deposition. Oxford series on advanced manufacturing Band 11, Clarendon Press, Oxford, 1994
- [ZEPO16] ZEPON, G.: Spray forming of wear and corrosion resistant bimetallic pipes – from the alloy design to the semi-industrial process. PhD thesis, Federal University of São Carlos, 2016
- [ZHAO09] ZHAO, X.; XU, J.; ZHU, X.; ZHANG, S.: Effect of atomization gas pressure variation on gas flow field in supersonic gas atomization. Science in China Series E: Technological Sciences, (52)10, 2009, S. 3046–3053
- [ZHAO12] ZHAO, W.; CAO, F.; NING, Z.; ZHANG, G.; LI, Z.; SUN, J.: A computational fluid dynamics (CFD) investigation of the flow field and the primary atomization

of the close coupled atomizer. Computers & Chemical Engineering, (40), 2012, S. 58–66

[ZHEN11] ZHENG, B.; LAVERNIA, E. J.: Handbook of Atomization and Sprays, chapter Melt Atomization. Springer Science+Business, LLC, Luxembourg, 2011, S. 837–848

[ZIES02] ZIESENIS, J.: Weiterentwicklung der PDA-Meßtechnik zur on-line Prozeßkontrolle beim Sprühkompaktieren. PhD thesis, Universität Bremen, 2002

[ZIES03] ZIESENIS, J.; BAUCKHAGE, K.: Spray Forming: Controlling the Atomization Result with Regard to Particle Properties. Particle & Particle Systems Characterization, (20)4, 2003, S. 290–297

Appendix

Experimental setup

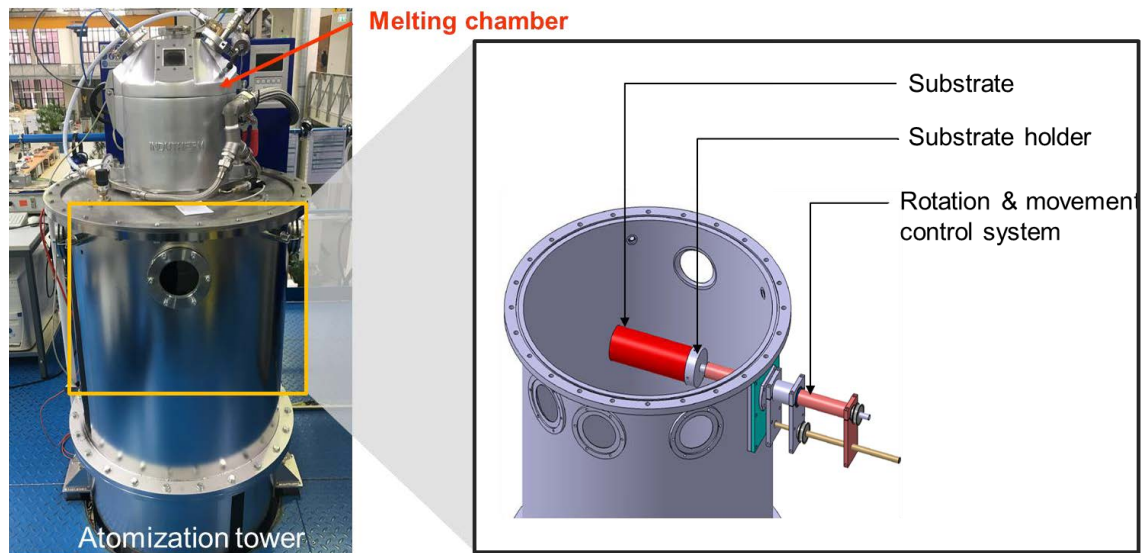


Figure A-1: Atomization facility at the University of Bremen (PA7).

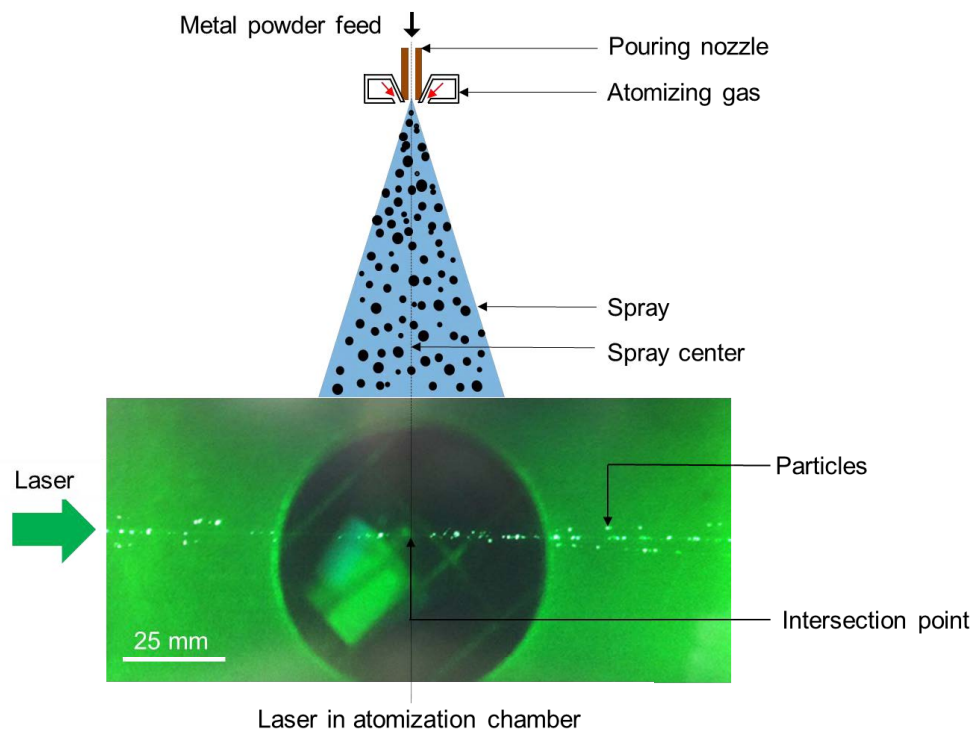


Figure A-2: Measurement of particle velocity in the spray chamber with cold particles (size fraction 63 – 90 μm) inside the spray chamber (PA5).

Table appendix

Table A-1 Process parameters and results of the spray forming experiments with CCA and FFA (section 5.1, Alloy: AISI 52100).

Parameters (Exp. ID number)	Symbol	Unit	PA7-032	PA7-041	PA7-107	PA7-130	PA7-246	PA7-247
Pouring temperature	—	°C	1713	1713	1713	1713	1730	1730
Feed stock mass	—	g	2847	3030	3030	3020	3730	3730
Atomizer	—	—	CCA	CCA	CCA	CCA	FFA	FFA
Pouring nozzle diameter	\varnothing_n	mm	2	2	2	2	2.5	2.5
Melting environment	—	—	Ar	Ar	Ar	Ar	Ar	Ar
Atomization gas	—	—	N ₂	N ₂	N ₂	N ₂	N ₂	N ₂
Atomization gas pressure	p_G	MPa	1.6	0.8	0.8	0.8	2.0	2.0
Spray distance	z	mm	130	130	160	140	120	120
Substrate thickness	s	mm	2.9	5.0	5.0	6.3	5	5
Transitional velocity of substrate	v_s	mm/s	2	2	1.5	1.5	3	2
Rotational speed of substrate	v_r	rps	3.4	3.5	3.5	3.5	3.5	3.5
Gas flow rate	\dot{M}_G	kg/h	590	316	316	316	285	285
Melt flow rate (feed stock mass/ spray time)	\dot{M}_L	kg/h	205	153	155	178	179	198
Gas-to-melt mass flow ratio	GMR	—	2.9	2.1	2.0	1.8	1.6	1.4
Deposit thickness	y	mm	—	—	—	—	—	—
Max. deposit surface temperature	$T_{D,max}$	°C	—	—	—	—	—	—
Max. substrate temperature	$T_{S,max}$	°C	—	—	—	—	—	—

Table A-2 Process parameters and results of the spray forming experiments with CCA (Alloy: AISI 52100).

Parameters (Exp. ID number)	Symbol	Unit	Run 1 (PA7-168)	Run 2 (PA7-169)	Run 3 (PA7-170)	Run 4 (PA7-173)	Run 5 (PA7-174)
Pouring temperature	–	°C	1730	1730	1730	1730	1730
Gas temperature	T_G	°C	RT	RT	RT	RT	RT
Feed stock mass	–	g	3450	5400	5380	3460	5380
Atomizer	–	–	CCA	CCA	CCA	CCA	CCA
Pouring nozzle diameter	\varnothing_n	mm	2.5	2.5	2.5	2.5	2.5
Melting environment	–	–	Ar	Ar	Ar	Ar	Ar
Atomization gas	–	–	N ₂	N ₂	N ₂	N ₂	N ₂
Atomization gas pressure	p_G	MPa	1.0/1.2 ³	0.8/1.0 ³	0.8	0.8/1.2 ³	0.8/1.0
Spray distance	z	mm	130	130	130	130	130
Substrate thickness	s	mm	5	5	5	5	5
Translational velocity of substrate	v_s	mm/s	2.0	3	3	3	2.5
Rotational speed of substrate	v_r	rps	3.5	3.5	3.5	3.5	3.5
Gas mass flow rate	\dot{M}_G	kg/h	385 / 453	316 / 385	316	316 / 453	316 / 385
Melt mass flow rate	\dot{M}_L	kg/h	282	286	198	258	222
Gas-to-melt ratio	GMR	–	1.4 / 1.6	1.1 / 1.3	1.6	1.3 / 1.9	1.2 / 1.5
Deposit thickness	y	mm	13 – 15	8.5 – 11.5	6.5 – 7.5	7.5 – 9.4	9.7 – 11
Max. deposit surface temperature	$T_{D,max}$	°C	1385 / 1425	1350 / 1390	1325 / 1345	1330 / 1350	1342 / 1350
Max. substrate temperature	$T_{S,max}$	°C	783	–	780	725	875

³ Gas pressure was changed after 50% of the spray time.

Table A-3 LDA parameters for mean particle velocity measurement.

Parameters	Unit	Value
Laser output	%	100
Photo-multiplier tube (PMT) Voltage	V	500
Burst Threshold	mV	160
Band Pass Filter	Hz	10 – 65 M (50 – 400 m/s)
SNR	–	Mild
Velocity Minimum	m/s	46
Velocity Maximum	m/s	400

Table A-4 Process parameter for atomized powder at different gas temperatures with CCA (Alloy: AISI 316L).

Parameters (Exp. ID number)	Symbol	Unit	Run A (PA7-224)	Run B (PA7-225)	Run C (PA7-226)
Pouring temperature	–	° C	1680	1680	1680
Gas temperature	T_G	° C	RT	225	330
Pouring nozzle diameter	\varnothing_n	mm	2.5	2.5	2.5
Melting environment	–	–	Ar	Ar	Ar
Atomization gas	–	–	N ₂	N ₂	N ₂
Atomization gas pressure	p_G	MPa	1.6	1.6	1.6
Gas flow rate	\dot{M}_G	kg/h	595	456	415
Mean melt flow rate (feed stock mass / run time)	\dot{M}_L	kg/h	420	440	430
Gas-to-melt mass flow ratio	GMR	–	1.41	1.05	0.96

Table A-5a Process parameters and results of the spray forming experiments with hot gas and cold gas and cold gas (CCA, Alloy: AISI 52100).

Parameters (Exp. ID number)	Symbol	Unit	Run H1 (PA7-186)	Run H2 (PA7-187)	Run H3 (PA7-188)	Run H4 (PA7-230)	Run H5 (PA7-232)	Run H6 (PA7-228)	Run H7 (PA7-229)
Pouring temperature	–	° C	1730	1730	1730	1730	1730	1730	1730
Gas temperature	T_G	° C	250	300	305	300	300	RT	RT
Feed stock mass	–	g	3030	5330	2470	3200	3160	2775	3210
Atomizer	–	–	CCA-HG	CCA-HG	CCA-HG	CCA-HG	CCA-HG	CCA	CCA
Pouring nozzle diameter	\varnothing_n	mm	2.5	2.5	2.5	2.5	2.5	2.5	2.5
Melting environment	–	–	Ar	Ar	Ar	Ar	Ar	Ar	Ar
Atomization gas	–	-	N ₂	N ₂	N ₂	N ₂	N ₂	N ₂	N ₂
Atomization gas pressure	p_G	MPa	0.8	1.2/1.0 ⁴	0.8	0.6	0.8	0.8	1.2/1.0 ⁴
Spray distance	z	mm	130	130	130	130	130	130	130
Substrate thickness	s	mm	5	5	5	5	5	5	5
Translational velocity of substrate	v_s	mm/s	3	3	2.5	2	2	3	3
Rotational speed of substrate	v_r	rps	3.5	3.5	3.5	3.5	3.5	3.5	3.5
Gas flow rate	\dot{M}_G	kg/h	240	330/280	230	180	230	320	450/390
Mean melt flow rate (feed stock mass / run time)	\dot{M}_L	kg/h	180	230	170	180	180	270	310
Gas-to-melt mass flow ratio	GMR	–	1.3	1.4 / 1.2	1.3	1.0	1.2	1.2	1.5/1.2
Deposit thickness	y	mm	5.5	9 / 6.5	5	7.3	6.5	7	8
Max. deposit surface temperature	$T_{D,max}$	°C	1320	1430/1330	1000	1415	1410	1465	1480
Max. substrate temperature	$T_{S,max}$	°C	830	930/950	750	870	840	860	980

⁴ Gas pressure was changed after 50% of the spray time.

Table A-5b Process parameters and results of the spray forming experiments with larger substrate (CCA, alloy: AISI 52100).

Parameters (Exp. ID number)	Symbol	Unit	Run H8 (PA7-268)	Run H9 (PA7-269)	Run H10 (PA7-270)	Run H11 (PA7-271)	Run H12 (PA7-189)	Run H13 (PA7-258)
Pouring temperature	–	° C	1730	1730	1730	1730	1730	1730
Gas temperature	T_G	° C	RT	RT	330	335	280	RT
Feed stock mass	–	g	5160	5190	5190	5200	2525	2800
Atomizer	–	–	CCA	CCA	CCA-HG	CCA-HG	CCA-HG	CCA-HG
Pouring nozzle diameter	\varnothing_n	mm	2.5	2.5	2.5	2.5	2.5	2.5
Melting environment	–	–	Ar	Ar	Ar	Ar	Ar	Ar
Atomization gas	–	-	N ₂	N ₂	N ₂	N ₂	N ₂	N ₂
Atomization gas pressure	p_G	MPa	0.8	0.8	0.8	0.6	0.8	0.8
Spray distance	z	mm	130	140	130	130	–	–
Substrate thickness	s	mm	3.5	3.5	3.5	3.5	3.5	3.5
Translational velocity of substrate	v_s	mm/s	1.5	2	1.5	2	–	–
Rotational speed of substrate	v_r	rps	3.5	3.5	3.5	3.5	–	–
Gas flow rate	\dot{M}_G	kg/h	320	320	220	175	178	316
Mean melt flow rate (feed stock mass / run time)	\dot{M}_L	kg/h	285	265	245	225	186	280
Gas-to-melt mass flow ratio	GMR	–	1.11	1.19	0.90	0.78	0.96	1.14
Deposit thickness	y	mm	12.5	11	11.5	8	–	–
Max. deposit surface temperature	$T_{D,max}$	° C	1440	1390	1420	1370	–	–
Max. substrate temperature	$T_{S,max}$	° C	1030	1000	1100	1040	–	–

Table A-6 RRSB parameters used in the numerical set-up.

p_G [MPa]	T_G [K]	d_{\min} [μm]	d_{\max} [μm]	d_{mean} [μm]	Spread parameter
0.6	293	2	237	92	4.93
0.8	293	2	237	86	4.79
1.0	293	2	219	76	4.56
0.6	573	2	257	58	4.43
0.8	573	2	237	54	4.33
1.0	573	2	221	50	4.27
0.6	873	2	253	47	4.44
0.8	873	2	237	44	4.35
1.0	873	2	221	41	4.25

Table A-7 Process parameters used in the numerical set-up.

P_G (MPa)	T_G (K)	\dot{M}_G (kg/h)	\dot{M}_L (kg/h)	$v_{G, \max}$ (m/s)	GMR
0.6	293	248	220	592	1.13
0.8	293	319	265	602	1.20
1.0	293	390	300	625	1.30
0.6	573	177	177	829	1.00
0.8	573	227	206	842	1.10
1.0	573	278	235	876	1.18
0.6	873	142	142	1031	1.00
0.8	873	183	166	1066	1.10
1.0	873	224	210	1090	1.07

Table A-8 Materials properties for spray-formed alloys.

Material properties	Symbol	Unit	AISI 52100	Low C steel	Al 5083	Al 6082
Solidus temperature	T_{sol}	$^{\circ}\text{C}$	1300	-	591	555
Density	ρ	g/cm^3	7.81	8	2.66	2.7
Sp. heat capacity	c_p	$\text{J}/\text{g } ^{\circ}\text{C}$	0.475	0.45	0.9	0.896

Table A-9 Process parameters for spray forming runs for spray forming of Al-alloys.

Parameters (Exp. ID number)	Symbol	Unit	Run A1 (PA9-826)	Run A2 (PA9- 824)	Run A3 (PA9 - 825)
Alloy	—	—	AlMg4.5Mn0.7 (5083)	AlMg4.5Mn0.7 (5083)	AlMgSi1 (6082)
Liquidus temperature	T_{liq}	° C	640	640	555
Pouring temperature	—	° C	850	850	750
Feed stock mass	—	g	7500	8700	7600
Atomizer	—	—	CCA	CCA	CCA
Pouring nozzle diameter	\varnothing_n	mm	2.5	2.5	2.5
Melting environment	—	—	N ₂	N ₂	N ₂
Atomization gas	—	—	N ₂	N ₂	N ₂
Atomization gas pressure	p_G	MPa	0.5	0.7	0.7
Spray distance	z	mm	120	120	120
Substrate thickness	s	mm	3.5	3.5	3.5
Transitional velocity of substrate	v_s	mm/s	2	2	2
Rotational speed of substrate	v_r	rps	3.5	3.5	3.5
Gas flow rate	\dot{M}_G	kg/h	215	280	280
Melt flow rate (feed stock mass/ spray time)	\dot{M}_L	kg/h	145	145	150
Gas-to-melt mass flow ratio	GMR	—	1.5	1.9	1.9
Deposit thickness	y	mm	—	—	—
Max. deposit surface temperature	$T_{D,max}$	°C	—	—	—
Max. substrate temperature	$T_{S,max}$	°C	—	—	—

Symbols and Abbreviations

Symbol	Description	Unit
Roman Letters		
a_2, b_2, c_2	Constant used to calculate enthalpy change	-
a^*, b^*, c^*, d^*	Constant used to calculate deposit surface temperature	-
A_d	Surface area of the droplet	m ²
$a_{dif.}$	Constant used to calculated particle deformation time	-
A_n	Nozzle outlet section / Area of flow (outflow function)	m ²
c_p	Specific heat capacity	J/kgK
C_d	Discharge coefficient	-
c_{pD}	Specific heat capacity of deposit	J/kgK
c_{pS}	Specific heat capacity of substrate	J/kgK
d_d	Droplet diameter	m
$d_{d,0}$	Droplet diameter with cold gas	m
d_f	Frequency of the Doppler burst	Hz
d_m	Mean particle diameter	m
$d_{50,3}$	Mass median particle diameter	m
D_l	Liquid stream diameter	m
h	Heat transfer coefficient	W/m ² K
h_0^*	Non-dimensional specific enthalpy	-
h_{surf}^*	Dimensionless enthalpy of deposit surface	-
K	Constant to calculate the mass median particle diameter (Lubanska equation)	-

Symbol	Description	Unit
m	Constant for melt mass flow calculation	-
\dot{M}_G	Gas mass flow rate	kg/h
$\dot{M}_{G,0}$	Gas mass flow rate cold gas	kg/h
\dot{M}_L	Melt mass flow rate [kg/h]	kg/h
n	Constant for melt mass flow calculation	-
p_{Asp}	Aspiration pressure	Pa
p_G	Atomizing gas pressure	Pa
p_{chamber}	Over pressure in the melting crucible	Pa
Q_3	Cumulative mass distribution (volume-based)	-
Re	Reynolds number	-
s	Substrate thickness	m
Sa	Arithmetical mean height	m
t	Time	s
t_d	Droplet deformation time	s
T_0	Ambient gas temperature	°C
T_d	Particle temperature	°C
T_D	Deposit surface temperature	°C
$T_{D,0}$	Deposit surface temperature with cold gas	°C
T_G	Gas temperature (hot gas)	°C
$T_{G,0}$	Gas temperature with cold gas atomization	°C
T_{liq}	Liquidus temperature	°C
T_M	Melt temperature	°C

Symbol	Description	Unit
T_s	Substrate temperature	°C
T_{sol}	Solidus temperature	°C
T_{∞}	Ambient temperature	°C
u_g	Gas velocity	m/s
u_{gl}	Gas velocity at impact with liquid melt stream	m/s
u_l	Liquid stream velocity	m/s
u_{rel}	Relative velocity	m/s
V	Volume	m ³
v_d	Particle velocity	m/s
$v_{d,0}$	Particle velocity with cold gas	m/s
$v_{d,m}$	Mean particle velocity	m/s
v_s	Translational velocity of the substrate	m/s
v_r	Rotational speed of substrate	rps
y	Deposit thickness	m
z	Spray distance	m

Symbol	Description	Unit
Greek Letters		
α	Deposition angle	$^{\circ}$
λ	Wave length	m
ν_g	Kinematic viscosity of the gas	m^2/s
ν_l	Liquid kinematic viscosity or melt droplet kinematic viscosity	m^2/s
ρ	Fluid density	kg/m^3
ρ_D	Density of deposit material	kg/m^3
ρ_s	Density of substrate material	kg/m^3
ρ_l	Liquid density or melt droplet density	kg/m^3
ρ_g	Gas density	kg/m^3
σ	Stefan-Boltzmann constant	-
σ_l	Liquid surface tension or melt droplet surface tension	N/m
δ	Relative density	-
Δh	Change of specific enthalpy	J
ΔH	Change of enthalpy	J/kgK
ΔT	Temperature difference	$^{\circ}\text{C}$
ΔT_D	Change of deposit surface temperature	$^{\circ}\text{C}$
θ	Doppler shift angle	$^{\circ}$
ψ_{max}	Outflow function	-
\varnothing_n	Pouring nozzle diameter	m
\varnothing_s	Substrate diameter	m

Symbol	Description	Unit
Abbreviations		
CCA	Close-coupled atomizer	-
CCD	Charge-coupled device	-
CFD	Computational fluid dynamics	-
DTT	Ratio of deposit surface temperature and solidus temperature	-
EDX	Energy-Dispersive X-Ray Spectroscopy	-
FFA	Free-fall atomizer	-
<i>GMR</i>	Gas-to-melt mass flow ratio	-
HG	Hot gas atomization	-
LDA	Laser Doppler anemometry	-
PDA	Phase Doppler anemometry	-
RRSB	Rosin-Rammler-Sperling-Bennet	-
RT	Atomization at ambient / room temperature	-
SDAS	Secondary dendrite arm spacing	-
SEM	Secondary Electron Microscopy	-
$T_{D,avg}$	Local average deposit surface temperature	°C
$T_{D,max}$	Maximum deposit surface temperature	°C
$T_{S,max}$	Maximum substrate temperature	°C
We_g	Gas Weber number	-
We_l	Liquid Weber number	-

Figures

Figure 1-1:	Samples from spray-formed steel tube produced by a close-coupled atomizer.	3
Figure 2-1:	Comparison of conventional cast and spray-formed (rapidly solidified) FeTiB ₂ (HMS = High Modulus Steel) a) microstructure as-casted, b) microstructure as-sprayed, and c) stress-strain curves. The figure is adopted from [SPRI17].	5
Figure 2-2:	Schematic diagram of the spray forming set up (PA7 at University of Bremen) with a close-coupled atomizer for steel. The figure is adopted from [HUSS20a].	7
Figure 2-3:	Schematic a) annular atomizer b) multi jet atomizer with melt and gas exits.	12
Figure 2-4:	Schematic diagram of a) free-fall atomization, b) close-coupled atomization. The figures are adopted from [CIFT20].	12
Figure 2-5:	Typical particle size distributions with free-fall atomizer (FFA) and close-coupled atomizer (CCA) for CuSn6 for identical gas pressure ($p_G = 1.6$ MPa).	13
Figure 2-6:	Process video images showing the melt building up at the nozzle due to flow separation for the given nozzle geometries as well as for a) cold and b) hot gas conditions. The figure is adopted from [SCHW17].	15
Figure 2-7:	Aspiration pressure at the melt pouring nozzle exit (without melt in cold condition) for CCA (CD-CCA-0.8) nozzles at cold gas and hot gas conditions. The figure is adopted from [SCHW17].	15
Figure 2-8:	Gas mass flow rate for a CCA as a function of atomization gas pressure and temperature. HG ($T_G \sim 300$ °C) and RT ($T_G \sim 20$ °C) stand for hot gas atomization and atomization at ambient temperature. Measured (meas.) and calculated (calc.) gas mass flow rates at ambient temperature are compared with gas mass flow rates at elevated gas temperatures. Argon was used as process gas. The figure is adopted from [CIFT20].	17
Figure 2-9:	The mass median particle diameter $d_{50,3}$ of $\{(Fe_{0.6}Co_{0.4})_{0.75}B_{0.2}Si_{0.05}\}_{96}Nb_4$ powders as a function of a) melt mass flow rate, b) gas-to-melt mass flow ratio (GMR). The averaged hot gas temperatures and gas mass flow rates are listed. The lines serve only as visual guides. An increased GMR and gas temperature result in smaller $d_{50,3}$ values. [CIFT20].	18
Figure 2-10:	Cold and hot porosity in spray-formed deposits. The figure is adopted from [UHLE14].	20
Figure 2-11:	Relative density of different alloys in the as-sprayed condition [MCHU08a].	21

Figure 2-12	a) Schematic formation of rough surface and shadowing effect by higher impact angle (deposition angle) [HU00], b) porosity of spray-formed rings (material: IN718) as a function of impact angle α [UHLE07a]. 22
Figure 2-13	Influence of the average liquid fraction in the spray on the average porosity in the spray-formed tubes and billets [WARN97]. The figure is adopted from [HENE17]. 23
Figure 2-14	Influence of substrate temperature and impact speed on the deformation behaviour of droplets during impact (tin on stainless steel substrates [DHIM05]). 25
Figure 2-15	Influence of the deposit surface temperature on the porosity of spray-formed rings (Ni based alloy). The figure is adopted from [UHLE07a]. . 26
Figure 2-16	Effect of the dimensionless enthalpy of deposit surface on porosity of Al-bronze, Sn-bronze and nitriding steel (adapted from [MEYE14]). 27
Figure 2-17	Spray-formed a) tubular deposit of AISI 52100 (100Cr6) tool steel, b) porosity distribution in deposit thickness, c) cross-section of the ring segment with hot porosity (gaseous) in the deposit center and cold porosity in the vicinity of the substrate. The figure is adopted from [BUCH03, GRAN17]. 29
Figure 2-18	a) Temperature distribution through the longitudinal section of a tubular preform (AISI 52100), b) cooling behaviour at different regions in the deposit. The figure is adopted from [CUI05b]. 29
Figure 2-19	Calculated fraction of overspray for coating of thin tubes with a conventional free-fall-atomizer [ELLE14]. 30
Figure 2-20	a) Effect of spray distance on yield of tubular deposits by close-coupled atomizer (alloy: Cu-15.5wt%Sn), b) rough deposit surface at short spray distance; c) and d) higher porosity in the vicinity of the substrate. e) better surface at long spray distance, f) and g) lower porosity in the vicinity of the substrate. D – substrate diameter, p – atomization gas pressure. The figures are adopted from [ELLE14]. 31
Figure 2-21	Porosity in tubular deposit a) interfacial porosity in bimetallic spray-formed tube [ZEPO16], b) interfacial crack in cladding of two dissimilar steels [LEE18]. The figures are adopted from [ZEPO16] and [LEE18]. . 32
Figure 2-22	PDA results in copper (Cu) spray with a free-fall atomizer in the deposition zone. The figure is adopted from [ZIES03] in [KHAT17]. 34
Figure 2-23	Particle size, velocity and temperature measurement in metal droplet spray a) comparison of pyrometer (DPV-2000) and PDA, b) influence of the different alloys. The figures are adopted from [KRAU02]. 35
Figure 3-1:	Graphical outline of the course of the thesis. In the PhD dissertation a close-coupled atomizer is adopted to spray form tubular deposits. The smaller droplet size by a close-coupled atomizer influence the porosity. Hot gas introduction reduces the droplet size and increase the droplet

	velocity, which further reduce the deposit surface temperature and the droplet deformation time. With faster droplet deformation highly dense materials can be produced at lower temperatures. (T_G – gas temperature, \dot{M}_G – gas mass flow rate, d_d – droplet diameter at hot gas, v_d – droplet velocity at hot gas, t_d – droplet deformation time at hot gas, T_D – deposit surface temperature at hot gas, Δh – specific enthalpy change, subscript 0 means cold gas atomization condition).	38
Figure 4-1:	Overview of the used methodology and experimental procedure in this PhD thesis.....	41
Figure 4-2:	Line-scan range of the pyrometer and position of thermocouples in the substrate. The figure is adapted from [HUSS20a].....	45
Figure 4-3:	Arrangement and measuring principle of Laser Doppler Anemometer (LDA) in back scattering arrangement. The figure is adopted from [DANT20].....	46
Figure 4-4:	Schematic diagram of LDA particle velocity measurement (back scattering arrangement) in the spray chamber. The figure is adopted from [HUSS20b].....	47
Figure 4-5:	a) Photo and (b) contour of a spray-formed tubular AISI 52100 steel deposit (PA7-230).	47
Figure 4-6:	a) Ring of a spray-formed tubular deposit (GMR: 1.6, atomization gas temperture: RT, PA7-170); b) ring segment before macro-etching; c) after macro-etching. Micrographs are taken at three positions (P1, P2 and P3). P1 is near the outer surface, P2 is at the deposit core and P3 is near the inner surface. The figures are adopted from [HUSS20a].....	48
Figure 4-7:	Schematic diagram of scanning white-light interferometer.	49
Figure 4-8:	Porosity in terms of surface area in deposit thickness direction from substrate to outer surface ($GMR = 1.6$, PA7-170). The figure is adapted from [HUSS20a].....	50
Figure 4-9:	Measuring principle of laser diffraction analysis of metal powders.....	52
Figure 5-1:	Micrographs of the representative tubular AISI 52100 deposit spray-formed with a) close-coupled atomizer (CCA) and b) free-fall atomizer (FFA). Here, PA7 is the atomization setup name and the three digit number is designated for individual run number.....	54
Figure 5-2:	Porosity distribution of tubular AISI 52100 steel deposits spray-formed with close-coupled atomizer (CCA) and free-fall atomizer (FFA). Deposit section taken from deposit start position measured by image analysis (measurement field: $\sim 370 \mu\text{m} \times 370 \mu\text{m}$). The process parameters with Exp. ID is listed in the Appendix (Table A1). * Data from Cui et al. [CUI04] for comparison.....	55
Figure 5-3:	Micrographs of the spray-formed tubular AISI 52100 deposit (Run 3 (PA7-170)/ GMR: 1.6) with a close-coupled atomizer, before and after	

	etching. The positions are same as Figure 4-6. The figure is adopted from [HUSS20a].	58
Figure 5-4:	a) Porosity distribution of tubular AISI 52100 (100Cr6) steel deposits spray-formed under different process conditions with a close-coupled atomizer; b) enlarged area of the porosity profile 0% - 5%. Two samples were taken from each run. The first one is from deposit start position and the second one is from deposit end position. The figure is adopted from [HUSS20a].	60
Figure 5-5:	Porosity versus deposit longitudinal distance at Run 2 (PA7-169, GMR of 1.1 at deposit start and GMR of 1.3 at deposit end). a) mean porosity in the vicinity of the substrate and melt mass flow rate (calculated); b) thickness of the porous layer (with porosity > 0.5%) in the vicinity of the substrate. The figure is modified and reprinted from [HUSS20a].	61
Figure 5-6:	Adhered spherical particles on the substrate near deposition zone (PA7-232).	61
Figure 5-7:	Pressure difference in the melt during atomization by close-coupled atomizer.	62
Figure 5-8:	Relationship between the gas-to-melt ratio (<i>GMR</i>) and the mean porosity in the vicinity of the substrate at deposit start positions of spray-formed tubular 52100 deposits with close-coupled atomizer. The figure is adopted from [HUSS20a].	63
Figure 5-9:	a) Substrate temperature at position T1, T2, T3, and, T4 (Run 3/PA7-170). The end of deposition means end of melt flow. b) For comparison of the temperature profiles, the time at the maximum substrate temperature is set to zero ($T_{S,max} = 0$ s). The figures are adopted and modified from [HUSS20a].	65
Figure 5-10:	Deposit surface temperature at position T1, T2, and T3 (Run 3/PA7-170). For comparison of the temperature profiles, the time at the maximum deposit surface temperature is set to zero ($T_{D,max} = 0$ s). The figure is adopted from [HUSS20a].	66
Figure 5-11:	Maximum deposit surface temperature $T_{D,max}$ versus deposit thickness y for spray forming of tubes with a close-coupled atomizer. The figure is adopted from [HUSS20a].	67
Figure 5-12:	Maximum deposit surface temperature $T_{D,max}$ versus gas-to-melt ratio <i>GMR</i> at similar wall thickness y . In this figure the data from Figure 5-11 with similar wall thickness y is plotted. The figure is adopted from [HUSS20a].	68
Figure 5-13:	a) Deposit surface cooling rate versus deposit thickness; b) deposit surface cooling rate versus <i>GMR</i> (at similar wall thickness); c) maximum substrate temperature versus deposit thickness; d) maximum substrate temperature versus <i>GMR</i> ; e) ratio of maximum deposit surface	

	temperature versus ratio of deposit thickness and substrate thickness. The figures are adopted from [HUSS20a].....	69
Figure 5-14:	Grain size versus a) local average deposit surface temperature, b) GMR of spray-formed tubular AISI 52100 deposits with close-coupled atomizer. The figure (a) is adopted from [HUSS20a].	70
Figure 5-15:	a) Porosity in relation to the deposit surface temperature during spray forming (GMR: 1.1 – 1.9, Run 1 – Run 5); b) enlarged area of the porosity profile. The black dots are taken from the deposit start positions and the red pluses are taken from the deposit end positions. The figure is adapted from [HUSS20a].....	72
Figure 5-16:	Comparison of the experimental and the model maximum deposit surface temperatures for AISI 52100 steel.	74
Figure 5-17:	Numerical results of gas velocity at different atomization gas temperatures. a) Image of gas velocity distribution in spray chamber with atomization gas pressure of 1.6 MPa; and gas velocity and gas mass flow rate as a function of atomizing gas temperature with atomization gas pressure of 0.8 MPa (b) and 1.6 MPa (c). Simulation data from [HUSS22] performed by L. Buss.	77
Figure 5-18:	Correlation between the gas mass flow rate and the melt mass flow rate at different atomization gas temperature. A linear model is estimated based on the experimental results (Run H1 to H13).	79
Figure 5-19:	a) Particle (size fraction 0 – 200 μm) size distribution as accumulated mass percentage distribution, b) oxygen and nitrogen content at different atomizing gas temperature T_G of 316L stainless steel (size fraction of 20 – 63 μm), c) particle size distribution of size fraction 20 – 63 μm . The figures are adopted from [HUSS20b].	80
Figure 5-20:	SEM images of the atomized AISI 316L stainless steel particles (size fraction 20 – 63 μm), a) at atomization gas temperature T_G of 20 °C; b) at atomization gas temperature T_G of 330 °C with close-coupled atomizer.	81
Figure 5-21:	Mean particle size $d_{m,RRSB}$ at different atomizing gas temperatures (T_G – 20 °C, 300 °C, and 600 °C) a) at different gas pressures; b) at different gas mass flow rates. The particle size distributions are estimated by RRSB-functions from the experimental results (PA7-258 and PA7-189). Particle size distribution calculated by L. Buss.	81
Figure 5-22:	a) Particle trajectory in the gas jet (CFD simulation). Mean particle velocity measured with LDA and simulation of single particle b) as a function of atomizing gas pressure p_G , c) as a function of gas mass flow rate \dot{M}_G with cold gas at RT (293 K) and with hot gas at ~300 °C (573 K) (AISI 52100 steel powders, size fraction of 63 to 90 μm) at $z = 130$ mm. The figures are adopted from [HUSS20b] simulation data by L. Buss. ...	83

Figure 5-23:	Calculated mean velocity of the AISI 52100 particles at different atomizing gas temperatures T_G (20 °C, 300 °C, and 600 °C); a) at $p_G = 0.6$ MPa, b) at $p_G = 0.8$ MPa, and c) at $p_G = 1.0$ MPa in the spray forming zone of the atomization chamber. Simulation by L. Buss.	84
Figure 5-24:	a) Calculated mean particle velocity $v_{d,m}$ versus the atomization gas temperature T_G (20 °C, 300 °C, and 600 °C) at different gas pressures p_G (0.6 MPa, 0.8 MPa, and 1.0 MPa) at a distance $z = 130$ mm from the nozzle (deposition zone); b) particle deformation time t_d at different atomization gas temperatures T_G (20 °C, 300 °C, and 600 °C) and gas pressures p_G (0.6 MPa, 0.8 MPa, and 1.0 MPa) at the deposition zone. Simulation by L. Buss.	85
Figure 5-25:	Calculated mean particle temperatures of the AISI 52100 particles at different atomizing gas temperatures T_G (20 °C, 300 °C, and 600 °C); a) at $P_G = 0.6$ MPa, b) at $P_G = 0.8$ MPa, and c) at $P_G = 1.0$ MPa in the spray forming zone of the atomization chamber. Simulation by L. Buss.	86
Figure 5-26:	Calculated mean particle cooling rates of the AISI 52100 particles at different atomizing gas temperatures T_G (20 °C, 300 °C, and 600 °C); a) at $P_G = 0.6$ MPa, b) at $P_G = 0.8$ MPa, and c) at $P_G = 1.0$ MPa in the spray forming zone of the atomization chamber, and d) relationship between particle cooling rate and atomization gas temperature. Simulation by L. Buss.	87
Figure 5-27:	Calculated mean enthalpy change of the AISI 52100 spray at different atomization gas temperatures T_G (20 °C, 300 °C, and 600 °C) and atomization gas pressures ($P_G = 0.6, 0.8$, and 1.0 MPa) in the spray forming zone ($z = 130$ mm) of the spray chamber. Simulation by L. Buss.	88
Figure 5-28:	a) Deposit thickness y versus maximum deposit surface temperature $T_{D,max}$, b) gas mass flow rate \dot{M}_G versus melt flow rate \dot{M}_L in spray forming with a CCA in cold gas atomization ($T_G = RT$, GMR: 1.2 – 1.5) and hot gas atomization ($T_G = 280 \pm 30$ °C, GMR: 1.0 – 1.4). The figures are adopted from [HUSS20b].....	90
Figure 5-29:	a) Deposit surface at two different deposit surface temperatures for different atomizing conditions; b) relationship between the maximum deposit surface temperature $T_{D,max}$ with the deposit surface roughness (S_a). Surface roughness measured by white light interferometry. The figures are reprinted from [HUSS20b].....	90
Figure 5-30:	Ring segment of the deposit a) polished un-etched (P1 is near the outer surface, P2 is at the deposit center and P3 is neat to the substrate), b) etched at P2 region (pearlitic microstructure); c) magnified image at P1, P2 and P3 areas of the deposits (Run H5/PA7-232 at HG and Run H6/PA7-228 at RT). The figures are adopted from [HUSS20b].	92
Figure 5-31:	Mean porosity of deposit sections from the vicinity of the substrate to the outer surface. Two samples are taken from Run H5/PA7-232 and	

	Run H6/PA7-228 (Run H5 at $T_G = 300\text{ }^{\circ}\text{C}$ and Run H6 at $T_G = \text{RT}$). The figures are adopted from [HUSS20b].	93
Figure 5-32:	Relationship between average grain size and local average deposit surface temperature (Run H1 to Run H7). At hot gas (HG) atomization $T_G = 280 \pm 30\text{ }^{\circ}\text{C}$, GMR: 1 to 1.4 and at cold gas atomization $T_G = 20\text{ }^{\circ}\text{C}$, GMR: 1.2 to 1.5. The figure is modified reprinted from [HUSS20b].	94
Figure 5-33:	Mean porosity of deposit sections as a function of average grain size from the vicinity of the substrate to the outer surface. At hot gas (HG) atomization $T_G = 250 - 310\text{ }^{\circ}\text{C}$, GMR: 1 to 1.4 and at cold gas atomization $T_G = 20\text{ }^{\circ}\text{C}$, GMR: 1.2 to 1.5. The figure is reprinted from [HUSS20b].	95
Figure 5-34:	Relative density δ of the spray-formed deposits in relationship to the local deposit surface temperature $T_{D,avg}$ for cold gas ($T_G = 20\text{ }^{\circ}\text{C}$, GMR: 1.2 to 1.5) and hot gas atomization ($T_G = 280 \pm 30\text{ }^{\circ}\text{C}$, GMR: 1 to 1.4) in the deposit center areas. The porous regions in the vicinity of the the substrate and in the deposit surface zone are excluded. The process parameters can be found in Table A-5. The figure is reprinted from [HUSS20b].	96
Figure 5-35:	Effect of substrate pre-heating on the porosity in the vicinity of the substrate. Substrate heating with hot N_2 gas from the atomizer. Samples taken 20 mm away from the deposit starting end (start position).	98
Figure 5-36:	Mean porosity of deposit sections as a function of average grain size from the vicinity of the substrate to the outer surface for hot gas (HG) $T_G = 290 \pm 40\text{ }^{\circ}\text{C}$, GMR: 0.8 to 1.4 and cold gas atomization $T_G = 20\text{ }^{\circ}\text{C}$, GMR: 1.1 to 1.5. Process parameters in Appendix (Table A-5a and 5b).	99
Figure 5-37:	Relationship between relative density δ and local deposit surface temperature $T_{D,avg}$ of the spray-formed deposits via cold gas ($T_G = 20\text{ }^{\circ}\text{C}$, GMR: 1.1 to 1.2) and hot gas atomization ($T_G = 330\text{ }^{\circ}\text{C}$, GMR: 0.8 to 0.9) in the deposit center areas. Process parameters are listed in the Appendix (Table A-5). The porous regions near the substrate and in the deposit surface zone are excluded.	100
Figure 5-38:	Comparison of the experimental and the model relative density in the deposit center for AISI 52100 steel. Process parameters can be found in Appendix (Table A-5). The porous regions near the substrate and in the deposit surface zone are excluded.	101
Figure 5-39:	Schematic diagram of the spray forming set up (tilting crucible technique, SK-2/PA9 at University of Bremen) of tubular deposit with a close-coupled atomizer for Al-alloys.	104
Figure 5-40:	a) spray-formed deposit, b) deposit segment at the deposit end (Run A2/PA9-824). P1 is in the vicinity of the substrate, P2 is at the deposit center, and P3 is near the outer surface.	105

Figure 5-41:	Magnified images of the un-etched polished deposit segment in P1, P2 and P3 areas (Run A2_End_PA9-824). In the vicinity of the substrate (P3 area) the pores are irregular shape (mainly cold porosity), the deposit center (P2 area) is almost pore free. At the surface region (P1 area) circular hot pores are observed.	105
Figure 5-42:	Optical micrograph of etched (see Table 4-4) samples in different positions. All the samples show equiaxed uniform grain structure.	106
Figure 5-43:	Intermetallic phases of Al-6082 alloy a) as-casted material shows complex-shaped larger intermetallic phases [MORW09]; b) and c) as-sprayed materials shows uniformly distributed smaller intermetallic phases; d) etched microstructure show larger intermetallic phases are at grain boundaries and smaller intermetallic phases are dispersed within the grain.	107
Figure 5-44:	a) Porosity distribution of tubular deposits (Al-5083 and Al-6082) spray-formed under different process conditions using a close-coupled atomizer; b) enlarged area of the porosity profile 0% – 5%. Two samples are taken from each run. The first sample is taken from the deposit start position and the second one is taken from the deposit end position (Figure 5-40).	108
Figure 5-45:	a) Average grain size of the spray-formed deposit at near substrate region, center region and near surface region, b) relationship between deposit thickness and average grain size.	109
Figure 5-46:	Deposit thickness versus a) calculated maximum deposit surface temperature and b) DTT for Al-alloys tubular deposits.	110
Figure 5-47:	Mean porosity versus calculated DTT for Al-alloys (Al-5083 and Al-6082).	111
Figure A-1:	Atomization facility at the University of Bremen (PA7).	131
Figure A-2:	Measurement of particle velocity in the spray chamber with cold particles (size fraction 63 – 90 μm) inside of the spray chamber (PA5).	131

Tables

Table 2-1	Process parameters in spray forming process of tubular deposits.	8
Table 2-2	Comparison between free-fall and close-coupled atomizers.	14
Table 4-1	Nominal chemical composition of AISI 52100 (100Cr6).	44
Table 4-2	Nominal chemical composition of AISI 316L (Fe – balance)	44
Table 4-3	Nominal chemical composition of spray-formed Al alloys in wt.% (Al – balance).	44
Table 4-4	List of etching solutions and conditions for different materials.	50
Table 4-5	Error in adopted measurement techniques.	52
Table 5-1	Key process parameters varied in section 5.1.	53
Table 5-2	Key process parameters varied in section 5.2.	56
Table 5-3	Grain size at different spray forming condition in spray-formed tubular AISI 52100 deposits.	57
Table 5-4	Process parameters related to the maximum deposit surface temperature.	73
Table 5-5	Key process parameters varied in section 5.3.	76
Table 5-6	Key process parameters varied in section 5.3.4.	89
Table 5-7	Effect of hot gas atomization on key parameters/factors by CCA compared to FFA.	102
Table 5-8	Key process parameters varied in section 5.4.	103
Table A-1	Process parameters and results of the spray forming experiments with CCA and FFA (section 5.1, Alloy: AISI 52100).	132
Table A-2	Process parameters and results of the spray forming experiments with CCA (Alloy: AISI 52100).	133
Table A-3	LDA parameters for mean particle velocity measurement.	134
Table A-4	Process parameter for atomized powder at different gas temperatures with CCA (Alloy: AISI 316L).	134
Table A-5	Process parameters and results of the spray forming experiments with hot gas and cold gas and cold gas (CCA, Alloy: AISI 52100)... ..	135
Table A-6	RRSB parameters used in the numerical set-up.	137
Table A-7	Process parameters used in the numerical set-up.	137

Table A-8	Materials properties for spray-formed alloys.....	137
Table A-9	Process parameters for spray forming runs for spray forming of Al-alloys.....	138

List of Publications

- [1] Hussain, S.; Cui, C.; Temple, N.; Uhlenwinkel, V.; Mädler, L.: Porosity and microstructure of steel tubes spray-formed by close-coupled atomizer, Journal of Materials Processing Technology 276 (2020) 116407
<https://doi.org/10.1016/j.jmatprotec.2019.116407>
- [2] Hussain, S.; Cui, C.; He, L.; Mädler, L.; Uhlenwinkel, V.: Effect of hot gas atomization on spray forming of steel tubes using a close-coupled atomizer (CCA), Journal of Materials Processing Technology 282 (2020) 116677
<https://doi.org/10.1016/j.jmatprotec.2020.116677>
- [3] Yao, D.; Hussain, S.; Buss, L.; Uhlenwinkel, V.; Fritsching, U.: Numerical investigation of the heat transfer of an atomizer gas jet impinging perpendicular on a circular cylinder, International Journal of Thermal Sciences 176 (2022) 107531
<https://doi.org/10.1016/j.ijthermalsci.2022.107531>
- [4] Hussain, S.; Buss, L.; Yao, D.; Fritsching, U.; Uhlenwinkel, V.: Droplet velocity and thermal state from hot gas atomization of steel melt: Impact on the quality of the spray-formed tubular deposit, Advanced Powder Technology 33(6) (2022) 103640
<https://doi.org/10.1016/j.appt.2022.103640>

Student contributions

The following students have contributed by some of their experimental support, results analysis and discussions. None of the students have officially submitted any thesis according to the FB04 Production Engineering, University of Bremen student regulations. Reference [1] has been treated according to the Faculty of Engineering's Co-op Program at the University of Alberta, Edmonton, Canada. References [2,3] worked as student research assistant under SFB 1232, TP:1. Their contributions are gratefully acknowledged.

- [1] Temple, N.; Porosity analysis of spray-formed steel tubes using two-dimensional image analysis. University of Alberta Co-op Program, December 2017.
- [2] Kamrujjaman, M.; Student research assistant, SFB – 1232, University of Bremen, June 2018 to July 2020.
- [3] Das, R.; Student research assistant, University of Bremen, April 2021 to September 2021.

Declaration

I hereby declare, that I have written this PhD thesis on my own and have not used any other but the mentioned tools. Those works or text passages which have been included word by word or by content accordingly from other sources have been indicated.

Hiermit erkläre ich, dass ich die vorliegende Dissertation selbständig verfasst und keine anderen als die angegebenen Hilfsmittel verwendet habe. Die den benutzten Werken wörtlich oder inhaltlich entnommenen Stellen als solche kenntlich gemacht hat.

Bremen, 20 November 2022

.....

(signature)